UNIVERSITÀ DEGLI STUDI DI TORINO

DOCTORAL THESIS

New pieces in the radio galaxy feedback puzzle

Author:
Ana Jimenez-Gallardo

Supervisors:
Prof. Francesco Massaro
Dr. M. Almudena Prieto

Advisors:
Dr. Eleonora Sani
Dr. Chiara Mazzucchelli

Physics Department

May 31, 2022

Abstract

Radio galaxies lie at the highest extremes of black hole mass among Active Galactic Nuclei (AGN). Therefore, their interaction with their environment, the so-called feedback mechanisms, can greatly impact galaxy evolution. Feedback mechanisms are reflected in the multiphase gas in which radio galaxies are embedded, thus, studying the origin and emission mechanisms responsible for different gas phases can give an overview on how radio galaxies affect their environments. This is the main goal of this Ph.D. research.

More specifically, this work focuses on unveiling the origin and emission mechanisms underlying large-scale (>100 kpc) extended X-ray emission, signatures of radio mode feedback, such as ionized gas filaments and X-ray cavities, and optical extended emission-line regions (EELRs), as well as on studying how radio jets affect the gas surrounding radio galaxies.

To improve our understanding of the multiphase gas surrounding radio galaxies, I carried out multiwavelength analyses focused on a radio and X-ray comparison for emission at larger scales (>100 kpc), and on optical and X-ray comparisons for smaller scales (<100 kpc). Additionally, I took advantage of the vast suite of observations already available for the revised version of the Third Cambridge Catalog of radio sources (3CR) at all frequencies. In particular, the 3CR catalog was chosen since it is a paramount tool to study the physics of the most powerful radio sources.

Firstly, I carried out the X-ray analysis of the 9 last 3CR sources with optical counterparts of the 3CR *Chandra* Snapshot Survey, a campaign dedicated to completing the X-ray coverage of the 3CR sample. This sample covers the highest redshift range of the survey, with $1.5 < z < 2.5$. The analysis consisted in the comparison of X-ray *Chandra* and radio Very Large Array (VLA), images to detect X-ray counterparts of radio cores and lobes, and extended X-ray emission possibly associated with thermal radiation of the intracluster medium (ICM). Thus, I detected X-ray counterparts of 7 radio cores and of radio lobes in 6 out of the 9 sources.

To unveil the origin of large-scale extended X-ray emission surrounding radio galaxies, I carried out an X-ray analysis of the *Chandra* images of 35 3CR radio galaxies with FR II radio morphologies. Large-scale extended X-ray emission could be due to either thermal, non-thermal processes, or a mixture of both. In the first scenario, whenever a source is part of a galaxy cluster, the thermal radiation from the intracluster medium (ICM) could explain the observed extended X-ray emission. Contrary, extended X-ray emission can also be dominated by non-thermal radiation when it is due to inverse Compton scattering of cosmic microwave background photons (IC/CMB) from radio lobes. Additionally, I aimed at understanding how extended X-ray emission affects the detection of the X-ray counterparts of radio hotspots. I found extended X-ray emission surrounding ~90 % of sources in the sample, with ~71 % of them mostly explained by IC/CMB from lobes, while ~17 % appear to be dominated by thermal emission from ICM. Lastly, while carrying out this analysis, I discovered X-ray extended emission at ~446 kpc of 3CR 103 and at ~128 kpc of 3CR 4303, which could indicate the presence of merging galaxy groups/clusters. Nevertheless, future optical spectroscopic observations are needed to verify this hypothesis.

At smaller scales, I carried out a dedicated analysis of the ionized gas spatially associated with X-ray features in radio galaxies harbored in cool core galaxy clusters, signatures

of radio mode feedback. Firstly, I studied the spatial association of ionized gas and cold X-ray filaments in 3CR 318.1. Then, I analyzed the spatial association of ionized gas with an X-ray cavity in 3CR 196.1. Both of these features were studied by carrying out joint analyses of MUSE and *Chandra* observations. Regarding the filaments in 3CR 318.1, I concluded that they most likely originated from the cooling of AGN-driven outflows due to their alignment with the radio jets and their low optical velocity dispersion. Additionally, the dominant mechanism underlying the filamentary emission is a combination of photoionization due to star formation, self-ionizing cooling ICM, and a contribution of ionization due to shocks. Then, regarding 3CR 196.1, the multiwavelength analysis revealed the possible presence of ionized gas filling an X-ray cavity. While ionized gas filaments are typically found surrounding X-ray cavities, finding ionized gas filling an X-ray cavity is a rare occurrence. I conclude that this ionized gas spatially associated with an X-ray cavity could preferentially be explained either by different episodes of AGN activity or by the cooling of AGN outflows.

Lastly, I extended previous analyses of ionized gas in 3CR 318.1 and 3CR 196.1 to a sample of 15 3CR radio sources. Thus, I carried out an analysis of MUSE and *Chandra* observations to study the origin and emission mechanisms of EELRs surrounding radio galaxies and associated with small-scale diffuse X-ray emission. The sample included High-Excitation Radio Galaxies (HERGs), Low-Excitation Radio Galaxies (LERGs), and Broad-Line Radio Galaxies (BLRGs). I found similar morphologies of optical EELRs and the X-ray emission associated with them, as previously reported in the literature. Additionally, when comparing [O III]λ5007 and soft X-ray fluxes, I found a trend for HERGs, suggesting a common origin of optical and X-ray emission, which I conclude is most likely nuclear photoionization. On the other hand, I found a trend for LERGs and BLRGs with optical to X-ray flux ratios suggesting a higher ionization state than that of HERGs. This, in turn, could imply some contribution of ionization due to jet-driven shocks. Nevertheless, the trend found for LERGs and BLRGs needs to be taken with caution since (i) it is mostly based on upper limits for [O III]λ5007 fluxes, (ii) the current sample only includes 4 LERGs and 3 BLRGs, (iii) thermal X-ray ICM emission can be detected surrounding all LERGs and most BLRGs in the sample, which could influence the measured X-ray fluxes. This last point could have arisen due to LERGs and BLRGs in our sample having X-ray observations with significantly longer exposure times than HERGs. Thus, further optical observations of LERGs and more uniform X-ray observations for LERGs and HERGs will be needed to verify different origins of their EELRs.

This works highlights different aspects of the gas surrounding radio galaxies, the study of which is crucial to understanding feedback processes and, therefore, galaxy evolution. Although a complete picture has not been achieved yet, this work is further proof of the major progress that multifrequency observations of samples such as the 3CR catalog can provide. However, it also evidenced how the statistics of current studies on powerful radio galaxies are hindered by the number of objects in the 3CR catalog. Thus, the next step to improving our understanding of powerful radio galaxies will be the creation of an equivalent catalog to the 3CR, but including sources in the southern hemisphere, the G4Jy-3CRE. Such a catalog will provide the community with the statistics needed to verify and refine results achieved through the 3CR catalog. Additionally, listing sources in the southern hemisphere will allow the whole catalog to be observed with state-of-the-art and upcoming astronomical facilities, such as ALMA, VLT, ELT, or SKA.

Guidelines to the reader

This thesis is mostly based on original results either published or submitted to peer-refereed journals.

In *Chapter One*, I present an introduction to active galactic nuclei, with emphasis on the radio galaxies, the focus of this work. The current understanding of feedback processes in radio galaxies, i.e., how radio galaxies interact with their environment, is also included. Lastly, I present the Third Cambridge Catalog, the sample of radio sources used throughout this work.

In *Chapter Two*, I summarize the radiative processes responsible for the emission of radio galaxies at different wavelengths. This summary includes the description of synchroton radiation, inverse Compton scattering and thermal bremsstrahlung. This chapter concludes with the description of emission line regions in radio galaxies.

Chapter Three, the last introductory chapter, collects all information regarding observations used throughout this work, including descriptions of the main characteristics of LOFAR, VLA, VLT/MUSE and *Chandra*. Additionally, I briefly introduce archival resources used to carry out this work. Lastly, data reduction and analysis procedures followed are also described.

Chapter Four is dedicated to the analysis of *Chandra* observations of the highest redshift 3CR sources, with special emphasis on the detection of X-ray counterparts of radio structures.

Chapter Five collects the analysis of the large-scale soft X-ray emission surrounding FR II radio galaxies with no counterpart at GHz frequencies, as detected during the 3CR *Chandra* Snapshot Survey. The origin of this extended emission, whether thermal or non-thermal, is discussed. Lastly, the nuances of hotspot detection against this extended X-ray emission are also exposed.

Chapter Six collects the analyses of 3CR 318.1 and 3CR 196.1 aimed at understanding the origin and emission mechanisms underlying different gas phases. These multi-wavelength analyses exemplify two different radio mode feedback manifestations, gas filaments and X-ray cavities.

Chapter Seven is dedicated to the *Chandra*-MUSE analysis of a sample of 16 radio sources to establish the ionization mechanisms underlying extended optical emission line regions and its link with small-scale soft X-ray emission in radio galaxies.

Lastly, *Chapter Eight* is dedicated to conclusions of previous chapters.

List of publications

1. **A. Jimenez-Gallardo**, E. Sani, F. Ricci, C. Mazzucchelli, B. Balmaverde, F. Massaro, A. Capetti, W. R. Forman, R. P. Kraft, G. Venturi, M. Gendron-Marsolais, M. A. Prieto, A. Marconi, H. A. Peña-Herazo, S. A. Baum, C. P. O'Dea, L. Lovisari, R. Gilli, E. Torresi, A. Paggi, V. Missaglia, G. R. Tremblay, B. J. Wilkes, & G. Miley, *The cavity of 3CR 196.1: Hα emission spatially associated with an X-ray cavity"*, 2022, ApJ, submitted.

2. B. Balmaverde, A. Capetti, R. D. Baldi, S. Baum, M. Chiaberge, R. Gilli, **A. Jimenez-Gallardo**, A. Marconi, F. Massaro, E. Meyer, C. ODea, G. Speranza, E. Torresi, & G. Venturi, *"The MURALES survey. VI. Properties and origin of the extended line emission structures in radio galaxies"*, 2022, A&A, 662, A23.

3. V. Missaglia, F. Massaro, E. Liuzzo, A. Paggi, R. P. Kraft, W. R. Forman, **A. Jimenez-Gallardo**, J. P. Madrid, F. Ricci, C. Stuardi, B. J. Wilkes, S. A. Baum1, C. P. O'Dea, J. Kuraszkiewicz, G. R. Tremblay, A. Maselli, A. Capetti, E. Sani, B.Balmaverde, & D. E. Harris, *"Hidden treasures in the unknown 3CR extragalactic radio sky: a multi-wavelength approach"*, 2021, ApJS, 255, 18.

4. **A. Jimenez-Gallardo**, F. Massaro, B. Balmaverde, A. Paggi, A. Capetti, W. R. Forman, R. P. Kraft, R. D. Baldi, V. H. Mahatma, C. Mazzucchelli, V. Missaglia, F. Ricci, G. Venturi, S. A. Baum, E. Liuzzo, C. P. O'Dea, M. A. Prieto, H. J. A. Röttgering, E. Sani, W. B. Sparks, G. R. Tremblay, R. J. van Weeren, B. J. Wilkes, J. J. Harwood, P. Mazzotta, & J. Kuraszkiewicz, *"Raining in MKW 3 s: A Chandra-MUSE Analysis of X-Ray Cold Filaments around 3CR 318.1"*, 2021, ApJL, 912, L25.

5. **A. Jimenez-Gallardo**, F. Massaro, A. Paggi, R. D'Abrusco, M. A. Prieto, H. A. Peña-Herazo, V. Berta, F. Ricci, C. Stuardi, B. J. Wilkes, C. P. O'Dea, S. A. Baum, R. P. Kraft, W. R. Forman, C. Jones, B. Mingo, E. Liuzzo, B. Balmaverde, A. Capetti, V. Missaglia, M. J. Hardcastle, R. D. Baldi, & L. K. Morabito, *"Extended X-Ray Emission around FR II Radio Galaxies: Hot Spots, Lobes, and Galaxy Clusters"*, 2021, ApJS, 252, 31.

6. **A. Jimenez-Gallardo**, F. Massaro, M. A. Prieto, V. Missaglia, C. Stuardi, A. Paggi, F. Ricci, R. P. Kraft, E. Liuzzo, G. R. Tremblay, S. A. Baum, C. P. O'Dea, B. J. Wilkes, J. Kuraszkiewicz, W. R. Forman, & D. E. Harris, *"Completing the 3CR Chandra Snapshot Survey: Extragalactic Radio Sources at High Redshift"*, 2020, ApJS, 250, 7.

7. F. Massaro, A. Capetti, A. Paggi, R. D. Baldi, A. Tramacere, I. Pillitteri, R. Campana, **A. Jimenez-Gallardo**, & V. Missaglia, *"Deciphering the Large-scale Environment of Radio Galaxies in the Local Universe. II. A Statistical Analysis of Environmental Properties"*, 2020, ApJS, 247, 71.

8. **A. Jimenez-Gallardo**, F. Massaro, A. Capetti, M. A. Prieto, A. Paggi, R. D. Baldi, R. Grossova, L. Ostorero, A. Siemiginowska, & S. Viada, *"COMP2CAT: hunting compact double radio sources in the local Universe"*, 2019, A&A, 627, A108.

Acknowledgements

This work would not have been possible without the tireless efforts of my supervisor, Francesco Massaro. You are always thinking about my future and ten steps ahead of everyone. Without you, I would not have had half the wonderful experiences I lived these past years and I would have visited quite a few less continents. From discussing science and inspiring me with your contagious enthusiasm for everything you do, to telling anecdotes and jokes, you were, without a doubt, an outstanding supervisor that I hope will keep being one of my closest collaborators. I would like to thank Almudena Prieto, who made this opportunity possible and whose discussion was able to give me a different view on my research.

A great part of this work would not have been possible without the help, knowledge and support of Eleonora Sani and Chiara Mazzucchelli, that I got to experience thanks to the ESO studentship. Both of you are among the kindest and most talented people that I know. I will be forever grateful for all the chats we shared, your trust in my decisions and your efforts to make my stay in Chile one of the best years in my life. Together with all the friends I made at ESO, you made me feel right at home and I consider myself incredibly lucky for having met you.

I was fortunate enough to have conversations with some of the brightest and kindest people in the field. Among all these people I would like to highlight Bill Forman, Ralph Kraft and Raffaele D'Abrusco, who hosted me at CfA and provided me with invaluable discussions that enriched my work immensely, Alessandro Paggi, who was always there to help me and teach me and who is always full of fun facts, Alessandro Capetti, whose didactic approach to discussions I always appreciated, and Barbara Balmaverde, who provided me with the chance to work with MUSE data and discover a new aspect of radio galaxies that I love. I truly believe that my work would be nothing like it is today without all of you. Working with you has truly been a pleasure and I hope we keep collaborating in projects to come.

During these past years I had the pleasure of meeting some of my greatest friends, who kept me sane through the hard days. In particular I would like to thank Harold Peña-Herazo, for always being there for a coffee and a chat, Romana Grossová, for forcing me to go past my comfort zone, Raniere de Menezes, for all your jokes that proved memorable at schools, Valentina Missaglia, for always being there to show me cat pictures, Alejandro Santamaría, for your constant banter and teasing, and Francesca Lucertini, for making me the official Cocò. All of you made these years go by in a flash and I cannot wait to see you again.

I would also like to thank my sister and all my "non-coworker" friends, specially Pablo Quiles, María García, and Miriam Rodríguez, for always being there for me. You made me laugh when times got the hardest, kept me present when I wanted to avoid everything, and were always there even when I was not at my best. Lastly, I want to thank my parents. You have always believed in me more than I do and have taught me to push myself further than I ever thought possible. I was extremely fortunate to be born in a house full of love, with parents that taught me the value of kindness, hard work and modesty, and, for that I will be forever grateful.

Contents

Chapter 1

Introduction

1.1 Active Galactic Nuclei

Active galactic nuclei (AGN) constitute the most powerful, long-lived sources in the Universe. They are located at the center of galaxies and their emission often outshines that of their host galaxies. AGN have a broad range of luminosities (from $\sim 10^{40}$ to 10^{47} erg s^{-1}), exceeding by at least two orders of magnitude the typical luminosities of regular galaxies. Additionally, in contrast with non-active galaxies whose emission is mostly restricted to the UV, optical, and infrared, AGN emit across the whole electromagnetic spectrum. These differences imply that AGN emission cannot be explained by nuclear reactions on their own, as in non-active galaxies, and, thus, the introduction of a much more efficient emission mechanism is needed.

Nowadays, the emission mechanism generally accepted as responsible for the AGN emission is the accretion of material onto a Super-Massive Black Hole (SMBH; $\gtrsim 10^6$ M$_\odot$) at the center of the host galaxy. This accretion onto a black hole results in the conversion of a fraction of the gravitational potential of the accreted matter into luminosity. Thus, assuming that the black hole accretion rate is $\dot{M}_{acc}$, the bolometric luminosity emitted due to accretion is:

$$L_{bol} = \eta \dot{M}_{acc} c^2 \tag{1.1}$$

with c the speed of light and η the efficiency of the conversion of the gravitational potential into radiation. Since the potential energy U of an element of mass m_{acc} being accreted into the black hole at a distance r is given by:

$$U = \frac{G\, m_{acc}\, M_{BH}}{r} \tag{1.2}$$

where M_{BH} is the black hole mass, the luminosity yielded by this energy will be:

$$L_{bol} \simeq \frac{dU}{dt} = \frac{G\, \dot{m}_{acc}\, M_{BH}}{r} \tag{1.3}$$

Thus, comparing equations 1.1 and 1.3, the accretion efficiency is:

$$\eta \simeq \frac{G\, M_{BH}}{r c^2} = \frac{R_S}{2r} \tag{1.4}$$

with R_S being the Schwarzschild radius. Assuming the distance r at which most of the optical continuum is expected to be $r = 5R_S$ (Peterson 1997), the efficiency of the accretion is ~10%. This efficiency makes the accretion of material onto a black hole the most efficient astrophysical energy source and the only one able to reproduce the luminosities observed in AGN.

Therefore, black hole accretion rates deeply affect the evolution of AGN and their environments. In particular, if material is being accreted at such a rate that radiation pressure dominates above gravity, part of such material will be expelled by radiative-driven outflows, thus, effectively self-regulating the accretion rate. The limit at which the free-fall of material, F_{grav}, is counteracted by radiative pressure, F_{rad}, is known as "Eddington limit":

$$F_{rad} = F_{grav} \Rightarrow \frac{L_{Edd}\sigma_T}{4\pi r^2 c} = \frac{GM_{BH}m_p}{r^2} \tag{1.5}$$

where L_{Edd} is the luminosity emitted by a source accreting at the Eddington limit and σ_T is the Thomson cross-section. Therefore:

$$L_{Edd} = \frac{4\pi c G M_{BH} m_p}{\sigma_T} \simeq 1.3 \cdot 10^{38} \frac{M_{BH}}{M_\odot} \text{ erg s}^{-1} \tag{1.6}$$

The accretion rate associated to the Eddington luminosity, i.e., the Eddington accretion rate is defined as:

$$\dot{M}_{Edd} = \frac{L_{Edd}}{\eta c^2} \tag{1.7}$$

Lastly, the Eddington ratio, defined as:

$$\lambda = \frac{L_{bol}}{L_{Edd}} \tag{1.8}$$

is related to the relative accretion rate of an AGN.

AGN can deeply impact their environments either by removing material from them through black hole accretion, or by depositing material and energy in their environments through jets or outflows. The interactions of AGN and their environments are known as feedback processes and they will be discussed in detail in § 1.3.3.

1.1.1 The AGN zoo: classes and observational properties

Since AGN are observed in a broad range of frequencies, they were originally classified differently in different bands. Nevertheless, the two broader classification schemes were developed on the basis of their radio emission and of their optical/UV spectra.

On the basis of their radio emission, AGN are often classified as radio-loud or radio-quiet. While in radio-loud AGN the emission is mostly dominated by jets/lobes, the jet/lobe emission from radio-quiet AGN can be neglected. Traditionally, this distinction is made according to the radio-loudness parameter, R, which is given by the ratio of the radio flux at 5 GHz and the optical flux in the B band. Thus, radio-loud AGN are those with $R \geq 10$ (Kellermann et al. 1989). However, in recent years, this classification is being abandoned in favor of a more physically based classification, i.e., the presence or absence of strong relativistic jets. Thus, following this new scheme, AGN can be classified as "jetted" or "non-jetted" (see e.g., Padovani 2017).

On the basis of their optical/UV emission lines, AGN can be classified as:

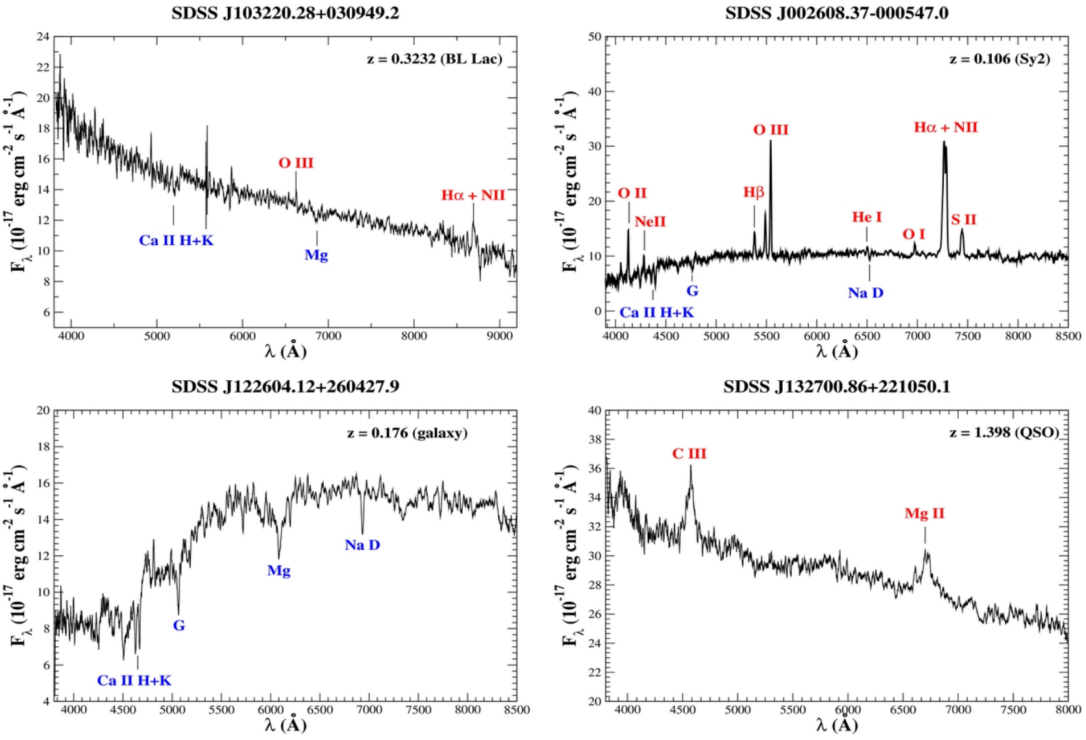

Figure 1.1: Examples of different AGN spectra, including a blazar (top-left), a Seyfert (top-right), a QSO (bottom-right), and a non-active galaxy (bottom-left). Main emission (red) and absorption (blue) spectral features seen are marked in each case.

- **Type I or broad-line AGN** (see bottom-right panel of Fig. 1.1), which show broad ($FWHM > 3000$ km s^{-1}) emission lines in their optical spectra.
- **Type II or narrow-line AGN** (see top-right panel of Fig. 1.1), which lack broad emission lines, only showing narrow optical components.
- **Type 0 or blazars** (see top-left panel of Fig. 1.1), which lack any strong emission or absorption features in their optical spectra.

However, the most widely used classification of AGN includes:

1. **Seyfert galaxies:** Although the first Seyfert galaxies were seen as peculiar emission lines in different nebulae at the beginning of the 1900s (Fath 1909, Slipher 1917, Hubble 1926, Humason 1932 and Mayall 1934), they were not established as such until 1943 by Carl Keenan Seyfert. With $L_{bol} < 10^{46}$ erg s^{-1} and absolute B magnitude $M_B > -23$, Seyfert galaxies are radio-quiet AGN characterized by strong optical emission lines. These emission lines can be either permitted broad lines together with permitted and forbidden narrow lines (Seyfert 1), or only narrow lines (Seyfert 2; see top-right panel of Fig. 1.1), as firstly discovered in 1974 by Khachikian and Weedman. Their host galaxies are predominantly early-type spirals (Sargent 1970, Green 1976, Adams 1977, Heckman 1978, Simkin et al. 1980, Yee 1983, MacKenty 1990, Kotilainen & Ward 1994 and Xanthopoulos 1996).
2. **Quasi-Stellar Objects (QSOs):** The first QSO was discovered by Schmidt in 1963 as a "stellar-like" object associated with the radio source 3C 273. Other QSOs

where shorty detected (see e.g., Greenstein 1963), including those with no radio emission associated (see e.g., Sandage et al. 1965 and Schmidt 1966), as well as the first $z \sim 2$ QSO (Sandage et al. 1965). More powerful than Seyfert galaxies (with $L_{bol} > 10^{46}$ erg s^{-1} and $M_B < -23$), they have star-like morphologies and emission lines similar to those of Seyfert 1 galaxies (see bottom-right panel of Fig. 1.1). According to their radio power, they can either be radio-quiet or radio-loud (also known as Quasars).

3. **LINERs:** Low Ionization Nuclear Emission Regions, as firstly described by Heckman (1980), show spectra similar to Seyfert 2 galaxies, but with faint ionization lines. As it is the case of Seyferts, LINERs are radio-quiet AGN whosehosts are also often early-type spirals.

4. **Blazars:** Originally, the only type of blazars thought to exist were BL Lac, compact, flat-spectrum radio sources with violent flaring activity and featureless optical spectra (Strittmatter et al. 1972). However, this classification was extended after the discovery of BL Lac-like objects with broad spectral lines (see Moore & Stockman 1981 and Impey & Tapia 1988). Nowadays, blazars are identified as radio-loud AGN that present rapid optical variability and highly polarized emission. They constitute the largest population of gamma-ray sources. An example of the spectrum of a BL Lac is shown in the top-left panel of Fig. 1.1)

5. **Radio galaxies:** Radio sources were detected for the first time during the 1940s (see e.g., Jansky 1933, Reber 1944, Hey et al. 1946 and Bolton 1948), however, these objects were not established as extragalactic until the discovery of the optical counterpart of Cygnus A by Baade & Minkowski (1954a,b). Although fainter than QSOs, radio galaxies are referred to as the radio-loud counterpart to Seyfert galaxies due to their optical spectra. A large percentage of these objects show jets and resolved radio structures. They also differ from Seyfert galaxies in their hosts, since radio galaxies tend to be hosted in giant elliptical galaxies (see Capetti et al. 2017a,b). However, similarly to Seyferts, radio galaxies can be classified into Broad-Line radio galaxies (BLRGs) and Narrow-Line radio galaxies (NLRGs). These objects are the focus of this Ph.D. research and are discussed in detail in following sections.

A summary of this classification is shown in Fig. 1.2.

1.1.2 The unification scenario of active galaxies

Despite the varied taxonomy presented, most of this variety can be explained, at zero-order, by an orientation-based unified model. This model, firstly presented in works such as Lawrence (1987), Antonucci et al. (1993) and Urry & Padovani (1995), is based on the idea that most differences observed in AGN are due to observing different AGN components at different viewing angles. The unified model relies on the presence of a dusty toroidal structure surrounding the accretion disk that blocks our view of the central AGN. A schematic representation of this model is shown in Fig. 1.3. According to this model, the components of an AGN are:

- **Accretion disk and hot corona:** Material accreting into the black hole forms a disk known as accretion disk. The accretion disk surrounding the SMBH can either be geometrically-thin, optically-thick, and radiatively efficient (as proposed by

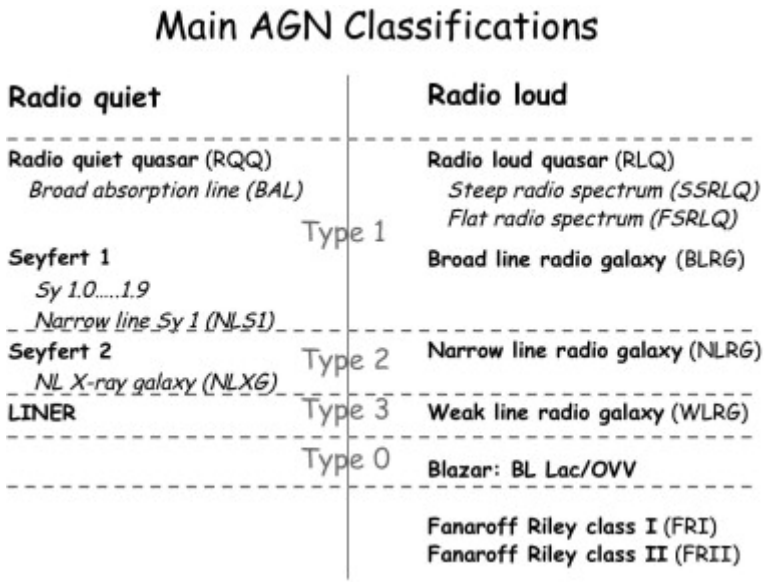

Figure 1.2: Schematic representation of main AGN radio and optical classifications taken from Tadhunter (2008).

Shakura & Sunyaev 1973 for luminous and normal AGN), or geometrically-thick, optically-thin, and less efficient (also known as an advection-dominated accretion flow or ADAF, as proposed by Narayan & Yin 1994 for low-luminosity AGN). Located at sub-parsec scales, this component is responsible for the thermal continuum emission observed in UV and optical. Then, Liang (1979) proposed the presence of a hot corona (T $\sim 10^7$ K) made of relativistic, non-thermal electrons, which has been proposed to be located above and below the SMBH. Photons from the accretion disk will then be scattered by electrons in the hot corona through Inverse Compton scattering (see Chapter 2), explaining part of the X-ray emission observed in AGN, particularly in radio-quiet AGN.

- **Broad Line Region (BLR):** A population of dense (n_e $\sim 10^{10}$ cm^{-3}) gas clouds at a distance of 0.01 - 0.1 pc from the SMBH, with velocity dispersion in the order of thousands of km s^{-1} (see Peterson 2006 for a review). This region is responsible for the broad permitted lines observed in the optical spectra of some AGN.

- **Dusty torus or obscuring structure:** A region of dusty molecular gas situated at scales of 1 to tens of pc. This region absorbs part of the photons from the accretion disk, corona, and BLR and re-emits them as thermal infrared emission. However, part of the emission due to previous components also escapes along the polar axis of the torus. Although the presence of a dusty torus was introduced by Antonucci et al. (1993) to explain the type I/II AGN dichotomy, current works have been able to obtain images of tori in Seyfert/LINER galaxies with spatial resolutions below 10 pc (see Combes et al. 2019).

- **Narrow Line Region (NLR):** A lower density (n_e $\sim 10^3$ - 10^6 cm^{-3}) population of gas clouds at 0.1 - 1 kpc from the SMBH, with velocity dispersions on scales of the hundreds of km s^{-1}. These clouds are ionized by the emission escaping along the polar axis of the dusty torus, originating narrow forbidden and permitted optical

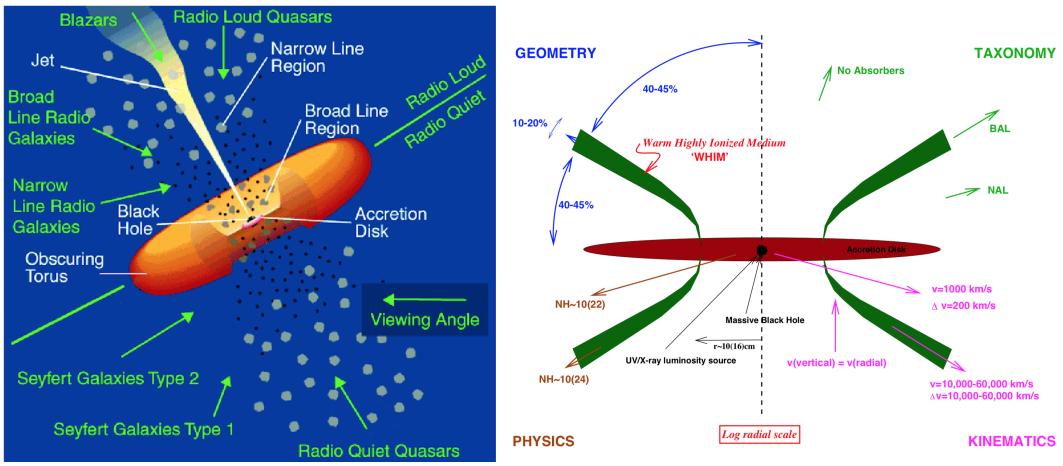

Figure 1.3: Schematic drawings of the unification scheme of AGN from Urry & Padovani (1995) (left) and Elvis (2000) (right). Left panel shows the structure of an AGN, as well as the type of AGN seen depending on the viewing angle. Right panel shows the spectroscopic appearance of the source, outflowing gas velocities, and typical column densities of the gas according to the angle of the observer's line of sight. Components in the images are not to scale.

emission lines (see e.g., Ferland & Osterbrock 1986 and Capetti et al. 1996 for works on NLRs).

- **Large-scale radio structures:** Apart from the previously discussed components, radio galaxies also show large-scale radio structures such as jets or lobes. These components are described in detail in § 1.2.

Following this scheme, whenever an AGN is observed edge-on, the dusty torus obscures the accretion disk, the corona, and the BLR, and the only features observed are narrow lines due to the NLR, typical of type 2 AGN (Seyfert 2 galaxies, NLRGs, and QSOs). However, if the torus presents some inclination with respect to the line of sight, both the BLR and the NLR are visible and, therefore, sources are seen as type 1 AGN (Seyfert 1 galaxies, BLRGs, and QSOs). Lastly, if the axis of the torus is aligned with the line of sight, face-on nuclei and jets are observed and, due to relativistic beaming effects, the observed spectra will be dominated by non-thermal jet emission, as it is the case for blazars. A schematic view of the unification scenario is shown in Fig. 1.3.

1.2 Focusing on radio galaxies

Throughout this thesis, I focus on radio galaxies, which lie at the highest extremes of the black hole mass and Eddington ratio distributions of AGN.

1.2.1 The historical radio classification

In 1974, Fanaroff & Riley proposed a classification scheme for radio galaxies with large-scale radio structures that is still the most used nowadays. This classification is based on the morphology of the extended structures of radio galaxies at 178 MHz, in particular,

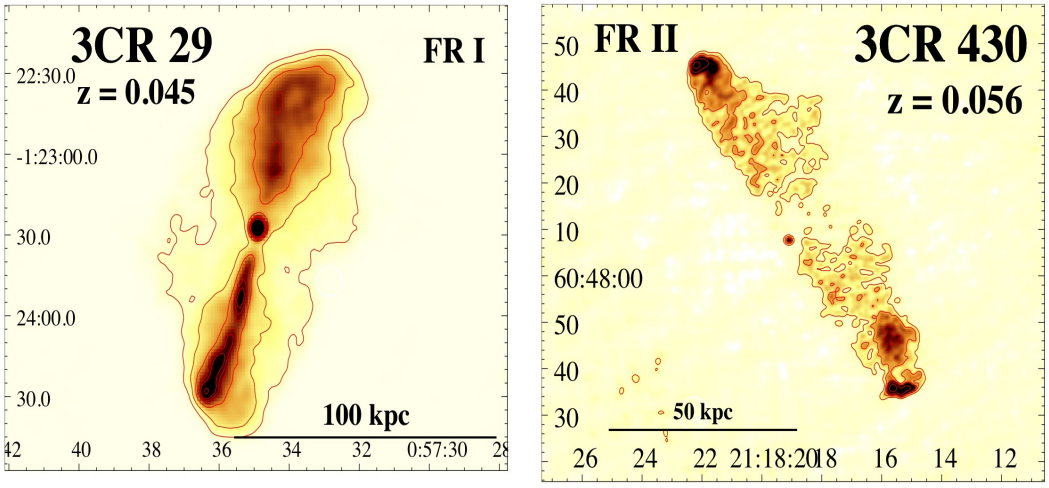

Figure 1.4: 4.8 GHz radio maps of radio galaxies with typical FR I (left) and FR II (right) radio morphologies, following the classification scheme introduced by Fanaroff & Riley (1974).

on the ratio R_{FR} of the distance between the highest surface brightness peaks on opposite sides of the host galaxy to the total extent of the radio emission. According to this classification, there are two main classes of radio galaxies:

- **FR I or edge-darkened**: radio galaxies with $R_{FR} < 0.5$. Their radio luminosity decreases along the jets, which typically end in diffuse lobes or extended emission. An example of a radio galaxy with a typical FR I radio morphology is 3CR 29, shown in the left panel of Fig. 1.4.

- **FR II or edge-brightened**: radio galaxies with $R_{FR} < 0.5$. Their radio luminosity increases along the jets or lobes, which typically show hotspots at their edges. An example of a radio galaxy with a typical FR II radio structure is 3CR 430, shown in the right panel of Fig. 1.4.

Fanaroff & Riley (1974) also discovered a link between this morphological classification and the total radio power, with FR Is being typically less powerful at 178 MHz than FR IIs. Additionally, Ledlow & Owen (1996) showed that the FR I to FR II division appears even sharper when comparing the hosts' optical luminosity and their total radio power. Nevertheless, this division disappears when including lower luminosity radio galaxies (see, e.g., Best 2009, Lin et al. 2010, Wing & Blanton 2011 and Capetti et al. 2017b).

This radio galaxy classification is often associated with Mpc-scale environments, i.e., whether radio galaxies are isolated or reside in galaxy groups/clusters. In particular, works such as Zirbel (1997) reported richer environments surrounding FR I radio galaxies than FR II. A more in-depth discussion on the topic of radio galaxy environment is presented in § 1.3.

Apart from the traditional FR I/FR II division, further morphological classifications arose in the last decades to include more varied morphologies, including wide-angle tailed radio galaxies (Owen & Rudnick 1976 and O'Donoghue et al. 1990), hybrid radio sources (Gopal-Krishna & Wiita 2000), and compact radio galaxies (Ghisellini et al. 2011, Sadler et al. 2014 and Baldi et al. 2015).

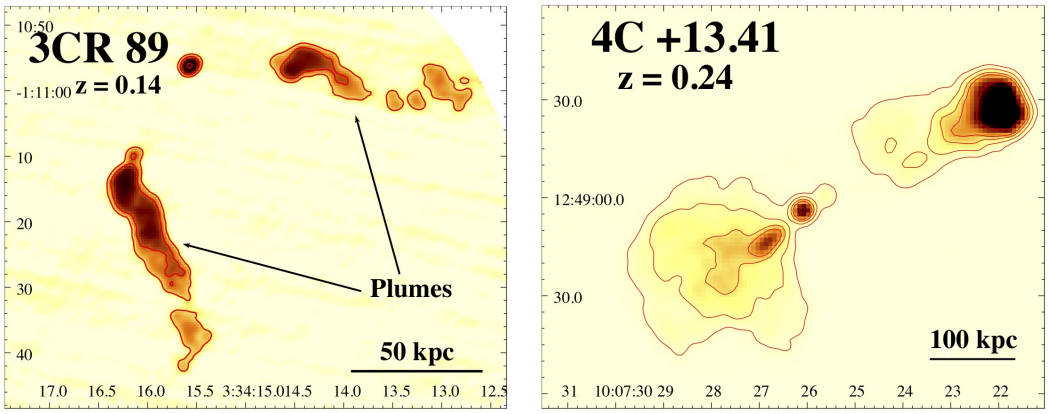

Figure 1.5: Left: 1.4 GHz radio map of the wide-angle tail 3CR 89. WATs often display diffuse radio lobes known as plumes. Right: 1.4 GHz radio map of the HYMOR 4C +13.41. Its western lobe is edge-brightened, while it eastern lobe is edge-darkened.

Wide-angle tailed radio galaxies or WATs, observed for the first time by Owen & Rudnick (1976), are radio galaxies with curved radio structures. Their jets are well collimated on kpc scales, flaring further away into diffuse plumes. WATs are typically found in rich environments. An example of a radio galaxy with a WAT radio morphology is 3CR 89, shown in the left panel of Fig. 1.5.

Later on, Gopal-Krishna & Wiita (2000) introduced a new classification for those radio galaxies in which each radio lobe presents a different FR morphology. They proposed to call these radio galaxies "HYbrid MOrphology Radio Sources" or HYMORS. An example of a HYMOR is 4C +13.41, shown in the right panel of Fig. 1.5. Additionally, they proposed that these different lobe morphologies in the same source could be explained by differences in their environments instead of in the SMBH activity.

Lastly, Ghisellini et al. (2011) started using the term "FR 0" as a way to link the population of low luminosity (10^{20-22} W Hz^{-1} at 1.4 GHz) sources with FR I radio morphologies described by Baldi & Capetti (2009) to the FR morphological classification. Apart from their lower radio luminosities, sources with FR 0 radio morphologies are also characterized by a lack of extended features above a few kpc.

1.2.2 An optical perspective: HERGs *vs.* LERGs

Apart from the traditional radio classification of radio galaxies, Laing et al. (1994) introduced a new classification based on the ratios of optical emission lines, as firstly noticed by Hine & Longair (1979). Thus, Laing et al. (1994) introduced Low Excitation Radio Galaxy (LERG) and High Excitation Radio Galaxy (HERG) classes. Typical LERG and HERG optical spectra are shown in Fig. 1.6. Later on, Buttiglione et al. (2010) established clearer criteria to distinguish between these sub-classes with:

$$-1 \lesssim \log([\mathrm{O\ III}]/\nu L_{178\,\mathrm{MHz}}) \lesssim 0.5, \text{ for HERGs,}$$
$$-2 \lesssim \log([\mathrm{O\ III}]/\nu L_{178\,\mathrm{MHz}}) \lesssim -0.5, \text{ for LERGs.}$$

Additionally, all HERGs appear to be associated with bright radio galaxies with FR II radio morphologies, while LERGs can have either FR I or FR II radio morphologies, with

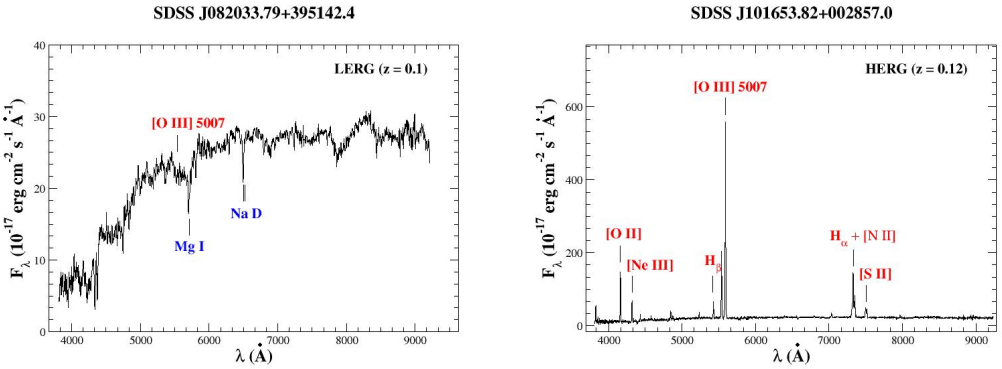

Figure 1.6: Examples of typical LERG (left) and HERG (right) spectra from Jimenez-Gallardo et al. (2019).

any radio luminosity. The difference between HERGs and LERGs seems to lie in differences in their accretion mechanisms, with HERGs accreting cold gas at high rates and LERGs accreting hot gas at low rates (see e.g., Hardcastle et al. 2007a, Buttiglione et al. 2010 and Best & Heckman 2012).

1.2.3 The radio structure: jets, hotspots, and lobes

The main components found in radio galaxies are core, jets, lobes, jet knots, and hotspots. An example of these components is shown in the 4.8 GHz radio map of Cygnus A in Fig. 1.7. Radio emission of most of these components is thought to be synchrotron radiation due to the spectral shape and the polarization of their emission. Details on the synchrotron emission are collected in Chapter 2.

Radio core

Radio cores are bright compact (with sizes below a few parsecs) structures coincident with the nucleus of the host galaxy, believed to be the synchrotron self-absorbed bases of jets (see Chapter 2). Radio galaxy cores are characterized by flat radio spectra due to the convolution of the synchrotron spectra from progressively larger regions along the expanding jet that have progressively lower turnover frequencies (see Blandford & Königl 1979).

Jets

Jets are structures that extend from the radio core, often in pairs, and appear to trace the path of collimated outflows from the central AGN. Nevertheless, the production mechanism of the jets is still disputed (see Blandford et al. 2019 for a review). Following the definition of Bridle (1986), jets are defined as features at least four times as long as they are wide and distinguishable from other extended components. Some radio galaxies can show surface brightness peaks either along the jet or at the jet termination. Whenever these surface brightness peaks are situated along the jet, they are known as **"jet knots"**, while if they are situated at the jet termination, they are called **"hotspots"**. Historically,

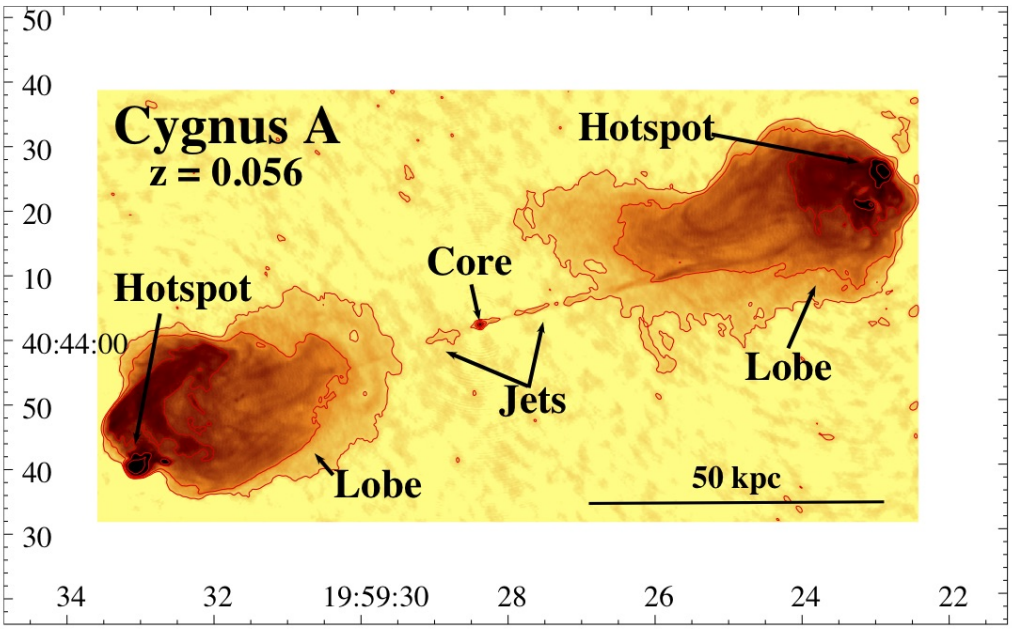

Figure 1.7: 4.8 GHz radio map of Cygnus A showing the main components that can be found in a radio galaxy: core, jets, lobes, and hotspots.

jets have been classified as either being "strong-flavored" (i.e., with projected magnetic fields parallel to the jet axis and average opening angles $< 5°$) or "weak-flavored" (i.e., with large opening angles, $> 8°$, and projected magnetic fields perpendicular to the jet), as defined by Bridle (1992).

Radio lobes

Radio lobes are extended regions of diffuse radio emission, on scales of tens of kpc, whose edge is mostly well-defined and with intensity tending to zero toward it. As revealed from in-depth studies of well-known radio lobes (such as those of Cygnus A, by Perley et al. 1984, or 3C 353, by Swain et al. 1996), radio lobes tend to have steep radio spectra ($\alpha > 0.7$, see Chapter 2) and filamentary structures.

Plumes are diffuse radio lobes, such as those observed in radio galaxies with WAT radio morphologies, as shown in the left panel of Fig. 1.5.

Hotspots

Hotspots were defined by Leahy (1993) as surface brightness peaks at the jet termination with no significant diffuse radio emission beyond them and detected above ten times the rms noise level at frequencies above ~1 GHz. Hotspots are also relatively "compact" (i.e., enclosed in circular regions of ~2-4″ radius) and distinct from radio lobes. They are thought to be associated with the re-acceleration of high-energy particles (see e.g., Hardcastle et al. 2007b). Compact surface brightness peaks that are not situated at the jet termination are known as "jet knots".

1.3 Where radio galaxies are born, grow and die

Interactions between radio galaxies and their environment are often invoked to explain different radio galaxy morphologies. One of the clearer examples is the hypothesis of radio galaxies with FR I radio morphologies inhabiting denser environments than those with FR II radio morphologies to explain the disruption of their jets (see e.g., Bicknell 1994 and Laing & Bridle 2008). Other widely accepted examples include explaining the bending of jets in narrow-angle tail radio galaxies as the consequence of ram pressure (see e.g., Sakelliou & Merrifield 200 and Blanton et al. 2015), or explaining the difference in the two lobes in HYMORS as differences in the environment on opposite sides of the radio galaxy (see e.g., Harwood et al. 2020). Thus, the environment of radio galaxies can yield important clues to the origin of different radio morphologies. Additionally, jets deposit most of their energy at kpc-scales, being their large-scale environment a key factor in the feedback processes responsible for their triggering and fueling. The main evidence of these interactions can be seen in the multiphase gas haloes radio galaxies are embedded in, including the hot plasma of the intracluster medium (ICM) and the warm ionized gas in Extended Emission Line Regions (EELRs).

1.3.1 The environment of radio galaxies at kpc scales

In the last decades, several optical campaigns revealed the presence of EELRs in radio galaxies (see e.g., Baum et al. 1988), similar to those found in Seyfert galaxies (see e.g., Fosbury 1986, van Breugel et al. 1986, Stockton & MacKenty 1987). These EELRs, traced by ionization lines such as [O II], [O III], Hα and [N II], extend on scales of a few tens of kpc and have been proven to be spatially associated with diffuse soft X-ray emission, which suggests a link between their origin (see e.g., Bianchi et al. 2006, Massaro et al. 2009a, Hardcastle et al. 2010, 2012, McDonald et al. 2010, 2012 and Balmaverde et al. 2012). One of the best examples of this link can be seen in 3CR 171 and 3CR 305, shown in Fig. 1.8.

There is still no consensus on the dominant ionizing mechanism responsible for EELRs in radio galaxies. The most likely origins of EELRs are either nuclear photoionization or ionization due to jet-driven shocks of cold extranuclear gas that could potentially have been accreted into the elliptical host from a gas-rich companion (see e.g., Baum & Heckman 1989 and Tadhunter et al. 1998).

However, there is also a fraction of radio galaxies with EELRs surrounded by multiphase gas halos. This is the case of those radio galaxies that are hosted by brightest cluster galaxies (BCGs) of cool core clusters (i.e., galaxy clusters with low central entropy, decreasing central temperatures, and short central cooling times, see Hudson et al. 2010). These multiphase halos of gas, known as ICM are composed of a mix of hot plasma at a temperature of several keV ($\sim 10^7$ K), warm ionized and neutral gas (at $\sim 10^4$ K, often forming filaments), and cold ($\sim$10 K) molecular gas clouds. The main hypothesis for the origin of the warm and cold phases is the cooling and condensation of the hot plasma, often in the shape of filaments (see e.g., Gaspari et al. 2017, 2018, Qiu et al. 2020, 2021). One of the most remarkable examples of these filaments can be found in NGC 1275 in the center of the Perseus galaxy cluster (Lynds 1970, Conselice et al. 2001 and Fabian et al. 2008), where ionized gas filaments are spatially associated with an X-ray excess (Fabian et al. 2011). The same situation occurs for other BCGs, where a tight connection between

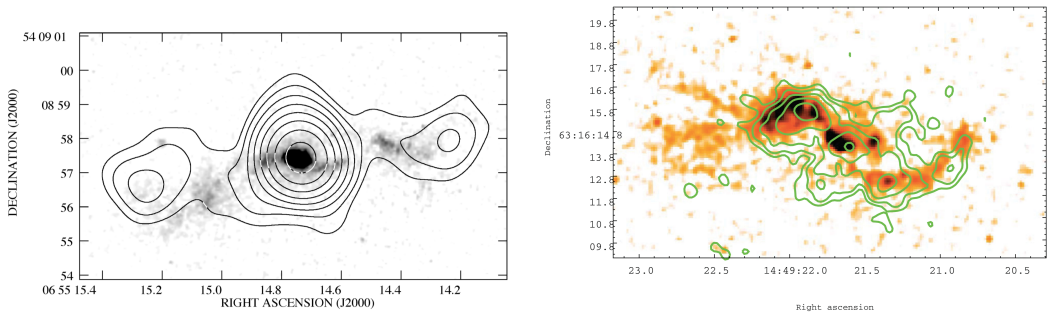

Figure 1.8: [O III] HST image with 0.5 - 5 keV *Chandra* contours of 3CR 171 (left) and 3CR 305 (right), from Hardcastle et al. (2010) and Hardcastle et al. (2012), respectively. These images show the spatial correlation of X-ray emission and the EELRs.

X-ray and optical filamentary emission was found (McDonald et al. 2010).

EELRs are commonly found surrounding X-ray cavities (see e.g., Fig. 1.9, taken from Blanton et al. 2011 and Balmaverde et al. 2018, as well as works by Tremblay et al. 2015 and Olivares et al. 2019), or spatially associated with radio emission whenever the sources lie at higher redshifts (known as the "alignment effect"; see e.g., Fosbury 1986, Hansen et al. 1987, Baum et al. 1988, McCarthy 1988, Baum et al. 1990, Tremblay et al. 2009 and Baldi et al. 2019). Nevertheless, the effect of radio jets in EELRs is not yet fully understood.

1.3.2 Harbouring radio galaxies

A few decades after its creation, the FR classification of radio galaxies was linked to their Mpc-scale environment, with radio galaxies with FR I radio morphologies being found generally more often in groups or galaxy clusters than radio galaxies with FR II radio morphologies (see, e.g., Zirbel 1997). This is supported by a recent work carried out with the LOFAR sample (Mingo et al. 2019) at $z < 0.4$ by Croston et al. (2019), where it was found that radio galaxies with higher 150 MHz radio luminosities tend to inhabit richer environments, in addition to radio galaxies with FR I radio morphologies being found in richer environments than radio galaxies with FR II radio morphologies. However, works by Massaro et al. (2019) and Massaro et al. (2020) showed that, at low-redshift ($z < 0.15$), all radio galaxies, independently of their radio morphology, tend to inhabit galaxy-rich large-scale environments.

Regarding their optical properties, Ineson et al. (2013, 2015) found that LERGs tend to inhabit richer environments than HERGs, with LERGs also showing a strong link between radio luminosity and environmental richness, and HERGs showing no such correlation.

Galaxy clusters where these radio galaxies reside contain large amounts of hot (10^7 - 10^8 K) X-ray emitting ICM. The gas mass of groups ranges from ~10^{12} - 10^{13} $M_\odot$, while it can exceed 10^{14} $M_\odot$ in galaxy clusters (Forman & Jones 1990). In the cases where the galaxy cluster is relaxed (i.e., it has reached dynamic equilibrium) Cavaliere & Fusco-Femiano (1976, 1978) proposed that, if both the ICM and the members of a galaxy cluster respond to the same gravitational potential and assuming an isothermal distribution and spherical symmetry of the gas, the density radial profile of the ICM, ρ_{gas}, follows a "β model":

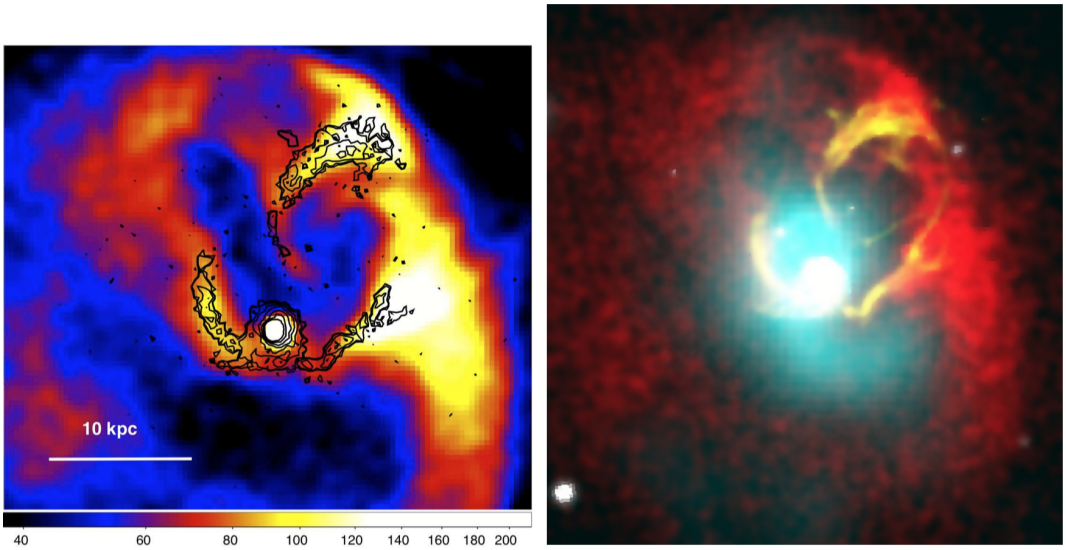

Figure 1.9: Images of the central region of the A2052 galaxy cluster in which Hα filaments are spatially aligned with edges of an X-ray cavity. Left: 0.3 - 10 keV *Chandra* image with Hα contours overlaid taken from Blanton et al. (2011). Right: Composite image from Balmaverde et al. (2018) showing Hα + [N II] filaments in yellow, surrounding an X-ray cavity (*Chandra* X-ray emission is shown in red). Additionally, optical continuum image in the *r*-band from the the Sloan Digital Sky Survey and radio map from the Very Large Array are shown in white and cyan, respectively.

$$\rho_{gas}(r) = \rho_0 \left[1 + \left(\frac{r}{r_c}\right)^2\right]^{-3\beta/2} \tag{1.9}$$

where ρ_0 is the central density, r_c is the core radius of the gas distribution, and the parameter $\beta = \mu m_p \sigma_v^2/(k_B T)$ represents the ratio of the specific energy in galaxies to the specific energy in gas, with μ being the mean molecular mass, σ_v, the galaxy velocity dispersion and T, the gas temperature. Although assuming an isothermal and spherical gas distribution is not often justified, β profiles are still widely used as a first approximation since they can provide radial density profiles from the X-ray surface brightness profile of the ICM (see e.g., Lovisari et al. 2015). ICM thermal emission in the X-rays surrounding 3CR 320 is shown in Fig. 1.10.

1.3.3 Feedback processes: radiative *vs.* kinetic feedback

The interaction of radio galaxies with their environment can play an important role in galaxy evolution by influencing the star formation in their host galaxies. From quenching star formation (negative feedback) by expelling the gas reservoir of the galaxy and preventing it from cooling to outflows enhancing star formation (positive feedback) by compressing the molecular gas, feedback processes can drastically impact galaxy evolution (for a more detailed overview, see reviews by McNamara & Nulsen 2007, Alexander & Hickox 2012 and Morganti 2017). Although positive AGN feedback is thought to be episodic (see e.g., Feain et al. 2007 and Kalfountzou et al. 2017), negative AGN feedback is key to explaining the lack of predicted high-mass galaxies (see e.g., Kormendy & Ho

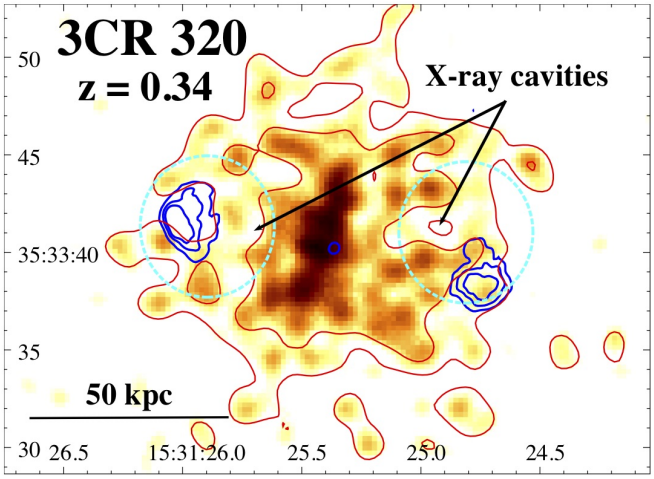

Figure 1.10: 0.5 - 3 keV *Chandra* image of 3CR 320 with 4.8 GHz contours overlaid in blue. The position of the X-ray cavities (firstly reported by Massaro et al. 2013 and studied in detail by Vagshette et al. 2019) are marked in cyan.

2013).

Negative AGN feedback is thought to happen in two different ways, radiative mode and kinetic mode, which are illustrated schematically in Fig. 1.11.

Radiative mode feedback

During radiative mode feedback (also known as quasar mode or wind mode and first proposed by Silk & Rees 1998), high accretion rates originate powerful outflows that expel cold gas in the SMBH environment. Thus, radiative feedback causes the depletion of the gas reservoir for star formation and black hole accretion, which also limits AGN activity. This feedback is mostly associated with high-luminosity AGN.

Radio mode feedback

This mode of feedback (also known as kinetic mode or jet mode) is associated with BCGs of cool core galaxy clusters. In this mode, AGN jets mechanically transfer energy to the gas surrounding the BCG, preventing it from cooling. If AGN feedback was not present, surrounding gas would experience rapid radiative cooling and would collapse into the host galaxy, originating vast cooling flows and triggering star formation of the galaxy (see e.g., McNamara & Nulsen 2007, 2012, Cavagnolo et al. 2010, Fabian 2012, Gitti et al. 2012, and Morganti 2017). The best evidence of radio mode feedback is the presence of X-ray cavities associated with radio lobes, first reported by Böhringer et al. (1996) and Churazov et al. (2000). The most accepted interpretation for this spatial association is that radio jets inflate expanding radio bubbles that are responsible for displacing the hot ICM. Some of the most remarkable examples of cavities include those of Perseus (see Fabian et al. 2003, 2006 and Graham et al. 2008), M87 (see e.g., Forman et al. 2005, 2017), Hydra A (Nulsen et al. 2005a), Hercules A (Nulsen et al. 2005b), MS0735.6+7421 (McNamara et al. 2005, 2009), NGC 5813 (Randall et al. 2011, 2015), A2052 (Blanton et al. 2011), A2597 (Tremblay et al. 2012), and NGC 4636 (Jones et al. 2002).

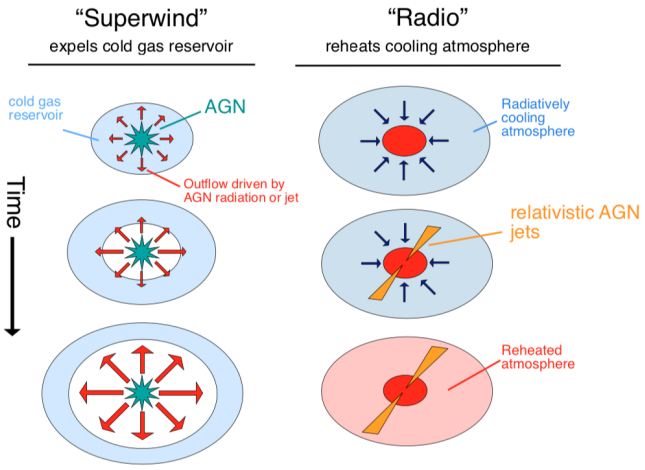

Figure 1.11: Diagrams illustrating the two main modes of AGN negative feedback. "Superwind"-mode or radiative-mode feedback is shown on the left, while "radio"-mode or kinetic-mode is shown on the right.

1.4 The Third Cambridge Catalog

The Third Cambridge Catalog of radio sources and its revised versions (3C, 3CR and 3CRR; Edge et al. 1959, Bennett 1962, Spinrad et al. 1985 and Laing et al. 1983) have proven to be incredibly valuable in the study of the nature and evolution of radio galaxies and their relationship with their environments (see e.g., Schmidt 1963, Shields 1999, Fabian 2012, Kraft et al. 2012, and Tadhunter 2016). Considered the definitive listing of the brightest radio sources in the Northern Hemisphere, built first from radio sources detected at 159 MHZ, and later updated with observations at 178 MHz, the 3CR catalog collects all radio sources with flux density above 9 Jy and declination above 5°. The 3CR catalog, in particular, lists 298 radio galaxies and radio-loud QSOs. Some of the keys to its success include its wide ranges in radio power and redshift, as well as the vast suite of multifrequency observations carried out in the last decades.

1.4.1 An historical introduction

The discoveries of extraterrestrial radio waves in 1935 by Jansky and of some radio sources such as Cygnus (Hey et al. 1946), Virgo A, and Centaurus A (Bolton et al. 1949), resulted in the first attempts to create systematic surveys to study extragalactic radio sources. After two first attempts, in 1959, members of the Radio Astronomy Group at the University of Cambridge published the first reliable radio survey of the northern sky, the 3C catalog (Edge et al. 1959). The 3C catalog listed 471 radio sources detected at 159 MHz using the Cambridge Interferometer at the Mullard Radio Astronomy Observatory, Cambridge.

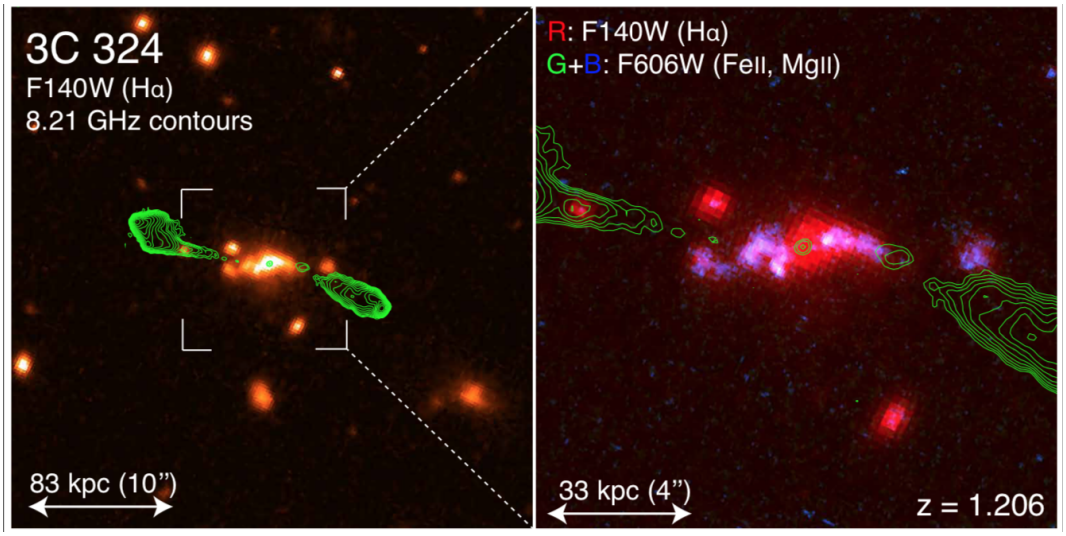

Figure 1.12: 3CR 324 optical and infrared observations from HST with radio contours overlaid from Hilbert et al. (2016).

1.4.2 Revised versions of the 3C

Using observations at 178 MHz, in 1962, Bennett created the "revised 3C Catalog of radio sources", or 3CR catalog. This catalog listed 328 radio sources (29 of them, galactic) in the Northern sky with flux density above 9 Jy. The main differences between the 3C and the 3CR catalogs are the inclusion of new sources that had been missed in the original catalog, as well as the exclusion of those sources that were below the flux limit of the original catalog or those that were previously unresolved blends of adjacent sources.

However, due to the shortcomings of original observations, some sources that met the flux and declination limits of the 3CR catalog were missed. Thus, in 1983, Laing et al. created an additional revision, called the 3CRR catalog, a formally complete sample. This revision included all extragalactic radio sources in the northern sky with flux density at 178 MHz above 10.9 Jy, declination $\delta > 10°$, and Galactic latitudes above 10° or below -10°.

1.4.3 The vast suite of multifrequency observations

Thanks to being considered the definitive listing of the brightest radio sources in the Northern Hemisphere, a vast suite of multifrequency observations of 3CR sources were carried out in the last decades. These multifrequency observations include:

- **Radio observations:** such as the ones presented in Law-Green et al. (1995), Hardcastle & Worrall (2000), Giovannini et al. (2005), Kotyla et al. (2016), and Balmaverde et al. (2019).
- **Infrared observations:** like those carried out by Madrid et al. (2006), Baldi et al. (2010), Werner et al. (2012), and Dicken et al. (2014).
- **Optical and UV observation:** such as the ones in Fig. 1.12, taken from Hilbert et al. (2016) and those in works by Hiltner & Roeser (1991), de Koff et al. (1996),

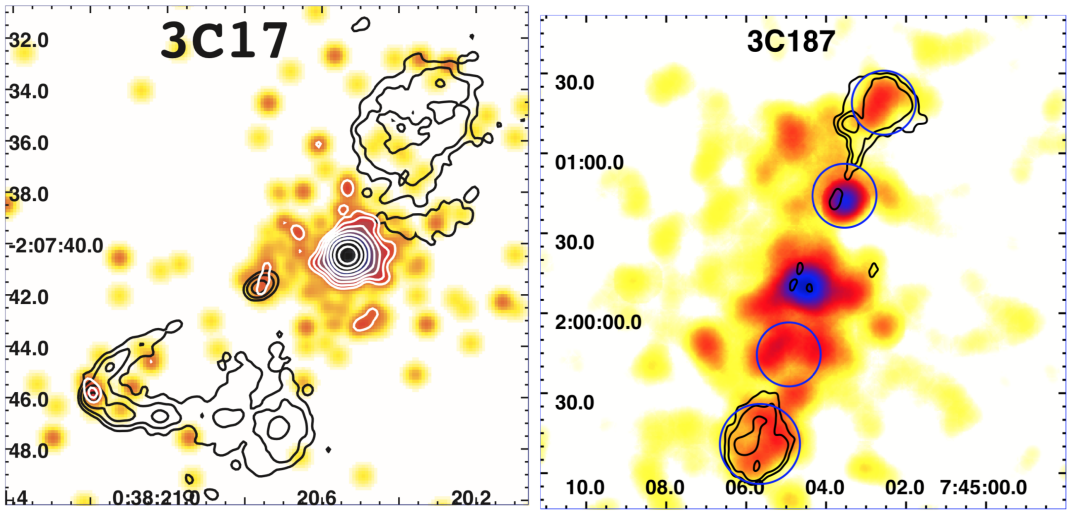

Figure 1.13: X-ray images with radio contours overlaid taken from the 3CR *Chandra* Snapshot Survey (Massaro et al. (2010, 2013)).

Chiaberge et al. (2000), Allen et al. (2002), Privon et al. (2008), Baldi & Capetti (2008), Buttiglione et al. (2009, 2011), Tremblay et al. (2009), and Baldi et al. (2019).

- **X-ray observations:** like the ones presented in Prieto (1996), Evans et al. (2006), Hardcastle et al. (2006), Balmaverde et al. (2012), Wilkes et al. (2013), Maselli et al. (2016), and Kuraszkiewicz et al. (2021).

1.4.4 The 3CR *Chandra* Snapshot Survey

Despite this large suite of available multifrequency observations, before *Chandra* GO Cycle 9 only ~60% of 3CR sources had archival *Chandra* observations and only ~30% had been observed with XMM-*Newton* (see e.g., Massaro et al. 2018, for a recent summary). Therefore, in 2007, the 3CR *Chandra* Snapshot Survey began to complete the 3CR catalog's X-ray coverage (Massaro et al. 2010).

The 3CR *Chandra* Snapshot Survey (Massaro et al. 2010, 2012, 2013, 2015, 2018, Stuardi et al. 2018 and Jimenez-Gallardo et al. 2020) aimed at obtaining snapshot observations for all the sources in the catalog not observed by *Chandra* before 2009. Exposure times of these snapshots range from ~8 to ~38 ks, to take into account the decreasing efficiency of the ACIS detector and estimated count rates. Currently, all identified sources in the 3CR catalog have been observed in the X-rays (see Jimenez-Gallardo et al. 2020) and the sample is being completed with the 25 unidentified sources (that is, lacking an optical counterpart for their radio cores), 16 of which are already approved for future *Chandra* observations (see the first part of these observations in Missaglia et al. 2021). 3CR *Chandra* Snapshot Survey observations of 3CR 17 and 3CR 187 are shown in Fig. 1.13.

Several important results have been achieved to date thanks to this snapshot survey, including X-ray follow-up observations of interesting targets (such as 3CR 171 by Hardcastle et al. 2010 and Balmaverde et al. 2012, 3CR 305 by Hardcastle et al. 2012, 3CR 105

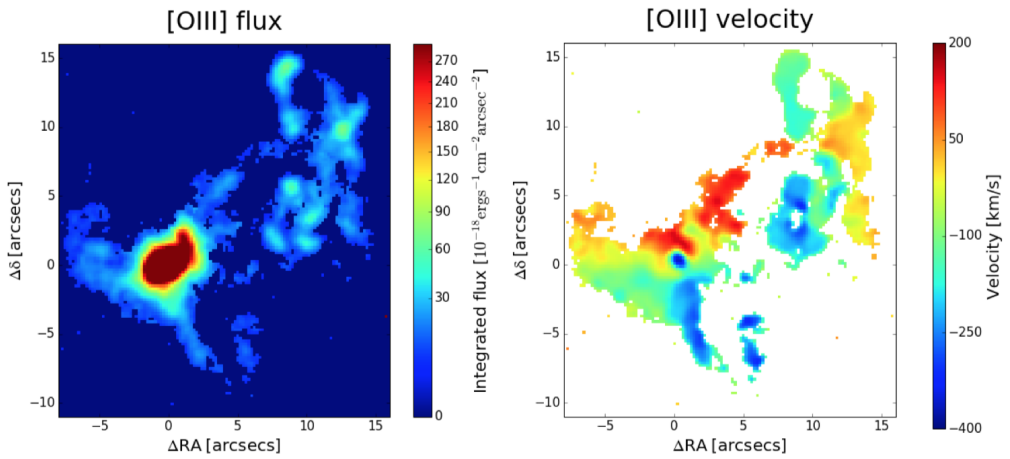

Figure 1.14: [O III] emission and velocity of 3CR 459 from the MURALES survey (Balmaverde et al. 2018b).

and 3CR 445 by Orienti et al. 2012 and 3CR 227 and 3CR 295 by Migliori et al. 2020). Furthermore, this survey led to the discovery of X-ray counterparts of radio jet-knots and hotspots (see e.g., Massaro et al. 2015), as well as diffuse X-ray emission around several radio sources (Massaro et al. 2009a, 2018 and Stuardi et al. 2018) due to the presence of ICM (see e.g., 3CR 89, 3CR 196.1 and 3CR 320 by Dasadia et al. 2016, Ricci et al. 2018 and Vagshette et al. 2019, respectively, and 3CR 17 by Massaro et al. 2009b and Madrid et al. 2018, to name a few examples) or to Inverse Compton scattering (IC) of photons from the Cosmic Microwave Background (CMB) in their lobes (IC/CMB; see e.g., 3CR 459 by Maselli et al. 2018). In addition, several radio galaxies with FR II radio morphologies, observed during the 3CR *Chandra* Snapshot Survey, show diffuse X-ray emission with no apparent radio counterparts at GHz frequencies (see e.g., Massaro et al. 2013 and Stuardi et al. 2018).

1.4.5 The MURALES survey

With a similar mindset, in 2018, Balmaverde et al. started the MURALES (MUse RAdio Loud Emission line Snapshot) survey aiming at observing the 3CR radio sources with the Multi-Unit Spectroscopic Explorer (MUSE) at the Very Large Telescope (VLT). The MURALES survey has collected to date MUSE observations for 37 3CR sources with $z < 0.3$ and visible from the southern hemisphere (i.e., $\delta < 20°$). Some of the main results of this project include the possible discovery of a dual AGN at the center of 3CR 459 (see Balmaverde et al. 2018b), the observations of extended emission line structures connected to the radio morphologies of 3CR radio galaxies (see Balmaverde et al. 2019, 2021), such as the ones seen in 3CR 317 (see also Balmaverde et al. 2018) or 3CR 227 (see also Prieto et al. 1993), as well as the identification of gaseous "superdisks" as emission line structures in radio galaxies with FR II radio morphologies (see Balmaverde et al. 2022). Examples of MURALES survey observations are shown in Figs. 1.14 and 1.15.

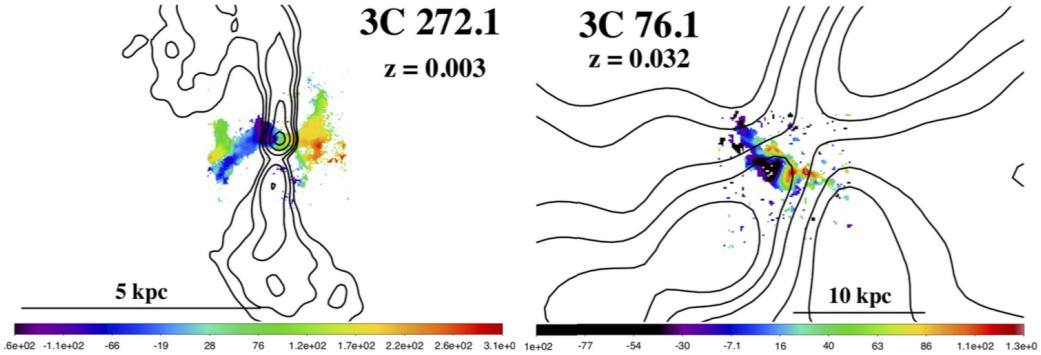

Figure 1.15: [N II] velocity maps of 3CR 272.1 and 3CR 76.1 from the MURALES survey with radio contours overlaid (Balmaverde et al. 2022).

1.5 The unsolved puzzle: open questions

Despite the fast progress in the study of radio galaxies in the last decades, there still remain several unanswered questions. Some of them include:

1. What is the origin of extended soft X-ray emission surrounding radio galaxies?
2. How do jets interact with the small and large-scale environment of radio galaxies and how does this interaction affect galaxy evolution?
3. What is the origin of the different gas phases radio galaxies are embedded in? In particular, what is the origin of EELRs and their associated soft X-ray emission? And what is the origin of ionized gas filaments with X-ray counterparts seen in cool-core galaxy clusters?
4. Are X-ray counterparts of jets and jet knots due to synchrotron or IC/CMB radiation? Are the emission processes underlying jet X-ray radiation the same for low and high-power radio sources?
5. How prevalent is the effect of positive feedback in radio galaxies?
6. What is the evolutionary path of radio galaxies? Are small-size radio sources like Gigahertz Peaked-Spectrum and Compact Steep-Spectrum sources the predecessors of large radio galaxies?
7. Is there a definite distinction in the environments of radio galaxies with FR I and FR II radio morphologies? And in the environments of radio galaxies optically classified as LERGs and HERGs?

In this thesis, I focus on delving into the first three questions.

Bibliography

Adams, T. F. 1977, ApJS, 33, 19

Alexander, D. M. & Hickox, R. C. 2012, New Astron. Rev., 56, 93

Allen, M. G., Sparks, W. B., Koekemoer, A., et al. 2002, ApJS, 139, 411

Antonucci, R., et al. 1993, ARA&A, 31, 473

Baade, W. & Minkowski, R. 1954, ApJ, 119, 206

Baade, W. & Minkowski, R. 1954, ApJ, 119, 215

Baldi, R. D. & Capetti, A. 2008, A&A, 489, 989

Baldi, R. D. & Capetti, A. 2009, A&A, 508, 603

Baldi, R. D., Chiaberge, M., Capetti, A., et al. 2010, ApJ, 725, 2426

Baldi, R. D., Capetti, A. & Giovannini, G., 2015, A&A, 576, A38

Baldi, R. D., Rodríguez Zaurín, J., Chiaberge, M., et al. 2019, ApJ, 870, 53

Balmaverde, B., Capetti, A., Grandi, P., et al. 2012, A&A, 545, A143

Balmaverde, B., Capetti, A., Marconi, A., et al. 2018, A&A, 612, A19

Balmaverde, B., Capetti, A., Marconi, A., et al. 2018, A&A, 619, A83

Balmaverde, B., Capetti, A., Marconi, A., et al. 2019, A&A, 632, A124

Balmaverde, B., Capetti, A., Marconi, A., et al. 2021, A&A, 645, A12

Balmaverde, B., Capetti, A., Baldi, R. D., et al. 2022, A&A, accepted

Baum, S. A., Heckman, T. M., Bridle, A., et al. 1988, ApJS, 68, 643

Baum, S. A. & Heckman, T. M., 1989, ApJ, 336, 681

Baum, S. A., Heckman, T. & van Breugel, W. 1990, ApJS, 74, 389

Bennett, A. S. 1962, MNRAS, 125, 75

Best, P. N., 2009, Astronomische Nachrichten, 330, 184

Best, P. N. & Heckman, T. M. 2012, MNRAS, 421, 1569

Bicknell, G. V., 1994, ApJ, 422, 542

Blandford, R. D. & Königl, A. 1979, ApJ, 232, 34

Blandford, R., Meier, D. & Readhead, A. 2019, ARA&A, 57, 467

Blanton, E. L., Randall, S. W., Clarke, T. E., et al. 2011, ApJ, 737, 99

Blanton, E. L., Paterno-Mahler, R., Wing, J. D., et al. 2015, in Extragalactic Jets from Every Angle, vol. 313, ed. Massaro, F., Cheung, C. C., Lopez, E. & Siemiginowska, A., 315

Böhringer, H., Neumann, D. M., Schindler, S., et al. 1996, ApJ, 467, 168

Bolton, J. G. 1948, Nature, 162, 141

Bolton, J. G., Stanley, G. J. & Slee, O. B. 1949, Nature, 164, 101

Bridle, A. H., 1986, Canadian Journal of Physics, 64, 353

Bridle, A. H., 1992, in American Institute of Physics Conference Series, Vol. 254, Jets on large scales, ed. Holt, S. S., Neff, S. G. & Urry, C. M., 386

Buttiglione, S., Capetti, A., Celotti, A., et al. 2009, A&A, 495, 1033

Buttiglione, S., Capetti, A., Celotti, A., et al. 2010, A&A, 509, A6

Buttiglione, S., Capetti, A., Celotti, A., et al. 2011, A&A, 525, A28

Capetti, A. and Axon, D. J. and Macchetto, F., et al. 1996, ApJ, 469, 554

Capetti, A., Massaro, F. & Baldi, R. D. 2017, A&A, 598, A49

Capetti, A., Massaro, F. & Baldi, R. D. 2017, A&A, 601, A81

Cavagnolo, K. W., McNamara, B. R., Nulsen, P. E. J., et al. 2010, ApJ, 720, 1066

Cavaliere, A. & Fusco-Femiano, R. 1976, A&A, 500, 95

Cavaliere, A. & Fusco-Femiano, R. 1978, A&A, 70, 677

Chiaberge, M., Capetti, A. & Celotti, A. 2000, A&A, e

Churazov, E., Forman, W., Jones, C., et al. 2000, A&A, 356, 788

Combes, F., García-Burillo, S., Audibert, A., et al. 2019, A&A, 623, A79

Conselice, C. J., Gallagher, J. S., III & Wyse, R. F. G. 2001, AJ, 122, 2281

Croston, J. H., Hardcastle, M. J., Mingo, B., et al. 2019, A&A, 622, A10

Dasadia, S., Sun, M., Morandi, A., et al. 2016, MNRAS, 458, 681

Davis, J. E. 2001, ApJ, 562, 575

De Lucia, G., Poggianti, B. M., Aragón-Salamanca, A., et al. 2005, ApJ, 626, 733

Dicken, D., Tadhunter, C., Morganti, R., et al. 2014, ApJ, 788, 98

Edge, D. O., Shakeshaft, J. R., McAdam, W. B., et al. 1959, MmRAS, 69, 37

Elvis, M. 2000, ApJ, 545, 63

Evans, D. A., Worrall, D. M., Hardcastle, M. J., et al. 2006, ApJ, 642, 96

Fabian, A. C., Sanders, J. S., Allen, S. W., et al. 2003, MNRAS, 344, L43

Fabian, A. C., Sanders, J. S., Taylor, G. B., et al. 2006, MNRAS, 366, 417

Fabian, A. C., Johnstone, R. M., Sanders, J. S., et al. 2008, Nature, 454, 968

Fabian, A. C., Sanders, J. S., Williams, R. J. R., et al. 2011, MNRAS, 417, 172

Fabian, A. C. 2012, ARA&A, 50, 455

Fanaroff, B. L. & Riley, J. M. 1974, MNRAS, 167, 31P

Fath, E. A. 1909, Lick Observatory Bulletin, 149, 71

Feain, I. J., Papadopoulos, P. P., Ekers, R. D., et al. 2007, ApJ, 662, 872

Ferland, G. J. & Osterbrock, D. E. 1986, ApJ, 300, 658

Forman, W. & Jones, C. 1990, in Clusters of Galaxies, ed. Oegerle, W. R., Fitchett, J. & Danly, L., 257

Forman, W., Jones, C., Churazov, E., et al. 2005, ApJ, 665, 1057

Forman, W., Churazov, E., Jones, C., et al. 2017, ApJ, 844, 122

Fosbury, R. A. E. 1986, in Astrophysics and Space Science Library, Vol. 121, Large scale ionized gas in radio galaxies and quasars, ed. Giuricin, G., Mezzetti, M., Ramella, M. & Mardirossian, F., 297

Gaspari, M., Temi, P. & Brighenti, F. 2017, MNRAS, 466, 677

Gaspari, M., McDonald, M., Hamer, S. L., et al. 2018, ApJ, 854, 167

Ghisellini, G., 2011, in 25th Texas Symposium on Relativistic AstroPhysics (Texas 2010), Vol. 1381, Extragalactic relativistic jets, ed. Aharonian, F. A., Hofmann, W. & Rieger, F. M., 180

Giovannini, G., Taylor, G. B., Feretti, L., et al. 2005, ApJ, 618, 635

Gitti, M., Brighenti, F. & McNamara, B. R. 2012, Advances in Astronomy, 950641

Gopal-Krishna & Wiita, P. J. 2000, A&A, 363, 507

Graham, J., Fabian, A. C. & Sanders, J. S. 2008, MNRAS, 386, 278

Green, R. F. 1976, PASP, 88, 665

Greenstein, J. L. 1963, Scientific American, 209, 6

Grimes, J. A., Rawlings, S., & Willott, C. J., 2004, MNRAS, 349, 503

Hammer, F. & Le Fevre, O. 1990, ApJ, 357, 38

Hansen, L., Norgaard-Nielsen, H. U. & Jorgensen, H. E. 1987, A&AS, 71, 465

Hardcastle, M. J. & Worrall, D. M. 2000, MNRAS, 314, 359

Hardcastle, M. J., Evans, D. A. & Croston, J. H. 2006, MNRAS, 370, 1893

Hardcastle, M. J., Evans, D. A. & Croston, J. H. 2007, MNRAS, 376, 1849

Hardcastle, M. J., Croston, J. H. & Kraft, R. P. 2007, ApJ, 669, 893

Hardcastle, M. J., Evans, D. A. & Croston, J. H. 2009, MNRAS, 396, 1929

Hardcastle, M. J., Massaro, F. & Harris, D. E., 2010, MNRAS, 401, 2697

Hardcastle, M. J., Massaro, F. & Harris, D. E., 2012, MNRAS, 424, 1774

Harris, D. E. & Krawczynski, H., 2002, ApJ, 565, 242

Harris, D. E. & Krawczynski, H., 2006, ARA&A, 44, 463

Harwood, J. J., Vernstrom, T. & Stroe, A., 2012, MNRAS, 491, 803

Heckman, T. M. 1978, PASP, 90, 241

Heckman, T. M. 1980, A&A, 500, 187

Hes, R., Barthel, P. D. & Fosbury, R. A. E. 1996 A&A, 313, 423

Hewett, P. C. & Wild, V. 2010, MNRAS, 405, 2302

Hewitt, A. & Burbidge, G. 1991, ApJS, 75, 297

Hey, J. S., Parsons, S. J. & Phillips, J. W. 1946, Nature, 158, 4007

Hiltner, P. R. & Roeser, H. J. 1991, A&A, 244, 37

Hilbert, B., Chiaberge, M., Kotyla, J. P., et al. 2016, American Astronomical Society, 225, 12

Hine, R. G. & Longair, M. S. 1979, MNRAS, 188, 111

Hubble, E. P. 1926, ApJ, 64, 321

Hudson, D. S., Mittal, R., Reiprich, T. H., et al. 2010, A&A, 513, A37

Humason, M. L. 1932, PASP, 44, 260

Impey, C. D. & Tapia, S. 1988, ApJ, 333, 666

Ineson, J., Croston, J. H., Hardcastle, M. J., et al. 2013, ApJ, 770, 136

Ineson, J., Croston, J. H., Hardcastle, M. J., et al. 2015, MNRAS, 453, 2682

Jackson, N. & Rawlings, S. 1997, MNRAS, 286, 241

Jansky, K. G. 1933, Nature, 132, 66

Jimenez-Gallardo, A., Massaro, F., Capetti, A., et al. 2019, A&A, 627, A108

Jimenez-Gallardo, A., Massaro, F., Prieto, M. A., et al. 2020, ApJS, 250, 7

Jones, C., Forman, W.,Vikhlinin, A., et al. 2002, ApJL, 567, L115

Kalberla, P. M. W., Burton, W. B., Hartmann, D., et al. 2005, A&A, 440, 775

Kalfountzou, E., Stevens, J. A., Jarvis, M. J., et al. 2017, MNRAS, 471, 28

Kellermann, K. I., Sramek, R., Schmidt, M., et al. 1989, AJ, 98, 1195

Khachikian, E. Y. & Weedman, D. W. 1974, ApJ, 192, 581

Kormendy, J. & Ho, L. C. 2013, ARA&A, 51, 511

Kotilainen, J. K. & Ward, M. J. 1994, MNRAS, 266, 953

Kotyla, J. P., Hilbert, Chiaberge, M., Baum, S., et al. 2016, American Astronomical Society, 826, 46

Kraft, R. P., Birkinshaw, M., Nulsen, P. E. J., et al. 2012, ApJ, 749, 19

Kuraszkiewicz, J., Wilkes, B., Atanas, A., et al. 2021, ApJ, 913, 134

Laing, R. A., Riley, J. M. & Longair, M. S. 1983, MNRAS, 204, 151

Laing, R. A., Jenkins, C. R., Wall, J. V., et al. 1994, Astronomical Society of the Pacific Conference Series, 54, 201

Laing, R. A. & Bridle, A. H. 2008, in Extragalactic Jets: Theory and Observation from Radio to Gamma Ray, vol. 386, ed. Rector, T. A. & De Young, D. S., 70

Law-Green, J. D. B., Leahy, J. P., Alexander, P., et al. 1995, MNRAS, 274, 939

Lawrence, A., 1987, PASP, 99, 309

Leahy, J. P., 1993, in Jets in Extragalactic Radio Sources, Vol. 421, DRAGNs, ed. Röser, H.-J. & Meisenheimer, K., 1

Ledlow, M. J. & Owen, F. N., 1996, AJ, 112, 9

Liang, E. P. T. 1979, ApJL, 231, L111

Lin, Y.-T., Shen, Y., Strauss, M. A., et al. 2010, ApJ, 723, 1119

Lonsdale, C. J., Barthel, P. D. & Miley, G. K. 1993, ApJS, 87, 63

Lovisari, L., Reiprich, T. H. & Schellenberger, G. 2015, A&A, 573, A118

Lynds, R. 1970, ApJL, 159, L151

MacKenty, J. W. 1990, ApJS, 72, 231

Madrid, J. P., Chiaberge, M., Floyd, D., et al. 2006, ApJS, 164, 307

Madrid, J. P., Donzelli, C. J., Rodríguez-Ardila, A., et al. 2018, ApJS, 238, 31

Maselli, A., Kraft, R. P., Massaro, F. & Hardcastle, M. J. 2018, A&A, 619, A75

Massaro, F., Chiaberge, M., Grandi, P., et al. 2009, ApJL, 692, L123

Massaro, F., Harris, D. E., Chiaberge, M., et al. 2009, ApJ, 696, 980

Massaro, F., Harris, D. E., Tremblay, G. R., et al. 2010, ApJ, 714, 589

Massaro, F., Harris, D. E. & Cheung, C. C. 2011, ApJS, 197, 24

Massaro, F., Tremblay, G. R., Harris, D. E., et al. 2012, ApJS, 203, 31

Massaro, F., Harris, D. E., Tremblay, G. R., et al. 2013, ApJS, 206, 7

Massaro, F., Masetti, N., D'Abrusco, R., et al. 2014, AJ, 148, 66

Massaro, F., Harris, D. E., Liuzzo, E., et al. 2015, ApJS, 220, 5

Massaro, F., Missaglia, V., Stuardi, C., et al. 2018, ApJS, 234, 7

Massaro, F., Álvarez-Crespo, N., Capetti, A., et al. 2019, ApJS, 240, 20

Massaro, F., Capetti, A., Paggi, A., et al. 2020, ApJS, 247, 71

Maselli, A., Massaro, F., Cusumano, G., et al. 2016, MNRAS, 460, 3829

Mayall, N. U. 1934, PASP, 46, 271

McCarthy, P. J., Spinrad, H., Djorgovski, S., et al. 1987, ApJL, 319, L39

McCarthy, P. J. 1988, PhD thesis, AA (California Univ., Berkeley)

McDonald M., Veilleux, S., Rupke, D. S. N., et al. 2010, ApJ, 721, 1262

McDonald M., Veilleux, S. & Rupke, D. S. N. 2012, ApJ, 746, 153

McNamara, B. R., Nulsen, P. E. J., Wise, M. W., et al. 2005, Nature, 433, 7021

McNamara B. R. & Nulsen, P. E. J. 2007, ARA&A, 45, 117

McNamara, B. R., Kazemzadeh, F., Rafferty, D. A., et al. 2009, ApJ, 698, 594

McNamara B. R. & Nulsen, P. E. J. 2012, New Journal of Physics, 14, 5

Migliori, G., Orienti, M., Coccato, L., et al. 2020, MNRAS, 495, 1593

Mingo, B., Hardcastle, M. J., Croston, J. H., et al. 2014, MNRAS, 440, 269

Mingo, B., Watson, M. G., Rosen, S. R., et al. 2016, MNRAS, 462, 2631

Mingo, B., Croston, J. H., Hardcastle, M. J., et al. 2019, MNRAS, 488, 2701

Missaglia, V., Massaro, F., Liuzzo, E., et al. 2021, ApJS, 255, 18

Morganti, R. 2017, Frontiers in Astronomy and Space Sciences, 4, 42

Moore, R. L. & Stockman, H. S. 1981, ApJS, 243, 60

Narayan, R. & Yi, I. 1994, ApJL, 428, L13

Nulsen, P. E. J., McNamara, B. R., Wise, M. W., et al. 2005a, ApJ, 628, 629

Nulsen, P. E. J., Hambrick, D. C., McNamara, B. R., et al. 2005b, ApJL, 625, L9

O'Dea, C. P. 1998, PASP, 110, 747

O'Donoghue, A. A., Owen, F. N. & Eilek, J. A. 1990, ApJS, 72, 75

Olivares, V., Salome, P., Combes, F., et al. 2019, A&A, 631, A22

Orienti, M., Prieto, M. A., Brunetti, G., et al. 2012, MNRAS, 419, 2338

Owen, F. N. & Rudnick, L. 1976, ApJL, 205, L1

Padovani, P. 2017, Nature Astronomy, 1, 0194

Panessa, F., Bassani, L., Landi, R., et al. 2016 MNRAS, 461, 3153

Perley, R. A., Dreher, J. W. & Cowan, J. J. 1984 ApJL, 285, L35

Perryman, M. A. C., Lilly, S. J., Longair, M. S., et al. 1984 MNRAS, 209, 159

Peterson, B. M., 1997, An Introduction to Active Galactic Nuclei

Peterson, B. M., 2006, in Physics of Active Galactic Nuclei at all Scales, vol. 693, ed. Alloin, D., 77

Prieto, M. A., Walsh, J. R., Fosbury, R. A. E., 1993, MNRAS, 263, 10

Prieto, M. A., 1996, MNRAS, 282, 421

Privon, G. C., O'Dea, C. P., Baum, S. A., et al. 2008, ApJS, 175, 423

Qiu, Y., Bogdanović, T., Li, Y., et al. 2020, Nature Astronomy, 4, 900

Qiu, Y., Hu, H., Inayoshi, K., et al. 2021, ApJL, 917, L7

Randall, S. W., Forman, W. R., Giacintucci, S., et al. 2011, ApJ, 726, 86

Randall, S. W., Nulsen, P. E. J., Jones, C., et al. 2015, ApJ, 805, 112

Reber, G. 1944, ApJ, 100, 279

Ricci, F., Lovisari, L., Kraft, R. P., et al. 2018, AAS, 867, 35

Sadler, E. M., Ekers, R. D., Mahony, E. K., et al. 2014, MNRAS, 438, 796

Sakelliou, I. & Merrifield, M. R. 2000, MNRAS, 311, 649

Sandage, A., Véron, P. & Wyndham, J. D., et al. 1965, ApJ, 142, 1307

Sargent, W. L. W., 1970, ApJ, 160, 405

Seyfert, C. K., 1943, ApJ, 97, 28

Schmidt, M. 1963, Nature, 197, 1040

Schmidt, M. 1966, ApJ, 144, 443

Shakura, N. I. & Sunyaev, R. A. 1973, A&A, 500, 33

Shields, G. A. 1999, PASP, 111, 661

Silk, J. & Rees, M. J. 1998, A&A, 331, L1

Simkin, S. M., Su, H. J. & Schwarz, M. P. 1980, ApJ, 237, 404

Slipher, V. M. 1917, Lowell Observatory Bulletin, 3, 59

Spinrad, H., Djorgovski, S., Marr, J. & Aguilar, L. 1985, PASP, 97, 932

Stickel, M. & Kuehr, H. 1996, A&AS, 115, 1

Stockton, A. & MacKenty, J. W. 1987, ApJ, 316, 584

Strittmatter, P. A., Serkowski, K., Carswell, R., et al. 1972, ApJL, 175, L7

Stuardi, C., Missaglia, V., Massaro, F., et al. 2018, ApJS, 235, 32

Swain, M. R., Bridle, A. H. & Baum, S. 1996, in American Astronomical Society Meeting Abstracts, 189

Tadhunter, C. N., Morganti, R., Robinson, A., et al. 1998, MNRAS, 298, 1035

Tadhunter, C. 2008, New Astron. Rev., 52, 227

Tadhunter, C. 2016, A&ARv, 24, 10

Torresi, E. 2018, arXiv e-prints, 1809.08074

Tremblay, G. R., Chiaberge, M., Sparks, W. B., et al. 2009, ApJS, 183, 278

Tremblay, G. R., O'Dea, C. P., Baum, S. A., et al. 2012, MNRAS, 424, 1026

Tremblay, G. R., O'Dea, C. P., Baum, S. A., et al. 2015, MNRAS, 451, 3768

Urry, M. & Padovani, P., 1995, PASP, 107, 803

Ursini, F., Bassani, L., Panessa, F., et al. 2018, MNRAS, 481, 4250

Vagshette, N. D., Naik, S., Patil, M. K., et al. 2019, MNRAS, 485, 1981

van Breugel, W. J. M., Fillippenko, A. V., McCarthy, P. J., et al. 1986, in Bulletin of the American Astronomical Society, Vol. 18, Spectroscopically Identical, High-Excitation Emission-Line Regions Associated with a Jet in the Radio Galaxy 3C 321, 1005

Véron-Cetty, M. P. & Véron, P. 2006, A&A, 455, 773

Werner, M. W., Murphy, D. W., Livingston, J. H., et al. 2012, ApJ, 759, 86

Wilkes, B. J., Kuraszkiewicz, J., Haas, M., et al. 2013, ApJ, 773, 15

Wing, J. D. & Blanton, E. L. 2011, AJ, 141, 88

Worrall, D. M. 2009, A&ARv, 17, 1

Xanthopoulos, E. 1996, MNRAS, 280, 1

Yee, H. K. 1983, ApJ, 272, 473

Zirbel, E. L. 1997, ApJ, 476, 489

Chapter 2

Radiative Processes

In this chapter, I present a brief summary of the radiative processes at work in radio galaxies, as revealed by radio, optica,l and X-ray observations. I present the main formulae, however, more in-depth information can be found in Rybicki & Lightman (1979), Longair (2011) and Ghisellini (2013).

2.1 Synchrotron radiation

Synchrotron radiation is electromagnetic energy emitted by relativistic charged particles gyrating in a magnetic field (see Fig. 2.1). This type of non-thermal emission (i.e., emission due to a distribution of particles with a non-Maxwellian energy spectrum) is responsible for the rasio emission of lobes.

2.1.1 Basic formulae for synchrotron radiation

Considering an electron of mass m and charge e, moving in a uniform magnetic field $\mathbf{B}$, its motion can be described as:

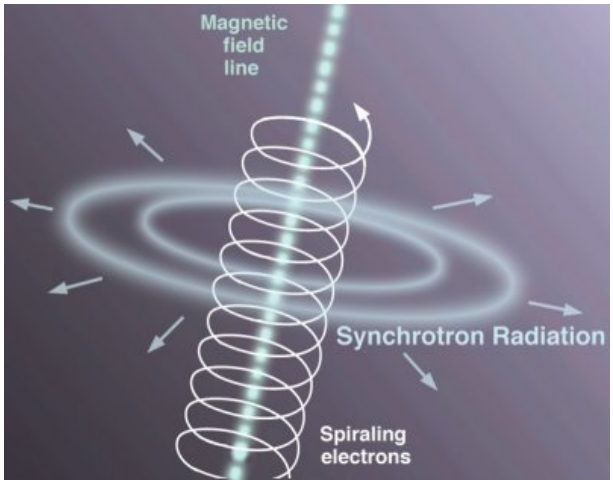

Figure 2.1: Motion of an electron centripetally accelerated by a magnetic field.

$$\begin{cases} \frac{d}{dt}(\gamma m \mathbf{v}) = \frac{e}{c}\mathbf{v} \times \mathbf{B} \\ \frac{d}{dt}(\gamma m c^2) = e\mathbf{v} \cdot \mathbf{E} \end{cases} \tag{2.1}$$

where the second equation implies that the Lorentz factor, γ, as well as the norm of the velocity, $|\mathbf{v}|$ are constant. Thus:

$$\gamma m \frac{d}{dt}(\mathbf{v}) = \frac{e}{c}\mathbf{v} \times \mathbf{B} \Rightarrow \begin{cases} \frac{dv_{\parallel}}{dt} = 0 \\ \frac{d\mathbf{v}_{\perp}}{dt} = \frac{e}{\gamma m c^2}\mathbf{v}_{\perp} \times \mathbf{B} \end{cases} \tag{2.2}$$

where $v_{\parallel}$ and $\mathbf{v}_{\perp}$, are the parallel and perpendicular velocity components with respect to the magnetic field, with θ_p, the pitch angle between the velocity and the magnetic field.

Therefore both $v_{\parallel}$ and $v_{\perp}$ are constant and the solution to equation 2.2 is an helical motion of the charged particle around the field lines, with an acceleration perpendicular to both, velocity and magnetic field vectors, and a rotation frequency:

$$\nu_g = \frac{eB}{2\pi\gamma mc} = \frac{\nu_L}{\gamma} \quad \text{with} \quad \nu_L = \frac{eB}{2\pi mc} \tag{2.3}$$

where ν_L is the Larmor frequency, which in cgs units is given by:

$$\nu_L = 2.80 \cdot 10^6 \, B(\mathrm{G}) \sin\theta_p \, \mathrm{Hz} \tag{2.4}$$

Using the Larmor formula, the total emitted power is provided by:

$$P_{syn} = \frac{dE}{dt} = \frac{2}{3} r_e^2 c \beta^2 \gamma^2 B^2 \sin^2\theta_p = 1.59 \cdot 10^{-15} \beta^2 \gamma^2 B^2(\mathrm{G}) \sin^2\theta_p \, \mathrm{erg\ s^{-1}} \tag{2.5}$$

with $r_e = \frac{e^2}{mc^2}$.

Integrating over all pitch angles, the total power emitted for an isotropic distribution of velocities is given by:

$$\left\langle P_{syn} \right\rangle = \frac{4}{3} \sigma_T c \beta^2 \gamma^2 u_B = 1.06 \cdot 10^{-15} \beta^2 \gamma^2 B^2(\mathrm{G}) \, \mathrm{erg\ s^{-1}} \tag{2.6}$$

where $u_B = \frac{B^2}{8\pi}$.

For a single utrarelativistic ($\beta \sim 1$), the synchrotron spectrum is given by:

$$\frac{dP}{d\nu} = c_0 F_{syn}\left(\frac{\nu}{\nu_c}\right) \tag{2.7}$$

with:

$$c_0 = \frac{\sqrt{3} e^3 B \sin\theta_p}{mc^2} = 2.34 \cdot 10^{-22} B(\mathrm{G}) \sin\theta_P \, \mathrm{erg\ s^{-1}\ Hz^{-1}}, \tag{2.8}$$

$$\nu_c = \frac{3}{2}\gamma^2 \nu_L \sin\theta_P = 4.20 \cdot 10^6 \gamma^2 B(\mathrm{G}) \sin\theta_P \, \mathrm{Hz} \tag{2.9}$$

the synchrotron critical frequency, and

$$F_{syn}\left(\frac{\nu}{\nu_c}\right) = F_{syn}(\chi) = \chi \int_{\chi}^{\infty} K_{5/3}(\eta) d\eta \tag{2.10}$$

the synchrotron kernel (see left panel of Fig. 2.2), where $K_{5/3}$ is the modified Bessel function of 5/3 order.

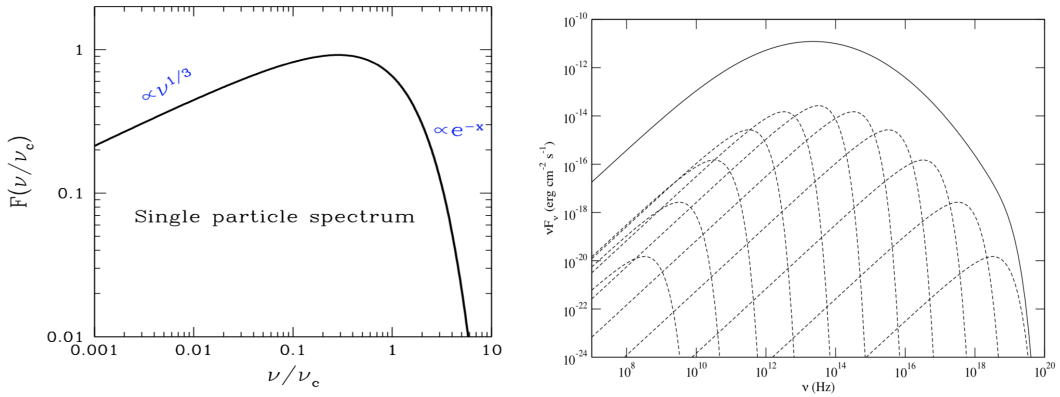

Figure 2.2: Left: Synchrotron kernel $F_{syn}(\nu/\nu_c)$ as given by equation 2.10, taken from Ghisellini (2013). Right: Synchrotron spectrum assuming a power-law electron distribution.

The single electron synchrotron spectrum peaks at a frequency $\nu_m \sim 0.29\nu_c$ and, integrating eq. 2.7, the total power emitted by a single ultrarelativistic electron is given by:

$$P_{syn} = \int \frac{dP}{d\nu} = 2\sigma_T c\beta^2\gamma^2 u_B \tag{2.11}$$

Lastly, the synchrotron cooling time of ultrarelativistic electrons can be written as:

$$t_{cool} = \frac{\gamma mc^2}{P} \Rightarrow t_{cool,syn} = 5.16 \cdot 10^8 \gamma^{-1} B^{-2}(\mathrm{G}) \sin^{-2}\theta_P \ \mathrm{s} \tag{2.12}$$

Assuming an isotropic electron distribution $n(\gamma)$, the synchrotron emission coefficient is given by:

$$\epsilon_{syn} = \frac{1}{4\pi}\int_{\gamma_{min}}^{\gamma_{max}} n(\gamma)\frac{dP}{d\nu}(\gamma)d\gamma = \frac{c_0}{4\pi}\int_{\gamma_{min}}^{\gamma_{max}} n(\gamma)F_{syn}\left(\frac{\nu}{\nu_c(\gamma)}\right)d\gamma \tag{2.13}$$

This emission coefficient corresponds to the superposition of the spectra emitted by each electron over the electron distribution. In the case where electrons follow a power-law distribution, the synchrotron spectrum is shown on the right panel of Fig. 2.2.

Lastly, for a power-law electron distribution $n(\gamma) \propto \gamma^{-p}$, the synchrotron spectrum can be written as:

$$S_{syn}(\nu) \propto \nu^{-\alpha} \tag{2.14}$$

where α is known as the spectral index and it is related to the electron distribution index as $\alpha = \frac{p-1}{2}$.

2.1.2 Equipartition magnetic field

An estimate of the magnetic field can be obtained from synchrotron emission by assuming the equipartition condition. Here I will present a simplified and summarized explanation, however, the detailed derivation can be found in Govoni & Feretti (2004). The equipartition condition implies that the total energy content of a synchrotron emitting source can be

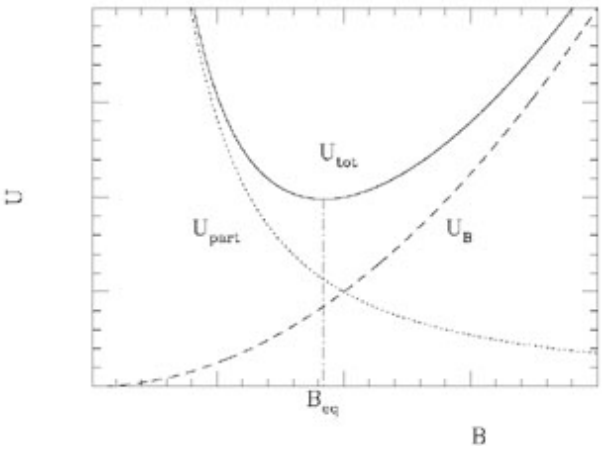

Figure 2.3: Energy content of a synchrotron source, together with the energy contributions of magnetic field, U_B, and relativistic particles, $U_{part} = U_{el} + U_{pr} = (1 + k)U_{el}$, as a function of the magnetic field (from Govoni & Feretti 2004). The minimum of the total energy is reached at the equipartition value, B_{eq}.

estimated as its minimum value, which is reached when the contributions of the magnetic field and the relativistic particles are approximately equal (see Fig. 2.3):

$$U_B = \frac{3}{4}(1 + k)U_{el} \tag{2.15}$$

where U_B and U_{el} are the energy contributions of magnetic field and electrons, respectively, and k is the fraction of the electron energy contributed by heavy particles.

U_B and U_{el} can be written as:

$$U_B = \frac{B^2}{8\pi}\Phi V \tag{2.16}$$

where Φ is the filling factor (i.e., the fraction of the volume occupied by the magnetic field) and V, the source volume, and as:

$$U_{el} = c_{12}(\alpha, \nu_1, \nu_2)L_{syn}B^{-3/2} \tag{2.17}$$

with $c_{12}(\alpha, \nu_1, \nu_2)$, a tabulated constant depending on the spectral index and the frequency range and L_{syn}, the synchrotron luminosity.

Thus, the equipartition magnetic field is given by:

$$B_{eq} = (6\pi(1 + k)c_{12}L_{syn}\Phi^{-1}V^{-1})^{2/7} \tag{2.18}$$

2.2 Inverse Compton scattering

Inverse Compton scattering is the interaction of photons and charged particles resulting in photons being scattered and gaining energy from charged particles. A particular case of inverse Compton scattering, and the one I will concern myself with, occurs in radio galaxies. In this case, non-thermal electrons scatter Cosmic Microwave Background (CMB) photons up to X-ray energies. This mechanism is the one responsible for the X-ray counterparts of radio lobes.

2.2.1 An overview of inverse Compton process

The inverse Compton scattering can be treated in two regimes, the Thomson and the Klein-Nishina regimes.

Thomson regime

In the Thomson regime, the energy of the incoming photon in the rest-frame of the electron (K') is $E'_0 << mc^2$. In this case, the Thomson cross-section, σ_T can be used to describe the scattering probability. In this regime, the scattering rate in the laboratory frame K for an isotropic distribution of photons, $n(E_0)$, can be written as:

$$\frac{dN}{dt} = \sigma_T c \int n(E_0) dE_0 \tag{2.19}$$

Then, the total power going into the X-ray photons is given by:

$$P_{IC} = \frac{4}{3} c \sigma_T \gamma^2 \beta^2 \int E_0 n(E_0) dE_0 \tag{2.20}$$

and the IC spectrum in the Thomson limit is given by:

$$F_{IC} = \frac{3}{4} \frac{\sigma_T c n(E_0)}{\gamma^2 E_0} f\left(\frac{E}{4E_0\gamma^2}\right) \tag{2.21}$$

with $f(x) = 2x \ln x + x + 1 - 2x^2$, and $x = \frac{E}{4E_0\gamma^2}$.

Klein-Nishina regime

If $\gamma E_0 \sim mc^2$, the Thomson regime is no longer valid and the IC process is defined by the Klein-Nishina formula. In that case, the IC photon spectrum is described by:

$$F_{IC} = \frac{3\sigma_T c}{4\gamma^2} \frac{n(E_0)}{E_0} \cdot \left[2q \ln q + (1+2q)(1-q) + \frac{1}{2} \frac{(\Gamma q)^2}{1+\Gamma q}(1-q)\right] \tag{2.22}$$

with

$$\Gamma = \frac{4\gamma E_0}{mc^2}, \quad q = \frac{E}{(\gamma mc^2 - e)\Gamma} \tag{2.23}$$

This spectrum is shown in Fig. 2.4.

IC spectrum from an electron distribution

Assuming a power-law electron distribution, $n(\gamma) \propto \gamma^{-p}$, then, the inverse Compton spectrum can be written as:

$$S_{IC} \propto E^{-\alpha} \tag{2.24}$$

with $\alpha = \frac{p-1}{2}$, the Inverse Compton spectral index.

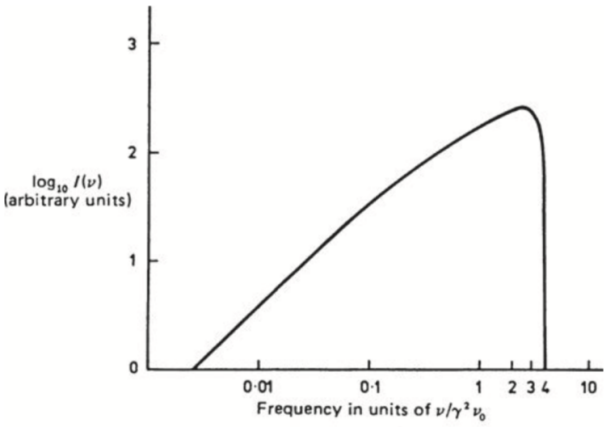

Figure 2.4: Spectrum of the inverse Compton scattering, where ν_0 is the frequency of the unscattered radiation (figure taken from Blumenthal & Gould 1970).

2.3 Thermal Bremsstrahlung

Thermal Bremsstrahlung or free-free radiation is emitted from ionized hot gas since it is produced from the acceleration of a charged particle moving in the electric field generated by another charge. In particular, this type of radiation is the one responsible for the X-ray emission seen from the ICM in galaxy clusters.

2.3.1 Free-free emission

Here I present a simplified summary of the Bremsstrahlung emission using a classical treatment and using corrections (the Gaunt factors) to achieve the quantum results. For a more detailed approach, see Rybicki & Lightman (1979) and Longair (2011).

The simplest approach to the free-free emission consists on an electron moving with velocity v and colliding, with an impact parameter b (see left panel of Fig. 2.5), with a nucleus with a charge Ze. In that case, the radiated power is given by the Larmor formula:

$$P_{BR} = \frac{2}{3}\frac{e^2}{c^3}\left(\frac{Ze^2}{mx^2}\right)^2 \tag{2.25}$$

with x is the distance of the electron to the nucleus. Since $P_{BR} \propto x^{-4}$, the irradiated energy will only be significant for $x \sim b$, and, thus, the typical duration of the interaction is given by:

$$\Delta t \sim 2\frac{b}{v} \tag{2.26}$$

Therefore, the total energy radiated during the interaction will be:

$$P_{BR}\Delta t \sim \frac{4}{3}\frac{Z^2e^6}{c^3m^2b^3v} \tag{2.27}$$

In the frequency space, this function is approximately constant until a frequency $\nu_{max} \simeq \frac{1}{2\Delta t} = \frac{v}{4b}$, after which it decreases exponentially. Thus, the radiated energy per collision and frequency interval can be simplified as:

$$\frac{P_{BR}\Delta t}{\Delta\nu} \approx \frac{16}{3}\frac{Z^2e^6}{c^3m^2b^2v^2} \tag{2.28}$$

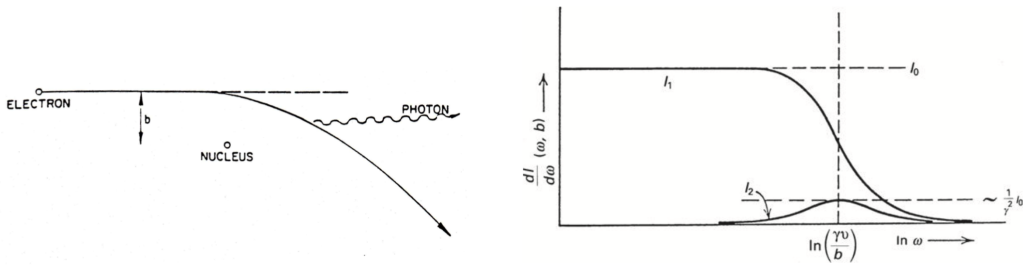

Figure 2.5: Left: Scheme of a single electron and nucleus collision with impact parameter b. Right: Bremsstrahlung spectrum due to parallel (I_1) and perpendicular (I_2) components of the electron acceleration.

For a plasma with an ion density n_Z, and an electron density n_e, if all electrons move at velocity v, the emissivity, $J_{BR}(v)$, is given by:

$$J_{BR}(v) \simeq \frac{32\pi^2}{3\sqrt{3}} \frac{Z^2 n_e n_Z e^6}{m^2 c^3} \frac{1}{v} g_{ff} \tag{2.29}$$

where $g_{ff} = \frac{\sqrt{3}}{\pi} \ln \frac{b_{max}}{b_{min}}$ is the Gaunt factor, a tabulated function of the electron energy and frequency of the emission. An example of Bremsstrahlung spectrum is shown on the right panel of Fig. 2.5.

The relativistic Bremsstrahlung emissivity for a power-law electron distribution, $n(E) = n_0 E^{-p}$, integrated over all electrons with energies Ehv, can be written as:

$$J_{BR}(v) \approx 5 \cdot 10^{-42} \frac{n_Z}{p-1} n_0 (hv)^{-p} hv \left[\frac{\text{erg}}{\text{cm}^3 \text{ s Hz}}\right] \propto \nu^{-(p-1)} \tag{2.30}$$

2.3.2 Thermal emission in galaxy clusters: temperature and density

For a thermal plasma at a temperature T where electrons follow a Maxwellian velocity distribution:

$$n_e(v)dv = 4\pi n_e \left(\frac{m}{2\pi kT}\right)^{3/2} v^2 e^{-\frac{mv^2}{2kT}} dv \tag{2.31}$$

the emissivity is given by:

$$J_{BR}(\nu, T) = 6.8 \cdot 10^{-38} Z^2 n_e n_Z T^{-1/2} e^{-\frac{hv}{kT}} g_{ff}(\nu, T) \text{ erg cm}^{-3}\text{s}^{-1}\text{Hz}^{-1} \tag{2.32}$$

In X-ray frequencies, the Gaunt factor can be written as $g_{ff}(\nu, T) = \frac{\sqrt{3}}{\pi} \ln \frac{kT}{h\nu}$.

Eq. 2.32 can be used to derive the temperature and the electron density of the plasma in the ICM, by fitting observed X-ray spectra, such as the case of the Perseus cluster shown in Fig. 2.6. Additionally, thanks to ICM being characterized by gravitational processes and Bremsstrahlung emission, self-similarity and, thus, scaling relations can be applied to galaxy clusters. Therefore, X-ray luminosity scales with ICM temperature as:

$$L_X \propto T_{gas}^2 (1+z)^{3/2} \tag{2.33}$$

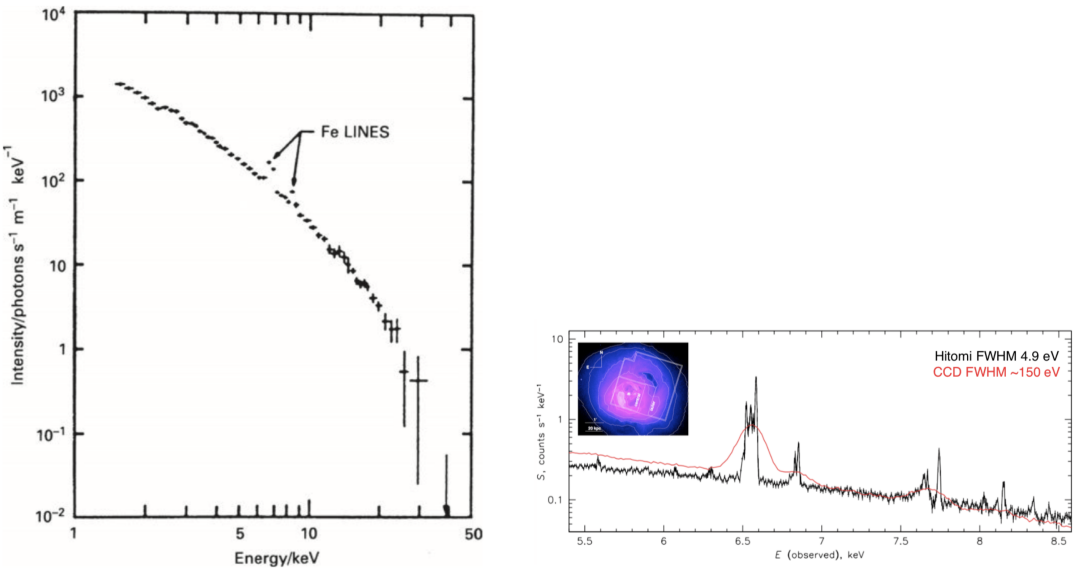

Figure 2.6: X-ray spectrum of the Perseus cluster from Mushotzky (1980) and Hitomi Collaboration (2016). By fitting the X-ray continuum with a thermal Bremsstrahlung model, a temperature of $kT = 6.5$ keV (or $T = 7.5 \cdot 10^7$ K) can be found for the hot plasma.

2.4 Extended emission line regions in radio galaxies

Extended Emission Line Regions (EELRs) in radio galaxies similar to those found in Seyfert galaxies were discovered in the last decades thanks to several observational optical campaigns (see e.g., Fosbury 1986, van Breugel et al. 1986, Stockton & MacKenty 1987). EELRs extend on scales of a few tens of kpc and can be traced by ionization lines such as Hβ, [O II], [O III], Hα, [N II] and the [S II].

In contrast with Seyfert galaxies, for which the emission mechanism underlying their EELRs is widely believed to be nuclear photoionization (see e.g., Bianchi et al. 2006), the emission mechanism and origin of the gas responsible for the EELRs in radio galaxies are still debated. Some of the plausible origins for EELRs include (i) nuclear photoionization of the narrow line region, (ii) hot gas shocked and driven out of the host galaxy by an outflow or jet, (iii) collisionally ionized gas escaping from the nucleus, and (iv) cooling of a hotter medium into warm ionized gas and collapsing into the nucleus (Baum & Heckman 1989, Tadhunter et al. 1998, Hardcastle et al. 2010, 2012, Balmaverde et al. 2012, and Reynaldi & Feinstein 2013).

BPT diagnostic diagram

Optical emission lines characteristic of the EELRs provide an optical spectroscopic classification method for radio galaxies. Firstly proposed by Baldwin et al. (1981), BPT diagrams are diagnostic tools that use selected optical emission line ratios to classify AGN. These diagrams are able to distinguish H II regions from gas clouds ionized by nuclear activity, i.e., due to the presence of an AGN, according to their [O III]/Hβ and [N II]/Hα (Kewley et al. 2001). Additionally, Kewley et al. 2006 proposed that AGN can be classified as Seyferts or LINERS according to their [O III]/Hβ, [S II]/Hα and [O I]/Hα ratios.

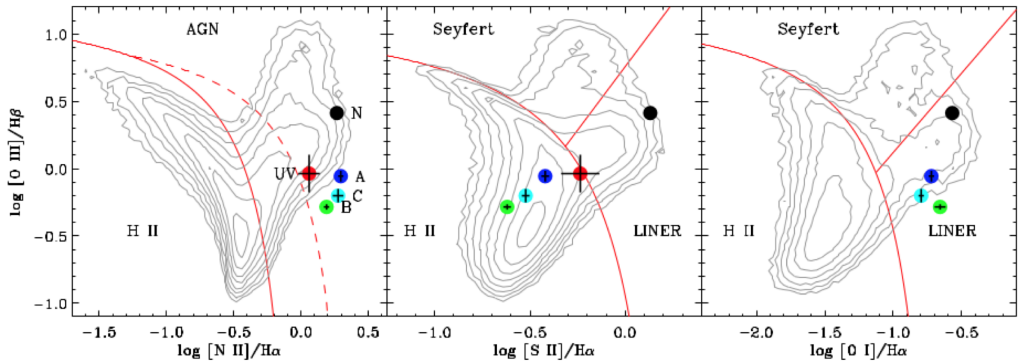

Figure 2.7: Example of a BPT diagram taken from Balmaverde et al. (2018). The colored dots mark the position of different regions of 3CR 317. The red solid curves represent the Kewley et al. (2001) theoretical upper bound for pure star formation, the red straight line shows the Kewley et al. (2006) separation between AGN and LINERs, while the dashed red curve in the [N II]λ6584 BPT is the Kauffmann et al. (2003) empirical classification separating star-forming galaxies and AGN. Contours represent the iso-densities of all SDSS/DR7 emission line galaxies (Capetti & Baldi 2011).

An example of a BPT diagram is shown in Fig. 2.7.

Ionized gas: density and mass

As shown by Osterbrock (1989) different optical emission lines can provide estimations of key parameters of the ionized gas. Throughout this work in particular, I used the ratio of the [S II] doublet 6716 and 6731 Å, R = [S II]λ6716/λ6731, to estimate the density of an emission line nebula as:

$$n_e = \frac{cR - ab}{a - R} \tag{2.34}$$

with $a = 0.4315$, $b = 2107$ and $c = 627.1$, as more recently obtained by Sanders et al. (2016). However, this estimation is only valid for $0.4375 < R < 1.4484$.

Additionally, the total mass of the ionized gas can be estimated from the total Hβ luminosity and the electron density (Osterbrock 1989) using:

$$M = 7.5 \cdot 10^{-3} \left(\frac{10^4}{n_e} \frac{L_{\mathrm{H}\beta}}{L_\odot} \right) \mathrm{M}_\odot \tag{2.35}$$

Bibliography

Baldwin, J. A., Phillips, M. M. & Terlevich, R. 1981, PASP, 93, 5

Balmaverde, B., Capetti, A., Grandi, P., et al. 2012, A&A, 545, A143

Balmaverde, B., Capetti, A., Marconi, A., et al. 2018, A&A, 612, A19

Baum, S. A. & Heckman, T. M., 1989, ApJ, 336, 681

Bianchi, S., Guainazzi, M. & Chiaberge, M. 2006, A&A, 448, 499

Blumenthal, G. R. & Gould, R. J. 1970, Reviews of Modern Physics, 42, 237

Capetti, A. & Baldi, R. D. 2011, A&A, 529, A126

Fosbury, R. A. E. 1986, in Astrophysics and Space Science Library, Vol. 121, Large scale ionized gas in radio galaxies and quasars, ed. Giuricin, G., Mezzetti, M., Ramella, M. & Mardirossian, F., 297

Ghisellini, G. 2013, Radiative Processes in High Energy Astrophysics

Govoni, F. & Feretti, L. 2004, International Journal of Modern Physics D, 13, 8

Hardcastle, M. J., Massaro, F. & Harris, D. E., 2010, MNRAS, 401, 2697

Hardcastle, M. J., Massaro, F. & Harris, D. E., 2012, MNRAS, 424, 1774

Hitomi Collaboration, 2016, Nature, 535, 117

Kauffmann, G., Heckman, T. M., Tremonti, C., et al. 2003, MNRAS, 346, 1055

Kewley, L. J., Heisler, C. A., Dopita, M. A, et al. 2001, ApJS, 132, 37

Kewley, L. J., Groves, B., Kauffmann, G., et al. 2006, MNRAS, 372, 961

Longair, M. S. 2011, High Energy Astrophysics

Mushotzky, R. 1980, The X-ray spectra of clusters of galaxies, in X-ray Astronomy, eds: Giacconi, R. & Setti, G., pp. 171–179. Dordrecht: Reidel

Osterbrock, D. E. 1989, Astrophysics of gaseous nebulae and active galactic nuclei (Mill Valley, CA: University Science Books)

Reynaldi, V. & Feinstein, C. 2013, MNRAS435, 1350

Rybicki G. B. & Lightman A. P. 1979, Radiative processes in astrophysics

Sanders, Ryan L., Shapley, A. E., Kriek, M., et al. 2016, ApJL, 825, L23

Stockton, A. & MacKenty, J. W. 1987, ApJ, 316, 584

Tadhunter, C. N., Morganti, R., Robinson, A., et al. 1998, MNRAS, 298, 1035

van Breugel, W. J. M., Fillippenko, A. V., McCarthy, P. J., et al. 1986, in Bulletin of the American Astronomical Society, Vol. 18, Spectroscopically Identical, High-Excitation Emission-Line Regions Associated with a Jet in the Radio Galaxy 3C 321, 1005

Chapter 3

Telescopes, instruments and data reduction procedures

In this chapter, I present a brief description of all resources used to carry out this Ph.D., including telescopes, instruments, archival resources, and main data reduction procedures. Unless otherwise stated, I adopted cgs units for numerical results and assumed a flat cosmology with $H_0 = 69.6$ km s^{-1} Mpc^{-1}, $\Omega_M = 0.286$ and $\Omega_\Lambda = 0.714$ (Bennett et al., 2014). Spectral indices, α, are defined by flux density, $S_\nu \propto \nu^{-\alpha}$.

3.1 Radio wavelengths

3.1.1 The Low-Frequency Array: LOFAR

LOFAR is a radio telescope network operating between 10 and 240 MHz and consisting of an interferometric array of dipole antennas. The array spans several countries, including the Netherlands, France, Germany, Ireland, Latvia, Poland, Sweden, the UK, and Italy. LOFAR antennas are distributed in 52 stations, each of them having two types of antennas: High Band Antennas (HBA, operating between 110 and 240 MHz) and Low Band Antennas (LBA, operating between 10 and 90 MHz).

Thanks to having a densely populated core of antennas and to its long baselines, LOFAR provides the highest sensitivity and angular resolution achieved in the low-frequency regime yet. Furthermore, its sub-arcsec angular resolution in the high band combined with its large field of view make LOFAR especially tailored to all-sky surveys. An example of an *uv* coverage plot and its corresponding synthesized beam for LOFAR are shown in Fig. 3.1. Furthermore, angular resolution and sensitivity as functions of frequency for different configurations[1] are shown in Fig. 3.2.

Low-frequency radio observations are particularly interesting in the study of radio galaxies since they provide insight into the older electron populations. The comparison of low-frequency and high-frequency observations of 3CR 223.1 is shown in Fig. 3.3.

[1] http://old.astron.nl/radio-observatory/astronomers/lofar-imaging-capabilities-sensitivity/lofar-imaging-capabilities/lofa

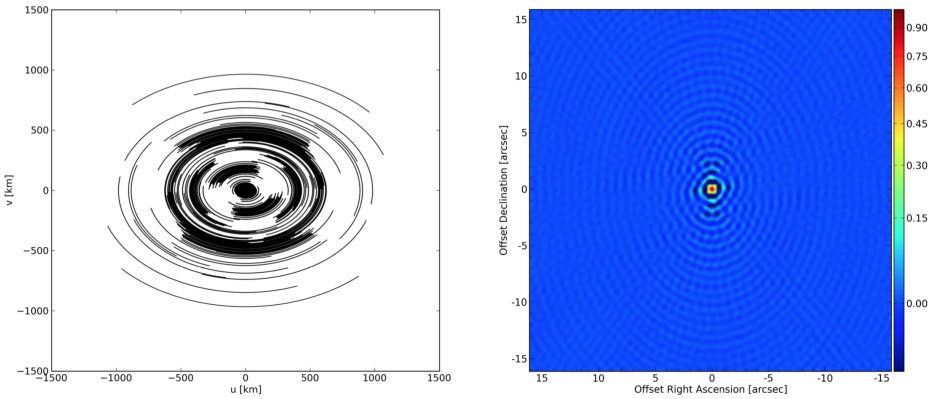

Figure 3.1: *uv* coverage (left) and synthesized beam (right) calculated for a source at a 48° declination and for a 6 h track, including all LOFAR observations (van Haarlem et al. 2013).

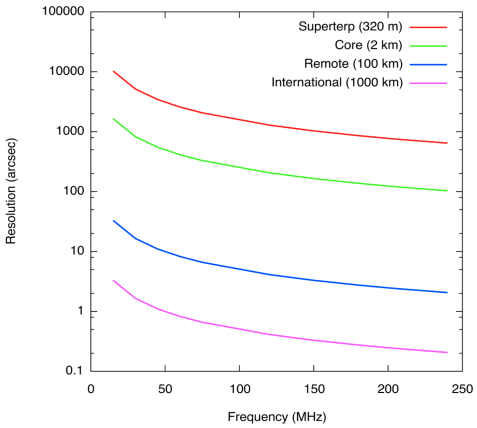

		Sensitivity			
Freq. (MHz)	λ (m)	Superterp (mJy)	NL Core (mJy)	Full NL (mJy)	Full EU (mJy)
15	20.0	...	...	...	...
30	10.0	36	9.0	5.7	3.8
45	6.67	29	7.4	4.7	3.1
60	5.00	25	6.2	3.9	2.6
75	4.00	44	10.8	6.8	4.5
120	2.50	1.5	0.38	0.30	0.20
150	2.00	1.3	0.31	0.24	0.16
180	1.67	1.5	0.38	0.30	0.20
200	1.50	(2.5)	(0.62)	(0.48)	(0.32)
210	1.43	(2.5)	(0.62)	(0.48)	(0.32)
240	1.25	(5.6)	(1.4)	(1.1)	(0.73)

Figure 3.2: Indicative LOFAR angular resolution and sensitivity for different frequencies, maximum baselines, *L*, and configurations.

3.1.2 The Karl Jansky Very Large Array: VLA

The Karl G. Jansky Very Large Array (VLA) is a radio astronomy interferometer of the National Radio Astronomy Observatory (NRAO) operating between 74 MHz and 50 GHz. The VLA consists of twenty-eight 25-meter antennas forming a Y-shaped array, with two 21-km arms and an 18-km one.

Antennas can be distributed along the array in four different main configurations that rotate throughout 16 months. The different configurations of the VLA allow for different balances between angular resolution, and surface brightness sensitivity, with maximum baselines ranging from ~1 km to ~36 km and reaching angular resolutions between 0.2″ and 0.04″. Maximum and minimum baselines, angular resolution and spatial sensitivity of the main VLA configurations available are shown in Tables 3.1. While the D configuration has the worst angular resolution of all configurations, it also provides the best spatial sensitivity, making it ideal for detecting diffuse emission. On the other hand, configuration A, despite having the worst spatial sensitivity, provides the best angular resolution, thus, this configuration is preferred to resolve finer structures.

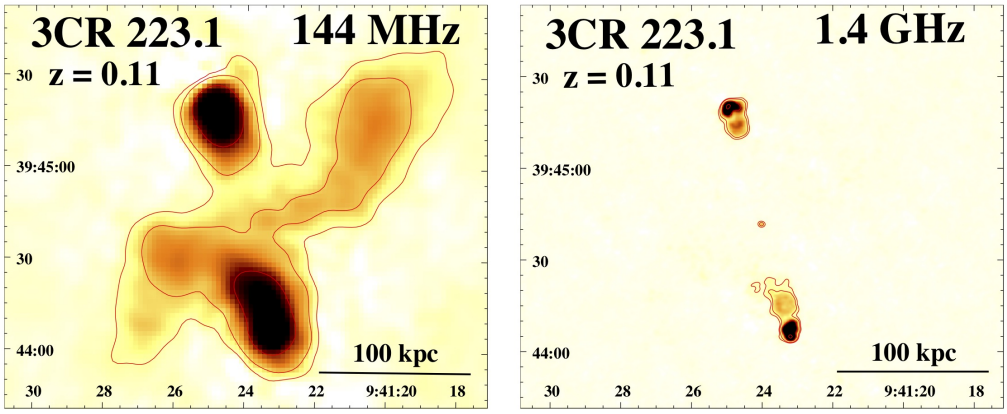

Figure 3.3: Low (left) and high (right) frequency observations of 3CR 223.1 from LOFAR and VLA, respectively.

3.1.3 Archival resources

In addition to LOFAR and VLA observations, this work took advantage of archival radio observations from the Tata Institute of Fundamental Research (TIFR) Giant Metrewave Radio Telescope (GMRT) Sky Survey (TGSS[2]) and the Multi-Element Radio-Linked Interferometer Network (MERLIN[3]), an array of seven radio telescopes with a maximum baseline of 217 km, operating between 151 MHz and 24 GHz.

The TGSS survey is a compilation of observations taken with GMRT at 150 MHz. TGSS observations have a resolution of 25″ by 25″ and a median noise of 3.5 mJy/beam. An example of the comparison of TGSS observations and radio observations at 1.4 GHz is shown in Fig. 3.4.

Table 3.1: Main VLA configurations

VLA Configuration	B_{max} (km)	B_{min} (km)	Resolution (arcsec)	LAS (arcsec)
A	36	0.7	1.3	36
B	11	0.2	4.3	120
C	3	0.04	14	970
D	1	0.04	46	970

Table 3.1: Maximum and minimum baselines, B_{max} and B_{min}, angular resolutions and largest angular scales detectable (LAS) of the main four VLA configurations.

3.2 Optical frequencies

3.2.1 The Multi Unit Spectroscopic Explorer: MUSE

MUSE (Bacon et al. 2010) is an Integral-Field Spectrograph located in the Very Large Telescope (VLT) UT4. MUSE consists of 24 integral field spectrograph units (IFUs) op-

[2]http://tgssadr.strw.leidenuniv.nl/doku.php
[3]http://www.e-merlin.ac.uk

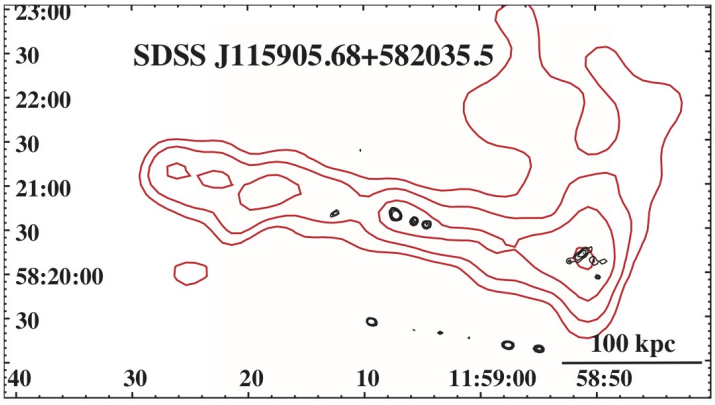

Figure 3.4: 1.4 GHz (black) and 150 MHz (red) contours of SDSS J115905.68+582035.5. 150 MHz were drawn from TGSS archival observations.

erating in the optical. It works by splitting its field of view into 24 channels, further sliced into 48 slices that are injected into a spectrograph, producing a total of 1152 medium resolution spectra. Two different observation modes are available with MUSE: Wide Field Mode (WFM) and Narrow Field Mode (NFM), both designed to take advantage of the Ground Atmospheric Layer Adaptive Corrector for Spectroscopic Imaging (GALACSI). Both, MUSE spectral resolution and efficiency are shown in Fig. 3.5 as functions of wavelength.

Table 3.2: MUSE technical specifications

WFM	
Field of View	1 arcmin^2
Spatial sampling	0.2″/pixel
Spatial resolution (FWHM)	0.3″ - 0.4″
Resolving power	1770 (4800 Å) – 3590 (9300 Å)
Limiting magnitude	V_{AB} = 22.64 mag (5500 Å)
(1 hr, airmass = 1.0,	R_{AB} = 22.70 mag (6500 Å)
seeing 0.8″V)	I_{AB}= 22.28 mag (7849 Å)
NFM	
Field of View	7.42″ x 7.43″
Spatial sampling	0.025″/pixel
Spatial resolution (FWHM)	55 mas - 80 mas
Resolving power	1740 (4800 Å) – 3450 (9300 Å)
Predicted limiting flux in 1 hr	$2.3{\cdot}10^{-18}$ erg cm^{-2} s^{-1}
Predicted limiting mag in 1 hr	R_{AB} = 22.3 mag
Predicted limiting surface brightness in 1 hr	R_{AB} = 17.3 mag arcsec^{-2}

Table 3.2: Main technical details of the two MUSE observation modes: WFM and NFM.

In WFM, a 1 arcmin^2 field of view is sampled at 0.2″/pixel, using GALACSI, the UT4 4 Laser Guide Stars (4LGS), and its Deformable Secondary Mirror (DSM) to provide Ground Layer Adaptive Optics (GLAO). In contrast, NFM provides a Laser Tomography Adaptive Optics (LTAO) corrected 7.5 arcsec^2 field of view, sampled at 0.025″/pixel.

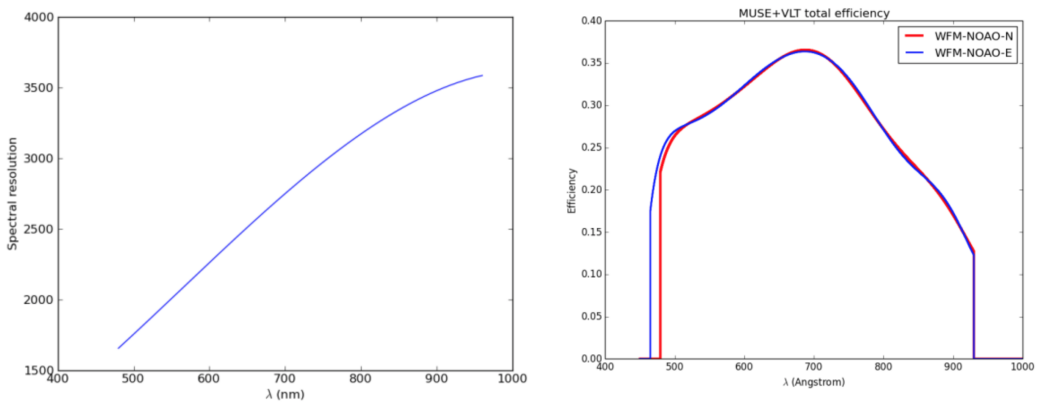

Figure 3.5: MUSE spectral resolution (left) and efficiency (right) as functions of wavelength.

MUSE images presented in this work were all taken in WFM. Main details about both observation modes are shown in Table 3.2

3.2.2 Archival resources

Apart from MUSE observations, this work also makes use of archival optical observations from the Panoramic Survey Telescope and Rapid Response System (Pan-STARRS[4]) and the Sloan Digital Sky Survey (SDSS[5]).

The Pan-STARRS archive collects wide-field images in five broadband filters (g, r, i, z and y) obtained using the 1.8 m Pan-STARRS1 telescope. The rest of the optical data used in this work was obtained from the SDSS, which is a survey aimed at mapping in detail one-quarter of the sky and at obtaining spectra of a selected number of sources. The final release of the SDSS includes 12000 square degrees of imaging and spectra of 930000 galaxies, 120000 quasars, and 460000 stars.

3.3 High energies

3.3.1 *Chandra* X-ray observatory

NASA's *Chandra* X-ray observatory, launched in 1999, is a Flagship-class space telescope still in operation. Its mission is to observe the high-energy Universe, providing better spatial resolution than any other X-ray telescope before.The *Chandra* observatory has three major elements, the spacecraft system, the X-ray telescope, and the science instruments. A summary of *Chandra* technical specifications is shown in Table 3.3.

The spacecraft system includes thrusters, thermal control systems, power supply elements, pointing, and aspect systems, as well as communication, control, and data management systems. All these elements together provide the necessary structures for the X-ray telescope and the science instruments to work.

[4]https://catalogs.mast.stsci.edu/panstarrs/
[5]http://skyserver.sdss.org/dr10/en/tools/chart/listinfo.aspx

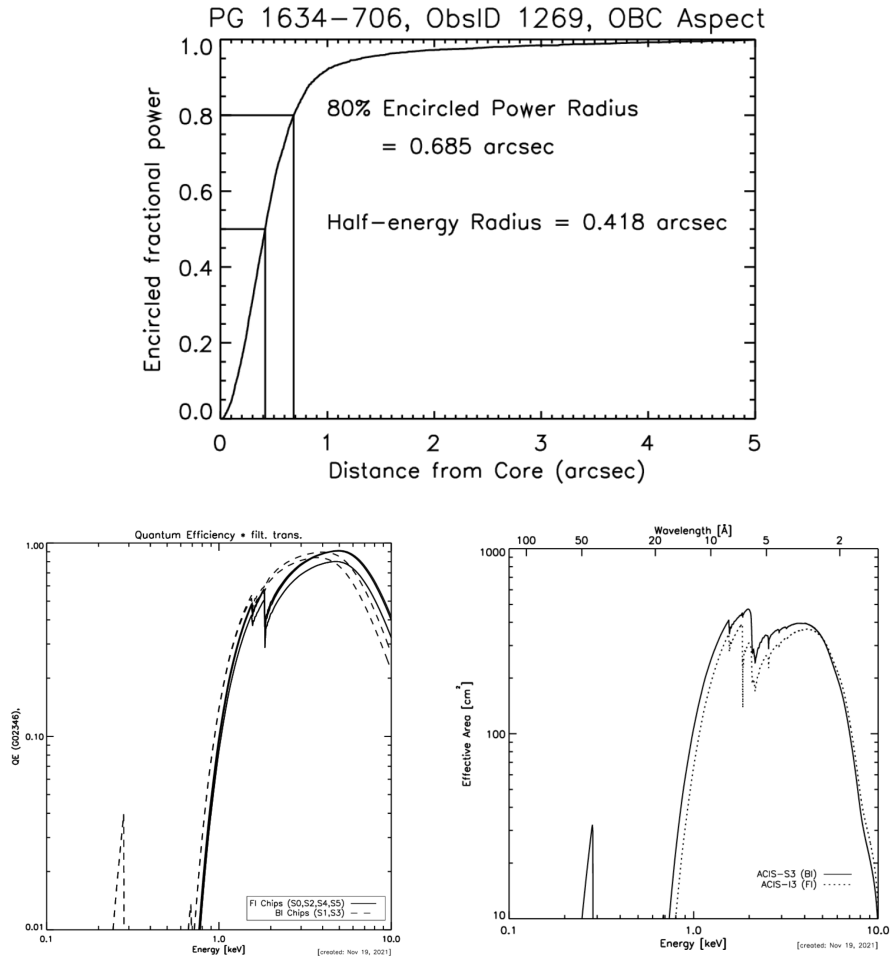

Figure 3.6: Encircled broad-band energy vs. radius for an ACIS observation of a point source (left), ACIS CCDs quantum efficiency (middle) and effective area of the ACIS CCDs (right) as a function of the energy.

The *Chandra* X-ray telescope consists of four sets of nested 2-cm cylindrical paraboloid/hyperboloid mirror pairs coated with 33 nm of iridium. Mirrors are mounted on the High-Resolution Mirror Assembly (HRMA). The very precise polishing of these mirrors provide *Chandra* with its unmatched spatial resolution, with $\sim 90\%$ of the on-axis *Chandra* point-spread function (PSF) enclosed in a circular region of $2''$ radius (see Fig. 3.6).

Chandra has four science instruments on board:

- The High-Resolution Camera (HRC) is an X-ray imager composed of two clusters of 69 million, tiny lead-oxide glass tubes. This instrument allows to determine the position of an X-ray source very precisely, thanks to having the highest spatial resolution of all *Chandra* instruments.

- The Advanced CCD Imaging Spectrometer (ACIS) is formed by an array of ten 1024 by 1024 pixels charged coupled devices (CCDs), two back-illuminated (BI) and eight front-illuminated (FI). Apart from producing X-ray images, this instrument records the energy of each X-ray photon detected. ACIS quantum efficiency and effective area as functions of energy are shown in Fig. 3.6.

- The two high-resolution spectrometers aboard of *Chandra* are the High Energy Transmission Grating Spectrometer (HETGS) and the Low Energy Transmission Grating Spectrometer (LETGS). These two instruments are diffraction gratings that can be used together with either HRC or ACIS to provide higher spectral resolution than ACIS.

A summary of the main technical details of *Chandra* science instruments is shown in Table 3.3. All *Chandra* images in this work were obtained using ACIS.

Table 3.3: *Chandra* technical specifications

ACIS	
Energy range	0.2 - 10 keV
Pixel size	0.492″
ACIS-I array size	16.9′ by 16.9′
ACIS-S array size	8.3′ by 50.6′
Sensitivity	$4{\cdot}10^{-15}$ erg cm^{-2} s^{-1} in 104 s (0.4 to 6.0 keV)
HRC	
Energy range	0.08 - 10 keV
Spatial resolution	0.4″
HRC-I field of view	30′ by 30′
HRC-S field of view	6′ by 90′
Limiting sensitivity	$9{\cdot}10^{-16}$ erg cm^{-2} s^{-1}
HETGS	
Energy range	0.4 - 10 keV
Spectral resolution	60 - 1000
LETGS	
Energy range	0.09 - 3 keV
Spectral resolution	40 - 2000

Table 3.3: Main technical details of the four instruments aboard of *Chandra*: ACIS, HRC, HETGS and LETGS.

3.4 Analyzed sources

In this section, I present a summary of the information regarding all sources discussed in this work. Tables 3.4, 3.6, and 3.8 collect the main characteristics of those sources in Chapters 4, 5, 6, and 7; while the main parameters of *Chandra*, MUSE, VLA, and LOFAR observations used are shown in Tables 3.5, 3.7, and 3.9.

3.4.1 Sample in Chapter 4

Sources presented in Chapter 4 are the last 9 sources to be introduced to the 3CR *Chandra* Snapshot Survey, with $1.5 < z < 2.5$ and known optical counterparts, observed by *Chandra* during Cycle 20.

Table 3.4: Characteristic of all sources in Chapter 4.

3CR Name	Radio/optical Class	R.A. (J2000) (hh mm ss)	Dec. (J2000) (dd mm ss)	z	kpc scale (kpc/arcsec)
239	FR II/HERG	10 11 45.284	+46 28 18.79	1.781	8.598
249	LDQ	11 02 03.774	-01 16 16.67	1.554	8.612
257	RG	11 23 09.391	+05 30 18.50	2.474	8.245
280.1	LDQ	13 00 33.364	+40 09 07.28	1.667	8.615
322	FR II	15 35 01.269	+55 36 52.33	1.681	8.614
326.1	RG	15 56 10.170	+20 04 20.73	1.825	8.586
418	QSO	20 38 37.042	+51 19 12.43	1.686	8.613
454	CSS	22 51 34.722	+18 48 40.02	1.757	8.603
454.1	CSS	22 50 33.067	+71 29 18.02	1.841	8.582

Table 3.4: Column description: (1) Source name; (2) radio and optical classification; (3,4) coordinates; (5) redshift; (6) kpc scale.

Table 3.5: Observation log of all sources in Chapter4.

3CR Name	*Chandra* Obs. ID.	*Chandra* exposure time (ks)	MUSE seeing (arcsec)	VLA freq. (GHz)	Beam size (arcsec)	LOFAR freq. (MHz)	Beam size (arcsec)
239	21395	18	–	1.4	1.29	–	–
249	21396	18	–	4.9	0.46	–	–
257	21397	18	–	4.9	0.47	–	–
280.1	21398	18	–	1.4	1.54	–	–
322	21399	18	–	4.8	0.55	–	–
326.1	21400	18	–	4.8	1.51	–	–
418	21401	18	–	4.8	0.39	–	–
454	21403	18	–	8.4	0.26	–	–
454.1	21402	18	–	4.8	0.42	–	–

Table 3.5: Column description: (1) Source name; (2) *Chandra* Observation ID; (3) *Chandra* exposure time; (4) MUSE seeing; (5) VLA frequency; (6) VLA beam size; (7) LOFAR frequency; (8) LOFAR beam size.

3.4.2 Sample in Chapter 5

The sample used in Chapter 5 includes 35 3CR radio galaxies with a classical FR II radio morphology (i.e., edge-brightened, Fanaroff & Riley 1974) and angular sizes larger than 5″ observed during the 3CR *Chandra* Snapshot Survey before Cycle 20, for which a dedicated study was neither published nor in preparation (i.e., 3CRR sources, 3CR 187, 3CR 196.1, and 3CR 320).

Table 3.6: Characteristic of all sources in Chapter 5.

3CR Name	Radio/optical Class	R.A. (J2000) (hh mm ss)	Dec. (J2000) (dd mm ss)	z	kpc scale (kpc/arcsec)
18	FR II/BLRG	00 40 50.53	+10 03 26.65	0.188	3.167
44	FR II/HERG	01 31 21.65	+06 23 43.14	0.66	7.059
52	FR II/HERG	01 48 28.91	+53 32 28.04	0.29	4.389
54	FR II/HERG	01 55 30.26	+43 45 59.05	0.827	7.694
63	FR II/HERG	02 20 54.30	-01 56 50.65	0.175	2.990
69	FR II/HERG	02 38 02.66	+59 11 50.50	0.458	5.878
103	FR II	04 08 03.22	+43 00 33.93	0.33	4.796

107	FR II/HERG	04 12 22.62	-00 59 32.69	0.785	7.556
114	FR II/LERG	04 20 22.23	+17 53 56.86	0.815	7.655
133	FR II/HERG	05 02 58.47	+25 16 25.27	0.2775	4.254
135	FR II/HERG	05 14 08.36	+00 56 32.48	0.1273	2.294
165	FR II/LERG	06 43 07.40	+23 19 02.60	0.2957	4.449
166	FR II/LERG	06 45 24.10	+21 21 51.27	0.2449	3.883
169.1	FR II/HERG	06 51 14.83	+45 09 28.48	0.633	6.931
180	FR II/HERG	07 27 04.88	-02 04 30.34	0.22	3.581
197.1	FR II/HERG	08 21 33.60	+47 02 37.15	0.1282	2.307
198	FR II/HERG	08 22 33.58	+05 56 30.82	0.0814	1.545
223.1	FR II/HERG	09 41 24.02	+39 44 41.71	0.1075	1.979
268.2	FR II/HERG	12 00 58.73	+31 33 21.55	0.362	5.096
272	FR II/HERG	12 24 28.44	+42 06 36.51	0.944	8.005
287.1	FR II/HERG	13 32 53.27	+02 00 45.86	0.2156	3.526
293.1	FR II/HERG	13 54 40.52	+16 14 43.15	0.709	7.272
306.1	FR II/HERG	14 55 01.41	-04 20 59.94	0.441	5.751
313	FR II/HERG	15 11 00.04	+07 51 50.15	0.461	5.900
332	FR II/HERG	16 17 42.54	+32 22 34.39	0.151	2.649
357	FR II/LERG	17 28 20.11	+31 46 02.55	0.166	2.866
379.1	FR II/HERG	18 24 33.00	+74 20 58.87	0.256	4.013
403.1	FR II/LERG	19 52 30.44	-01 17 22.35	0.0554	1.083
411	FR II/HERG	20 22 08.43	+10 01 11.38	0.467	5.943
430	FR II/LERG	21 18 19.10	+60 48 07.68	0.0555	1.086
434	FR II/LERG	21 23 16.24	+15 48 05.80	0.322	4.718
435A	FR II/BLRG	21 29 05.45	+07 32 59.75	0.471	5.971
435B	FR II	21 29 06.10	+07 32 54.80	0.865	7.804
456	FR II/HERG	23 12 28.08	+09 19 26.39	0.233	3.741
458	FR II/HERG	23 12 52.08	+05 16 49.80	0.289	4.378

Table 3.6: Column description: (1) Source name; (2) radio and optical classification; (3,4) coordinates; (5) redshift; (6) kpc scale.

Table 3.7: Observation log of all sources in Chapter 5.

3CR Name	*Chandra* Obs. ID.	*Chandra* exposure time (ks)	MUSE seeing (arcsec)	VLA freq. (GHz)	Beam size (arcsec)	LOFAR freq. (MHz)	Beam size (arcsec)
18	9293	8	0.53	1.4	1.70	150	6
44	16048	12	–	1.4	1.46	–	–
52	9296	8	–	1.4	3.59	–	–
54	16049	12	–	8.0	0.40	150	6
63	12722	8	0.49	1.4	1.36	–	–
69	18092	12	–	4.9	5.00	–	–
103	13874	12	–	1.4	3.27	–	–
107	16052	12	–	4.9	0.46	–	–
114	16053	12	–	1.4	1.27	–	–
133	9300	8	–	1.4	0.98	–	–
135	9301	8	0.52	8.4	0.66	–	–
165	9303	8	–	1.4	3.36	–	–
166	12727	8	–	1.4	1.37	–	–
169.1	16056	12	–	1.4	1.37	–	–
180	12728	8	1.45	8.4	0.36	–	–
197.1	9306	8	–	4.8	1.32	–	–
198	12730	8	0.78	4.8	25.9	150	6
223.1	9308	8	–	1.4	1.67	150	6
268.2	13876	12	–	1.4	1.61	150	6
272	16061	12	–	1.4	5.40	150	6

287.1	9309	8	0.65	1.4	5.00	–	–
293.1	16066	12	–	1.4	5.40	150	6
306.1	13885	12	–	4.8	1.75	–	–
313	13886	12	–	8.4	2.43	150	6
332	9315	8	–	1.4	4.40	150	6
357	12738	8	–	4.8	1.92	150	6
379.1	12739	8	–	4.8	1.55	–	–
403.1	12741	8	0.80	0.3	7.03	–	–
411	13889	12	–	1.4	1.30	–	–
430	12744	8	–	4.8	1.34	150	6
434	13878	12	–	1.4	1.40	–	–
435A	13890	12	–	4.8	1.76	–	–
435B	13890	12	–	4.8	1.76	–	–
456	12746	8	1.27	1.4	1.43	–	–
458	12747	8	0.50	1.4	6.40	–	–

Table 3.7: Column description: (1) Source name; (2) *Chandra* Observation ID; (3) *Chandra* exposure time; (4) MUSE seeing; (5) VLA frequency; (6) VLA beam size; (7) LOFAR frequency; (8) LOFAR beam size.

3.4.3 Sample in Chapters 6 and 7

Sources presented in Chapter 6 are two radio galaxies harbored in cool core galaxy clusters and showing signatures of feedback, ionized gas filaments and an X-ray cavity. Additionally, the sample used throughout Chapter 7 includes 15 radio galaxies at $z < 0.3$ presenting resolved optical and X-ray diffuse emission and for which diffuse X-ray emission is not dominated by thermal ICM.

Table 3.8: Characteristic of all sources in Chapters 6 and 7.

3CR Name	Radio/optical Class	R.A. (J2000) (hh mm ss)	Dec. (J2000) (dd mm ss)	z	kpc scale (kpc/arcsec)
15	FR I/LERG	00 37 04.11	-01 09 08.47	0.073	1.398
17	FR II/BLRG	00 38 20.53	-02 07 40.50	0.22	3.581
18	FR II/BLRG	00 40 50.53	+10 03 26.65	0.188	3.167
29	FR I/LERG	00 57 34.90	-01 23 27.44	0.045	0.890
33	FR II/HERG	01 08 52.88	+13 20 14.36	0.060	1.167
40	FR I/LERG	01 26 00.62	-01 20 42.56	0.018	0.268
63	FR II/HERG	02 20 54.30	-01 56 50.65	0.175	2.990
76.1	FR I	03 03 15.00	+16 26 19.19	0.032	0.643
78	FR I/LERG	03 08 26.21	+04 06 39.37	0.029	0.585
79	FR II/HERG	03 10 00.09	+17 05 58.53	0.256	4.012
88	FR II/LERG	03 27 54.20	+02 33 42.16	0.030	0.604
89	FR I	03 34 15.57	-01 10 56.15	0.139	2.470
98	FR II/HERG	03 58 54.43	+10 26 02.58	0.030	0.604
105	FR II/HERG	04 07 16.45	+03 42 25.73	0.089	1.673
135	FR II/HERG	05 14 08.36	+00 56 32.48	0.1273	2.294
180	FR II/HERG	07 27 04.88	-02 04 30.34	0.22	3.581
196.1	HYMOR	08 15 27.793	-03 08 26.68	0.198	3.299
198	FR II/HERG	08 22 33.58	+05 56 30.82	0.0814	1.545
227	FR II/BLRG	09 47 45.13	+07 25 20.97	0.086	1.623
264	FR I/LERG	11 45 05.02	+19 36 22.76	0.022	0.447
272.1	FR I/LERG	12 25 03.73	+12 53 13.17	0.003	0.062
287.1	FR II/HERG	13 32 53.27	+02 00 45.86	0.2156	3.526
296	FR I/LERG	14 16 52.95	+10 48 26.75	0.025	0.507

300	FR II/HERG	14 22 59.86	+19 35 36.70	0.27	4.171
318.1		15 21 51.879	+07 42 32.03	0.0453	0.896
327	FR II/HERG	16 02 27.35	+01 57 56.22	0.105	1.939
348	FR I/LERG	16 51 08.13	+04 59 33.81	0.155	2.706
353	FR II/LERG	17 20 28.17	-00 58 46.56	0.030	0.604
386	FR II	18 38 26.23	+17 11 50.07	0.017	0.348
403	FR II/HERG	19 52 15.80	+02 30 24.31	0.089	1.149
424	FR II/LERG	20 48 12.09	+07 01 17.17	0.127	2.287
442	FR II/LERG	22 14 46.88	+13 50 27.57	0.026	0.526
445	FR I/BLRG	22 23 49.55	-02 06 13.03	0.056	1.094
456	FR II/HERG	23 12 28.08	+09 19 26.39	0.233	3.741
458	FR II/HERG	23 12 52.08	+05 16 49.80	0.289	4.378

Table 3.8: Column description: (1) Source name; (2) radio and optical classification; (3,4) coordinates; (5) redshift; (6) kpc scale.

Table 3.9: Observation log of all sources in Chapters 6 and 7.

3CR Name	*Chandra* Obs. ID.	*Chandra* exposure time (ks)	MUSE seeing (arcsec)	VLA freq. (GHz)	Beam size (arcsec)	LOFAR freq. (MHz)	Beam size (arcsec)
15	17128	130	0.65	8.4	0.34	–	–
17	9292	8	0.49	4.9	0.42	–	–
18	9293	8	0.53	1.4	1.70	150	6
29	12721	8	0.51	4.9	5.09	–	–
33	6910	20	0.63	4.9	1.35	–	–
40	7823	65	0.40	1.4	4.66	–	–
63	12722	8	0.49	1.4	1.36	–	–
76.1	9298	8	0.62	1.4	4.02	–	–
78	4157	55	0.53	4.9	4.67	–	–
79	12723	8	0.66	1.4	1.50	–	–
88	11977	50	0.59	4.9	4.42	–	–
89	14028	39	0.64	1.4	1.47	–	–
98	10234	30	0.66	8.4	2.00	–	–
105	9299	8	0.71	8.4	2.20	–	–
135	9301	8	0.52	8.4	0.66	–	–
180	12728	8	1.45	8.4	0.36	–	–
196.1	12729	8	0.48	8.4	0.30	–	–
198	12730	8	0.78	4.8	25.9	150	6
227	6842	30	0.91	1.4	2.04	–	–
264	4916	40	0.85	4.9	1.31	–	–
272.1	20543	55	0.39	4.9	4.35	–	–
287.1	9309	8	0.65	1.4	5.00	–	–
296	3968	50	1.08	8.4	0.75	–	–
300	9311	8	0.41	8.4	2.10	–	–
318.1	900	60	1.38	1.4	4.54	–	–
327	6841	40	0.70	8.4	2.20	–	–
348	6257	50	1.76	1.4	1.93	–	–
353	7886	72	1.30	8.4	0.44	–	–
386	10232	30	0.61	1.4	4.06	–	–
403	2968	50	0.54	8.4	0.75	–	–
424	12743	8	0.98	8.4	0.25	–	–
442	6392	36	0.61	1.4	7.50	–	–
445	7869	50	1.48	1.4	4.90	–	–
456	12746	8	1.27	1.4	1.43	–	–
458	12747	8	0.50	1.4	6.40	–	–

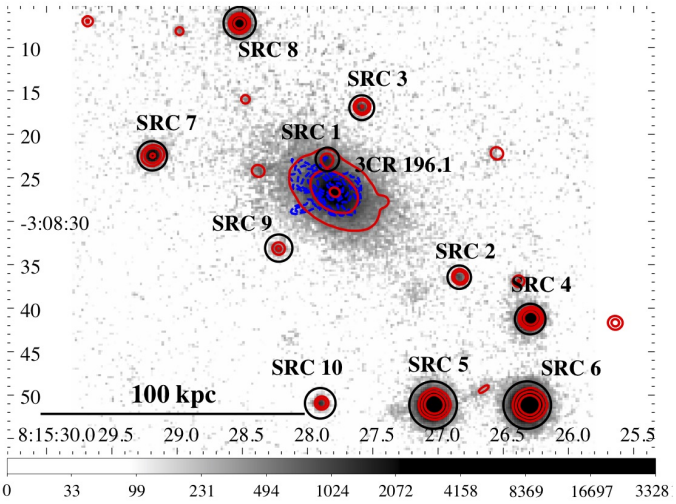

Figure 3.7: *r*-band PanSTARRS image of 3CR 196.1 with white light MUSE contours overlaid in red and Hα + [N II] contours overlaid in blue. With the final shift applied to the MUSE cube (3.1″) I obtained a good alignment for the rest of field sources, with an rms of 0.18″.

.

Table 3.9: Column description: (1) Source name; (2) *Chandra* Observation ID; (3) *Chandra* exposure time; (4) MUSE seeing; (5) VLA frequency; (6) VLA beam size; (7) LOFAR frequency; (8) LOFAR beam size.

3.5 Data reduction procedures

3.5.1 MUSE data sets

Astrometric registration

Astrometry in MUSE data is known to be off by several arcseconds, therefore performing an astrometric registration with MUSE data is a crucial step in the data reduction and large shifts are expected. MUSE astrometric registration was carried out by comparing VLA[6], Pan-STARRS[7] *r*-band, MUSE, and *Chandra* images. Lastly, I verified that the final shifts provided a good alignment for the rest of field sources. As an example, the results of the astrometric registration for 3CR 196.1 are shown in Fig. 3.7.

Continuum subtraction and spectral fitting

I obtained the fully reduced data cubes from the ESO archive[8]. I subtracted the continuum spaxel by spaxel from the archival MUSE reduced data in two different ranges, the

[6]https://science.nrao.edu/facilities/vla/archive/index
[7]https://catalogs.mast.stsci.edu/panstarrs/
[8]http://archive.eso.org/scienceportal/home

blue range, from 5370 to 6170Å, and the red range, from 7170 to 8680Å, by fitting the continuum in each range using a power law. I fitted the Hβ and [O III]$\lambda\lambda$4960, 5008 lines in the continuum subtracted blue range and the [O I]λ6300, Hα, [N II]$\lambda\lambda$6548, 6584 and [S II]$\lambda\lambda$6718, 6733 lines in the continuum subtracted red range. In general, I fitted each line with a single Gaussian component, fixing the wavelength separation between lines and the line ratio of [N II]$\lambda\lambda$6548, 6584 and [O III]$\lambda\lambda$4960, 5008 components, to their theoretical value of 1/3 (adopting CASE B, see Osterbrock & Ferland 2006).

3.5.2 *Chandra* observations

Chandra data reduction for all selected observations was carried out following the same procedures described in the *Chandra* Interactive Analysis of Observations (CIAO; Fruscione et al. 2006) threads[9] and using CIAO v4.11 and *Chandra* Calibration Database v4.8.2. Here, I report basic details and differences, specifically adopted to achieve my goals, with respect to previous analyses (see e.g., Massaro et al. 2010 and Massaro et al. 2011b for additional information).

Astrometric registration between radio and X-ray images was performed by adopting the same procedure used by previous papers on the 3CR *Chandra* Snapshot Survey (see Massaro et al. 2010; Massaro et al. 2012; Massaro et al. 2013; Massaro et al. 2018; Stuardi et al. 2018) and deviating from those results by $< 1''$. Frequencies and beam sizes of radio maps, obtained from the VLA archive, used in each case, are reported in Tables 3.5, 3.7, and 3.9.

The *Chandra* native pixel size for the ACIS instrument is $0.492''$, while the half-energy radius is $0.418''$, so data are under-sampled[10]. To recover the resolution, images were often regridded to 1/2, 1/4, or 1/8 of the native ACIS pixel size, according to the angular sizes of radio sources and to their number of counts (see also Massaro et al. 2012, 2013 for more details).

In the cases where I removed point-like sources from the *Chandra* images (either to highlight the presence of X-ray extended emission or to create X-ray surface brightness profiles), the procedure adopted is reported in the following. I detected point-like sources in the range 0.5 - 7 keV using the WAVDETECT task, available in CIAO, with a sequence of $\sqrt{2}$ wavelet scales, from 1 to 16 to cover different size sources, and a false-positive probability threshold set to the value of 10^{-6}, which is the value recommended for a 1024 $\times$ 1024 image in the CIAO threads[11] to make sure I do not over-subtract point sources. Next, I generated corresponding elliptical regions using the ROI task and with the DMFILTH task I built the final point-like source subtracted images. DMFILTH replaces counts in each region where a point-like source is detected, as defined by ROI, by sampling the Poisson distribution of the pixel values in concentric background regions. As an example in Fig. 3.8, I show the field of 3CR 313, marking the point-like sources detected by WAVDETECT.

Since some of the background and foreground X-ray sources could be active galaxies (see e.g., Horst et al. 2008, Eckart et al. 2010, Massaro et al. 2011a, and Assef et al. 2013), I tested if the X-ray sources detected with *wavdetect* have a mid-infrared counterpart in the recent release of the Wide-field Infrared Survey Explorer (*WISE*) catalog (i.e., *AllWISE*[12]).

[9] http://cxc.harvard.edu/ciao/threads/
[10] https://cxc.harvard.edu/proposer/POG/pdf/MPOG.pdf
[11] https://cxc.harvard.edu/ciao/threads/wavdetect/
[12] http://wise2.ipac.caltech.edu/docs/release/allwise/

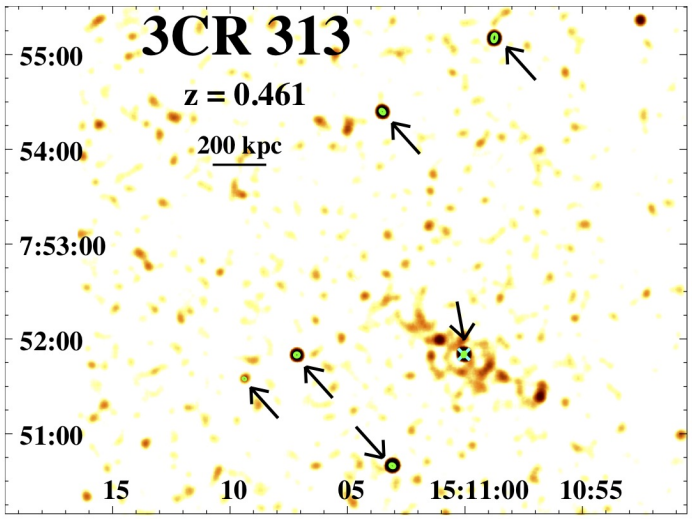

Figure 3.8: 0.5 - 3 keV *Chandra* image of 3CR 313. Point-like sources detected in the 3CR 313 field using WAVEDETECT are marked with black arrows. The image has been smoothed using a Gaussian kernel radius of 4.92″. The position of the nucleus is marked with a cross. Point sources marked are removed during the point source subtraction. This image shows how effective WAVDETECT is at detecting point sources with the parameters selected.

Within a circle of radius of 30″ centered in the 3CR sources all point sources from the *AllWISE* catalog with X-ray counterparts were detected by WAVDETECT. Therefore, this suggests that the thresholds chosen to run WAVDETECT are reliable.

Source detection

I defined the position of X-ray nuclei and lobes using radio maps. However, when the core was not detected in radio, the position of the X-ray nucleus was defined as the emission peak in the 5 - 7 keV band since I expect nuclei to have hard spectra in the X-ray band.

X-ray detection significance for any X-ray feature (i.e., nuclei, X-ray counterparts of hotspots or lobes, or thermal ICM emission) was estimated using the following procedure:

1. I computed the background, choosing an appropriate region;
2. I identified a region for the X-ray feature;
3. I computed the number of photons in the region containing the X-ray feature;
4. Assuming the number of photons in the background follows a Poissonian distribution with mean the number of photons that I measured for the background region, I compute the probability of detecting the observed number of photons in the region containing the X-ray feature. Detection probability is indicated using the Gaussian equivalent σ.

X-ray photometry: flux maps

X-ray flux maps were created by taking into account the exposure time and the effective area. I obtained maps in the X-ray energy ranges: 0.5 – 1 keV (soft), 1 – 2 keV (medium), and 2 – 7 keV (hard) by using monochromatic exposure maps set to the nominal energies of 0.75, 1.4, and 4 keV for the soft, medium and hard bands, respectively. All flux maps were converted from units of counts s^{-1} cm^{-2} to cgs units by multiplying each event by the nominal energy of each band, assuming that every event in the same band has the same energy (see Massaro et al. 2015).

Observed X-ray fluxes were measured using circular regions of 2″ radii centered on the X-ray nuclei and, for extended structures, circular regions containing the radio emission at more than three times the root mean square (rms) level of the background in the radio maps and centered on the peak of the radio emission. Typical background regions were chosen as circular regions at least as big as the radio sources and located on the same CCD chip, far enough from the radio galaxy (i.e., at least a few tens of arcsec) to avoid the smearing of the PSF on CCD borders and contamination from the source. Average background level in *Chandra* images is ~0.02 photons $pixel^{-1}$.

Fluxes were measured in each energy band and region using funtools[13] and assuming a flat energy response in each band as in previous analyses (see Massaro et al. 2015). Uncertainties were computed assuming Poisson statistics (i.e., square root of the number of photons) in the source and background regions. X-ray fluxes were not corrected for the Galactic absorption, as in previous analyses (see e.g., Massaro et al. 2015), since due to the low exposures of Chandra images used, this second-order correction is not significant with respect to the flux uncertainty. X-ray luminosities were not corrected for neutral hydrogen column densities (either galactic or intrinsic).

Spectral analysis

In the cases where I performed a spectral analysis of the thermal emission in X-ray images, I chose, as background a larger circle located where no point-like and/or extended X-ray sources are detected.

Background subtracted X-ray spectra in the 0.5–4 keV energy range were extracted using the CIAO routine SPECEXTRACT and analyzed using Sherpa v4.12.1 (Freeman et al. 2001). To ensure the validity of Gaussian statistics, spectral data were binned to at least 25 photons per bin.

I first try fitting the final spectra using an absorbed bremsstrahlung model, however, whenever it fails to reproduce the soft X-ray spectra below 2 keV, I adopt a collisional ionization gas model (XSAPEC[14]), absorbed by Galactic hydrogen column density (XSWABS[15]; Kalberla et al. 2005). This XSAPEC model has three free parameters: normalization, plasma temperature kT, and metal abundance Z.

Surface brightness profiles

I computed 0.5 - 3 keV, exposure corrected X-ray surface brightness profiles in two directions: (i) along the radio axis and (ii) perpendicular to the radio axis. To estimate the

[13] http://www.cfa.harvard.edu/~john/funtools
[14] https://cxc.cfa.harvard.edu/sherpa/ahelp/xsapec.html
[15] https://cxc.cfa.harvard.edu/sherpa/ahelp/xswabs.html

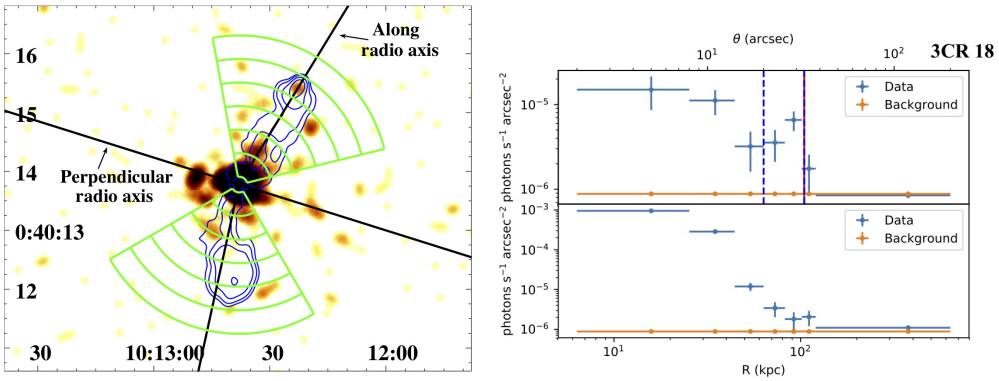

Figure 3.9: Left: Directions along and perpendicular to the radio axis chosen for 3CR 18, as well as bins along the radio axis. The image shows the X-ray emission between 0.5 and 3 keV with 1.4 GHz VLA contours overlaid in blue. *Chandra* image has a pixel size of 0.25″ and it was smoothed with a Gaussian kernel of 3″ radius. These directions and bins were chosen based on the radio morphology and used to make surface brightness profiles. Right: Surface brightness profiles of 3CR 18. The top profile corresponds to the profile along the radio axis, while the bottom one corresponds to the direction perpendicular to the radio axis. The orange points show the background level in each case. The red vertical line marks the extension of the radio emission along the radio axis while the dashed blue lines mark the position of the hotspots.

background, I used blank-sky files available in the *Chandra* Calibration Database. Final background event files were obtained by re-projecting blank-sky files to the same tangent planes as observations. Next, I renormalized exposure times of background event files, making observation count rates in the 9 - 12 keV band match background files count rates in the same band, where I expect emission to come mainly from particle background (same procedure adopted and described in Hickox & Markevitch 2006).

Left panel of Fig. 3.9 shows an example of the bins chosen for 3CR 18, while the right panel shows the resulting X-ray surface brightness profiles. I chose regions along the radio axis on the basis of the radio emission (as shown in the left panel of Fig. 3.9). Once these regions were chosen, I built radial bins with fixed widths of 4″ to 8″, depending on the scale of each source, up to the maximum extent of the radio contours. Beyond the radio structure, I extended the radial profiles until a signal-to-noise ratio (SNR) of three was achieved or once a maximum radius (set to be inside the CCD chip) was reached.

Bibliography

Assef, R. J., Stern, D., Kochanek, C. S., et al. 2013, ApJ, 772, 26

Bacon, R., Accardo, M., Adjali, L., et al. 2010, in Society of Photo-Optical Instrumentation Engineers (SPIE) Conference Series, Vol. 7735, Proc. SPIE, 773508

Bennett, C. L., Larson, D., Weiland, J. L., et al. 2014 ApJ, 794, 135

Eckart, M. E., McGreer, I. D., Stern, D., et al. 2010, ApJ, 708, 584

Freeman, P., Doe, S., & Siemiginowska, A. 2001, Proc. SPIE, 4477, 76

Fruscione, A., McDowell, J. C., Allen, G. E., et al. 2006, Society of Photo-Optical Instrumentation Engineers (SPIE) Conference Series, 6270, 62701V

Hickox, R. C. & Markevitch, M. 2006, ApJ, 645, 95

Horst, H., Gandhi, P., Smette, A., et al. 2008, A&A, 479, 389

Kalberla, P. M. W., Burton, W. B., Hartmann, D., et al. 2005, A&A, 440, 775

Massaro, F., Harris, D. E., Tremblay, G. R., et al. 2010, ApJ, 714, 589

Massaro, F., D'Abrusco, R., Ajello, M., et al. 2011, ApJ, 740, L48

Massaro, F., Harris, D. E. & Cheung, C. C. 2011, ApJS, 197, 24

Massaro, F., Tremblay, G. R., Harris, D. E., et al. 2012, ApJS, 203, 31

Massaro, F., Harris, D. E., Tremblay, G. R., et al. 2013, ApJS, 206, 7

Massaro, F., Harris, D. E., Liuzzo, E., et al. 2015, ApJS, 220, 5

Massaro, F., Missaglia, V., Stuardi, C., et al. 2018, ApJS, 234, 7

Osterbrock, D. E. & Ferland, G. J. 2006, Astrophysics of gaseous nebulae and active galactic nuclei (2nd ed.; Sausalito, CA: Science Books)

Stuardi, C., Missaglia, V., Massaro, F., et al. 2018, ApJS, 235, 32

van Haarlem, M. P., Wise, M. W., Gunst, A. W., et al. 2013, A&A, 556, A2

Chapter 4

Completing the 3CR X-ray observations at high redshift

This chapter is dedicated to the analysis of nine radio sources belonging to the Third Cambridge Revised catalog (3CR) observed with *Chandra* during Cycle 20 in the redshift range between 1.5 and 2.5. It is organized as follows. A brief overview of the sample selection is given in § 4.1 while results are described in § 4.2. Notes on the 9 3CR radio galaxies are collected in § 4.3. Then, § 4.4 is devoted to a summary and discussion of this chapter.

The main goal of this chapter is to complete the X-ray coverage of all identified, i.e., with optical counterpart, 3CR sources, which was completed up to $z < 0.15$ by 2018.

4.1 Sample selection

The last sources to be introduced to the 3CR *Chandra* Snapshot Survey were those with $1.5 < z < 2.5$ and known optical counterparts, observed by *Chandra* during Cycle 20. Sources fulfilling these criteria are 9, namely 3CR 239, 3CR 249, 3CR 257, 3CR 280.1, 3CR 322, 3CR 326.1, 3CR 418, 3CR 454, and 3CR 454.1. These are the highest redshift (from 1.554 to 2.474) sources listed in the 3CR *Chandra* Snapshot Survey.

This sample is particularly interesting since it covers the highest redshift identified extragalactic sources in the 3CR catalog and, therefore, these are the highest redshift sources observed so far during the 3CR *Chandra* Snapshot Survey. However, the high redshift prevents me from resolving hotspot emission from lobe emission and, therefore, I label as lobes all extended structures not being nuclei.

Out of the 9 sources included in the sample, only three, namely, 3CR 280.1, 3CR 418 and 3CR 454 were registered since radio nuclei could not be detected using radio maps available for the remaining sources. For sources registered, the total shift was of the order of 0.5″ or less, which corresponds to ~4 kpc at redshifts 1.5 - 2.5, consistent with previous campaign papers.

X-ray images of all sources in the sample with radio contours overlaid are shown in Figs. 4.1, 4.2, 4.3, 4.4, 4.5, and 4.6.

Table 4.1: X-ray emission from nuclei.

3CR name	Net counts	Detection Significance	$F^{*}_{0.5-1\ keV}$ (cgs)	$F^{*}_{1-2\ keV}$ (cgs)	$F^{*}_{2-7\ keV}$ (cgs)	$F^{*}_{0.5-7\ keV}$ (cgs)	$\log(N_H(z))$ (cm^{-2})	L_X (10^{44}erg s^{-1})	$L_{X,obs}$ (10^{44}erg s^{-1})
239	7.5 (2.7)	>5	–	0.6 (0.5)	4.4 (1.9)	5.0 (2.0)	22.863 - 23.845	0.283 - 0.940	0.189 - 0.300
249	11.5 (3.4)	>5	1.01 (1.08)	0.6 (0.4)	4.8 (1.8)	6.4 (2.1)	19.89 - 22.38	0.234 - 0.304	0.222 - 0.233
257	29.5 (5.4)	>5	–	3.18 (1.02)	15.5 (3.6)	18.7 (3.8)	23.412 - 23.813	3.192 - 6.087	1.791 - 2.528
280.1**	719.6 (26.8)	>5	91.4 (11.8)	123.0 (6.5)	251.7 (14.5)	466.2 (19.8)	20.01 - 21.507	17.675 - 17.914	16.607 - 17.482
322	3.6 (1.9)	4	–	–	3.6 (1.9)	3.6 (1.9)	19.991 - 24.001	0.090 - 0.839	0.088 - 0.207
326.1+	1.6 (1.3)	–	–	–	1.8 (1.4)	1.8 (1.4)	24.4 - 24.404	0.800 - 1.040	0.110 - 0.144
418***	1513.6 (38.9)	>5	22.4 (4.7)	166.0 (7.2)	784.8 (25.4)	973.3 (26.8)	22.871 - 23.023	69.445 - 73.719	39.229 - 39.418
454**	438.7 (20.9)	>5	50.7 (8.8)	70.8 (4.9)	155.2 (11.1)	276.7 (15.0)	19.902 - 22.338	12.269 - 13.608	10.728 - 11.388
454.1	–	–	–	–	–	–	–	–	–

Col. (1): 3CR name.
Col. (2): Background-subtracted number of photons within a circle of radius $r = 2''$ in the 0.5 - 7 keV band. Numbers between parenthesis correspond to the uncertainty in the number of photons computed assuming Poisson statistics.
Col. (3): Detection significance of the nucleus in the 0.5 - 7 keV band, assuming the background has a Poisson distribution with a mean scaled to a $2''$ radius circle.
Col. (4): Measured X-ray flux between 0.5 and 1 keV.
Col. (5): Measured X-ray flux between 1 and 2 keV.
Col. (6): Measured X-ray flux between 2 and 7 keV.
Col. (7): Measured X-ray flux between 0.5 and 7 keV.
Col. (8): Range of intrinsic column densities needed to obtain the X-ray fluxes reported assuming a model comprising Galactic absorption, a power-law with slope fixed to 1.8, and intrinsic absorption with column density $N_{H,int}$ at the source redshift z.
Col. (9): Range of X-ray luminosities in the 0.5 - 7 keV band without taking into account intrinsic or Galactic absorption.
Col. (10): Range of observed X-ray luminosities in the 0.5 - 7 keV band evaluated from the model with Galactic and intrinsic absorption.
Notes:
(*) Fluxes are given in units of 10^{-15}erg $cm^{-2}s^{-1}$ and 1σ uncertainties are given in parenthesis. The uncertainties in the flux measurements are computed as described in Chapter 3. Fluxes were not corrected for Galactic absorption and were obtained by assuming a flat energy response in each band.
(**) For 3CR 280.1 and 3CR 454 the number of photons allowed me to extract their spectra and I obtained acceptable fits (i.e., reduced $\chi^2 \simeq 0.9$) adopting an absorbed power-law model, with only Galactic column density. I found the best fit value of the photon index being 1.54 (0.09) and 1.59 (0.07) with an integrated flux equal to $3.19{\cdot}10^{-13}$ erg/cm^2/s and $5.51{\cdot}10^{-13}$ erg/cm^2/s for 3CR 280.1 and 3CR 454, respectively. Then, assuming a fixed value of the photon index of 1.8 I also estimated the value of the intrinsic absorption (i.e., N_H, int) consistent with those obtained with the photometric analysis (i.e., hardness ratios) within 1σ being $1.84(0.07){\cdot}10^{-22}$ and $0.97(0.04){\cdot}10^{-22}$ for 3CR 280.1 and 3CR 454, respectively.
(***) For 3CR 418 I also carried out a spectral analysis and fitting with an absorbed power-law model, both including the Galactic and the intrinsic absorption, with a fixed photon index of 1.8, I obtained an estimate of the pile-up fraction of 0.13 (0.03) and a value of $N_{H,int}$ equal to $4.52{\cdot}10^{-22}$ cm^{-2} consistent with what expected from the source count rate using PIMMS v4.10[1] and that of the *pileup_map* task. All are consistent with the photometric analysis.
(+) For 3CR 326.1 I report the upper limit of the intrinsic column density since the nucleus was not detected.

4.2 Detection of nuclei, lobes and diffuse emission

I defined the position of X-ray nuclei and of X-ray counterparts of radio lobes using VLA radio maps. Here, I define as X-ray counterparts of lobes all X-ray diffuse emission detected in the 0.5-7 keV energy range consistent/associated with extended radio structures since at these redshifts radio maps available do not have sufficient resolution to distinguish/identify hotspots. However, when the core was not detected in radio, the position of the X-ray nucleus was defined as the emission peak in the 5 - 7 keV band (in contrast to the 0.5 - 7 keV band used for images and for the rest of the analysis) since nuclei are expected to have hard spectra in the X-ray band. The positions found are consistent (within $2''$) with those of the host galaxies in Pan-STARRS[2](Chambers et al. 2016) and those reported in Spinrad et al. (1985). Then, observed X-ray fluxes were measured using circular regions of $2''$ radii centered on the X-ray nuclei and, for lobes, circular regions containing the radio emission at more than three times the rms level of the background in the radio maps and centered on the peak of the radio emission. Background regions were chosen as circular regions at least as big as the radio sources and located on the same CCD chip, far enough from the radio galaxy (i.e., at least a few tens of arcsec) to avoid the smearing of the PSF on CCD borders and contamination from the source. Average background level is ~0.02 photons $pixel^{-1}$.

Results for nuclei are reported in Table 4.1 while X-ray fluxes of radio lobe counterparts are given in Table 4.2. Lobes are labeled as a combination of one letter indicating their orientation and one number indicating their distance from the X-ray nuclei in arcseconds.

[2]https://catalogs.mast.stsci.edu/panstarrs/

Table 4.2: X-ray emission from radio extended structures (i.e., lobes).

3CR name	Component	Size (arcsec)	Net counts	Detection Significance	$F^{*}_{0.5-1\ keV}$ (cgs)	$F^{*}_{1-2\ keV}$ (cgs)	$F^{*}_{2-7\ keV}$ (cgs)	$F^{*}_{0.5-7\ keV}$ (cgs)	L_X (10^{44}erg s^{-1})
239	e4	3	7.9 (2.8)	5	2.1 (1.7)	1.1 (0.6)	1.5 (1.1)	4.7 (2.1)	1.0 (0.5)
249	n11	4	4.1 (2.0)	3	0.7 (1.0)	0.5 (0.5)	1.8 (1.8)	3.0 (2.1)	0.5 (0.3)
249	s12	2.5	9.3 (3.0)	>5	2.0 (1.5)	1.9 (0.7)	0.4 (0.8)	4.2 (1.8)	0.7 (0.3)
257	w6	2	8.5 (2.9)	>5	–	0.9 (0.6)	3.9 (1.7)	4.9 (1.8)	2.5 (0.9)
280.1	w12	4.5	7.8 (2.8)	4	–	1.4 (0.8)	4.6 (2.5)	6.1 (2.6)	1.2 (0.5)
280.1	e7	5	26.0 (5.1)	>5	3.6 (2.3)	2.3 (0.9)	15.5 (4.1)	21.4 (4.8)	4.1 (0.9)
322	n14	3.5	7.7 (2.8)	5	0.9 (1.1)	1.4 (0.7)	1.9 (1.5)	4.2 (2.0)	0.8 (0.4)
326.1	e3	2.5	4.3 (2.1)	4	2.3 (1.7)	0.2 (0.2)	1.3 (1.2)	3.8 (2.1)	0.9 (0.5)
326.1	w3	2	7.6 (2.8)	>5	2.8 (2.0)	1.4 (0.7)	0.7 (1.0)	4.9 (2.3)	1.2 (0.5)

Col. (1): 3CR name. Col. (2): Component name is a combination of one letter indicating the orientation of the radio structure and one number indicating the distance from the nucleus in arcseconds. Col. (3): Radius of the circle containing the 3 rms noise contours of the radio emission. Col. (4): Background-subtracted number of photons within the photometric circle in the 0.5 - 7 keV band. Numbers between parenthesis correspond to the uncertainty in the number of photons computed assuming Poisson statistics. Col. (5): Detection significance of the lobes in the 0.5 - 7 keV band, assuming the background has a Poisson distribution with a mean scaled to a 2″ radius circle. Col. (6): Measured X-ray flux between 0.5 and 1 keV. Col. (7): Measured X-ray flux between 1 and 2 keV. Col. (8): Measured X-ray flux between 2 and 7 keV. Col. (9): Measured X-ray flux between 0.5 and 7 keV. Col. (10): X-ray luminosity in the range 0.5 to 7 keV with the 1σ uncertainties given in parenthesis.
Note:
(*) Fluxes are given in units of 10^{-15}erg cm^{-2}s^{-1} and 1σ uncertainties are given in parenthesis. The uncertainties in the flux measurements were computed as described in Chapter 3. Fluxes were not corrected for Galactic absorption and were obtained by assuming a flat energy response in each band.

A comparison between radio and X-ray images was carried out to verify the presence of X-ray counterparts of radio structures and to identify those sources that present diffuse X-ray emission in the soft band that is extended beyond the position of the radio lobes. This diffuse emission could be either due to IC/CMB or to X-ray emission arising from ICM in galaxy clusters or a combination of both processes (see e.g., Croston et al. 2005). I expect this diffuse X-ray emission to peak in the soft band, regardless of its origin. To obtain the detection significance of the diffuse X-ray emission, regions were chosen as circles centered in the X-ray nuclei and including all the radio emission above a 3 rms level and excluding the regions chosen for the nuclei and the lobes.

An additional difference with respect to previous survey papers is the lack of spectral analysis. Since all sources in this sample are at high redshift, using only snapshot observations meant that the total number of photons received from each source was too small to carry out this kind of analysis.

4.2.1 Nuclei

I detected X-ray emission in the full band (0.5 - 7 keV) above a 3σ significance level for all the nuclei in the sample with the only exception of 3CR 326.1 and 3CR 454.1. Background-subtracted number of photons within a circle of $r = 2''$ as well as the nuclear fluxes in the soft (0.5 - 1 keV), medium (1 - 2 keV), hard (2 - 7 keV) and full (0.5 - 7 keV) bands and the X-ray luminosity for each source are shown in Table 4.1. In contrast with previous analyses (see, e.g., Massaro et al. 2012), I do not report the extent ratio of the sources (i.e., the ratio of photons in the 2″ circle and those in an annulus between 2″ and 10″) since nearly all sources in the sample are enclosed within 10″ from their X-ray nucleus.

Three out of the 7 nuclei detected in X-rays in the sample are affected by pileup

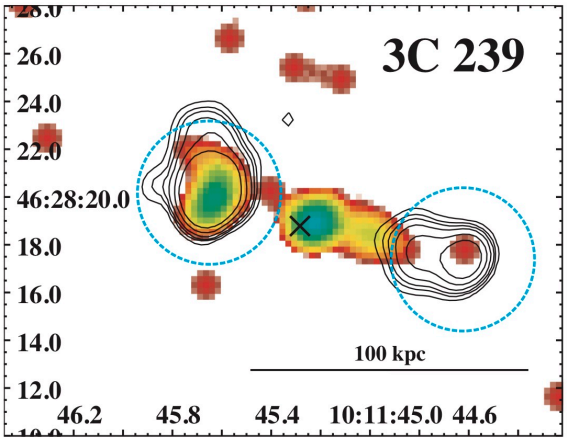

Figure 4.1: 0.5 - 7 keV *Chandra* image with 1.4 GHz VLA contours overlaid. The position of the X-ray nucleus is shown with a black X. Cyan dashed circles correspond to regions used to define lobes. The *Chandra* image has a pixel scale of 0.2″ and was smoothed with a 1.2″ radius Gaussian kernel. Radio contours were drawn at levels of 10, 20, 30, 50, 100, and 200 times the rms. The position of the X-ray nucleus was identified as the peak emission in the 5 - 7 keV band.

(see Davis 2001 for details about pileup), namely 3CR 280.1 (5%), 3CR 418 (10%), and 3CR 454 (3%). Therefore, X-ray fluxes obtained for these sources are underestimated.

As carried out for the analyses of 3CR sources at low redshifts (i.e., below 0.3) as well as in works such as those by Hardcastle et al. (2006, 2009), Mingo et al. (2014, 2016), Panessa et al. (2016), Ursini et al. (2018), and Butler (2019) on similar samples; I performed spectral simulations with SHERPA, using a model comprising Galactic absorption (fixed to the values reported in Table 4.1 for each source), a power-law with slope fixed to 1.8, and intrinsic absorption with column density $N_{H,int}$ at the source redshift z. I computed the ranges of the hardness ratios *HR* as the ratio between the fluxes in the soft (0.5 - 3 keV) and the hard band (3 - 7 keV) and, from those, I derived the range of intrinsic absorbing column density $N_{H,int}$ as reported in Table 4.1 for all detected nuclei, as well as the ranges of X-ray luminosities in the 0.5 - 7 keV band without taking into account any absorption (L_X) and from the model with Galactic and intrinsic absorptions ($L_{X,obs}$).

Moreover, for three sources (namely, 3CR 280.1, 3CR 418, and 3CR 454), the number of detected photons for their nuclei allowed me to carry out detailed spectral analyses as done for relatively bright 3CR sources at lower redshifts observed during the snapshot survey. All spectral fits in these cases were consistent with simple power-law with galactic absorption, where the photon index is consistent with that of typical AGNs (i.e., 1.8) within 3σ and, in agreement with the HR analysis, the column density from intrinsic absorption is negligible with respect to the Galactic one and/or unconstrained. A summary of these results is shown in Table 4.1.

4.2.2 Lobes

I detected 9 lobes above a 3σ confidence level in 6 of the sources in the sample. Sizes, background-subtracted number of photons, X-ray fluxes, and X-ray luminosities of the X-ray counterparts of radio lobes are listed in Table 4.2.

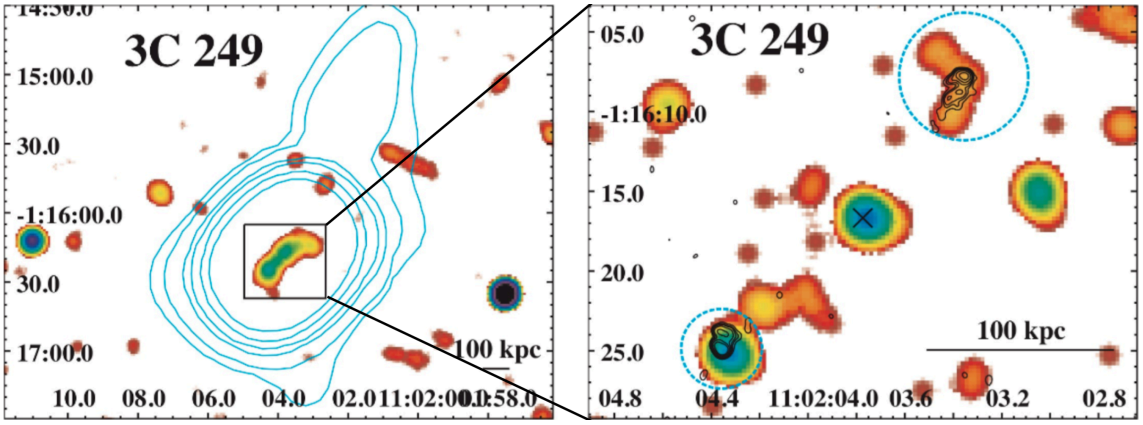

Figure 4.2: *Chandra* image with VLA contours overlaid in black and 150 MHz TGSS contours overlaid in cyan. When identified, the position of the X-ray nucleus is shown with a black X. Cyan dashed circles correspond to regions used to define lobes.
On the left, 0.5 - 3 keV *Chandra* image with 150 MHz TGSS contours overlaid. The *Chandra* image has a pixel scale of 1″ and was smoothed with an 8″ radius Gaussian kernel. 150 MHz contours were drawn at 5, 10, 30, 50, 100, and 200 times the rms. On the right, 0.5 - 7 keV *Chandra* image with 4.8 GHz VLA contours overlaid showing an inset of the image on the left. The *Chandra* image has a pixel scale of 0.2″ and was smoothed with a 1.6″ radius Gaussian kernel. 4.8 GHz contours were drawn at 10, 20, 30, 50, 100, and 200 times the rms.

4.2.3 Diffuse emission

X-ray detection of nuclei and lobes was carried out in the 0.5 - 7 keV band like in previous analyses for the 3CR *Chandra* Snapshot Survey; while I used the 0.5 - 3 keV band to detect the diffuse X-ray emission, since I expect this emission to peak in the soft band, regardless of its origin. This diffuse emission was estimated excluding the regions selected for nuclei and lobes.

Out of the 9 sources in the sample, I only detected diffuse X-ray emission in the soft band along the radio axis and beyond the lobe radio emission observed at GHz frequencies in 3CR 249, with a 2σ confidence level. This diffuse emission is shown in the left panel of Fig. 4.2, where the X-ray emission in the 0.5 - 3 keV band with 150 MHz TGSS radio contours overlaid is shown. Additionally, only two out of the 9 selected targets, namely 3CR 249 and 3CR 322 presented extended morphology in TGSS (see left panels of Figs. 4.2 and 4.4), while the rest are unresolved.

4.3 Notes on individual sources

3CR 239. This is a FR II radio galaxy at $z = 1.781$ (Laing et al. 1983) optically identified as a high-excitation radio galaxy (HERG; Jackson & Rawlings 1997). According to Hammer & Le Fevre (1990), this galaxy lies in a crowded field where there are two different populations of galaxies, one at the same redshift as 3CR 239 and one in the foreground. They suggested that the first population belongs to a galaxy cluster surrounding 3CR 239 which could be gravitationally lensed by the foreground population. The last statement

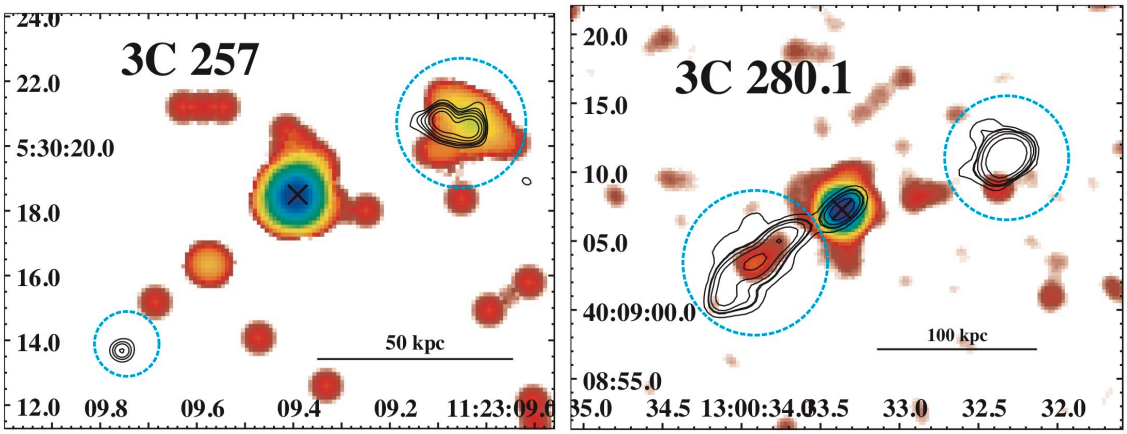

Figure 4.3: *Chandra* image with VLA contours overlaid in black. When identified, the position of the X-ray nucleus is shown with a black X. Cyan dashed circles correspond to regions used to define lobes.
3CR 257: 0.5 - 7 keV *Chandra* image with 4.8 GHz VLA contours overlaid. The *Chandra* image has a pixel scale of 0.1″ and was smoothed with a 0.8″ radius Gaussian kernel. Radio contours were drawn at levels of 10, 20, 30, 50, 100, and 200 times the rms.
3CR 280.1: 0.5 - 7 keV *Chandra* image with 1.4 GHz VLA contours overlaid. The *Chandra* image has a pixel scale of 0.2″ and was smoothed with a 1.2″ radius Gaussian kernel. Radio contours were drawn at levels of 10, 20, 30, 50, 100, and 200 times the rms.

was supported by Best et al. (1997) since they claim that a foreground galaxy within 5″ of the host of 3CR 239, next to the eastern lobe, could cause the presence of a double hotspot and arc-like structures in that lobe. *HST* images (Best et al. 1997) show a bright galaxy with two emission regions aligned with the radio axis and a string of emission to the southeast misaligned to the radio axis by ∼45°, as well as two faint tidal tails to the north and west of the galaxy, extending ∼40 kpc. These features could be the result of past galaxy collisions.

Both the nucleus and the eastern lobe of 3CR 239 were detected in the 0.5 - 7 keV band, using Poisson statistics (see Fig. 4.1). I could not find an archival radio map in which the radio core was detected, therefore, I considered the position of the X-ray nucleus that of the peak emission in the 5 - 7 keV band, in which the nucleus was detected at a 3σ confidence level. I did not detect the presence of diffuse X-ray emission beyond the radio lobes that could indicate the presence of ICM from a galaxy cluster.

3CR 249. This source is a lobe-dominated quasar at $z = 1.554$ (Law-Green et al. 1995). It has not been studied in detail in the literature and, as for the previous source, I could not find a radio map in which the radio core was detected. However, I obtained the position of the nucleus using hard X-rays (see right panel of Fig. 4.2), in which the nucleus was detected with a 2σ confidence level. I was able to detect the X-ray nucleus and both lobes in the 0.5 - 7 keV band. Additionally, diffuse X-ray emission was found beyond the position of the radio lobes in the 0.5 - 3 keV band (with a 2σ confidence level), as shown in the left panel of Fig. 4.2.

3CR 257. This is the highest redshift ($z = 2.474$) radio galaxy in the 3CR catalog. According to Hilbert et al. (2016), the IR image shows a distorted morphology (∼2″, which is equivalent to 16.5 kpc at the source redshift), which implies that the source could be undergoing a merging event. Additionally, it shows some optical emission suggesting

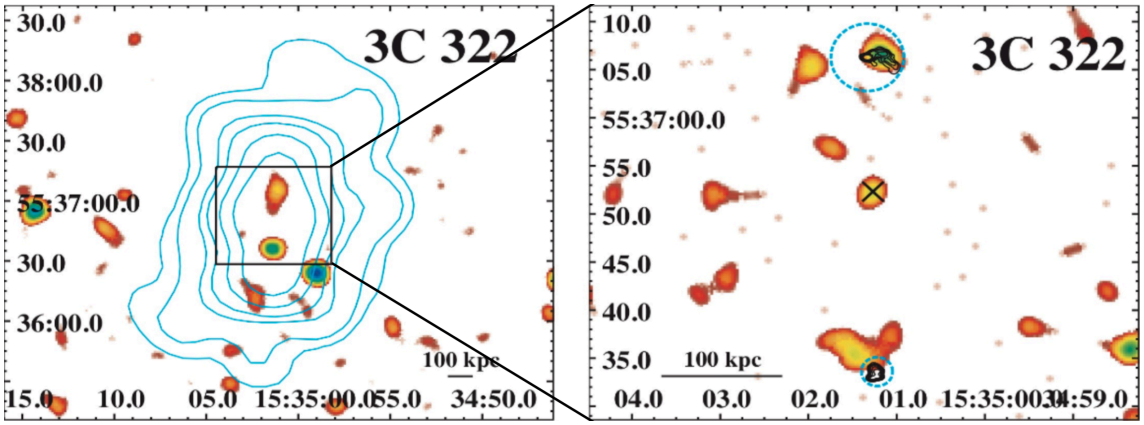

Figure 4.4: *Chandra* image with VLA contours overlaid in black and 150 MHz TGSS contours overlaid in cyan. When identified, the position of the X-ray nucleus is shown with a black X. Cyan dashes circles correspond to regions used to define lobes.
On the left, 0.5 - 3 keV *Chandra* image with 150 MHz TGSS contours overlaid. The *Chandra* image has a pixel scale of 1″ and was smoothed with an 8″ radius Gaussian kernel. 150 MHz contours were drawn at 5, 10, 30, 50, 100, and 200 times the rms. On the right, 0.5 - 7 keV *Chandra* image with 1.4 GHz VLA contours overlaid showing an inset of the image on the left. The *Chandra* image has a pixel scale of 0.2″ and was smoothed with a 1.6″ radius Gaussian kernel. 1.4 GHz contours were drawn at 10, 20, 30, 50, 100, and 200 times the rms.

ongoing star formation.

I defined the position of the X-ray nucleus using hard X-rays as in previous sources (in this band, the nucleus was detected with a 3σ confidence level). In the *Chandra* full band image, I detected the nucleus and the western lobe (see left panel of Fig. 4.3). I did not detect diffuse X-ray emission in the soft band.

3CR 280.1. This source is a lobe-dominated quasar at $z = 1.667$ (Laing et al. 1983 and Véron-Cetty & Véron 2006). The 5 GHz radio map in Lonsdale et al. (1993) shows a strong jet.

In this case, I was able to define the core position using the radio emission (in this position, the X-ray nucleus was detected in the 5 - 7 keV band above a 5σ confidence level). I detected the nucleus and both lobes in the 0.5 - 7 keV band (see right panel of Fig. 4.3). Furthermore, the eastern lobe of 3CR 280.1, which corresponds to the strong jet detected by Lonsdale et al. (1993) at radio frequencies, is the brightest lobe in the sample. The X-ray nucleus of 3CR 280.1 is affected by 5% pileup. Lastly, I did not detect diffuse X-ray emission in the 0.5 - 3 keV band.

3CR 322. This is a FR II radio galaxy at $z = 1.168$ (Law-Green et al. 1995). In the IR, this source appears as an extended object (~2″, which is equivalent to 17 kpc at the source redshift) with a core elongated in the northwest-southeast direction (Hilbert et al. 2016). According to Kotyla et al. (2016), it could be part of a galaxy cluster since there is an overdensity of galaxies on its field.

In the full X-ray band, I detected the nucleus (whose position I found using the peak emission in hard X-rays with a 4σ confidence level) and the north lobe (see right panel of Fig. 4.4). I found no diffuse emission in the 0.5 - 3 keV band that could indicate the presence of ICM from a galaxy cluster (see left panel of Fig. 4.4).

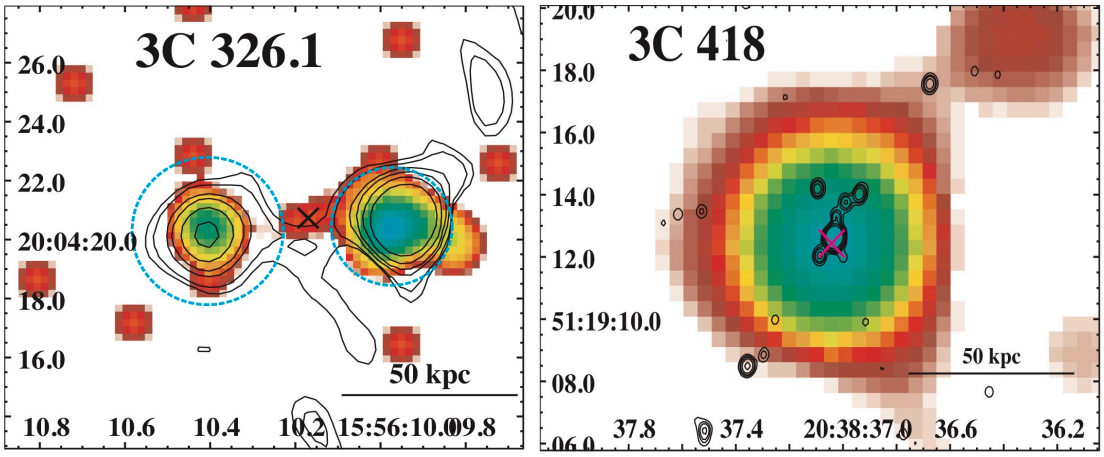

Figure 4.5: *Chandra* image with VLA contours overlaid. The position of the X-ray nucleus is shown with a black X (magenta for 3CR 418). Cyan dashes circles correspond to regions used to define lobes.
3CR 326.1: 0.5 - 7 keV *Chandra* image with 4.8 GHz VLA contours overlaid. The *Chandra* image has a pixel scale of 0.2″ and was smoothed with a 1.2″ radius Gaussian kernel. Radio contours were drawn at levels of 5, 10, 30, 50, 100, and 2000 times the rms.
3CR 418: 0.5 - 7 keV *Chandra* image with 4.8 GHz VLA contours overlaid. The *Chandra* image has a pixel scale of 0.5″ and was smoothed with a 3″ radius Gaussian kernel. Radio contours were drawn at levels of 10, 20, 30, 50, 100, and 200 times the rms.

3CR 326.1. This source is a FR II radio galaxy at $z = 1.825$. McCarthy et al. (1987) found that the host galaxy is surrounded by a giant Lyα cloud of ~100 kpc diameter, which could imply that it is a young and/or starforming galaxy. IR observations presented by Hilbert et al. (2016) show that the host is a dim galaxy, elongated in the east-west direction and surrounded by many small and irregular sources. Hilbert et al. (2016) also observed several clumps of UV emission due to, for example, star formation regions. Lastly, Kotyla et al. (2016) found an overdensity of sources in the field of 3CR 326.1, suggesting that it could be part of a galaxy cluster.

I defined the position of the X-ray nucleus of this source using the 5 - 7 keV band emission, in which the nucleus was detected with a 2σ confidence level. I was not able to detect the X-ray nucleus above a 3σ level of confidence, using the full band X-ray emission. I detected both lobes (see left panel of Fig. 4.5) with a confidence level of, at least, 4σ. As for 3CR 322, I did not detect diffuse emission that could indicate the presence of ICM to corroborate Kotyla et al. (2016) results.

3CR 418. This is a QSO at $z = 1.686$ (Véron-Cetty & Véron 2006). According to Hilbert et al. (2016) in the IR this source can be seen as a bright target submerged in a dense field, due to its location at a low galactic latitude; while in the 4.86 GHz VLA map the emission comes from the core and a small jet extending 6″ to the northwest.

Using the position of the radio core, I detected the X-ray nucleus in the 5 - 7 keV band above a 5σ confidence level. I also detected the nucleus in the full X-ray band and it was the brightest X-ray nucleus in the sample (see right panel of Fig. 4.5). Due to the small angular size of the radio emission of 3CR 418 (~3″), I did not attempt to detect X-ray counterparts of radio lobes or diffuse X-ray emission in the soft band. The X-ray nucleus of 3CR 418 is affected by 10% pileup.

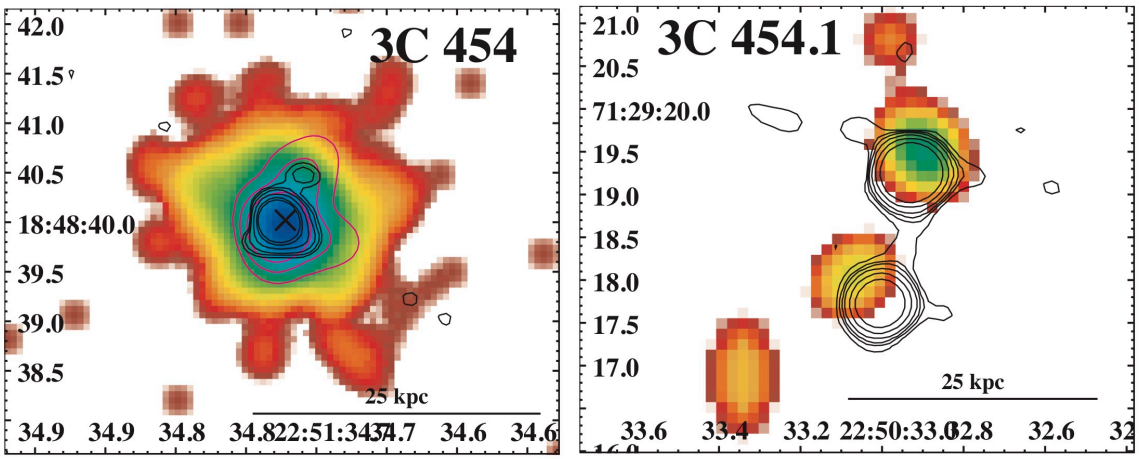

Figure 4.6: *Chandra* image with VLA contours overlaid in black (and magenta for 3CR 454). When identified, the position of the X-ray nucleus is shown with a black X. Cyan dashes circles correspond to regions used to define lobes.
3CR 454: 0.5 - 7 keV *Chandra* image with 4.8 GHz VLA and 8.4 GHz contours overlaid in magenta and black, respectively. The *Chandra* image has a pixel scale of 0.05″ and was smoothed with a 0.3″ radius Gaussian kernel. 4.8 GHz contours were drawn at levels of 20, 100, and 300 times the rms and 8.4 GHz were drawn at levels of 20, 30, 50, 100, 200, and 300 times the rms.
3CR 454.1: 0.5 - 7 keV *Chandra* image with 4.8 GHz VLA contours overlaid. The *Chandra* image has a pixel scale of 0.1″ and was smoothed with a 0.6″ radius Gaussian kernel. Radio contours were drawn at levels of 10, 20, 30, 50, 100, and 200 times the rms.

3CR 454. This source is a QSO at $z = 1.757$ (Véron-Cetty & Véron 2006) defined as a Compact Steep Spectrum (CSS) source by O'Dea (1998). Using the 0.5 - 7 keV *Chandra* image, I detected the nucleus above a 3σ confidence level (see left panel of Fig. 4.6). The position of this nucleus was given by the position of the radio core, in which the nucleus in the 5 - 7 keV was detected with a confidence level above 5σ. Radio lobes are not resolved in the radio map and, due to the small angular size of the radio emission of 3CR 454 (∼1.5″), I did not attempt to detect extended X-ray counterparts of radio lobes or diffuse X-ray emission in the 0.5 - 3 keV. The X-ray nucleus of 3CR 454 is affected by 3% pileup.

3CR 454.1. This is a FR II radio galaxy at $z = 1.841$ classified as a HERG by Stickel & Kuehr (1996) and as a CSS by O'Dea (1998). Using optical observations, Chiaberge et al. (2015) claimed that this source recently underwent merger activity. Lastly, Kotyla et al. (2016) found an overdensity of sources in its field.

In the case of 3CR 454.1, I was not able to identify the X-ray nucleus (see right panel of Fig. 4.6). The position reported by Spinrad et al. (1985) matches the northern X-ray peak, however, this peak is most likely the X-ray counterpart of the northern radio lobe. On the other hand, the position of the X-ray peak in the 5 - 7 keV band matches the position of the southern radio lobe, therefore I could not detect the X-ray nucleus of 3CR 454.1. I did not attempt to detect X-ray counterparts of radio lobes or diffuse X-ray emission in the soft band, due to the small angular size of the radio emission of 3CR 454.1 (∼3″).

4.4 Summary and discussion

I present the X-ray analyses carried out on the 9 remaining identified 3CR sources up to $z = 2.5$ (namely 3CR 239, 3CR 249, 3CR 257, 3CR 280.1, 3CR 322, 3CR 326.1, 3CR 418, 3CR 454, and 3CR 454.1) observed by *Chandra* during Cycle 20 as part of the 3CR *Chandra* Snapshot Survey. This sample is particularly interesting since it covers the highest redshift identified extragalactic sources in the 3CR catalog and, therefore, these are the highest redshift sources observed so far during the 3CR *Chandra* Snapshot Survey. However, the high redshift prevents me from resolving hotspot emission from lobe emission and, therefore, I label as lobes all extended structures not being nuclei.

All data presented, as well as all previous data from the 3CR *Chandra* Snapshot Survey are publicly available in the *Chandra* archive.

I present the main parameters of these newly observed sources. I followed the same data reduction and analysis procedures as in previous papers of the 3CR *Chandra* Snapshot Survey. I created flux maps in the soft (0.5 - 1 keV), medium (1 - 2 keV), and hard (2 - 7 keV) bands for detected nuclei and extended X-ray features (i.e., lobes) and reported their background-subtracted number of photons, detection significance, fluxes in each band, and X-ray luminosities.

I detected the X-ray nuclei using the 0.5 - 7 keV emission in all sources in the sample except for 3CR 326.1 and 3CR 454.1. Additionally, I detected X-ray counterparts of radio lobes, in the same band, in 6 of the 9 sources in the sample, namely 3CR 239, 3CR 249, 3CR 257, 3CR 280.1, 3CR 322, and 3CR 326.1. In particular, I detected both lobes in 3CR 249, 3CR 280.1, and 3CR 326.1. In the three sources left, the X-ray detected lobe was also the brightest in radio. Lastly, I found diffuse X-ray emission along the radio axis of 3CR 249 in the 0.5 - 3 keV band.

This work marks the completion of the *Chandra* Snapshot Survey of identified 3CR sources, carried out to guarantee the X-ray coverage of the entire 3CR extragalactic catalog with *Chandra*. Thanks to the last 9 observations presented here I completed the analysis of all identified sources listed in the 3CR.

From providing a first glimpse into interesting sources that warranted deeper observations, to providing data for more detailed studies, the 3CR *Chandra* Snapshot Survey has proven to be an extremely helpful tool in the study of radio sources (see e.g., Hardcastle et al. 2010, 2012, Balmaverde et al. 2012, Orienti et al. 2012, Ineson et al. 2013, Dasadia et al. 2016 and Madrid et al. 2018). So far, during the 3CR *Chandra* Snapshot Survey, a total of 122 sources with no previous observations in the *Chandra* archive have been observed. Using these observations, X-ray counterparts of 119 radio cores were detected.

According to the XJET database[3], thanks to the 3CR *Chandra* Snapshot Survey, 8 more radio jet knots with an X-ray counterparts in 7 different sources were detected, thus increasing their number by ~10% (see Massaro et al. 2011 for latest results on the XJET project). In addition, the number of sources having at least one X-ray detected hotspot have been doubled. Then, in all previous data papers of the 3CR *Chandra* Snapshot Survey, it was reported the discovery of X-ray counterparts of radio lobes in 11 3CR sources in addition to those listed in the literature. Additionally, X-ray emission arising from ICM in galaxy clusters was detected in 19 sources including those reported in the archival search (Massaro et al. 2015). Having such a large sample of X-ray counterparts of radio galaxies' components will allow for future studies on the origin of the X-ray

[3] http://hea-www.harvard.edu/XJET/

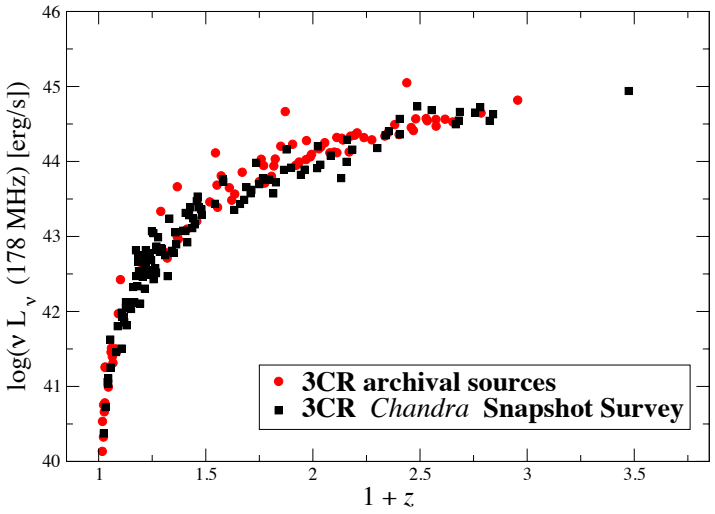

Figure 4.7: Radio luminosity at 178 MHz vs. redshift plot for the 3CR sources with observations in the *Chandra* archive (black circles) and those observed during the 3CR *Chandra* Snapshot Survey (red squares).

emission from jets and hotspots which is currently still uncertain, but believed to be non-thermal (see e.g., Harris & Krawczynski 2002, 2006 and Worrall 2009), the most likely scenarios being synchrotron emission or IC scattering.

I remark that the current summary about the X-ray detection of extended radio structures in 3CR sources does not include the following cases for which extensive analyses have been carried out in the literature, namely: 3CR 66A, 3CR 71 (a.k.a. NGC 1068), 3CR 84 (a.k.a Perseus A), 3CR 186, 3CR 231 (a.k.a. M82), 3CR 317 (a.k.a. Abell 2052), and 3CR 348 (a.k.a. Hercules A) as well as 3CR 236, 3CR 263, and 3CR 386 for which the multifrequency analysis is still ongoing (Birkinshaw priv. comm.).

In Fig. 4.7, I show the radio luminosity at 178 MHz obtained from Spinrad et al. (1985) versus redshift for 3CR sources with *Chandra* observations, comparing those observed during the 3CR *Chandra* Snapshot Survey and those with previous archival observations. This comparison shows that at redshift $z > 0.5$ snapshot observations pointed the faintest radio sources. In the left panel of Fig. 4.8, I show the redshift distribution of the 3CR sources before and after this survey was completed, including all sources analyzed here, and not considering those still unidentified (i.e., lacking an optical counterpart and thus a z estimate). The comparison between these two z distributions highlights the impact of the 3CR *Chandra* Snapshot Survey on the number of sources at moderate redshift (i.e., above 1.2) as well as in the low redshift range (i.e., between 0.1 and 0.5) which were significantly increased with respect to those listed in the *Chandra* archive. Finally, the right panel of Fig. 4.8 shows the distribution of X-ray nuclear luminosities as measured in all data papers published to date (Massaro et al. 2010, 2012, 2013, 2015, 2018 and Stuardi et al. 2018) and in this work.

Out of the 25 unidentified 3CR sources, 16 of them already have archival *Chandra* observations, observed in cycles 21 and 22, and four have observations in the XMM-

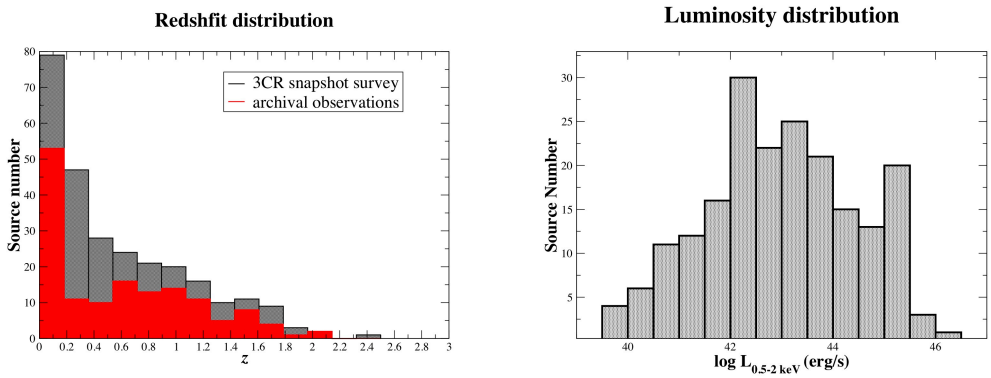

Figure 4.8: Left: Redshift distribution of sources in the 3CR *Chandra* Snapshot Survey (in grey) and in the *Chandra* archive before the Snapshot Survey (red). Right: Soft X-ray luminosity distribution of 3CR nuclei in the *Chandra* archive.

Newton archive. Furthermore, a paper with the analysis of the first seven sources was already published (Missaglia et al. 2021). Thus, only five of them have no X-ray observations available yet. Additionally, I am planning another forthcoming paper presenting a statistical study on the whole 3CR *Chandra* Snapshot Survey in which I plan to include the SED modeling of these sources.

Bibliography

Balmaverde, B., Capetti, A., Grandi, P., et al. 2012, A&A, 545, A143

Best, P. N., Longair, M. S. & Roettgering, H. J. A. 1997, MNRAS, 292, 758

Best, P. N., Peacock, J. A., Brookes, M. H. 2003, MNRAS, 346, 1021

Butler, A. R. 2019, University of Western Australia, https://ui.adsabs.harvard.edu/abs/2019PhDT.....145B

Chambers, K. C., Magnier, E. A., Metcalfe, N., et al. 2016, arXiv e-prints, 1612.05560

Chiaberge, M., Gilli, R., Lotz, J. M., et al. 2015, IOP Publishing, 806, 147

Croston, J. H., Hardcastle, M. J., Harris, D. E., et al. 2005, ApJ, 626, 733

Dasadia, S., Sun, M., Morandi, A., et al. 2016, MNRAS, 458, 681

Davis, J. E. 2001, ApJ, 562, 575

Fanaroff, B. L. & Riley, J. M. 1974, MNRAS, 167, 31P

Grimes, J. A., Rawlings, S., & Willott, C. J., 2004, MNRAS, 349, 503

Hammer, F. & Le Fevre, O. 1990, ApJ, 357, 38

Hardcastle, M. J., Evans, D. A. & Croston, J. H. 2006, MNRAS, 396, 1929

Hardcastle, M. J., Evans, D. A. & Croston, J. H. 2009, MNRAS, 396, 1929

Hardcastle, M. J., Massaro, F. & Harris, D. E., 2010, MNRAS, 401, 2697

Hardcastle, M. J., Massaro, F. & Harris, D. E., 2012, MNRAS, 424, 1774

Harris, D. E. & Krawczynski, H., 2002, ApJ, 565, 242

Harris, D. E. & Krawczynski, H., 2006, ARA&A, 44, 463

Hes, R., Barthel, P. D. & Fosbury, R. A. E. 1996 A&A, 313, 423

Hewett, P. C. & Wild, V. 2010, MNRAS, 405, 2302

Hewitt, A. & Burbidge, G. 1991, ApJS, 75, 297

Hilbert, B., Chiaberge, M., Kotyla, J. P., et al. 2016, American Astronomical Society, 225, 12

Ineson, J., Croston, J. H., Hardcastle, M. J., et al. 2013, ApJ, 770, 136

Jackson, N. & Rawlings, S. 1997, MNRAS, 286, 241

Kalberla, P. M. W., Burton, W. B., Hartmann, D., et al. 2005, A&A, 440, 775

Kotyla, J. P., Hilbert, Chiaberge, M., Baum, S., et al. 2016, American Astronomical Society, 826, 46

Laing, R. A. and Riley, J. M. and Longair, M. S. 1983, MNRAS, 204, 151

Law-Green, J. D. B., Leahy, J. P., Alexander, P., et al. 1995, MNRAS, 274, 939

Lonsdale, C. J., Barthel, P. D. & Miley, G. K. 1993, ApJS, 87, 63

Madrid, J. P., Donzelli, C. J., Rodríguez-Ardila, A., et al. 2018, ApJS, 238, 31

Massaro, F., Harris, D. E., Tremblay, G. R., et al. 2010, ApJ, 714, 589

Massaro, F., Harris, D. E. & Cheung, C. C. 2011, ApJS, 197, 24

Massaro, F., Tremblay, G. R., Harris, D. E., et al. 2012, ApJS, 203, 31

Massaro, F., Harris, D. E., Tremblay, G. R., et al. 2013, ApJS, 206, 7

Massaro, F., Harris, D. E., Liuzzo, E., et al. 2015, ApJS, 220, 5

Massaro, F., Missaglia, V., Stuardi, C., et al. 2018, ApJS, 234, 7

McCarthy, P. J., Spinrad, H., Djorgovski, S., et al. 1987, ApJL, 319, L39

Mingo, B., Hardcastle, M. J., Croston, J. H., et al. 2014, MNRAS, 440, 269

Mingo, B., Watson, M. G., Rosen, S. R., et al. 2016, MNRAS, 462, 2631

Missaglia, V., Massaro, F., Liuzzo, E., et al. 2021, ApJS, 255, 18

O'Dea, C. P. 1998, PASP, 110, 747

Orienti, M., Prieto, M. A., Brunetti, G., et al. 2012, MNRAS, 419, 2338

Panessa, F., Bassani, L., Landi, R., et al. 2016 MNRAS, 461, 3153

Perryman, M. A. C., Lilly, S. J., Longair, M. S., et al. 1984 MNRAS, 209, 159

Spinrad, H., Djorgovski, S., Marr, J. & Aguilar, L. 1985, PASP, 97, 932

Stickel, M. & Kuehr, H. 1996, A&AS, 115, 1

Stuardi, C., Missaglia, V., Massaro, F., et al. 2018, ApJS, 235, 32

Ursini, F., Bassani, L., Panessa, F., et al. 2018, MNRAS, 481, 4250

Véron-Cetty, M. -P. & Véron, P. 2006, A&A, 455, 773

Worrall, D. M. 2009, A&ARv, 17, 1

Chapter 5

Extended X-ray emission around 3CR radio galaxies

This chapter focuses on the analysis of the large-scale soft X-ray emission surrounding FR II radio galaxies with no GHz-counterparts, as detected during the 3CR *Chandra* Snapshot Survey. It is organized as follows. § 5.1 collects an overview of the sample selection, followed by the description of the X-ray analysis in § 5.2. Results on the detection of X-ray counterpart emission of hotspots as well as of diffuse X-ray emission, X-ray surface brightness profiles, and notes on individual sources are shown in § 5.3. § 5.4 is devoted to a radio and X-ray comparison, while § 5.5 and § 5.6 are optical and WISE overviews. Lastly, § 5.7 is dedicated to a summary and discussion of the chapter.

While carrying out the 3CR *Chandra* Snapshot Survey, several examples of FR II radio galaxies with diffuse X-ray emission with no apparent radio counterpart at GHz frequencies were found (see e.g., Massaro et al. 2013c and Stuardi et al. 2018).

Radio sources showing diffuse X-ray emission extending, well beyond the radio structure were discovered at high redshifts (i.e., $1.7 < z < 3.8$) in the last two decades (e.g., 3CR 294, HDF 130, 3CR 191, 3CR 432, 4C 60.07, 4C 03.24 and 4C 19.71 by Fabian et al. 2003, 2009, Erlund et al. 2006, and Smail et al. 2009, 2012, respectively). This X-ray emission could be due to either (i) the X-ray counterpart of extended steep-spectrum radio structures observable at MHz but not at GHz frequencies, (ii) the ICM whenever the source lies in a group/cluster of galaxies, or (iii) a mixture of both processes. Croston et al. (2005) studied X-ray lobe emission in 33 FR II radio sources, finding a high rate of lobe detection (at least one per source in 20 sources of their sample) and concluding that the main X-ray emission mechanism from lobes is IC/CMB. Following this result, Ineson et al. (2013, 2015, 2017) differentiated between thermal emission from the ICM and non-thermal emission from IC/CMB in a sample of radio galaxies based on their radio morphology. Thus, they considered that X-ray emission spatially associated with lobes was due to IC/CMB, while the rest of the extended X-ray emission was thermal emission from the ICM. Additionally, using a complete subset of 2 Jy sources (at $0.05 < z < 0.2$), Mingo et al. (2017) found lobe emission in FR II radio galaxies consistent with IC/CMB emission, confirming previous results by Croston et al. (2005).

Although this extended X-ray emission had been discovered during the 3CR *Chandra* Snapshot Survey around many of the 3CR sources (~50 sources out of 262 observed by 2018, Massaro et al. 2018), previous analyses were mainly focused on searching for X-ray counterparts of hotspots rather than ICM. Thus, I carried out a refined analysis

of a selected sample of FR II radio galaxies observed in the last decade during the 3CR *Chandra* Snapshot Survey with the main goals of:

1. testing for the presence of extended X-ray emission around FR II radio galaxies and comparing the structure of this emission with the radio morphology at GHz and at ~150 MHz frequencies (for those having available MHz observations);

2. investigating the origin of this extended emission (either as IC/CMB emission from lobes or as thermal emission from the ICM);

3. verifying previous claims of X-ray detected hotspots and checking if they could be related to fluctuations of the *local* X-ray background by refining the background regions and energy range used to claim their detection.

Table 5.1: Image parameters for X-ray and radio emission.

3CR Name	Radio freq. (GHz)	Beam size (arcsec)	Contour levels (mJy/beam)	Pixel size (arcsec)	Smoothing Gaussian kernel (arcsec)
18	1.4	1.70	5, 10, 20, 40, 80, 160, 320, 640	0.246	2.95
44	1.4	1.46	2, 4, 8, 20, 40, 80	0.492	5.90
52	1.4	3.59	10, 20, 80, 320, 640	0.984	9.84
54	8.0	0.40	0.2, 0.8, 3.2, 12.8, 51.2	0.492	6.89
63	1.4	1.36	1, 2, 4, 8, 16, 32, 64	1.968	23.62
69	4.8	5.00	2, 4, 8, 16, 32, 64	0.984	9.84
103	1.4	3.27	10, 20, 40, 80, 160, 320, 640	0.984	9.84
107	4.8	0.46	0.2, 0.4, 0.8, 1.6, 3.2, 6.4	0.123	1.48
114	1.4	1.27	2, 4, 8, 16, 32	0.246	3.44
133	1.4	0.98	8, 32, 64, 256, 512	0.123	1.48
135	8.0	0.66	0.02, 0.08, 0.32, 1.28	1.968	15.74
165	1.4	3.36	2, 8, 16, 32, 64	0.984	7.87
166	1.4	1.37	4, 8, 16, 32	0.492	3.94
169.1	1.4	1.37	2, 4, 8, 16, 32, 64	0.984	15.74
180	8.0	0.36	0.5, 0.7, 1, 2, 4	0.492	7.87
197.1	4.8	1.32	2, 3, 4, 5, 6, 8	0.492	3.94
198	4.8	25.9	1, 2, 4, 8, 10, 12	1.968	23.62
223.1	1.4	1.67	2, 4, 8, 20, 40, 80	0.492	3.94
268.2	1.4	1.61	2, 4, 8, 20, 40, 80	0.984	9.84
272	1.4	5.40	2, 4, 8, 20, 40, 80	0.984	9.84
287.1	1.4	5.00	2, 4, 8, 20, 40, 80	0.492	4.92
293.1	1.4	5.40	2, 8, 16, 32, 64	0.984	9.84
306.1	4.8	1.75	1, 2, 4, 8, 16	0.984	9.84
313	8.0	2.43	2, 4, 8, 32, 64, 128	0.984	11.81
332	1.4	4.40	2, 4, 8, 16, 32, 64	0.984	7.87
357	4.8	1.92	1, 2, 4, 8, 16	0.984	13.78
379.1	4.8	1.55	1, 2, 4, 8	0.984	11.81
403.1	0.3	7.03	16, 32, 64	0.984	13.78
411	1.4	1.30	4, 8, 16, 32, 64	0.123	1.48
430	4.8	1.34	1.5, 2, 4, 8, 16, 32, 64	0.984	15.74
434	1.4	1.40	4, 8, 16, 32, 64	0.246	3.44
435	4.8	1.76	1, 2, 4, 8, 16, 32	0.246	3.44
456	1.8	1.43	4, 16, 64, 256	0.123	1.72
458	1.4	6.40	2, 4, 8, 16, 32, 64	0.984	13.78

Table 5.1: Column description: (1) Source name; (2) radio frequency of contours in GHz; (3) beam size of the radio maps; (4) radio contour levels in mJy/beam; (5) pixel size of the X-ray image; (6) size of the Gaussian Kernel used for smoothing the X-ray image.

This last point arose since, although a significant number of X-ray counterparts were discovered at the locations of radio hotspots (~40; Massaro et al. 2013c), previous analyses of 3CR *Chandra* Snapshot Survey observations (reported in Massaro et al. 2010a, 2012, 2013c, 2018 and Stuardi et al. 2018) did not take into account the possibility that detected hotspots could be fluctuations of the extended X-ray emission due to (i) radiation arising from radio lobes and/or to (ii) the presence of ICM in those cases where the radio galaxy belongs to a galaxy cluster.

I computed surface brightness profiles of FR II radio galaxies with clearly detected extended X-ray emission along their radio axes and verified the presence of galaxy clusters by using archival optical observations to test for the presence of red sequences (i.e.,

a color-magnitude relation for galaxies belonging to the same galaxy cluster; see Visvanathan & Sandage 1977) in the fields of those galaxies with diffuse X-ray emission not spatially associated with the radio structure. Finally, I performed a comparison with low radio frequencies (i.e., ~150 MHz) TGSS[1]) and LOFAR[2] observations.

5.1 Sample selection

I initially selected all radio galaxies with a classical FR II radio morphology (i.e., edge-brightened, Fanaroff & Riley 1974) out of those listed in the 3CR catalog and observed during the 3CR *Chandra* Snapshot Survey before Cycle 20. Radio sources belonging to the 3CRR sample were not included since a dedicated paper is already in preparation (Wilkes et al. 2020). Criteria to select FR II radio sources on the basis of their radio morphology are as those adopted in Capetti et al. (2017). I restricted the sample to those radio galaxies with FR II morphology to achieve my goals. Additionally, I expect the physical mechanisms that give rise to potential X-ray emission in radio galaxies with FR II radio morphologies to be different from those of with FR I radio morphologies, because of differences in their particle content (see Croston et al. 2018).

The initial sample included 72 sources. Then, I excluded (i) sources with angular size (measured as the angular separation of the radio position of both hotspots) smaller than 5″ measured at GHz frequencies in VLA[3] radio maps and (ii) three sources, namely: 3CR 187, 3CR 196.1, and 3CR 320 for which deeper investigations have been already published or are in preparation (see Paggi et al., 2020, Ricci et al., 2018 and Vagshette et al., 2019, respectively). I chose to exclude sources with angular sizes below 5″ since, at the redshift range of the sample, it corresponds to 5 - 15 kpc and, therefore, I exclude compact radio sources. In addition, ~ 90% of the on-axis *Chandra* PSF is enclosed in a circular region of 2″ radius. Thus, selecting sources that extend beyond 5″ allowed me to detect extended X-ray emission.

The final sample thus included 35 radio galaxies with FR II radio morphologies, 24 optically classified as HERGs, 7 as LERGs, 2 as BLRGs (see e.g., Laing et al. 1994, Buttiglione et al. 2010, Baldi et al. 2019, for works on optical classification of radio galaxies) and 2 with no clear optical identification (3CR 103 and 3CR 435B). In total, these FR II radio galaxies have 71 hotspots since 3CR 133 shows a double hotspot.

In Fig. 5.1, I show *Chandra* 0.5 - 3 keV images for all sources in the sample, with different pixel sizes and smoothed with different Gaussian kernels, as reported in Table 5.1. Overlaid contours correspond to the radio emission at different frequencies, as reported in Table 5.1. Radio maps were obtained from the VLA archive. I removed point-like sources from these images (including the X-ray nuclei of the radio galaxies but not their hotspots) to highlight the presence of X-ray extended emission, although I only used the point-source subtracted images for visualization purposes (see Fig. 5.1) and to create X-ray surface brightness profiles.

I performed an astrometric registration as described in Chapter 3 for all sources in the sample except those due lacking core detections in radio observations, namely, 3CR 44, 3CR 165, 3CR 198, 3CR 272, 3CR 403.1, 3CR 434, 3CR 435A, and 3CR 456.

[1]http://tgssadr.strw.leidenuniv.nl/doku.php
[2]http://www.lofar.org
[3]http://archive.nrao.edu/nvas/

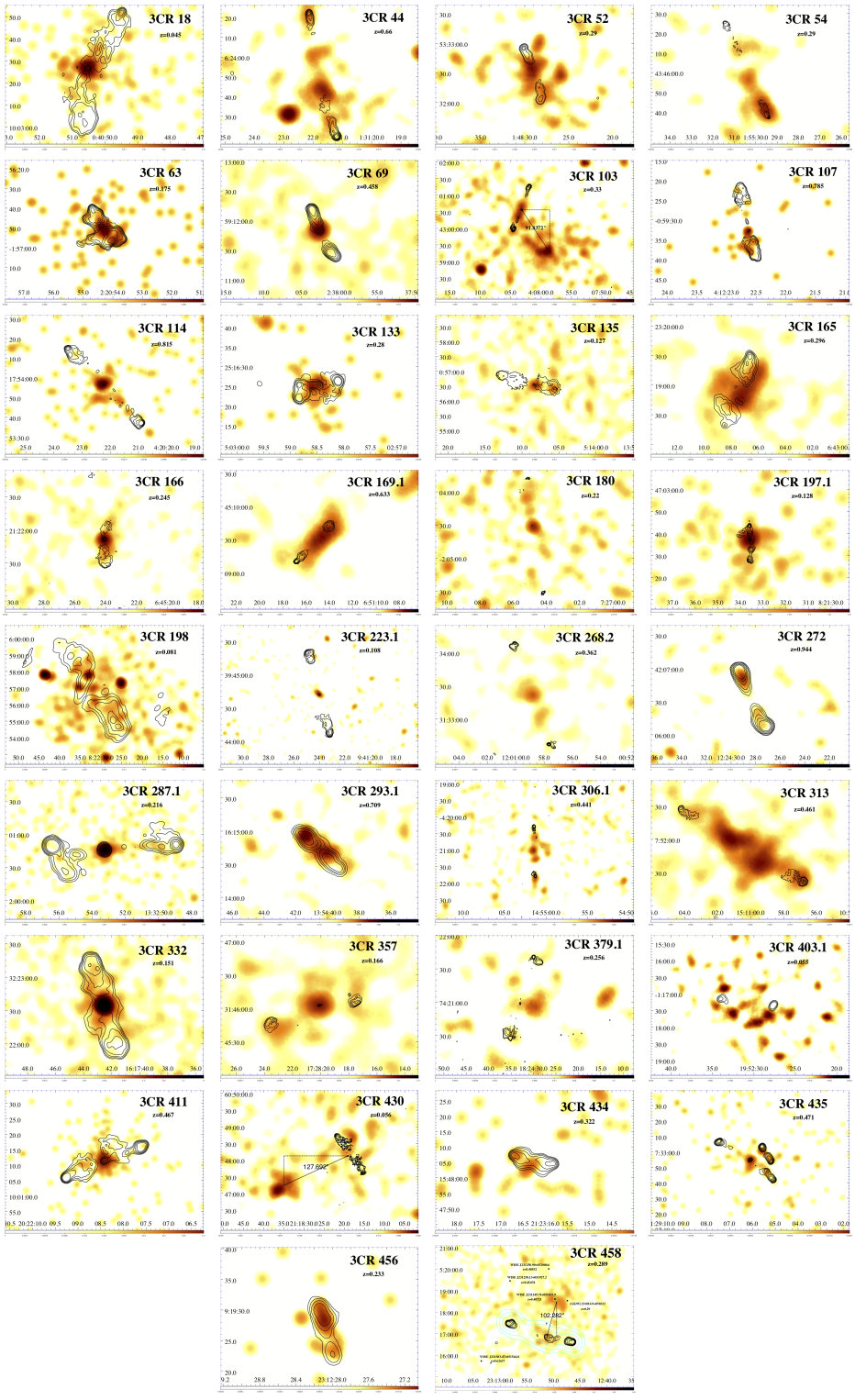

Figure 5.1: X-ray emission, point-source subtracted (see Chapter 3), in the 0.5 - 3 keV band with VLA radio contours overlaid for all sources in the sample. For 3CR 458, I also show the TGSS contours at levels of 40, 160, 640, 2560 mJy/beam. Pixel size of X-ray images, as well as frequency and contour levels for each source are shown in Table 5.1.

5.2 X-ray analysis

Throughout this analysis, I used unbinned and unsmoothed images. I chose to restrict the analysis to the 0.5 - 3 keV energy range since extended X-ray radiation is emitted predominantly in the soft band. This could only affect calculations for a source in a very dense environment. However, I do not expect that to be the case for sources in the sample because all sources were already inspected in the original data papers (see Ineson et al. 2013, 2015, 2017, and Croston et al. 2017).

To search for extended X-ray emission surrounding radio galaxies in the sample as well as the X-ray counterparts of radio hotspots, I considered three different regions (as shown in Fig. 5.2):

1. hotspot regions: circular regions of 2″ radius centered on the radio position of all hotspots and radio cores;

2. a rectangular region, defined along the radio axis on the basis of radio contours, excluding the regions corresponding to both the radio core and the hotspots;

3. a circular region centered on the radio core position and extended as the previous one, but excluding the rectangular region along the radio axis, radio core, and hotspots (circles of 2″ radius each).

The starting level of radio contours to select these regions was set to 5 times the root mean square of the radio map as reported in Table 5.1, which is usually ∼1 mJy/beam.

X-ray detection significance for hotspots was estimated following the procedure described in Chapter 3. For each hotspot region selected, I assume two different background regions: (i) the *standard* X-ray background measured in a circular region as large as the region perpendicular to the radio axis and located on the same CCD chip, far enough from the radio galaxy (i.e., at least a few tens of arcsec) to avoid the smearing of the PSF on CCD borders and contamination from the source, rescaled to the hotspot region size; and (ii) a so-called *local* background, defined as the region along the radio axis where IC/CMB could be present, also rescaled to the size of the hotspot region. In Table 5.2, I show the detection significance obtained for all features and in Table 5.3, I show the background-subtracted number of photons in each region, using the *standard* background.

As an example, in the left panel of Fig. 5.2, regions selected to carry out the analysis for 3CR 313 are shown over its 0.5 - 3 keV X-ray emission. On the other hand, in the right panel of Fig. 5.2 I show the *standard* X-ray background compared to the *local* background, also for 3CR 313.

I chose to label the region along the radio axis as *local* background only when this region was used as background. I used the number of photons in the *standard* X-ray background to also compute the detection significance of the extended X-ray emission along the radio axis and perpendicular to the radio axis.

Additionally, I built X-ray surface brightness profiles for the four sources in the sample with more than 100 photons along the radio axis, namely, 3CR 18, 3CR 198, 3CR 287.1, and 3CR 332.

5.3 Hotspots and diffuse X-ray emission

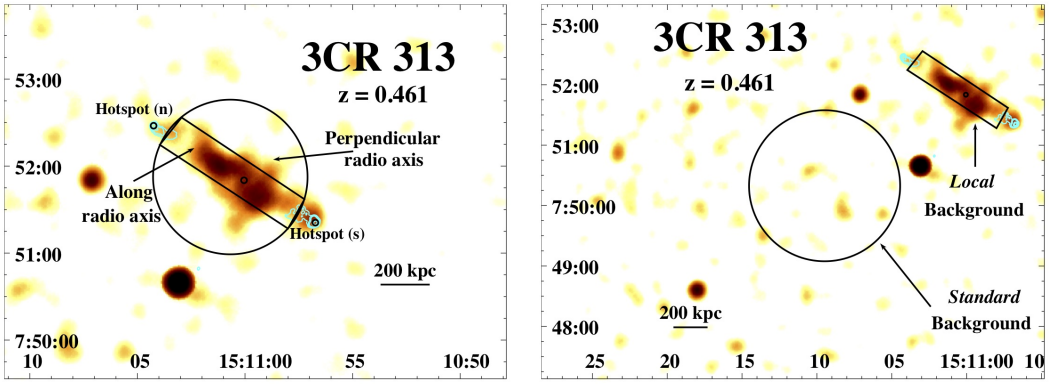

Figure 5.2: Left panel: Example of regions chosen for the detection of hotspots, as well as extended X-ray emission along the radio axis and perpendicular to the radio axis. The 0.5 - 3 keV X-ray emission was smoothed with a 12″ Gaussian kernel and with pixels of 1″. The 8 GHz radio emission is shown as blue contours whose levels are reported in Table 5.1. Similar regions to the ones shown were chosen for the other sources. Right panel: Example of regions chosen as background for 3CR 313 (in black) in the 0.5 - 3 keV band *Chandra* observation. The X-ray emission and radio contours are the same as those in the left panel. These background regions (and similar ones for the other sources) were used while carrying out the extended emission and hotspot detection analysis.

5.3.1 X-ray counterparts of hospots

Using the background estimated in the *standard* region, I detected 30 hotspots out of 35 sources in the sample, all above the 3σ confidence level and 4 of them above 5σ. If instead, I consider the background in the *local* region to guarantee that detected hotspots are not just due to background fluctuations of any diffuse emission, the number of detected hotspots decreases to 7 above the 3σ confidence level ($\sim$ 10% of the total number of hotspots). Therefore, ~75% of hotspots detected, without taking into account the *local* background, could be fluctuations of the extended X-ray emission along the radio axis.

Results of the detection analysis are shown in Table 5.2. I labeled hotspots using the same notation as in the XJET project[4] (Massaro et al. 2011b): their orientation (north, n, south, s, east, e, or west, w) followed by their angular separation (in arcsec) from the core of the radio galaxy.

In Table 5.3, I show a summary of the sources with newly detected hotspots compared with previous works on the 3CR *Chandra* Snapshot Survey. Previous works detected only 6 hotspots (~10 %) for the same sources/observations analyzed here, while only five of them are detected in the second version of the *Chandra* Source Catalog (CSC2[5]; see Evans et al. 2010 for the first version of the catalog and Evans et al. 2019, 2020 for the second release). However, the detection of these hotspots in the CSC2 is only marginal (below a 3σ confidence level) and, therefore, they could be spurious detections instead of X-ray counterparts of the radio hotspots. Using the *standard* background and restricting the energy to the soft band (in contrast with previous analyses, including that of CSC2, that used the full band), I detected new hotspots in 16 sources (see Table 5.3); while using the *local* background, I detected new hotspots in 2 sources and confirmed hotspots

[4]http://hea-www.harvard.edu/XJET/
[5]https://cxc.harvard.edu/csc/

Table 5.2: Detection significance for different radio components

3CR Name	$\sigma_{\parallel}$	$\sigma_{\perp}$	id_1	σ_1	σ_1^{loc}	id_2	σ_2	σ_2^{loc}
18	> 5	> 5	n29	4	–	s26	–	–
44	> 5	4	$n45^{C}$	3	–	s19	3	–
52	> 5	5	$n29^{*,C}$	–	–	s26	–	–
54	4	–	n34	–	–	$s19^{*}$	4	3
63	> 5	> 5	n11	–	–	s7	> 5	–
69	5	–	$n22^{W}$	–	–	s25	3	–
103	> 5	–	n45	–	–	s37	–	–
$107^{\dagger}$	> 5	–	n8	–	–	s7	–	–
114	5	3	n29	–	–	s24	–	–
133	> 5	> 5	w4	–	–	$e5^{C}$	> 5	–
135	–	–	e77	–	–	w43	–	–
165	> 5	> 5	n29	–	–	s48	–	–
166	> 5	5	n15	4	–	$s24^{W}$	–	–
169.1	3	–	n25	–	–	s22	3	–
180	3	–	n43	–	–	s63	–	–
197.1	> 5	> 5	n6	3	–	s10	3	–
198	> 5	4	n107	–	–	s176	–	–
223.1	3	–	n40	–	–	s38	–	–
268.2	5	–	n42	–	–	$s55^{*}$	3	3
272	4	–	n24	3	–	s32	3	–
287.1	> 5	5	$w65^{C}$	4	–	e47	3	–
293.1	5	4	n15	–	–	s29	–	–
306.1	> 5	–	n44	3	–	$s47^{C}$	–	–
313	> 5	4	$n90^{*}$	4	3	$s43^{*}$	4	3
332	> 5	5	$n34^{W}$	3	–	s34	–	–
357	> 5	–	w32	–	–	e44	–	–
379.1	–	3	n44	–	–	s32	–	–
403.1	3	> 5	e35	–	–	w72	–	–
411	> 5	> 5	w13	3	–	e13	–	–
430	–	> 5	n44	–	–	s41	–	–
434	3	–	w8	–	–	e5	4	3
435A	> 5	4	n9	3	–	s14	4	–
435B	> 5	> 5	e22	3	–	w22	4	–
456	4	> 5	n4	> 5	4	s3	4	–
458	5	–	$e75^{*}$	4	4	w122	–	–

Column description: (1) source name; (2) detection significance of the emission along the radio axis; (3) detection significance of the emission perpendicular to the radio axis; (4) first hotspot label; (5) detection significance of the first hotspot using the *standard* X-ray background; (6) detection significance of the first hotspot using the *local* background; (7) second hotspot label; (8) detection significance of the second hotspot using the *standard* X-ray background; (9) detection significance of the second hotspot using the *local* background.

Notes:

(†) Sources with extended X-ray emission previously reported in the survey papers.

(*) Hotspots detected in previous survey papers.

(^{C}) Hotspots detected in the *Chandra* Source Catalog.

(^{W}) Hotspots detected in *WISE*.

3CR 133 presents a double hotspot, e6, detected only over the *standard* background at 5σ level of confidence.

from previous analyses in 4 sources (see Table 5.3), discarding only one hotspot whose detection was claimed in previous survey papers (i.e., n29 in 3CR 52).

Photons in both hotspot regions as well as along the radio axis and in the region perpendicular to the radio axis (see § 5.2 for the definition of each region) and their corresponding background levels are reported in Table 5.3, together with an estimate of the ratio of photons along and perpendicular to the radio axis (ρ), defined as follows:

$$\rho = \frac{N_{ph,\parallel}}{N_{ph,\perp}} \cdot \frac{A_{\perp}}{A_{\parallel}} \tag{5.1}$$

where $N_{ph,\parallel}$ and $N_{ph,\perp}$ are the number of background-subtracted photons along the radio axis and in the region perpendicular to the radio axis, respectively, and $A_{\parallel}$ and $A_{\perp}$ are the areas of the regions along and perpendicular to the radio axis. This parameter gives me an estimate of the importance of the extended X-ray emission perpendicular to the radio axis with respect to the emission along the radio axis. In this table, I also compiled information about which sources present newly detected hotspots, which ones are in known optical galaxy clusters, and the dominant emission process responsible for the extended X-ray emission in each case, according to the detection significance of the extended emission along and perpendicular to the radio axis.

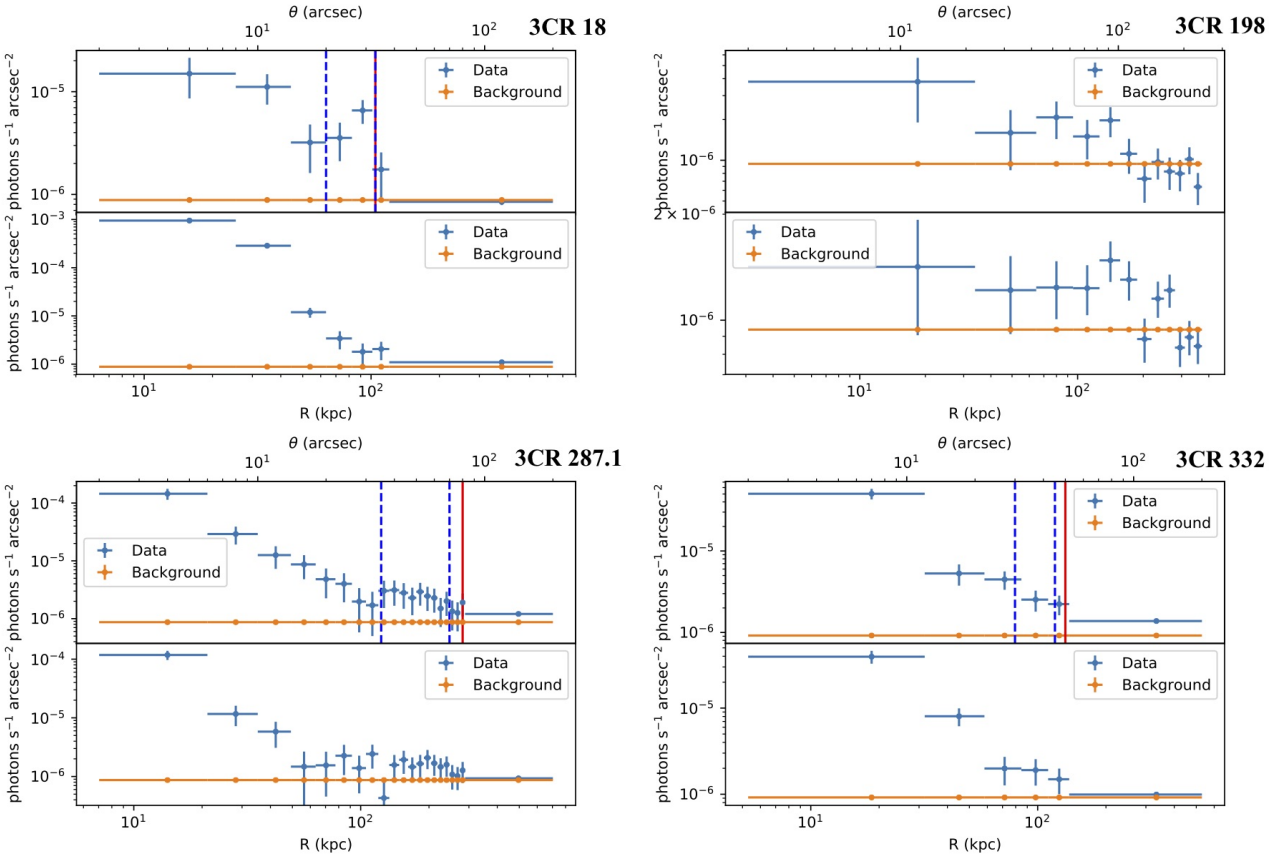

Figure 5.3: Surface brightness profiles for 3CR 18, 3CR 198, 3CR 287.1, and 3CR 332. The top profile in each figure corresponds to the profile along the radio axis, while the bottom profiles correspond to the profiles in the direction perpendicular to the radio axis. The orange points show the background level in each case. The red vertical line marks the extension of the radio emission along the radio axis while the dashed blue lines mark the position of the hotspots. All sources, except for 3CR 198 seem to have X-ray emission extended at least as much as the radio emission.

5.3.2 Lobe and intracluster medium X-ray emission

In comparison with the previous analyses carried out in the data papers of the 3CR *Chandra* Snapshot Survey, I restricted my analysis to the energy range 0.5 - 3 keV because the extended X-ray emission, both coming from the thermal ICM or from IC/CMB, peaks in the soft band. Furthermore, although hotspot emission could also be due to synchrotron radiation, the main contribution to the emission in these snapshot observations would be in the soft band, so restricting the energy band in the analysis does not affect the detection analysis of hotspots. This is supported by the fact that during the XJET project, carried out by Massaro et al. (2011b), only two hotspots out of the 32 detected in radio galaxies and quasars presented more counts in the hard band than in the soft band. In this work, the detection analysis was carried out using the full band (0.5 - 7 keV), observations had exposure times of less than 35 ks and the soft band was defined as 0.5 - 2 keV. Additionally, the hard band generally presents a higher background than the soft band.[6]

[6]These observations were taken during Cycles 9, 12, and 13, when the sensitivity of the soft band was not significantly degraded.

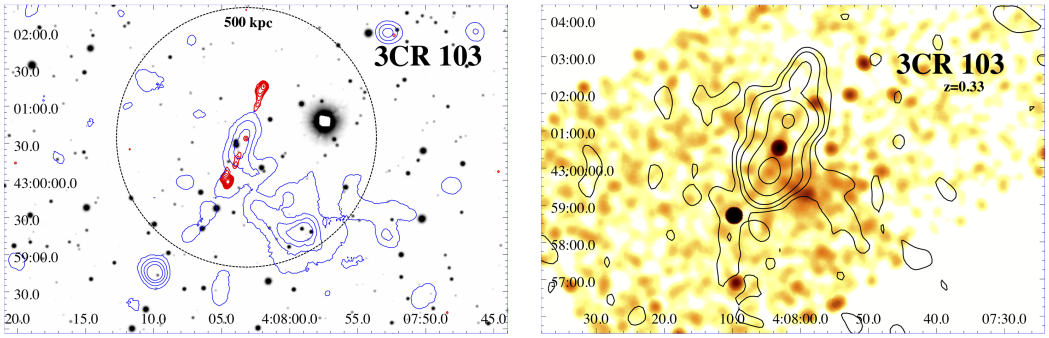

Figure 5.4: Left: Pan-STARSS optical image in the *R* band with VLA 1.4 GHz (in red) and *Chandra* 0.5 - 3 keV (in blue) contours overlaid of 3CR 103. Radio contours were drawn starting at 8 mJy/beam and increasing by a factor of 2. X-ray contours were drawn from the Chandra event file in the 0.5 - 3 keV energy range, smoothed with a 20″ Gaussian kernel at levels of 0.06, 0.08, 0.12, 0.24, 0.48, and 1.20 photons and with pixels of 2″. The dashed black circle has a 500 kpc radius. The X-ray contours show diffuse X-ray emission at 446 kpc to the southwest of 3CR 103 which could indicate that 3CR 103 belongs to a galaxy cluster. Right: *Chandra* image (exposure corrected) in the 0.5 - 3 energy range at center-band energy of 2.3 keV and smoothed with a Gaussian kernel of 13.8″ with TGSS contours overlaid in black drawn at 0.025, 0.05, 0.125, and 0.75 Jy/beam. TGSS radio map has a beam size of 25″. The 150 MHz emission coincident with the extended X-ray emission hints at the presence of a radio halo in a galaxy cluster.

Table 5.2 shows the results of the detection analysis for regions along the radio axis and perpendicular to the radio axis and hotspots, where $\sigma_{\parallel}$ and $\sigma_{\perp}$ are the detection significance of the emission along and perpendicular to the radio axis, and σ_i and σ_i^{loc} are the detection significance of hotspots against the *standard* background and against the *local* background, respectively. Sources and hotspots labeled with asterisks are those previously detected in the survey papers.

I detected extended X-ray emission (in the 0.5 - 3 keV range) along the radio axis against the *standard* background, for 32 out of 35 radio galaxies (i.e., ~90%) in the sample above 3σ level of confidence, while this number decreases to 24 (i.e., ~70%) when considering a threshold of 5σ.

On the other hand, I detected extended X-ray emission in the direction perpendicular to the radio axis, using the *standard* background, in 22 radio galaxies out of 35 above 3σ confidence level (~60%), 15 (~40%) when setting the level of confidence above 5σ.

5.3.3 X-ray surface brightness profiles

For sources with more than 100 photons along the radio axis (see Table 5.3), 3CR 18, 3CR 198, 3CR 287.1, and 3CR 332, I derived X-ray surface brightness profiles along the radio axis and in the direction perpendicular to the radio axis. Images are shown in Fig. 5.3 where the profile along the radio axis is represented on top of the one perpendicular to the radio axis, the extension of the radio emission is marked by a red vertical line, the blue dotted lines represent the hotspot region and the background level is indicated in orange. Although I only considered sources with the largest number of photons along the radio axis, the number of photons in each direction was still too low to obtain reliable results

from the β-profile fit (Cavaliere & Fusco-Femiano 1976, 1978). Although I cannot distinguish thermal and non-thermal emission using β-profile fits, the X-ray surface brightness profiles show that the X-ray emission is extended at least up to the radio structure extent in all cases but for 3CR 198.

5.3.4 Notes on individual sources

For a few targets, I found that the extended X-ray emission here discovered presents intriguing structures, namely 3CR 103, 3CR 268.2, 3CR 403.1, 3CR 430, and 3CR 458, with no associated Planck galaxy clusters (see Ade et al. 2016 and Piffaretti et al. 2011). These structures are discussed below.

3CR 103 (z = 0.33). I did not detect significant emission perpendicular to the radio axis arising from this galaxy, but I detected extended emission at 93″ (446 kpc at the source redshift) above 5σ confidence level to the southwest of the galaxy that could indicate the presence of a galaxy cluster. However, there is a bright star close to the position of the extended emission that prevented me from obtaining precise redshift estimates of nearby optical sources, necessary to verify the presence of a galaxy cluster/group and deserving future follow-up observations.

The left panel of Fig. 5.4 shows an optical image from Pan-STARRS of the field of 3CR 103 with radio contours (at 1.4 GHz) and X-ray contours (in the 0.5 - 3 keV band). The extended X-ray emission appears to be associated with the radio galaxy and seems to correspond to an overdensity of galaxies. Right panel of Fig. 5.4 shows the 0.5 - 3 keV X-ray emission of 3CR 103 with TGSS contours overlaid. Some radio emission can be seen matching the position of the extended X-ray emission, which could hint at the presence of a radio halo in a galaxy cluster (see e.g. Giovannini et al. 1993, Burns et al. 1995, Feretti et al. 1997a,b, Giovannini et al. 1999, Govoni et al. 2001, Feretti et al. 2012, and van Weeren et al. 2019).

3CR 268.2 (z = 0.362). I found no significant emission perpendicular to the radio axis. Nevertheless, I detected X-ray emission extended ~302″ (1.5 Mpc at the source redshift) above 5σ confidence level to the northeast of this source which could be due to the presence of an unrelated galaxy cluster (see Fig. 5.5). I explored the optical data available in the SDSS archive (see e.g., Ahn et al. 2012) and in Figure 5.5 I show the R band image of the field around 3CR 268.2. There are 8 sources with spectroscopic redshift estimates, two of them, marked in blue in Figure 5.5, have a velocity dispersion of ~725 km s^{-1}, thus corresponding to the typical velocity dispersion in groups and clusters of galaxies (see e.g., Moore et al. 1993, Eke et al. 2004, Berlind et al. 2006, and Massaro et al. 2019). This suggests the possible presence of a galaxy group surrounding 3CR 268.2. Moreover, Wen et al. (2012), using the photometric redshifts of the SDSS database, also claimed the presence of four candidate galaxy clusters highlighted with black circles in the same figure, namely: WHL J120053.9+313522 at z_{ph} = 0.2993, WHL J120105.4+313828 at z_{ph} = 0.3082 (which coincides with the position of the extended X-ray emission at 302″ from 3CR 268.2), WHL J120034.6+313051 at z_{ph} = 0.3528 (with a tentative association with a source having spectroscopic redshift 0.3645), and WHL J120037.1+313804 at z_{ph} = 0.3366, two of them marginally consistent with that of 3CR 268.2 lying at z = 0.362.

3CR 403.1 (z = 0.0554). I detected significant emission along and in the perpendicular direction to the radio axis. The extended X-ray emission is aligned with the GHz radio structure (see Fig. 5.1); however, the TGSS structure is perpendicular to the X-ray

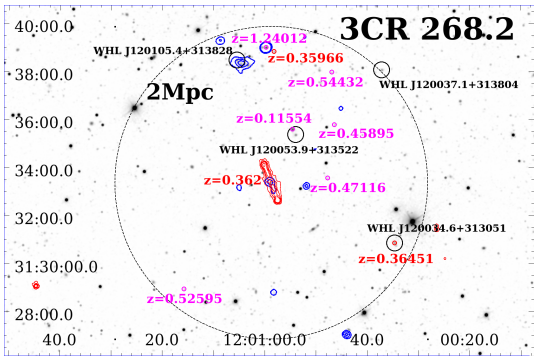

Figure 5.5: The SDSS *R* band image of the field around 3CR 268.2 (Ahn et al. 2012). Radio contours of the LoTSS dataset are marked in red as in Figure 5.8 to indicate the location of 3CR 268.2. Its redshift is also reported in red. The large dashed circle has a 2 Mpc radius computed at the central source redshift of 0.362 and centered on its position. Unrelated optical sources with spectroscopic redshifts are marked with magenta circles and two with a redshift difference less than 0.003 with respect to 3CR 268.2 are marked in red. Finally, black circles mark the location of the four candidate galaxy clusters found using photometric redshifts by Wen et al. (2012). Blue X-ray contours are drawn from the *Chandra* event file with a pixel size of 1″ and smoothed with a Gaussian kernel of 14″ at levels of 0.03, 0.05, and 0.07 photons. The candidate galaxy cluster WHL J120105.4+313828, at $z_{ph} = 0.3082$, in the northern direction appears to have an extended X-ray counterpart. The presence of sources at similar redshifts as the one of 3CR 268.2, suggests the presence of a galaxy group surrounding it.

extended emission as shown in Fig. 5.6. This could indicate the presence of a radio relic (see e.g., Rottgering et al. 1994, 1997, Bagchi et al. 1998, Feretti & Giovannini 1998, Giovannini et al. 1999, Feretti et al. 2012, and van Weeren et al. 2019).

3CR 430 ($z = 0.0555$). I detected significant emission perpendicular to the radio axis (above 5σ level of confidence) that could be due to ICM from a galaxy cluster at the same position as the radio galaxy. I additionally detected extended X-ray emission at 118″ (128 kpc at the source redshift) above 5σ confidence level to the southeast of this source that could hint at the presence of another galaxy cluster, possibly undergoing a merging process with the former. Assuming this emission comes from ICM from a galaxy cluster, the brightest cluster galaxy (BCG) would be J211836.50+604704.2 whose redshift is $z = 0.05593 \pm 0.00026$, which supports the hypothesis of these two galaxy clusters undergoing a merging process.

The left panel of Fig. 5.7 shows an optical image of the field of 3CR 430 with radio contours (at 4.9 GHz) and X-ray contours (in the 0.5 - 3 keV band). The right panel of Fig. 5.7 shows the 0.5 - 3 keV *Chandra* image of 3CR 430 with TGSS contours overlaid. Diffuse radio emission lying beyond the extended X-ray emission could indicate the presence of a radio relic if the X-ray emission arises indeed from two merging galaxy clusters.

3CR 458 ($z = 0.289$). I detected extended X-ray emission (460 kpc at the source redshift) above a 5σ confidence level at 105″ to the northwest of this source which could be due to the presence of another galaxy cluster that could be related to the radio galaxy (see Fig. 5.1). Wen & Han (2015) reported the presence of a galaxy cluster at $z = 0.407$ at the position of the extended emission, which would mean that this extended

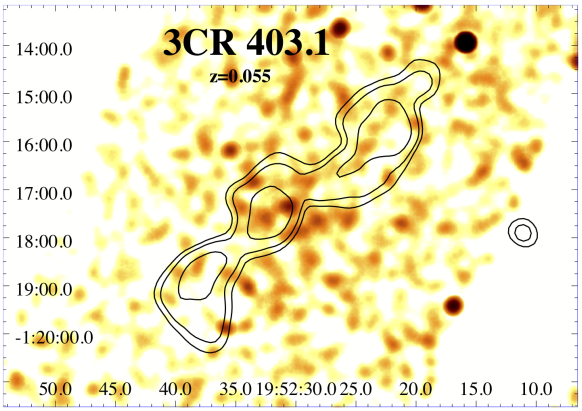

Figure 5.6: *Chandra* image (exposure corrected) in the 0.5 - 3 energy range and center-band energy of 2.3 keV with TGSS contours overlaid in black drawn at 0.025, 0.05, 0.125, and 0.75 Jy/beam. TGSS radio map has a beam size of 25″. The fact that the low-frequency radio emission is not co-spatial with the X-ray emission suggests the presence of a radio relic.

emission would be unrelated to the radio galaxy (at $z = 0.289$). However, there is also another galaxy for which the photometric redshift is known at the position of this extended emission (Gorshkov & Konnikova 1995). This galaxy, at $z = 0.29$, would be consistent with a source belonging to the same galaxy cluster as 3CR 458.

5.4 A radio and X-ray comparison

I compared *Chandra* observations with low radio frequency observations from TGSS and LOFAR at ~150 MHz. LOFAR observations were only available for 11 of the targets.

LOFAR observations are part of the forthcoming Data Release 2 (DR2) of LoTSS[7], i.e, a deep 120-168 MHz imaging survey. These datasets were processed by the international LOFAR collaboration as part of the LOFAR Data Release 1 and 2 (Shimwell et al. 2017, 2019 and Tasse et al. 2020, respectively).

Electrons responsible for IC/CMB emission from lobes in the soft X-rays (0.5 - 3 keV) are also responsible for the emission of synchrotron radiation at a frequency given by:

$$\nu_{syn}^{obs} = 3.72 \times 10^{-5} \nu_{IC}^{obs} \frac{B}{1+z} Hz \tag{5.2}$$

where ν_{syn}^{obs} is the observed frequency of the synchrotron radiation of the same electrons scattering the CMB at ν_{IC}^{obs} in the Thomson regime, while B is the magnetic field in Gauss and z the source redshift. Then, considering $\nu_{IC}^{obs} \sim 10^{17}$ Hz, and $B \sim 10$ μG (as found in the lobes of several radio galaxies by Ineson et al. 2017), I could detect synchrotron radiation from the same electrons emitting via IC/CMB in X-rays at radio frequencies of tens of MHz. Therefore, using radio observations at ~150 MHz allows me to get closer to the low-frequency regime needed to produce the IC/CMB radiation in the *Chandra*

[7]The DR2 v2.2 was run as part of the ddf pipeline (https://github.com/mhardcastle/ddf-pipeline) and the LoTSS DR1 consists of images at 6″ resolution and ~70 μJy/beam sensitivity covering an area of ~400 square degrees while the footprint of the DR2 will cover an area of approximately 5700 square degrees, both performed in the northern hemisphere.

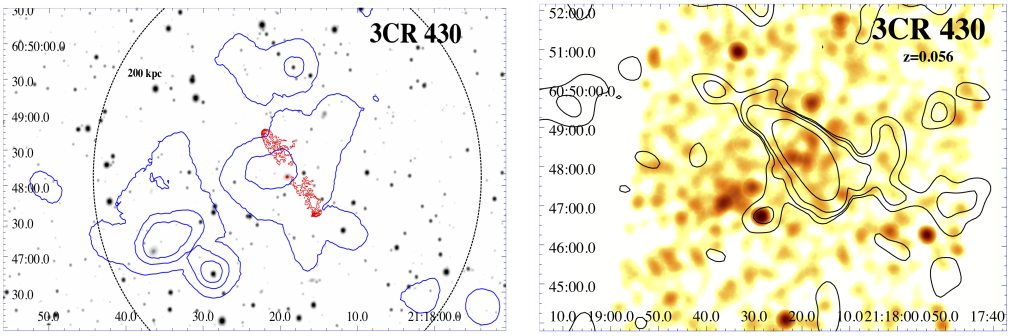

Figure 5.7: Left: Pan-STARSS optical image in the *R* band with VLA 1.4 GHz (in red) and Chandra 0.5 - 3 keV (in blue) contours overlaid of 3CR 430. Radio contours were drawn starting at 0.2 mJy/beam and increasing by a factor of 2. X-ray contours were drawn from the *Chandra* event file in the 0.5 - 3 keV energy range, smoothed with a 29.5″ Gaussian kernel at levels of 0.005, 0.08, 0.1 photons and with 2″ pixels. The dashed black circle has a 200 kpc radius. The two different extended X-ray emission structures could indicate the presence of two galaxy clusters undergoing a merging process. Right: *Chandra* image with 1″ pixels, exposure corrected in the 0.5 - 3 energy range at center-band energy of 2.3 keV and smoothed with a Gaussian kernel of 16″ with TGSS contours overlaid in white drawn at 0.025, 0.05, 0.125, and 0.75 Jy/beam. TGSS radio map has a beam size of 25″. TGSS contours mark the presence of radio emission unrelated to the extended X-ray emission, which could indicate the presence of a radio relic.

energy band. Thus, when I find low radio frequency lobe-emission co-spatial with the extended X-ray structure, I tend to favor a possible IC/CMB interpretation, if fainter or null cross-cone emission is present.

Sources for which LoTSS data were available are: 3CR 18, 3CR 54, 3CR 198, 3CR 223.1, 3CR 268.2, 3CR 272, 3CR 313, 3CR 332, and 3CR 357. LoTSS images are shown in Figure 5.8, where the X-ray emission, in the 0.5 - 3 keV band, can be seen with VLA contours in blue and 150 MHz LoTSS contours in black overlaid. X-ray and VLA image parameters are reported in Table 5.1, while LoTSS image parameters are collected in the caption of Fig. 5.8. In general, 150 MHz emission traces radio lobes along the whole radio axis, even where no high-frequency radio emission can be seen. The emission at 150 MHz matches the extent of the X-ray emission which is in line with IC/CMB being the dominant emission process occurring co-spatially with radio lobes.

All sources in the sample but 3CR 197.1 and 3CR 434 are extended in TGSS but only 3CR 44, 3CR 135, 3CR 268.2, 3CR 272, 3CR 287.1, 3CR 313, 3CR 332, 3CR 357, 3CR 379.1, and 3CR 458 present a double morphology at ∼150 MHz. I only show the TGSS data of 3CR 103 (right panel of Fig. 5.4), 3CR 403.1 (Fig. 5.6), 3CR 430 (right panel of Fig. 5.7), and 3CR 458 (last panel in Fig. 5.1) since I only used it to confirm the sources' double morphology.

5.5 An optical overview

I checked for the presence of "red sequences" (i.e., a color-magnitude relation followed by galaxies belonging to the same galaxy cluster; see Visvanathan & Sandage 1977 and De Lucia et al. 2007) in the fields of some sources in the sample to determine whether

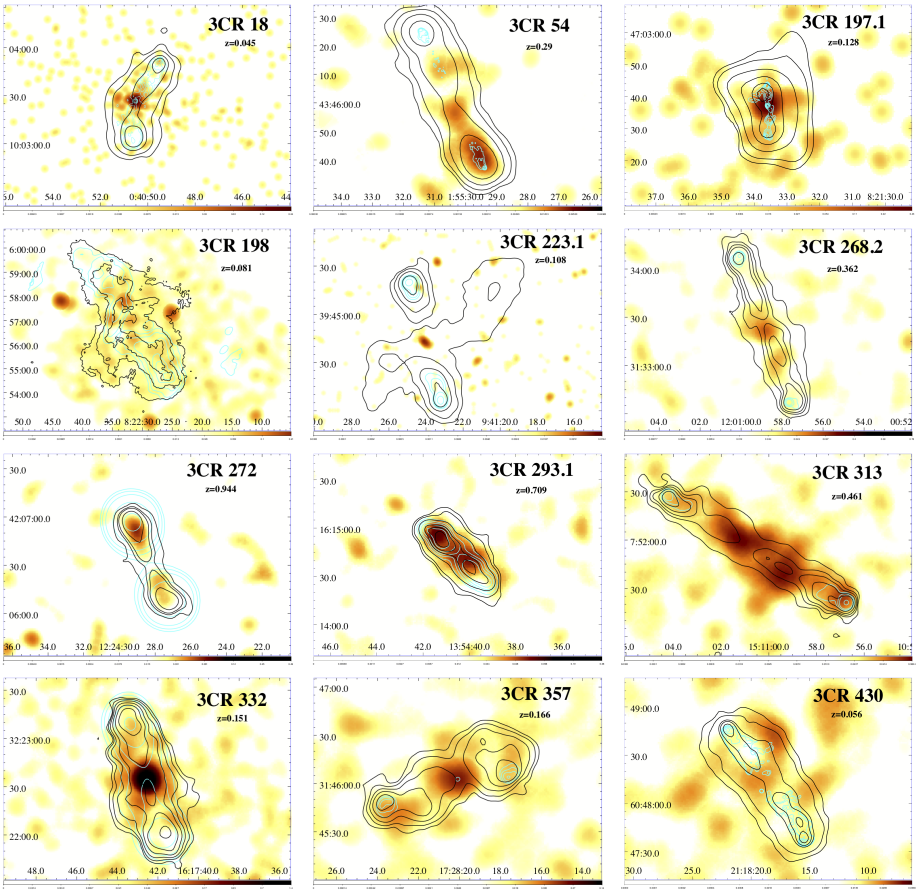

Figure 5.8: X-ray image, VLA contours (cyan) and 150 MHz contours (black). X-ray and VLA image parameters are shown in Table 5.1. LoTSS contours for each source are at 40, 160, 640, 1280 mJy/beam for 3CR 18; at 10, 40, 160, 640 mJy/beam for 3CR 54; at 40, 80, 240, 640, 1200, 1600 mJy/beam for 3CR 197.1; at 2, 8, 16 mJy/beam for 3CR 198; at 10, 40, 160, 640 mJy/beam for 3CR 223.1; at 10, 40, 80, 160, 640 mJy/beam for 3CR 268.2; at 10, 40, 80, 320 mJy/beam for 3CR 272; at 10, 20, 80, 320, 500, 800, 1300 mJy/beam for 3CR 293.1; at 40, 160, 320, 640, 1280 mJy for 3CR 313; at 10, 20, 40, 80, 160, 320 mJy for 3CR 332; at 20, 40, 80, 160, 320 mJy for 3CR 357, and at 100, 200, 800, 1200, 2000 mJy/beam for 3CR 430, respectively. LoTSS radio maps have beamsizes of 6″. 150 MHz emission traces better the lobe emission than the GHz emission and, thus, it suggests that the extended X-ray emission coincident with it is most likely due to IC/CMB from lobes.

these sources belong to galaxy clusters. Sources selected were those for which the ratio of photons along and perpendicular to the radio axis, $\rho < 1$ (Table 5.3) as defined in equation 5.1, meaning that the emission perpendicular to the radio axis is comparable to the emission along the radio axis, which hints at the presence of thermal emission from ICM in galaxy clusters. Magnitudes in the *r* and the *i* band (not corrected for Galactic absorption) for sources lying at > 500 kpc radius around the positions of the radio galaxies were obtained from Pan-STARRS[8].

I explored the red sequences in the fields of 3CR 103 (since I detected extended emis-

[8]https://catalogs.mast.stsci.edu/panstarrs/

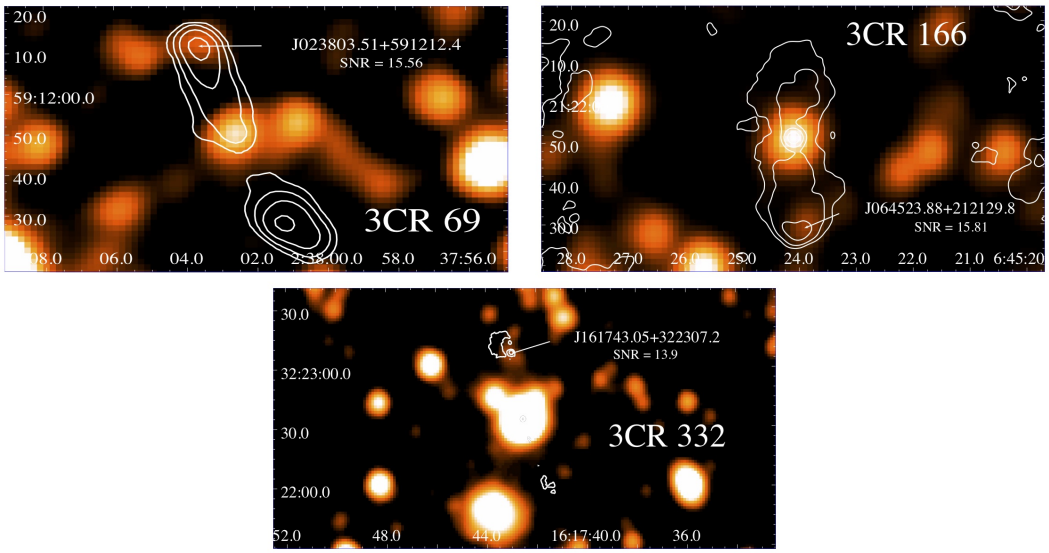

Figure 5.9: Top: 3.4 μm *WISE* image of 3CR 69 with 4.8 GHz VLA contours overlaid. Radio contours start at 2 mJy/beam and increase by a factor of four. VLA radio map has a beam size of 5″. Center: 3.4 μm *WISE* image of 3CR 166 with 1.4 GHz VLA contours overlaid. Radio contours start at 3 mJy/beam and increase by a factor of four. VLA radio map has a beam size of 1.4″. Bottom: 3.4 μm *WISE* image of 3CR 332 with 1.4 GHz VLA contours overlaid. Radio contours start at 1 mJy/beam and increase by a factor of four. VLA radio map has a beam size of 4.4″.

sion in the field with no redshift information that could be related to the radio galaxy), 3CR 379.1, 3CR 430. However, I was not able to identify red sequences in the fields of these sources. Nevertheless, spectroscopic follow-up observations would be crucial to confirm these results.

5.6 A WISE serendipitous discovery

I cross-matched the radio position of all hotspots in the radio galaxy sample with the *AllWISE* catalog aiming at finding their mid-IR counterparts. This was done while performing the test on the mid-IR counterparts of X-ray sources detected using the WAVDETECT algorithm.

I adopted a searching radius of 3.3″, chosen on the basis of previous analyses (see e.g., D'Abrusco et al. 2013, 2014; Massaro et al. 2014), since the chance probability to have spurious cross-matches between radio sources with an average positional uncertainty of the order of ∼1″ and their potential *WISE* counterparts is less than ∼1%, for angular separations below this value (see also Massaro et al. 2011a; D'Abrusco et al. 2012; Massaro et al. 2013a,b, for additional information on the method to compute the chance probability).

I found three hotspots, namely n22 in 3CR 69 (with $W1$ magnitude 15.553 ± 0.05), s24 in 3CR 166 ($W1 = 15.805 \pm 0.057$), and n34 in 3CR 332 ($W1 = 14.214 \pm 0.033$), having a clear mid-IR counterpart, all detected at 3.4 μm and 4.6 μm in *WISE* images, as shown in Fig. 5.9, respectively. The first two sources have a SNR greater than 15, while the third hotspot in 3CR 322 has a SNR of 13.9, all measured at 3.4 μm. These SNRs are generally

lower than those for example found for mid-IR counterparts of blazars with radio flux density of the order of a few mJy (see e.g. catalogs in D'Abrusco et al. 2014, 2019; de Menezes et al. 2019). Thus, although these SNRs are well above the *AllWISE* catalog threshold[9] I also carry out the following test to get a better idea of their significance. Since these hotspots have flux densities of the order of 1 mJy, I cross-matched all FIRST sources of 1 mJy (a total of 2907) with the *AllWISE* catalog within 3.3″. I found a total of 1407 cross-matches, all unique. Then I found that 124 out of 1407 (i.e., ∼8%) have SNR between 13 and 16, and ∼1/3 of all cross-matches are detected with SNR greater than 15, all computed at 3.4 μm that is the band with the largest number of constraints to claim a mid-IR detection. Thus I am confident that my claim on the discovery of mid-IR counterparts of three hotspots is reliable.

It is worth noting that mid-IR counterparts of hotspots and lobes of radio galaxies have already been observed in the past, especially for 3CR sources (Werner et al. 2012 and references therein). This serendipitous discovery proves that *WISE* is also able to detect them with a shallow mid-IR survey. Additionally, one hotspot in the sample was previously detected in the literature in the optical and near-IR, namely the eastern hotspot of 3CR 133 (Madrid et al. 2006). Lastly, de Koff et al. (1996) proposed a possible candidate for the optical counterpart of the western hotspot of 3CR 287.1.

5.7 Summary and discussion

I carried out a thorough analysis of 35 FR II radio galaxies with angular sizes above 5″, measured in the GHz radio maps, in the 3CR *Chandra* Snapshot Survey observed before Cycle 20 and not in the 3CRR catalog (excluding also 3CR 187, 3CR 196.1, and 3CR 320, for which detailed follow-up analyses have already been performed). My main goals were:

1. To study how the presence of this extended emission affects the detection of hotspots.
2. To investigate the origin of extended X-ray emission in radio galaxies (either non-thermal emission due to IC/CMB from lobes or thermal emission from ICM from galaxy clusters).

Throughout this analysis, I used 0.5 - 3 keV, background and point source subtracted, exposure-weighted observations from the *Chandra* Snapshot Survey, refining the previous analyses.

I found that ∼90% of galaxies in the sample presented significant (> 3σ confidence level) extended emission coincident with the radio axis (∼70% above a 5σ confidence level); while ∼60% presented significant extended emission in the direction perpendicular to the radio axis (∼40% above a 5σ confidence level). For those galaxies for which I detected extended X-ray emission perpendicular to the radio axis, at similar confidence levels as the emission along the radio axis, I tend to favor the scenario where the underlying emission process is thermal radiation from an ICM, while for sources where no significant emission perpendicular to the radio axis is detected I favor the scenario in which non-thermal IC/CMB emission is produced by electrons stored in the radio lobes.

In total, I found that IC/CMB is the most likely dominant emission process in ∼71% of sources, while for ∼17% of them, the dominant emission process is most likely thermal

[9]https://irsa.ipac.caltech.edu/Missions/wise.html,

Table 5.3: Summary of features detected in this work compared to detections reported in the literature.

3CR Name	Optical Classification	hotspot 1	hotspot 2	along radio axis	perpendicular radio axis	ρ	New hotspots standard, local	Optical Cluster	Dominant Process
18	BLRG	2.98 (1.90)	0.00 (0.14)	130.70 (13.69)	44.80 (9.89)	4.4	Y, –		IC/CMB
44	HERG	1.98 (1.56)	0.98 (1.14)	25.10 (8.00)	17.20 (8.82)	2.1	Y, –	✓	IC/CMB
52	HERG	0.00 (0.14)	0.98 (1.14)	21.00 (7.65)	20.40 (8.82)	1.6	–	✓	ICM
54	HERG	0.00 (0.14)	2.98 (1.90)	9.90 (5.37)	4.40 (5.53)	2.4	N, N		IC/CMB
63	HERG	0.00 (0.14)	4.98 (2.40)	16.60 (4.76)	9.20 (4.06)	3.9	Y, –		–
69	HERG	0.00 (0.14)	0.98 (1.14)	15.80 (6.86)	4.4 (5.89)	2.4	Y, –		IC/CMB
103		0.00 (0.14)	0.98 (1.14)	20.30 (8.07)	3.5 (9.43)	3.1	–		IC/CMB
107	HERG	0.00 (0.14)	0.98 (1.14)	6.70 (3.19)	1.40 (2.19)	7.4	–		IC/CMB
114	LERG	0.00 (0.14)	0.00 (0.14)	12.10 (5.58)	10.10 (9.14)	2.8	–		IC/CMB
133	HERG	0.00 (0.14)	2.98 (1.90)	11.90 (3.78)	6.70 (3.19)	4.1	N, –		IC/CMB
135	HERG	0.00 (0.14)	0.98 (1.14)	4.80 (8.61)	7.00 (15.42)	1.2	–	✓	–
165	LERG	0.00 (0.14)	0.98 (1.14)	39.20 (10.36)	54.20 (16.52)	2.1	–		ICM
166	LERG	1.98 (1.56)	0.00 (0.14)	28.20 (7.24)	13.10 (6.10)	2.5	Y, –		IC/CMB
169.1	HERG	0.00 (0.14)	0.98 (1.14)	6.30 (4.64)	6.50 (6.48)	1.8	Y, –		IC/CMB
180	HERG	0.00 (0.14)	0.00 (0.14)	6.50 (6.16)	16.00 (15.20)	1.5	–		IC/CMB
197.1	HERG	0.98 (1.14)	0.98 (1.14)	29.60 (5.10)	16.60 (5.79)	7.1	Y, –	✓	IC/CMB
198	HERG	0.00 (0.14)	0.00 (0.14)	129.60 (33.31)	124.90 (64.45)	1.4	–	✓	IC/CMB
223.1	HERG	0.00 (0.14)	0.00 (0.14)	9.80 (8.90)	12.50 (16.69)	1.4	–		IC/CMB
268.2	HERG	0.98 (1.14)	1.98 (1.56)	25.10 (11.70)	1.40 (12.05)	2.0	N, N		IC/CMB
272	HERG	0.98 (1.14)	0.98 (1.14)	10.50 (6.98)	9.30 (11.87)	1.8	Y, –		IC/CMB
287.1	HERG	0.00 (0.14)	0.98 (1.14)	167.20 (16.99)	27.20 (12.85)	7.2	Y, –		IC/CMB
293.1	HERG	0.00 (0.14)	0.00 (0.14)	14.40 (6.50)	17.00 (8.85)	1.7	–		IC/CMB
306.1	HERG	1.98 (1.56)	0.98 (1.14)	24.10 (9.22)	9.10 (11.71)	2.5	Y, –	✓	IC/CMB
313	HERG	2.98 (1.90)	2.98 (1.90)	93.60 (16.65)	41.8 (20.10)	2.7	N, N	✓	IC/CMB
332	HERG	1.98 (1.56)	0.00 (0.14)	203.80 (19.17)	47.60 (18.83)	7.1	Y, –	✓	IC/CMB
357	LERG	0.00 (0.14)	0.00 (0.14)	31.80 (12.40)	15.10 (15.39)	1.8	–	✓	IC/CMB
379.1	HERG	0.00 (0.14)	0.00 (0.14)	2.50 (5.90)	12.60 (9.22)	0.7	–		ICM
403.1	LERG	0.00 (0.14)	0.00 (0.14)	15.40 (9.94)	62.90 (21.67)	1.1	–	✓	ICM
411	HERG	1.98 (1.56)	0.98 (1.14)	68.80 (9.46)	55.30 (10.95)	1.2	Y, –		ICM
430	LERG	0.00 (0.14)	0.00 (0.14)	7.80 (7.44)	50.20 (16.19)	0.8	–		ICM
434	LERG	0.00 (0.14)	2.98 (1.90)	4.20 (3.13)	3.30 (5.54)	2.0	Y, Y	✓	–
435A	BLRG	0.98 (1.14)	1.98 (1.56)	6.70 (3.19)	6.60 (4.01)	3.7	Y, –		IC/CMB
435B		0.98 (1.14)	1.98 (1.56)	17.70 (5.99)	18.60 (7.82)	2.4	Y, –		IC/CMB
456	HERG	9.98 (3.30)	2.98 (1.90)	2.90 (2.05)	14.30 (5.30)	2.2	Y, Y		–
458	HERG	2.98 (1.90)	0.00 (0.14)	39.40 (15.58)	20.90 (20.03)	1.6	N, N	✓	IC/CMB

Column 1: source name. Column 2: optical classification. Columns 3-6: net source photons measured in the hotspots, along the radio axis and perpendicular to the radio axis with the corresponding background photons for those regions in parenthesis. Background here refers to the *standard* background. Column 7: ratio of photons along and perpendicular to the radio axis as defined by Eq. 5.1. Column 8: flag for sources with new hotspots detected using the *standard* and the *local* background. "Y" indicates a newly detected hotspot, "N" indicates a hotspot detected in this work that was previously detected by other works and "-" indicated a non-detection. Column 9: flag that indicates whether the presence of an optical galaxy cluster was previously reported. Column 10: Dominant emission process for the extended X-ray emission.

emission from the ICM (see Table 5.3). However, I could not establish which mechanism was responsible for the extended X-ray emission in the remaining ∼11%. Among sources optically classified LERGs, there is the same number of sources for which the dominant emission comes from non-thermal emission (IC/CMB) and from thermal emission (ICM). For HERGs, non-thermal emission (IC/CMB) dominates in six times more sources than thermal emission (ICM). This suggests that FR II-LERGs inhabit galaxy clusters more often than FR II-HERGs (see Massaro et al. 2019, 2020 for an in-depth analysis of the environments of radio galaxies). A summary of these results can be found in Table 5.3.

I confirmed the detection of 7 hotspots in the 0.5 - 3 keV band above 3σ confidence level, excluding the possibility of them being fluctuations of the extended X-ray emission that surrounds them. Using the soft energy band and the *local* background, I did not confirm one of the detected hotspots claimed in previous survey analyses (n29 in 3CR 52) but do claim newly detected hotspots in two sources. This demonstrates the relevance of taking into account the extended emission along the radio axis when detecting hotspots. Additionally, I detected the presence of extended X-ray emission that could arise from the ICM in the fields of 3CR 103 and 3CR 430.

Using X-ray surface brightness profiles, I concluded that the X-ray emission is extended up to extent of the radio structure in, at least, four sources. However, deeper X-ray observations are needed to distinguish between thermal and non-thermal emission processes.

I performed a multifrequency comparison to further constrain the origin of this emission. I compared low radio frequency and X-ray emission for those sources with LOFAR observations (3CR 18, 3CR 54, 3CR 198, 3CR 223.1, 3CR 268.2, 3CR 272, 3CR 313, 3CR 332,

and 3CR 357). In all cases, the low radio frequency morphology seems to trace the extended X-ray emission. Thus, in those cases, I tend to favor IC/CMB as the dominant emission process. I performed an optical investigation of the red sequences of sources in the field of 3CR 103, 3CR 379.1, and 3CR 430; however, it is not clear whether they belong to galaxy clusters/groups.

A summary of these results is presented in Table 5.3, where I show the number of photons in each region, with the number of background photons scaled to the size of the region in parenthesis. The parameter ρ defines the ratio of the emission along and perpendicular to the radio axis scaled to the sizes of the regions according to Eq. 5.1. I also collect in Table 5.3 information on sources that have newly detected hotspots, which ones are in known optical clusters and which is the dominant emission process in each case.

Lastly, during this analysis, I made the serendipitous discovery that three hotspots in the sample were detected in WISE, namely n22 in 3CR 69, s24 in 3CR 166, and n34 in 3CR 332.

Bibliography

Ade, P. A. R., Aghanim, N., Arnaud, M., et al. 2016, A&A, 594, A27

Ahn, C. P., Alexandroff, R., Allende Prieto, C., et al. 2012, ApJS, 203, 21

Allen, M. G., Sparks, W. B., Koekemoer, A., et al. 2002, ApJS, 139, 411

Assef, R. J., Stern, D., Kochanek, C. S., et al. 2013, ApJ, 772, 26

Bagchi, J., Pislar, V. & Lima Neto, G. B. 1998, MNRAS, 296, L23

Baldi, R. D. & Capetti, A. 2008, A&A, 489, 989

Baldi, R. D., Chiaberge, M., Capetti, A., et al. 2010, ApJ, 725, 2426

Baldi, R. D., Rodríguez Zaurín, J., Chiaberge, M., et al. 2019, ApJ, 870, 53

Balmaverde, B., Capetti, A., Grandi, P., et al. 2012, A&A, 545, A143

Balmaverde, B., Capetti, A., Marconi, A., et al. 2019, arXiv e-prints, 1903.10768

Bennett, A. S. 1962, MNRAS, 125, 75

Bennett, C. L., Larson, D., Weiland, J. L. & Hinshaw, G. 2014, ApJ, 794, 135

Berlind, A. A., Frieman, J., Weinberg, D. H., et al. 2006, ApJS, 167, 1

Burns, J. O., Roettiger, K., Pinkney, J., et al. 1995, ApJ, 446, 583

Buttiglione, S., Capetti, A., Celotti, A., et al. 2009, A&A, 495, 1033

Buttiglione, S., Capetti, A., Celotti, A., et al. 2009, A&A, 509, A6

Buttiglione, S., Capetti, A., Celotti, A., et al. 2011, A&A, 525, A28

Capetti, A., Massaro, F. & Baldi, R. D. 2017, A&A, 601, A81

Cavaliere, A. & Fusco-Femiano, R. 1976, A&A, 500, 95

Cavaliere, A. & Fusco-Femiano, R. 1978, A&A, 70, 677

Chambers, K. C., Magnier, E. A., Metcalfe, N., et al. 2016, arXiv e-prints, 1612.05560

Chiaberge, M., Capetti, A. & Celotti, A. 2000, A&A, 355, 873

Condon, J. J., Cotton, W. D., Greisen, E. W. , et al. 1998, AJ, 115, 1693

Croston, J. H., Hardcastle, M. J., Harris, D. E., et al. 2005, ApJ, 626, 733

Croston, J. H., Ineson, J., Hardcastle, M. J., et al. 2017, MNRAS, 470, 1943

Croston, J. H., Ineson, J. & Hardcastle, M. J. 2018, MNRAS, 476, 1614

D'Abrusco, R., Massaro, F., Ajello, M., et al. 2012, ApJ, 748, 68

D'Abrusco, R., Massaro, F., Paggi, A., et al. 2013, ApJS, 206, 12

D'Abrusco, R., Massaro, F., Paggi, A., et al. 2014, ApJS, 215, 14

D'Abrusco, R., Álvarez-Crespo, N., Campana, R., et al. 2019, ApJS 242, 4

Dasadia, S., Sun, M., Morandi, A., et al. 2016, MNRAS, 458, 681

De Lucia, G., Poggianti, B. M., Aragón-Salamanca, A., et al. 2005, ApJ, 626, 733

de Koff, S., Baum, S. A., Sparks, W. B., et al. 1996, ApJS, 107, 621

de Menezes, R., Peña-Herazo, H. A., Marchesini, E. J., et al. 2019, A&A 630, 55

Dicken, D., Tadhunter, C., Morganti, R., et al. 2014, ApJ, 788, 98

Eckart, M. E., McGreer, I. D., Stern, D., et al. 2010, ApJ, 708, 584

Edge, D. O., Shakeshaft, J. R., McAdam, W. B., et al. 1959, MmRAS, 69, 37

Eke, V. R., Baugh, C. M.,Cole, S., et al. 2004, MNRAS, 348, 866

Erlund, M. C., Fabian, A. C., Blundell, K. M., et al. 2006, MNRAS, 371, 29

Evans, D. A., Worrall, D. M., Hardcastle, M. J., et al. 2006, ApJ, 642, 96

Evans, I. N., Primini, F. A., Glotfelty, K. J., et al. 2010, ApJS, 189, 37

Evans, I. N., Allen, C., Anderson, C. S., et al. 2019, AAS/High Energy Astrophysics Division, 114.01

Evans, I. N., Primini, F. A., Miller, J. B., et al. 2020, American Astronomical Society Meeting Abstracts, 154.05

Fabian, A. C., Sanders, J. S., Crawford, C. S. & Ettori, S. 2003, MNRAS, 341, 729

Fabian, A. C., Chapman, S., Casey, C. M., et al. 2009, MNRAS, 395, L67

Fanaroff, B. L. & Riley, J. M. 1974, MNRAS, 167, 31P

Feretti, L., Boehringer, H., Giovannini, G., et al. 1997, A&A, 317, 432

Feretti, L., Giovannini, G. & Böhringer, H. et al. 1997, , 2, 501

Feretti, L. & Giovannini, G. 1998, Untangling Coma Berenices: A New Vision of an Old Cluster, 123

Feretti, L., Giovannini, G., Govoni, F. et al. 2012, A&ARv, 20, 54

Fruscione, A., McDowell, J. C., Allen, G. E., et al. 2006, Society of Photo-Optical Instrumentation Engineers (SPIE) Conference Series, 6270, 62701V

Giovannini, G., Feretti, L., Venturi, T., et al. 1993, ApJ, 406, 399

Giovannini, G., Tordi, M. & Feretti, L. 1999, , 4, 141

Giovannini, G., Taylor, G. B., Feretti, L., et al. 2005, ApJ, 618, 635

Gorshkov, A. G. & Konnikova, V. K. 1995, Astronomy Reports, 39, 257

Govoni, F., Enßlin, T. A., Feretti, L., et al. 2001, A&A, 369, 441

Haas, M., Willner, S. P., Heymann, F., et al. 2008, ApJ, 688, 122

Hardcastle, M. J. and Worrall, D. M. 2000, MNRAS, 314, 359

Hardcastle, M. J., Evans, D. A. & Croston, J. H. 2006, MNRAS, 370, 1893

Hardcastle, M. J., Massaro, F. & Harris, D. E., 2010, MNRAS, 401, 2697

Hardcastle, M. J., Massaro, F. & Harris, D. E., 2012, MNRAS, 424, 1774

Harris, D. E., Massaro, F. & Cheung, C. C. 2010, American Institute of Physics Conference Series, 1248, 355

Hickox, R. C. & Markevitch, M. 2006, ApJ, 645, 95

Hilbert, B., Chiaberge, M., Kotyla, J. P., et al. 2016, ApJS, 225, 12

Hiltner, P. R. & Roeser, H. J. 1991, A&A, 244, 37

Horst, H., Gandhi, P., Smette, A., et al. 2008, A&A, 479, 389

Ineson, J., Croston, J. H., Hardcastle, M. J., et al. 2013, ApJ, 770, 136

Ineson, J., Croston, J. H., Hardcastle, M. J., et al. 2015, MNRAS, 453, 2682

Ineson, J., Croston, J. H., Hardcastle, M. J., et al. 2017, MNRAS, 467, 1586

Kotyla, J. P., Chiaberge, M., Baum, S., et al. 2016, ApJ, 826, 46

Kuraszkiewicz, J., et al. 2020, in prep.

Laing, R. A. and Riley, J. M. and Longair, M. S. 1983, MNRAS, 204, 151

Laing, R. A., Jenkins, C. R., Wall, J. V., et al. 1994, Astronomical Society of the Pacific Conference Series, 54, 201

Leahy, J. P. 1993, Röser, H.-J., & Meisenheimer, K. (eds). 1993. Jets in Extragalactic Radio Sources. Berlin: Springer-Verlag

Madrid, J. P., Chiaberge, M., Floyd, D., et al. 2006, ApJS, 164, 307

Madrid, J. P., Donzelli, C. J., Rodríguez-Ardila, A., et al. 2018, ApJS, 238, 31

Maselli, A., Massaro, F., Cusumano, G., et al. 2016, MNRAS, 460, 3829

Maselli, A., Kraft, R. P., Massaro, F. & Hardcastle, M. J. 2018, A&A, 619, A75

Massaro, F., Chiaberge, M., Grandi, P., et al. 2009, ApJL, 692, L123

Massaro, F., Harris, D. E., Chiaberge, M., et al. 2009, ApJ, 696, 980

Massaro, F., Harris, D. E., Tremblay, G. R., et al. 2010a, ApJ, 714, 589

Massaro, F., Cheung, C. C. & Harris, D. E. 2010b, X-ray Astronomy 2009; Present Status, Multi-Wavelength Approach and Future Perspectives, 1248, 475

Massaro, F., Cheung, C. C. & Harris, D. E. 2010c, IAU Symposium, 275, 160

Massaro, F., D'Abrusco, R., Ajello, M., et al. 2011a, ApJ, 740, L48

Massaro, F., Harris, D. E. & Cheung, C. C. 2011b, ApJS, 197, 24

Massaro, F., Tremblay, G. R., Harris, D. E., et al. 2012, ApJS, 203, 31

Massaro, F., D'Abrusco, R., Paggi, A., et al. 2013a, ApJS, 206, 13

Massaro, F., D'Abrusco, R., Paggi, A., et al. 2013b, ApJS, 209, 10

Massaro, F., Harris, D. E., Tremblay, G. R., et al. 2013c, ApJS, 206, 7

Massaro, F., Masetti, N., D'Abrusco, R., et al. 2014, AJ, 148, 66

Massaro, F., Harris, D. E., Liuzzo, E., et al. 2015, ApJS, 220, 5

Massaro, F., Missaglia, V., Stuardi, C., et al. 2018, ApJS, 234, 7

Massaro, F., Àlvarez-Crespo, N., Capetti, A., et al. 2019, ApJS, 240, 20

Massaro, F., Capetti, A., Paggi, A., et al. 2020, ApJS, 247, 71

Migliori, G., Orienti, M., Coccato, L., et al. 2020, MNRASaccepted, arXiv: 2004.13756

Mingo, B., Hardcastle, M. J., Ineson, J., et al. 2017, MNRAS, 470, 2762

Mohr, J. J., Mathiesen, B. & Evrard, A. E. 1999, ApJ, 517, 627

Moore, B., Frenk, C. S. & White, S. D. M. 1993, MNRAS, 261, 827

Orienti, M., Prieto, M. A., Brunetti, G., et al. 2012, MNRAS, 419, 2338

Paggi, A., Massaro, F., Ricci, F., et al. 2020, in prep.

Piffaretti, R., Arnaud, M., Pratt, G. W., et al. 2011, A&A, 534, A109

Prieto, M. A., 1996, MNRAS, 282, 421

Privon, G. C., O'Dea, C. P., Baum, S. A., et al. 2008, ApJS, 175, 423

Ricci, F., Lovisari, L., Kraft, R. P., et al. 2018, ApJ, 867, 35

Rottgering, H., Snellen, I., Miley, G., et al. 1994, ApJ, 436, 654

Rottgering, H. J. A., Wieringa, M. H., Hunstead, R. W., et al. 1997, MNRAS, 290, 577

Schmidt, M. 1963, Nature, 197, 1040

Shields, G. A. 1999, PASP, 111, 661

Shimwell, T. W., Röttgering, H. J. A., Best, P. N., et al. 2017, A&A, 598, A104

Shimwell, T. W., Tasse, C., Hardcastle, M. J., et al. 2019, A&A, 622, A1

Smail, I., Lehmer, B. D., Ivison, R. J., et al. 2009, ApJL, 702, L114

Smail, I., Blundell, K. M., Lehmer, B. D. & Alexander, D. M. 2012, ApJ, 760, 132

Spinrad, H., Djorgovski, S., Marr, J. & Aguilar, L. 1985, PASP, 97, 932

Stuardi, C., Missaglia, V., Massaro, F., et al. 2018, ApJS, 235, 32

Tadhunter, C. 2016, A&ARv, 24, 10

Tasse, C., et al. 2020, in prep.

Tonry, J. L., Stubbs, C. W., Lykke, K. R., et al. 2012, ApJ, 750, 99

Tremblay, G. R., Chiaberge, M., Sparks, W. B., et al. 2009, ApJS, 183, 278

Vagshette, N. D., Naik, S., Patil, M. K., et al. 2019, MNRAS, 485, 1981

van Haarlem, M. P., Wise, M. W., Gunst, A. W., et al. 2013, A&A, 556, A2

van Weeren, R. J., de Gasperin, F., Akamatsu, H., et al. 2019, , 215, 16

Visvanathan, N. & Sandage, A. 1977, ApJ, 216, 214

Wen, Z. L., Han, J. L. & Liu, F. S. 2012, ApJS, 199, 34

Wen, Z. L. & Han, J. L. 2015, ApJ, 807, 178

Werner, M. W., Murphy, D. W., Livingston, J. H., et al. 2012, ApJ, 759, 86

Wilkes, B. J., Kuraszkiewicz, J., Haas, M., et al. 2013, ApJ, 773, 15

Wilkes, B. J., et al. 2020, in prep.

Chapter 6

Feedback in radio galaxies: the cases of 3CR 318.1 and 3CR 196.1

In this chapter, I present the multiwavelength study of two different manifestations of radio feedback processes in radio galaxies: the cold filaments around 3CR 318.1 and the X-ray cavity in 3CR 196.1. This chapter is organized as follows. § 6.1 collects the multifrequency analysis of the cold filaments found in 3CR 318.1, with § 6.1.1 presenting an overview on 3CR 318.1, § 6.1.2 collecting details on the analysis, and § 6.1.3 showing results on this analysis. § 6.2 is dedicated to the analysis of the ionized gas spatially associated with an X-ray cavity in 3CR 196.1. In particular, § 6.2.1 collects an overview on 3CR 196.1, § 6.2.2 explains details on the optical and X-ray analyses, and § 6.2.3 is dedicated to the results of these analyses. Lastly, § 6.3 is dedicated to the summary and discussion of this chapter.

6.1 Cold filaments around 3CR 318.1

During the MURALES survey, an optical filamentary structure was detected in 3CR 318.1 (Balmaverde et al. 2019), the BCG of the galaxy cluster MKW 3s (Morgan et al. 1975), in agreement with observations by Edwards et al. (2009). This structure consists of two ionized gas filaments extending ~25 kpc in the south and the southwest directions, both with almost constant velocities along their projected lengths (~230 km s^{-1} and ~280 km s^{-1}, respectively). The filament that points to the south presents a bright knot at its southern end. In contrast with the typical narrow-line regions seen in other radio galaxies, these filaments extend beyond tens of kiloparsecs and present drastically different emission line ratios (e.g., [O III]/H_β ~0.1 instead of the typical value of ~10).

Similar filamentary structures were discovered in other BCGs, like NGC 1275 in the center of the Perseus galaxy cluster (Lynds 1970, Conselice et al. 2001 and Fabian et al. 2008), spatially associated with an X-ray excess (Fabian et al., 2011). The same situation occurs for other BCGs, where a tight connection between X-ray and optical filamentary emission was found (McDonald et al., 2010).

However, the physical processes responsible for the ionization in these optical filaments are still debated. While Voit et al. (1994) proposed ionization due to cooling of the hot ICM as the excitation mechanism underlying these filaments; McDonald et al. (2010), who analyzed a sample of 23 filaments around BGCs, suggested that these types of filaments are due to ICM thermal conduction. In the case of the Perseus cluster, Fabian et al.

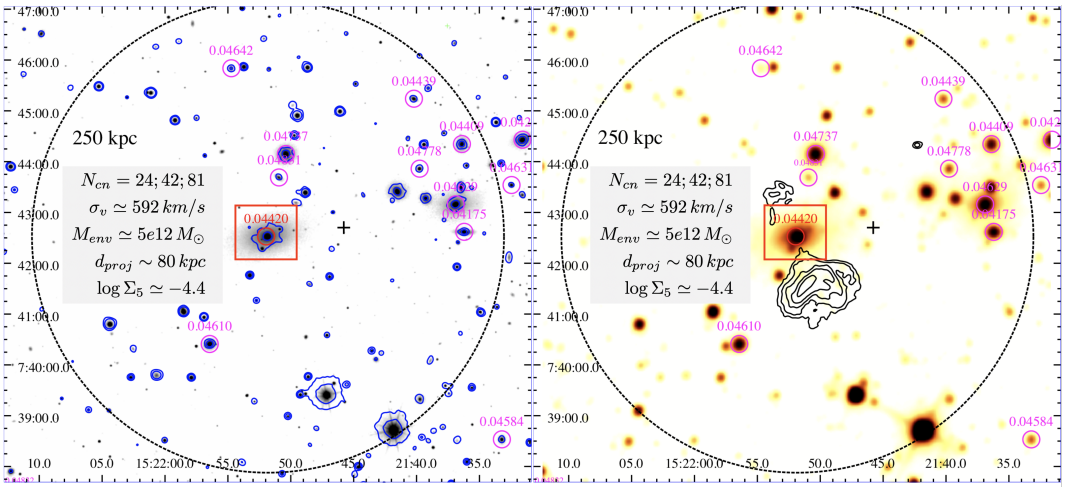

Figure 6.1: r-band SDSS image with SWIFT UV contours at 2600 Å overlaid in blue (left) and 3.4 μm WISE image with 328 MHz VLA radio contours overlaid in black (right), showing 3CR 318.1 at the center and other sources in the field. The red squares show the MUSE field of view. Radio contours were drawn at 5, 10, 20, 40, and 80 times the root mean square (rms) level of the background in the radio map (beam size of 5.4″). Sources in the field with known spectroscopic redshifts are marked in magenta. Ambient parameters, shown in both panels, were derived according to Massaro et al. (2019, 2020a,b). N_{cn} is the number of cosmological neighbors within a radius of 500 kpc, 1 Mpc and 2 Mpc, respectively, σ_v is the velocity dispersion of the cosmological neighbors, M_{env} is the environmental mass (i.e., galaxies, IGM and dark matter) estimated from the velocity dispersion, d_{proj} is the projected distance between the central radio galaxy and the centroid of the position of the cosmological neighbors within 2 Mpc (marked by the black cross) and Σ_5 is the cosmological parameter used to trace the dark matter halo density (see Sabater et al. 2013 and Worpel et al. 2013). SWIFT-UVOT data were reduced according to the standard procedure (see Massaro et al. 2008a,b, for more details).

(2011) rejected this scenario, due to the lack of a thick interface between the cold and hot gas, proposing that the origin of cold X-ray filaments is due to penetration of cold gas by the hot surrounding gas through reconnection diffusion.

Here, I present a comparison between optical and X-ray images of 3CR 318.1 to investigate the main ionization processes underlying the origin of these optical filaments, thus focusing only on the ∼30 kpc at the center of MKW 3s (for works on the large scale structures see e.g., Mazzotta et al. 2002, 2004 and Bîrzan et al. 2020).

6.1.1 An overview on 3CR 318.1

3CR 318.1 is the radio source associated with the nearby (z = 0.0453, which corresponds to 0.896 kpc/arcsec) galaxy NGC 5920, the BCG of the galaxy cluster MKW 3s. Based on its optical line emission, it can be classified as an extremely low-excitation galaxy (see Capetti et al. 2013). The central source presents a steep spectrum at low radio frequencies (i.e., $\alpha^{150\,\mathrm{MHz}}_{1.4\,\mathrm{GHz}} = 0.63$) with a luminosity of $\log L_{150\,\mathrm{MHz}} = 23.16$ W Hz^{-1} (Capetti et al. 2020). The surrounding diffuse radio emission also shows an extremely steep radio spectrum ($\alpha^{1.28\,\mathrm{GHz}}_{235\,\mathrm{MHz}} = 2.42$), leading to a classification of relic radio galaxy by Giac-

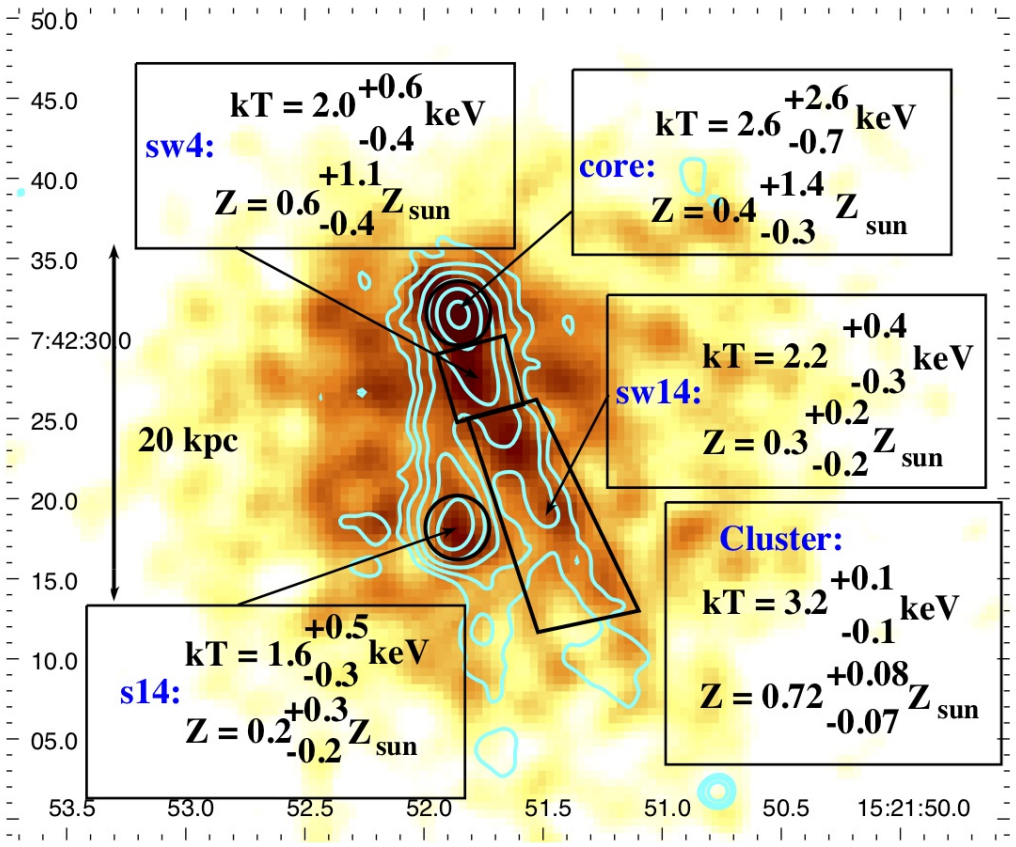

Figure 6.2: 0.5–3 keV *Chandra* image with [N II]λ6584 emission line contours overlaid in cyan. The *Chandra* image was smoothed with a 2″Gaussian kernel. [N II]λ6584 contours were drawn at 1, 2, 4, 8, 16 and 32 $\times 10^{-20}$ erg s^{-1} cm^{-2} (starting at 3 times the rms). Regions chosen for the X-ray spectral analysis and the results for each region are shown in black. The fit for each region yielded the following reduced $\chi^2_\nu = 1.304$ ($\nu = 8$), with 237 net photons, for the core, $\chi^2_\nu = 0.900$ ($\nu = 5$), with 167 net photons, for region s14, $\chi^2_\nu = 0.996$ ($\nu = 10$), with 268 net photons, for region sw4, $\chi^2_\nu = 0.588$ ($\nu = 36$), with 845 net photons, for region sw14, and $\chi^2_\nu = 0.906$ ($\nu = 207$) for the cluster region.

intucci et al. (2007). The host galaxy of 3CR 318.1 presents an AB UV magnitude at 2600 Å of 19.04 ± 0.04, corrected for Galactic reddening (Cardelli et al. 1989), with $E(B-V) = 0.0356 \pm 0.0010$[1]. This magnitude yields a UV luminosity at 2600 Å of $L_{UV} = (4.96 \pm 0.17) \times 10^{42}$ erg s^{-1}. An overview of 3CR 318.1 and its environment is shown in Fig. 6.1.

Peres et al. (1998) found that MKW 3s presents a moderate "cooling flow" ($\dot{M}$ ~170 M$_\odot$ yr^{-1}). Using deep (~57 ks) *Chandra* X-ray observations of the central 200 kpc, Mazzotta et al. (2002) identified the presence of a cavity, located at ~90 kpc south of the X-ray nucleus, hotter than the ~3 keV average cluster temperature and filled by radio emission arising from the southern lobe (Mazzotta et al. 2004), as recently confirmed by Bîrzan et al. (2020) using LOFAR observations.

[1]https://irsa.ipac.caltech.edu/applications/DUST/

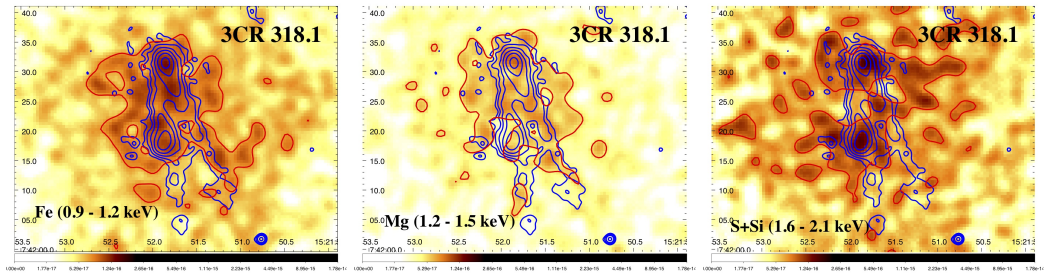

Figure 6.3: Narrow-band *Chandra* flux images in the 0.9–1.2 keV (left), 1.2–1.5 keV (center) and 1.6–2.1 keV (right) energy bands to show Fe, Mg and S+Si X-ray emissions with [N II]λ6584 contours overlaid. *Chandra* images were smoothed with a Gaussian kernel of 2″. [N II]λ6584 emission line contours are the same as in Fig. 6.2. X-ray emission due to Mg seems to trace the [N II]λ6584 morphology the best. X-ray fluxes along the filament (regions sw4 and sw14) are $F_{\rm Fe} = 2.9^{+0.2}_{-0.3} \times 10^{-14}$ erg s^{-1} cm^{-2} in the Fe band, $F_{\rm Mg} = 1.9^{+0.1}_{-0.1} \times 10^{-14}$ erg s^{-1} cm^{-2} in the Mg band, and $F_{\rm S+Si} = 2.3^{+0.1}_{-0.2} \times 10^{-14}$ erg s^{-1} cm^{-2} in the S+Si band.

6.1.2 A radio, optical and X-ray perspective

Here I focus on the analysis of the [N II]λ6584 emission since it is more luminous and extended than the Hα emission. The [N II]/Hα ratio is constant along the filaments with [N II]/Hα ~1.9.

I shifted the X-ray image 0.568″ to the northeast, then, I aligned the position of the optical host galaxy in the MUSE continuum image with the radio centroid shifting it by 1.62″. The comparison between registered X-ray and [NII]λ6584 optical images is shown in Fig. 6.2.

In the same figure, I show the regions selected to perform X-ray spectral analysis, based on the morphology of the [N II]λ6584 emission. These, labeled according to the nomenclature of Massaro et al. (2011), are:

1. two circles of 2″ radius, centered on (i) the radio core and (ii) the [N II]λ6584 emission line knot at the end of the south filament (core and s14, respectively);

2. two polygons along the southwest filament, namely: sw4 (inner 4 kpc) and sw14 (remaining 13 kpc).

I chose, as background for the spectral analysis of the filament regions, a larger circle located ~45″ to the northeast where no point-like and/or extended X-ray sources are detected, to obtain the spectrum of the excess emission only, instead of the line-of-sight average. I also performed the spectral analysis of the galaxy cluster emission, considering two polygonal regions, one on each side of the filaments and a background region at ~100″ to compare the inner and outer galaxy cluster emission.

I confirmed the presence of a soft X-ray (i.e., 0.5 - 3 keV) excess spatially coincident with the [N II]λ6584 filament (regions sw4 and sw14) at a level of confidence > 5σ with respect to the surrounding ICM emission.

Assuming the presence of emission lines below 2 keV, I created narrow band X-ray images, shown in Fig. 6.3 (see e.g., Massaro et al. 2013, 2015, 2018). I chose three energy ranges mainly attributable to (i) Fe (0.9–1.2 keV), (ii) Mg (1.2–1.5 keV) and (iii) S+Si

(1.6–2.1 keV) ionized elements. X-ray flux maps were created by using monochromatic exposure maps set to the nominal energies of 1, 1.3, and 1.8 keV for the Fe, Mg, S+Si, respectively, to take into account the detector effective area at different energies.

From the optical perspective, I modeled the main emission lines present in the MUSE spectra, i.e., $H\beta$, $H\alpha$, [O III]λ5007, [O I]λ6300, [N II]λ6584, and the [SII] doublet at $\lambda\lambda$6716, 6731, using Gaussian functions at different locations across the filament and the knot. Top panel of Fig. 6.4 shows the MUSE spectrum of the optical knot sw14, as an example. The $H\beta$ line was modeled using an additional broad component only present in the core and in region s4.

6.1.3 Results on the multifrequency analysis

I computed the emission line intensity ratios for all regions (see Fig. 6.2) and plotted them in the diagnostic diagrams defined by the intensity ratios shown in the bottom panels of Fig. 6.4, used to distinguish between different ionization mechanisms occurring in H II regions, AGN, or LINER/shocks (Baldwin et al. 1981 and Dopita & Sutherland 1995). Measurements obtained for all four regions in 3CR 318.1 are closely clustered and located where no emission line galaxies are found (see e.g., Kewley et al. 2006 and Capetti & Baldi 2011).

Similarly to what was found for filaments in different BCGs by McDonald et al. (2012), line ratios provide a contradictory classification: at the boundary between LINER and H II from the [O III]/Hβ vs [N II]/Hα and [O I]/Hα diagrams and in the region of ionization due to star-formation from the [S II]/Hα ratio.

I also estimated the gas density along the filaments, using the ratio of the [S II]λ6716 and the [S II]λ6731 lines (see Osterbrock 1989). Assuming a typical temperature of 10^4 K, I obtained $n_e \sim 1380$ cm^{-3} in the core and $n_e < 100$ cm^{-3} in s14 and along the filament (sw4 and sw14). I then estimated the total mass of the ionized gas as $M = 7.5 \times 10^{-3} \left(\frac{10^4}{n_e} \frac{L_{\mathrm{H}_\beta}}{L_\odot}\right)$ M$_\odot$, where L_{H_β} is the Hβ luminosity (see Osterbrock 1989). Thus, I estimated a total ionized gas mass of $M \sim 2 \times 10^5$ M$_\odot$ in the core, $M > 4 \times 10^5$ M$_\odot$ in s14, and $M > 10^6$ M$_\odot$ along the filament.

Simulations carried out by Qiu et al. (2019, 2020) show that cold filaments in cool core clusters can originate from warm AGN-driven outflows with shorter cooling than rising times. These simulations are consistent with the filaments in 3CR 318.1 extending in the direction of the southern radio lobe.

I performed the X-ray spectral analysis in all regions along optical filaments and in the galaxy cluster (excluding filaments, core, and knots). Best fit results, obtained with the absorbed XSAPEC model, are reported in Fig. 6.2. I also fitted regions sw4, and sw14 together and obtained a gas temperature of $2.4^{+0.3}_{-0.3}$ keV (with $Z = 0.5^{+0.3}_{-0.2}$ $Z_\odot$ and reduced $\chi^2_\nu = 0.857$ with $\nu = 59$ degrees of freedom) for the southwestern filament. This is colder than the surrounding ICM, which has $kT = 3.2^{+0.1}_{-0.1}$ keV (reduced $\chi^2_\nu = 0.906$; $\nu = 207$). The ICM temperature is consistent with the average temperature found by Mazzotta et al. (2002) for the inner regions of MKW 3s.

Metal abundance of the optical filament, $Z = 0.3^{+0.2}_{-0.2}$ for sw14 (with reduced $\chi^2_\nu = 0.588$; $\nu = 36$), appears to be marginally lower than that of the surrounding ICM ($Z = 0.72^{+0.08}_{-0.07}$). This is in agreement with literature results on other filaments (see e.g., Fabian et al. 2011 and McDonald et al. 2010).

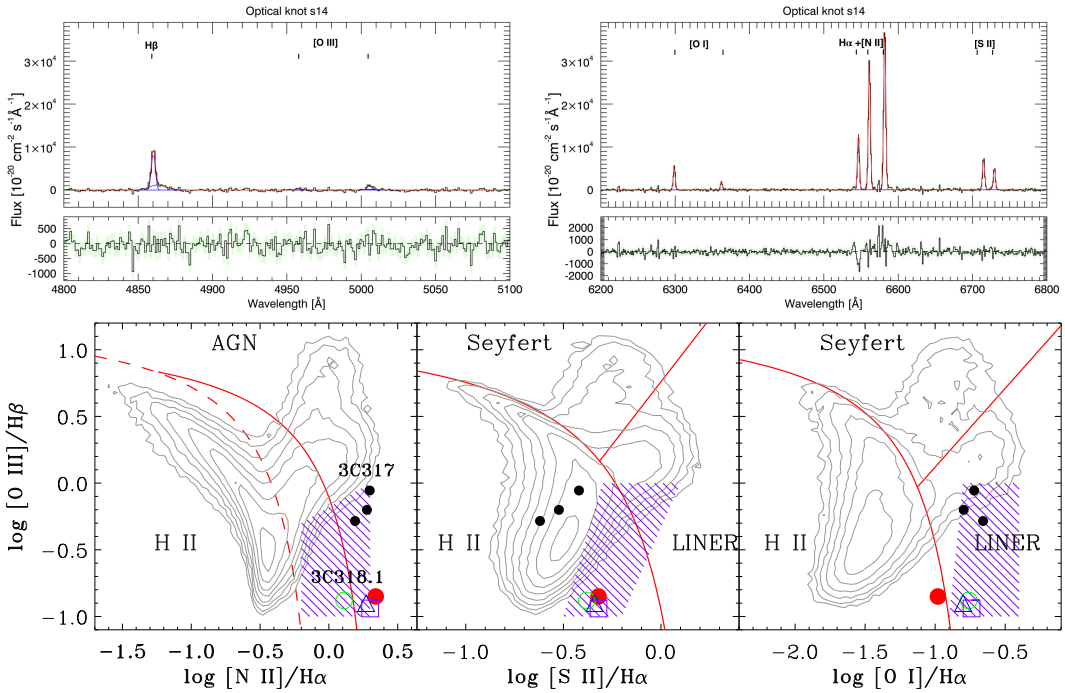

Figure 6.4: Top: MUSE spectrum (black histograms) of region s14, see Fig. 6.2, in rest frame, shown as an example. I show in red the Gaussian fit of the emission lines (top panels) and the residuals (bottom panels). Bottom: Location of 3CR 318.1 regions "core", s14, sw4 and sw14 (red filled circle, green circle, blue triangle, and magenta square, respectively) in the BPT diagnostic diagrams. The red solid curves represent the Kewley et al. (2001) theoretical upper bound for pure star formation, the red straight line shows the Kewley et al. (2006) separation between AGN and LINERs, while the dashed red curve in the [N II]λ6584 BPT is the Kauffmann et al. (2003) empirical classification separating star-forming galaxies and AGN. Contours represent the iso-densities of all SDSS/DR7 emission line galaxies (Capetti & Baldi 2011). The three black dots mark the location of the filaments in 3CR 317, the central galaxy of A2052, also observed as part of the MURALES survey (see Balmaverde et al. 2018). Purple dashed regions mark the location of filaments in other cool core galaxy clusters as measured by McDonald et al. (2012).

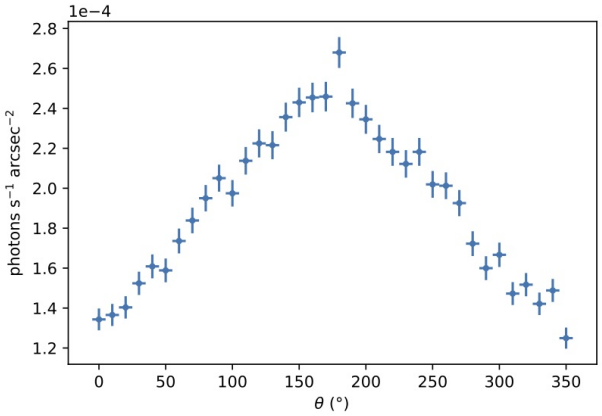

Figure 6.5: 0.5 - 3 keV, exposure corrected X-ray surface brightness profile with azimuthal bins of 10° centered on the core of 3CR 318.1. The bins were chosen so that the bin at 180° is the one containing the [N II]λ6584 filament. Background level is two orders of magnitude below the filament emission. The increase of surface brightness corresponds to the [N II]λ6584.

Assuming that narrow band images trace the X-ray emission lines, the Mg emission has a better spatial association with the optical filaments, while Fe and S+Si show X-ray emission more extended than the filaments, as well as strong emission at the core and the s14 (knot) regions (see Fig. 6.3). I computed the X-ray flux along the filament (regions sw4 and sw14) in the Fe, Mg and S+Si band and compared them with optical and X-ray fluxes. The X-ray fluxes along the filament (regions sw4 and sw14) are $F_{\rm Fe} = 2.9^{+0.2}_{-0.3} \times 10^{-14}$ erg s^{-1} cm^{-2} in the Fe band, $F_{\rm Mg} = 1.9^{+0.1}_{-0.1} \times 10^{-14}$ erg s^{-1} cm^{-2} in the Mg band, $F_{\rm S+Si} = 2.3^{+0.1}_{-0.2} \times 10^{-14}$ erg s^{-1} cm^{-2} in the S+Si band, and $F_{\rm 0.5\text{-}3\ keV} = 1.32^{+0.05}_{-0.08} \times 10^{-13}$ erg s^{-1} cm^{-2} in the soft band (0.5 - 3 keV). Detection significance of the excess X-ray emission along optical filaments is above 5σ confidence level for both Mg and Fe, while it is not significant for the S+Si narrow band image, thus the S+Si emission along the filament is consistent with the ICM emission.

I also obtained $F_{\rm H\alpha}/F_{\rm Fe} = 2.9^{+0.4}_{-0.4} \times 10^{-2}$ and $F_{\rm H\alpha}/F_{\rm 0.5\text{-}3\ keV} = 6.5^{+0.7}_{-0.8} \times 10^{-3}$. In contrast with the filaments of 3CR 318.1, Sanders & Fabian (2007) and Fabian et al. (2011) found that those in Perseus have soft X-ray emission of the same order as the Hα emission, while the Hα emission is an order of magnitude above the Fe emission, which highlights their much lower ionization state compared to that of the filaments in 3CR 318.1. Additionally, I obtained $F_{\rm [O\ III]}/F_{\rm 0.5\text{-}3\ keV} = 1.15^{+0.12}_{-0.14} \times 10^{-3}$, which is three orders of magnitude below the value obtained by Balmaverde et al. (2012) for the emission line regions in nine 3CR radio galaxies.

Lastly, I derived the 0.5–3 keV, exposure corrected, X-ray surface brightness profile with azimuthal bins of 10° centered on 3CR 318.1 core, excluding the inner 2″ and extending up to $\sim$ 30 kpc (see Jimenez-Gallardo et al. 2021 for additional details). I chose to make the bin containing the [N II]λ6584 filament correspond to the 180° bin. The resulting X-ray surface brightness profile is shown in Fig. 6.5. The background level is two orders of magnitude below the filament emission. The smooth increase of the surface brightness towards the [N II]λ6584 filament supports the hypothesis that the filament could have originated due to outflows in the direction of the radio jets.

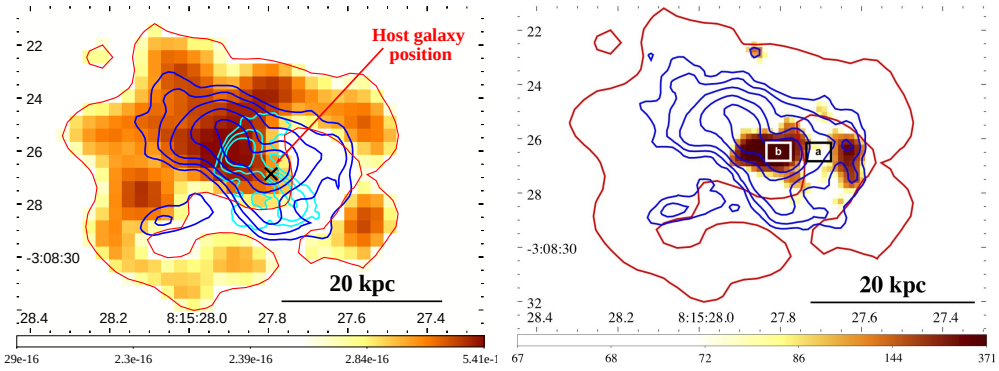

Figure 6.6: Left: Exposure-corrected 0.7 – 2 keV *Chandra* image of 3CR 196.1 with Hα + [N II]λ6584 (blue) and 8.4 GHz VLA (cyan) contours. The position of the centroid of the optical host, which corresponds to the radio core position is shown as a black cross. The *Chandra* image has a pixel scale of 0.492″ (corresponding to ∼1.6 kpc) and was smoothed with a 1.5″ radius Gaussian kernel. X-ray contours are drawn at $0.25 \cdot 10^{-15}$ erg cm^{-2} s^{-1}. Hα + [N II]λ6584 contours were drawn at 5, 10, 20, 50, and 100 times the rms. 8.4 GHz VLA contours were drawn at 5, 20, and 50 times the rms level of the background. Hα and the [N II]λ6584 emission presents an offset with respect to the borders of the X-ray cavity. The northeastern radio lobe is co-spatial with the X-ray emission peak, while the southwestern lobe is co-spatial with the X-ray cavity. Right: Redward [N II]λ6584 emission with the same exposure-corrected 0.7 – 2 keV *Chandra* contours (red) and Hα + [N II]λ6584 contours (blue) overlaid as in the left panel. The (a) and (b) regions marked in the figure show the extraction areas of the spectra in Fig. 6.7

.

6.2 In the cavity of 3CR 196.1

A recent analysis of radio, optical, and X-ray emission in 3CR 196.1 showed it is a promising source to investigate how radio jets affect EELRs, thanks to the discovery of an X-ray cavity at ∼10 kpc from the nucleus toward the southwest (see Ricci et al. 2018). Moreover, recent observations from VLT/MUSE (Bacon et al. 2010) obtained as part of the MURALES survey (Balmaverde et al. 2021) revealed that the Hα + [N II]λ6584 emission extends beyond the radio emission and appears, in projection, spatially associated with the X-ray cavity. This emission had not been detected in previous *HST* data originally published in Tremblay et al. (2009), due to *HST*'s lower sensitivity compared to MUSE. This spatial association of ionized gas with an X-ray cavity, instead of with its borders has been rarely reported in the literature (see e.g., A1668, Pasini et al. 2021).

To test where such optical emission stands with respect to the X-ray, I compared 3CR 196.1's optical, X-ray, and radio emission up to a few tens of kpc, taking advantage of the new VLT/MUSE observations. I focus on the comparison of X-ray and optical observations, previously investigated only separately (see Ricci et al. 2018 and Balmaverde et al. 2021).

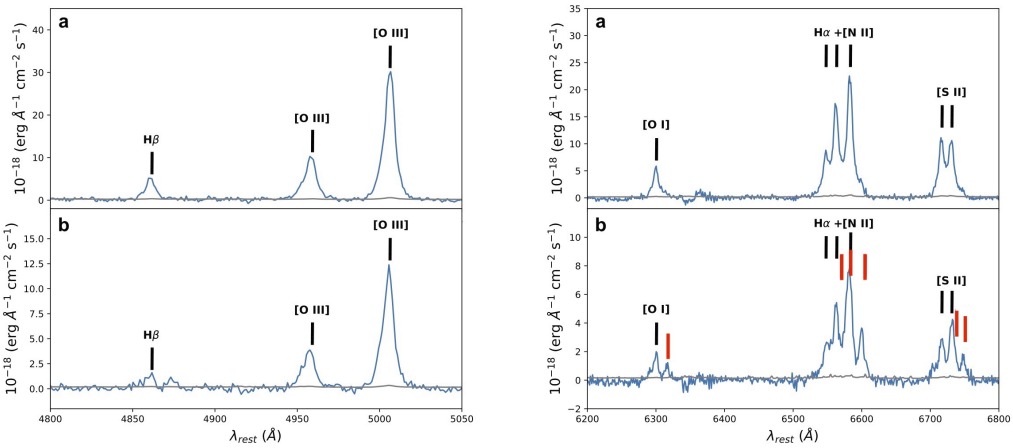

Figure 6.7: Spectra extracted from regions *a* and *b* (top and bottom panels in Fig. 6.6, right panel, respectively). The top spectrum could be fitted using a single Gaussian component for each line, while the bottom one shows an extra redward component in all lines except for Hβ and [O III]$\lambda\lambda$4960, 5008 lines. Black markers point to the rest-frame position of each line while red markers are located at 21 Å from rest-frame (~1000 km s^{-1}). Uncertainties in the spectra are shown in gray.

6.2.1 A brief overview of this hybrid radio galaxy

3CR 196.1 is the radio galaxy associated with the BCG of the galaxy cluster CIZA J0815.4-0303 (Kocevski et al. 2007). From an optical perspective, this radio galaxy is classified as a LERG (Buttiglione et al. 2010), while at radio frequencies it presents a HYMOR radio structure (see Gopal-Krishna & Wiita 2000), with a classical edge-darkened morphology, typical of FR Is, toward the southwest and a radio lobe, typical of FR IIs on the opposite side (Fanaroff & Riley 1974).

Near-infrared (Madrid et al. 2006) and optical continuum observations (Baum et al. 1988; de Koff et al. 1996) revealed that the host galaxy of 3CR 196.1 shows an elliptical morphology elongated from northeast to southwest, in the same direction as the radio jet. Optical images also revealed the presence of periodic shells possibly due to past merger events (Zirbel 1996), in agreement with centroid shifts measured using optical isophotes of its host galaxy (de Koff et al. 1996). Additionally, using *HST* emission line images, Baldi et al. (2019) measured a lower limit for the total ionized gas mass for 3CR 196.1 of $3.5{\cdot}10^5$ M$_\odot$, using the nuclear electron density.

Speranza et al. (2021) carried out an analysis of the newly obtained MUSE data focused on the [O III]λ5007 properties. During this analysis, they detected a broad [O III]λ5007 blue component with a maximum velocity of ~-640 km s^{-1}, extending toward the northeast, in the same direction as the radio jet.

Ricci et al. (2018) confirmed the presence of an X-ray surface brightness depression, previously suggested by Massaro et al. (2012), by carrying out a multiwavelength analysis of archival radio, optical, and X-ray observations. This surface brightness depression indicates the presence of a "butterfly-shaped" cavity at ~10 kpc from the nucleus (see left panel of Fig. 6.6). The temperature of the galaxy cluster (~4.2 keV) drops to ~2.8 keV in

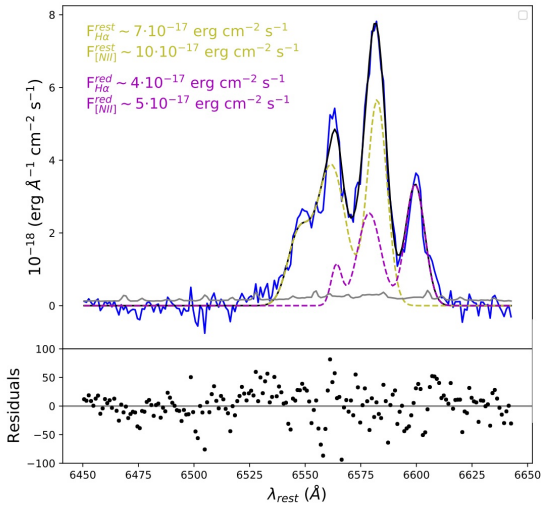

Figure 6.8: Fit to the spectrum extracted from a 2 x 2 spaxel region (0.4 x 0.4 arcsec^2), in region *b* (right panel of Fig. 6.6) using a Hα + [N II]λ6584 at rest frame (yellow) and another one redshifted ~21 Å. Uncertainties in the spectrum are shown in grey. Spectra in region *b* (see right panel of Fig. 6.6) cannot be reproduced using a single triplet.

the inner 30 kpc, suggesting that 3CR 196.1 is the brightest cluster galaxy of a cool core cluster. At scales of tens of kpc, the Hα + [N II]λ6584 emission observed with the *HST* is spatially aligned with the radio jet and lies in the base of the X-ray cavity. Lastly, Ricci et al. concluded that 3CR 196.1 could be an example where cold gas is being uplifted by radio lobes and that it could have undergone several AGN outbursts at multiple epochs. They also suggested its galaxy cluster may have experienced a merger episode, revealed by the spiral pattern seen in the X-ray observation, characteristic of gas sloshing (see, e.g., Markevitch & Vikhlinin 2007).

6.2.2 Optical and X-ray comparison

The final alignment after the astrometric registration and a 3.1″ shift (corresponding to ~10 kpc) is shown in the left panel of Fig. 6.6, where I show X-ray emission with Hα + [N II]λ6584 contours overlaid in blue, the position of the host marked with a black cross and 8.4 GHz VLA radio contours overlaid in cyan (see Balmaverde et al. 2021 for the Hα + [N II]λ6584 image).

I measured the redshift by using the Penalized Pixel-Fitting code (Cappellari 2017) to fit the stellar continuum and absorption features in a 2″ radius circular region centered on the host position. Following this procedure, I measured a value for the redshift of $z = 0.1982$, which I adopted throughout the analysis.

Although a single Gaussian is adequate to fit the spectral components in most spaxels, I found that the spectra in the central area have additional components in all spectral features, except for Hβ and [O III]$\lambda\lambda$4960, 5008. I detect these additional redward components at ~21 Å (i.e., ~1000 km s^{-1}) from rest-frame, in the regions shown in the right

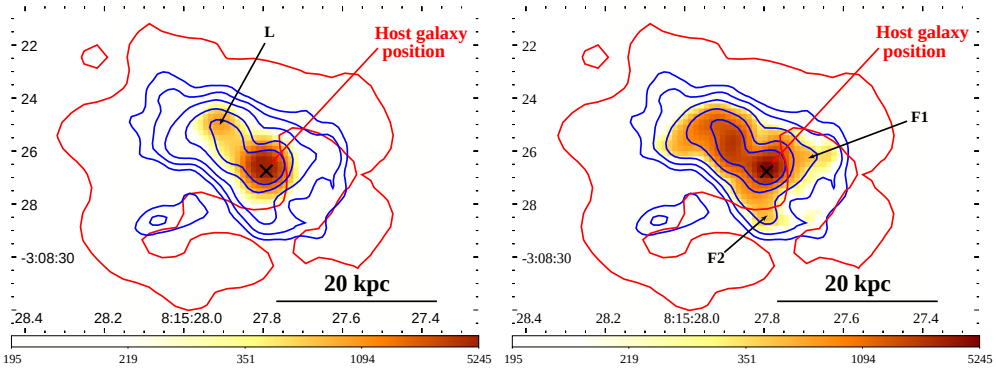

Figure 6.9: [O III]$\lambda\lambda$4960, 5008 (left) and [S II]$\lambda\lambda$6718, 6733 (right) emission with exposure-corrected 0.7 – 2 keV *Chandra* contours (red) and Hα + [N II]λ6584 contours (blue) overlaid. The position of the centroid of the optical host is indicated with a black cross. *Chandra* contours were smoothed with a 1.5″ Gaussian kernel radius and drawn in red at $0.25 \cdot 10^{-15}$ erg cm^{-2} s^{-1}. Hα + [N II]λ6584 contours were drawn at 5, 10, 20, 50, and 100 times the rms. Region L marks the region co-spatial with the northeastern radio lobe.

panel of Fig. 6.6. A comparison of the spectra extracted from regions without and with an extra redward component (regions *a* and *b* in the left panel of Fig. 6.6, respectively) is shown in Fig. 6.7, where the rest-frame wavelength of lines is marked in black and the wavelength at 21 Å from rest-frame is marked in red. Although there appears to be also a possible extra spectral feature corresponding to the Hβ line, this component is not detected (with a significance below 2σ). Additionally, in Fig. 6.8, I show an example of a fit using two Hα + [N II]λ6584 triplets, one at rest-frame and one redshifted by ~21 Å, of the spectrum extracted from a 0.4 x 0.4 arcsec^2 subregion from region *b* in the right panel of Fig. 6.6.

These redshifted spectral features are spectrally blended with emission at the systemic redshift, i.e., the redward and "rest-frame" components have an offset consistent with the separation between the Hα and the [N II]λ6584 lines (see Fig. 6.7). This offset, together with the fact that this redward component overlaps, in projection, the AGN emission, introduces a degeneracy in the intensities of the Hα, [N II]λ6584 and [S II]$\lambda\lambda$6718, 6733 lines that I cannot break without knowing a priori the ionization status of the source and the density of the gas. Thus, the limited spectral (~50 km s^{-1}) and spatial (~1″) resolution of MUSE cubes prevents me from breaking the degeneracy, and from providing a thorough analysis of the kinematics and ionization state of the gas.

6.2.3 The strange case of 3CR 196.1

I (i) detected Hα+[N II]λ6584 emission spatially associated with the X-ray cavity (see left panel of Fig. 6.6) and, at the same time, (ii) did not detect Hβ or [O III]λ5007 emission in the X-ray cavity region (see left panel of Fig. 6.9). A comparison between X-ray and Hα+[N II]λ6584, [O III]$\lambda\lambda$4960, 5008, and [S II]$\lambda\lambda$6718, 6733 is shown in the left panel of Fig. 6.6 and the left and right panels of Fig. 6.9, respectively.

The morphology of the Hα+[N II]λ6584 hints at differences in the density of the

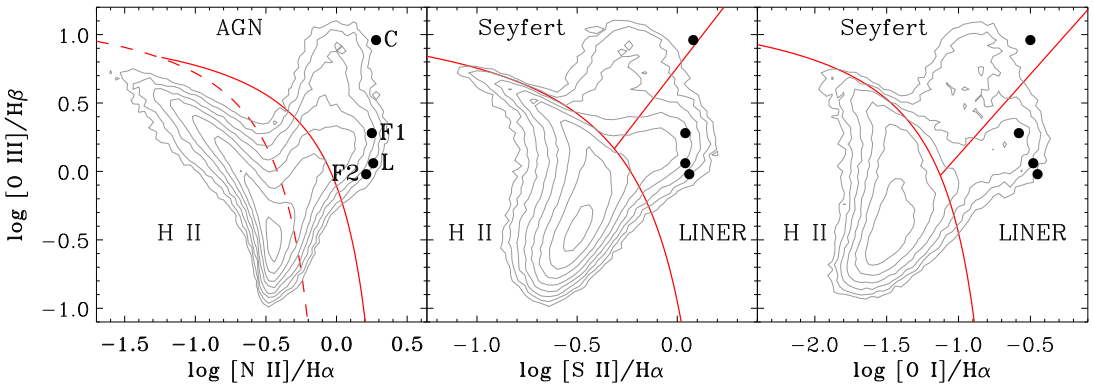

Figure 6.10: Location of 3CR 196.1 regions core, northeastern radio lobe and blue and red filaments (C, L, F1 and F2, respectively) in the BPT diagnostic diagrams. The red solid curves represent the Kewley et al. (2001) theoretical upper bound for pure star formation, the red straight line shows the Kewley et al. (2006) separation between AGN and LINERs, while the dashed red curve in the [N II]λ6584 BPT is the Kauffmann et al. (2003) empirical classification separating star-forming galaxies and AGN. Contours represent the iso-densities of all SDSS/DR7 emission line galaxies (Capetti & Baldi 2011). Extended ionized gas structures in 3CR 196.1 have an ionization state compatible with the LINER region of the BPT diagnostic diagrams, while the ionization state at optical host position is compatible with Seyfert-like ionization.

environment. In particular, the northeastern component (region L in the left panel of Fig. 6.9) being co-spatial with the northeastern radio lobe and with the highest X-ray surface brightness peak indicates a denser environment toward the northeast than toward the southwest, where the X-ray cavity is located.

All extended ionized gas features (regions L, F1 and F2, marked in Fig. 6.9) present LINER-like ionization states, as shown in the BPT diagram in Fig. 6.10 (see, e.g., Baldwin et al. 1981 and Kewley et al. 2006). The only region shown in Fig. 6.10 with a Seyfert-like ionization state is the region corresponding to the optical host position. The position in the BPT diagram of the extra redward component shown in Fig. 6.6, right panel, could not be established since the spectral and spatial blending does not allow me to obtain estimates of the line ratios in this region.

I decided to give an overview of the gas kinematics via velocity channel maps, as shown in Fig. 6.11 since the blending of the spectral components (see Fig. 6.8) prevents me from studying the kinematics of each component. This approach is commonly used for isolated lines. Thus, to avoid contamination due to the lines being part of a triplet, I considered different reference lines for blue and red-shifted emission. I considered as blue-shifted, emission blueward of the [N II]λ6548 rest frame line and, as red-shifted, emission redward of the [N II]λ6584 rest frame. Therefore, the central wavelength range including the emission of the Hα+[N II]λ6584, dominated by spectral blending, is not shown in the channel maps. Channel maps are shown in increments of 100 km s^{-1}, which correspond to two resolution elements, with the exception of the central channels that are shown in increments of 50 km s^{-1}.

Velocity channel maps show that the blue-shifted emission is co-spatial with the northern radio lobe (region L). Additionally, there seems to be a filament of blue-shifted emis-

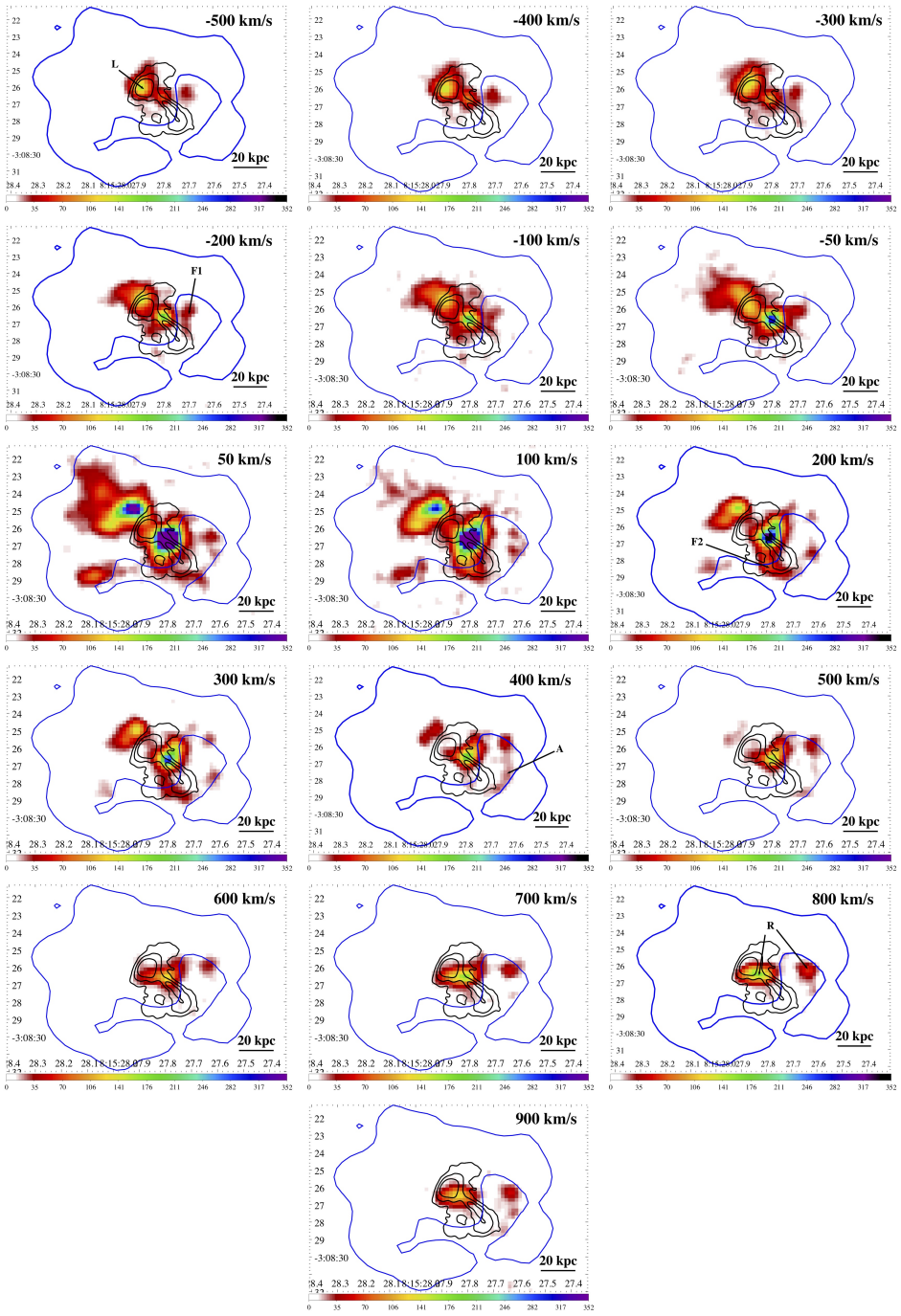

Figure 6.11: Hα + [N II]λ6584 flux in velocity bins of 100 km s^{-1}, with 8.4 GHz VLA (black) and exposure-corrected 0.7 - 2 keV *Chandra* (blue) contours overlaid. MUSE images have a pixel size of 0.2 arcsec/pixel. 8.4 GHz VLA contours were drawn at 5, 20, and 50 times the rms level of the background. *Chandra* contours were smoothed with a 1.5″ Gaussian kernel radius and drawn in red at $0.25 \cdot 10^{-15}$ erg cm^{-2} s^{-1}. Centers of the velocity bins are shown on the top right corners. Main features are labeled in figures, with L, the region co-spatial with the northeastern radio lobe, F1 and F2, the blue and red filaments that appear to surround the southwestern radio lobe, A, the arched emission that appears to trace the inner edge of the X-ray cavity, and R, the region polluted by the redward component.

sion on the outer edge of the southern radio lobe (F1). The red-shifted emission, up to ~300 km s^{-1}, shows some extended emission that appears to follow the northern radio jet and a filament that seems to wrap around the southern lobe (F2). There also appears to be some emission connecting filaments F1 and F2, which is most visible at ~400 km s^{-1} (A). This arched feature is apparently tracing the inner edge of the X-ray cavity. Lastly, at the reddest velocities (>500 km s^{-1}), the only emission that is detected corresponds to the redward [N II]λ6584 shown in the right panel of Fig. 6.6 and in the spectrum of region *b* in Fig. 6.7 (region R).

6.3 Summary and discussion

6.3.1 3CR 318.1

The MURALES survey revealed the presence of optical filaments in 3CR 318.1, the BCG of MKW 3s. Here I compared optical VLT/MUSE and X-ray *Chandra* observations to shed light on their physical origin.

From an optical perspective, intensity ratios of various rest-frame emission lines were used to distinguish between different ionization mechanisms. Possible explanations of filamentary emission include: ionization due to hot cooling ICM (Voit et al. 1994), ICM thermal conduction (McDonald et al. 2010), and reconnection diffusion (Fabian et al. 2011). However, individually, none of the ionization mechanisms listed can account for all line ratios simultaneously. As shown in Fig. 6.4, line ratios measured in 3CR 318.1 show extremely low values of [O III]/Hβ in the diagnostic diagrams, similarly, McDonald et al. (2012) found systematically lower [O III]/Hβ values in filaments of cool core galaxy clusters and higher values of [N II]/Hα, [O I]/Hα and [S II]/Hα than those found in galaxies in the SDSS. Although the diagnostic diagrams are used to discriminate between star-forming and AGN-dominated galaxies, they tend to fail when the ionization is due to more complex situations and/or different ionization mechanisms (see e.g., Stasińska et al. 2008, Capetti & Baldi 2011 and Balmaverde et al. 2018) and therefore they may have limited validity in assessing the ionization conditions of BCGs. Thus, the line ratios in 3CR 318.1 imply that the emission from the filaments is due to a combination of ionization mechanisms. McDonald et al. (2012) suggested that line ratios are due to a combination of star formation and ionization from slow shocks (~100 - 400 km s^{-1}; see also Allen et al. 2008). Since my results are similar to those of McDonald et al. (2012), I argue that their conclusion applies also to the case of 3CR 318.1. An additional contribution from self-ionizing cooling ICM is suggested by the low velocity dispersion (~ 60 km s^{-1}) of the optical filaments in 3CR 318.1, which implies a small contribution of shocks to the total ionization. Therefore, I conclude that the underlying ionization mechanisms include a combination of photoionization due to star formation, self-ionizing cooling ICM, and a small contribution of ionization due to slow shocks. Additionally, although McDonald et al. (2012) already found a decrease in the emission linewidth with radius, thanks to the MUSE data, it was discovered that this decrease occurs sharply in the case of 3CR 318.1 (from ~200 km s^{-1} in the core to ~60 km s^{-1} along the filaments; see Balmaverde et al. 2019).

I detected an excess of X-ray emission above the ICM along the [N II]λ6584 filaments. This X-ray filament is colder and despite the large uncertainties, appears to have a lower

metal abundance than the surrounding ICM, in agreement with literature results (McDonald et al. 2010). The association between the X-ray and optical filamentary morphologies, together with the radio structure, suggests that the filaments could have originated from AGN-driven outflows in the direction of the radio jet. This scenario is in agreement with the smooth 0.5 - 3 keV X-ray surface brightness profile at the location of the [N II]λ6584 filament and with simulations carried out by Qiu et al. (2019, 2020), in which cold filaments originate from warm outflows (10^4 - 10^7 K). Additionally, works such as Gaspari et al. (2018) and Voit (2021) predict that optical emission line nebulae would present velocity dispersions of ~100 - 200 km s^{-1} in the cases where the nebulae originated from compression and catastrophic cooling (see also Gaspari et al. 2012, 2013, 2015, 2017 and Voit et al. 2017 for previous works on multiphase condensation). However, the [N II]λ6584 filaments in 3CR 318.1 present very low velocity dispersions (~60 km s^{-1}; see Fig. 8 in Balmaverde et al. 2019), so the AGN uplift scenario could be favored.

6.3.2 3CR 196.1

I carried out a comparison of optical VLT/MUSE and X-ray *Chandra* observations of 3CR 196.1, the central radio galaxy associated with the cool core galaxy cluster CIZA J0815.4-0303, which exhibits a "butterfly-shaped" X-ray cavity at ~10 kpc toward the southwest of the nucleus.

Although ionized gas, co-spatial with rims of X-ray cavities or associated with radio emission, has been reported in the past, ionized gas spatially associated, and thus, potentially filling an X-ray cavity, is a rare occurrence with no clear explanation. In this work, I present the first detection of ionized gas spatially associated with an X-ray cavity, using Hα + [N II]λ6584 emission as a tracer.

Extended ionized gas features corresponding to regions L, F1, and F2 (in Fig. 6.9) appear to have LINER-like ionization states, as shown in Fig. 6.10. This LINER-like emission in extranuclear regions is often associated with large-scale outflows and shocks or with radio jet-shocked regions (see Kewley et al. 2006 and references therein).

The northeastern [O III]$\lambda\lambda$4960, 5008 emission (region L in Fig. 6.9, left panel) is, most likely, the optical counterpart of the northeastern radio lobe. However, LINER-like ionization could also be compatible with the presence of a second AGN in the northeastern region, which would be supported by the detection of possible signs of past mergers by Ricci et al. (2018). Nevertheless, current X-ray observations do not show evidence of any AGN nuclei, either corresponding to region L or to the position of the optical centroid, since X-ray emission is dominated by ICM emission. Additionally, the cluster appears relaxed at large scales and the stellar emission from the host galaxy does not appear disturbed, making the double AGN hypothesis unlikely.

During this analysis, I also discovered that, in the central and X-ray cavity regions, all spectral features, except for the Hβ and [O III]$\lambda\lambda$4960, 5008 lines, have an additional component at ~1000 km s^{-1} to the red of the rest-frame component (see right panel of Fig. 6.6 and Figs. 6.7 and 6.8). This additional redward component could be due to a background gas cloud since there does not appear to be a continuous range of velocities from rest-frame to the redward component and since the velocity of the redward component is above the sound speed at the center of the galaxy cluster (with c_s ~820 km s^{-1} for

kT ~2.8 keV; see McNamara & Nulsen 2007[2]). Despite that, the spatial resolution (~1″) of the current observations together with the blending of lines in the Hα + [N II]λ6584 complex due to the limited spectral resolution (~50 km s^{-1}) prevent an in-depth analysis on the kinematics and ionization state of the gas.

To characterize the emission spatially associated with the X-ray cavity, I computed the electron density using the [S II]$\lambda\lambda$6718, 6733 duplet ratio as described in Sanders et al. (2016). The [S II]$\lambda\lambda$6718, 6733 duplet is detected with enough signal-to-noise only in the blue and red filaments at the edges of the radio lobe (F1 and F2 in the right panel of Fig. 6.9). Therefore, I select two regions of the size of the PSF (~1.0 ″) over the filaments to compute the electron density. Thus the electron density within the cavity is < 350 e$^-$ cm^{-3}. Furthermore, the ionization state of the gas in filaments F1 and F2 is consistent with the AGN/LINER region of the BPT diagram.

The main possible explanations for detecting Hα + [N II]λ6584 emission spatially associated with an X-ray cavity instead of with its rim include:

1. The ionized gas is actually concentrated in filaments that wrap around the X-ray cavity, such as the ones shown in Fig. 6.11. However, due to projection effects, as well as to the presence of an additional redward component in the cavity region (see right panel of Fig. 6.6 and Fig. 6.7), the ionized gas appears to be co-spatial with the X-ray cavity. I tend to disfavor this scenario since it implies that I would be seeing the gas where it has the lowest column density along the line of sight, instead of at the edges, where its column density would be the highest.

2. The ionized gas is actually filling the X-ray cavity. In that case, there could be two possible explanations: (i) the gas has undergone multiple ionization events due to different AGN outbursts, or (ii) the ionized gas is forming filaments originating from the cooling of warm AGN outflows. Scenario (i) is compatible with an AGN outburst occurring after the one responsible for the X-ray cavity, since typical cycling times between quiescence and activity in radio galaxies are ~10^7-10^8 yr (see Shabala et al. 2008 and references therein) and the estimated age of the X-ray cavity is 12 Myr (Ricci et al. 2018). On the other hand, scenario (ii) is compatible with simulations by Qiu et al. (2020), which show that ionized gas present in the central 2 kpc of galaxy clusters (due to radiative feedback) could be lifted by AGN outflows, originating filaments. Additional simulations in Qiu et al. (2021) showed that these filaments could be shaped as rings perpendicular to the direction of the outflow, which would explain the arched feature (A in Fig. 6.11), that appears to connect filaments F1 and F2 (surrounding the southwestern radio lobe in Fig. 6.9, right panel) and that seems to trace the inner edge of the X-ray cavity.

To distinguish between these scenarios, I need longer *Chandra* observations to characterize, in more detail, the temperature and density profiles of the central ICM emission. To characterize the ionized gas, I would need deeper MUSE observations, and higher spatial resolution observations (either with the adaptive optics MUSE narrow-field mode, with the VLT Enhanced Resolution Imager and Spectrograph, or with the James Webb Space Telescope) would allow me to better understand the origin of the additional redward component found the spectra.

[2] $c_s = \sqrt{\frac{kT}{\mu m_p}} \simeq 1100 \left(\frac{kT}{5\ \mathrm{keV}}\right)^{1/2}$ km s^{-1}

Bibliography

Allen, M. G., Groves, B. A.,Dopita, M. A., et al. 2008, ApJS, 178, 20

Bacon, R., Accardo, M., Adjali, L., et al. 2010, in Society of Photo-Optical Instrumentation Engineers (SPIE) Conference Series, Vol. 7735, Proc. SPIE, 773508

Baldi, R. D., Rodríguez Zaurín, J., Chiaberge, M., et al. 2019, ApJ, 870, 53

Baldwin, J. A., Phillips, M. M. & Terlevich, R. 1981, PASP, 93, 5

Balmaverde, B., Capetti, A., Grandi, P., et al. 2012, A&A, 545, A143

Balmaverde, B., Capetti, A., Marconi, A., et al. 2018, A&A, 612, A19

Balmaverde, B., Capetti, A., Marconi, A., et al. 2019, A&A, 632, A124

Balmaverde, B., Capetti, A., Marconi, A., et al. 2021, A&A, 645, A12

Baum, S. A., Heckman, T. M., Bridle, A., et al. 1988, ApJS, 68, 643

Bîrzan, L. and Rafferty, D. A. and Brüggen, M., et al. 2020, MNRAS, 496, 2613

Buttiglione, S., Capetti, A., Celotti, A., et al. 2010, A&A, 509, A6

Capetti, A., Robinson, A., Baldi, R. D., et al. 2013, A&A, 551, A55

Capetti, A. & Baldi, R. D. 2011, A&A, 529, A126

Capetti, A., Brienza, M., Baldi, R. D., et al. 2020, A&A, 642, A107

Cappellari, M. 2017, MNRAS, 466, 798

Cardelli, J. A., Clayton, G. C. & Mathis, J. S. 1989, ApJ, 345, 245

Conselice, C. J., Gallagher, J. S., III & Wyse, R. F. G. 2001, AJ, 122, 2281

de Koff, S., Baum, S. A., Sparks, W. B., et al. 1996, ApJS, 107, 621

Dopita, M. A. & Sutherland, R. S. 1995, ApJ, 455, 468

Edwards, L. O. V., Robert, C., Mollá, M., et al. 2009, MNRAS, 396, 1953

Fabian, A. C., Johnstone, R. M., Sanders, J. S., et al. 2008, Nature, 454, 968

Fabian, A. C., Sanders, J. S., Williams, R. J. R., et al. 2011, MNRAS, 417, 172

Fanaroff, B. L. & Riley, J. M. 1974, MNRAS, 167, 31P

Gaspari, M., Ruszkowski, M. &Sharma, P. 2012, ApJ, 746, 94

Gaspari, M., Ruszkowski, M. & Oh, S. Peng 2013, MNRAS, 432, 3401

Gaspari, M., Brighenti, F. & Temi, P. 2015, A&A, 579, A62

Gaspari, M., Temi, P. & Brighenti, F. 2017, MNRAS, 466, 677

Gaspari, M., McDonald, M., Hamer, S. L., et al. 2018, ApJ, 854, 167

Giacintucci, S., Venturi, T., Murgia, M., et al. 2007, A&A, 476, 99

Gopal-Krishna & Wiita, P. J. 2000, A&A, 363, 507

Kauffmann, G., Heckman, T. M., Tremonti, C., et al. 2003, MNRAS, 346, 1055

Kewley, L. J., Heisler, C. A., Dopita, M. A, et al. 2001, ApJS, 132, 37

Kewley, L. J., Groves, B., Kauffmann, G., et al. 2006, MNRAS, 372, 961

Kocevski, D. D., Ebeling, H., Mullis, C. R., et al. 2007, ApJ, 662, 224

Jimenez-Gallardo, A., Massaro, F., Paggi, A., et al. 2021, ApJS, 252, 31

Lynds, R. 1970, ApJL, 159, L151

Madrid, J. P., Chiaberge, M., Floyd, D., et al. 2006, ApJS, 164, 307

Markevitch, M. & Vikhlinin, A. 2007, , 443, 1

Massaro, F., Tramacere, A., Cavaliere, A., et al. 2008a, A&A, 478, 395

Massaro, F., Giommi, P., Tosti, G., et al. 2008b, A&A, 489, 1047

Massaro, F., Harris, D. E. & Cheung, C. C. 2011, ApJS, 197, 24

Massaro, F., Tremblay, G. R., Harris, D. E., et al. 2012, ApJS, 203, 31

Massaro, F., Harris, D. E., Tremblay, G. R., et al. 2013, ApJS, 206, 7

Massaro, F., Harris, D. E., Liuzzo, E., et al. 2015, ApJS, 220, 5

Massaro, F., Missaglia, V., Stuardi, C., et al. 2018, ApJS, 234, 7

Massaro, F., Álvarez-Crespo, N., Capetti, A., et al. 2019, ApJS, 240, 20

Massaro, F., Capetti, A., Paggi, A., et al. 2020, ApJS, 247, 71

Massaro, F., Capetti, A., Paggi, A., et al. 2020, ApJL, 900, L34

Mazzotta, P., Kaastra, J. S., Paerels, F. B., et al. 2002, ApJL, 567, L37

Mazzotta, P., Brunetti, G., Giacintucci, S., et al. 2004, Journal of Korean Astronomical Society, 37, 381

McDonald M., Veilleux, S., Rupke, D. S. N., et al. 2010, ApJ, 721, 1262

McDonald M., Veilleux, S. & Rupke, D. S. N. 2012, ApJ, 746, 153

McNamara, B. R. & Nulsen, P. E. J. 2007, ARA&A, 45, 117

Morgan, W. W., Kayser, S. & White, R. A. 1975, ApJ, 199, 545

Osterbrock, D. E. 1989, Astrophysics of gaseous nebulae and active galactic nuclei (Mill Valley, CA: University Science Books)

Pasini, T., Gitti, M., Brighenti, F., et al. 2021, ApJ, 911, 66

Peres, C. B., Fabian, A. C., Edge, A. C., et al. 1998, MNRAS, 298, 416

Qiu, Y., Bogdanović, T., Li, Y., et al. 2019, ApJL, 872, L11

Qiu, Y., Bogdanović, T., Li, Y., et al. 2020, Nature Astronomy, 4, 900

Qiu, Y., Hu, H., Inayoshi, K., et al. 2021, ApJL, 917, L7

Ricci, F., Lovisari, L., Kraft, R. P., et al. 2018, ApJ, 867, 35

Sabater, J., Best, P. N. & Argudo-Fernández, M. 2013, MNRAS, 430, 638

Sanders, J. S. & Fabian, A. C. 2007, MNRAS, 381, 1381

Sanders, Ryan L., Shapley, A. E., Kriek, M., et al. 2016, ApJL, 825, L23

Shabala, S. S., Ash, S., Alexander, P., et al. 2008, MNRAS, 388, 625

Speranza, G., Balmaverde, B., Capetti, A., et al. 2021, A&A, 653, A150

Stasińska, G., Vale Asari, N., Cid Fernandes, R., et al. 2008, MNRAS, 391, L29

Tremblay, G. R., Chiaberge, M., Sparks, W. B., et al. 2009, ApJS, 183, 278

Voit, G. M., Donahue, M. & Slavin, J. D. 2012, ApJS, 759, 86

Voit, G. M., Meece, G., Li, Y., et al. 2017, ApJ, 845, 80

Voit, G. M. 2021, ApJL, 908, L16

Worpel, H., Brown, M. J. I., Jones, D. H., et al. 2013, ApJ, 772, 64

Zirbel, E. L. 1996, ApJ, 473, 713

Chapter 7

A Chandra-MUSE insight into radio galaxies

In this chapter, I tackle the question of the origin of Extended Emission Line Regions (EELRs) in radio galaxies using VLT/MUSE and *Chandra* observations of radio sources in the 3CR catalog. This chapter is organized as follows. In § 7.1, I give an overview of the sample selection, followed by the description of the optical and X-ray analysis in § 7.2. Results of the analysis are reported in § 7.3. Lastly, § 7.4 is dedicated to a summary and discussion of the chapter. At the redshifts in the sample, $0.003 \leq z \leq 0.27$, the scale is 0.062 - 4.171 kpc/arcsec.

Although in the last decades, several optical campaigns revealed the presence of EELRs in radio galaxies, similar to those found in Seyfert galaxies (see e.g., Fosbury 1986, van Breugel et al. 1986, Stockton & MacKenty 1987), extending on scales of a few tens of kpc and spatially associated with diffuse soft X-ray emission, there is still no consensus on the dominant ionizing mechanism underlying their emission. Nevertheless, the association of EELRs and diffuse soft X-ray emission suggests a link between the origin of X-ray and optical emission (see e.g., Massaro et al. 2009, Hardcastle et al. 2010, 2012, McDonald et al. 2010, 2012 and Balmaverde et al. 2012), with the most likely origin being nuclear photoionization (see e.g., Baum & Heckman 1989 and Balmaverde et al. 2012), as it is the case in Seyfert galaxies (see e.g., Bianchi et al. 2006), and ionization due to jet-driven shocks (see e.g., Hardcastle et al. 2010, 2012 and Reynaldi & Feinstein 2013).

Thus, aiming at solving the long-standing problem of the origin of the EELR, I carried out a systematic comparison of MUSE and *Chandra* data of 15 of the 3CR radio sources observed during the MURALES survey. This analysis includes the comparison of the optical and X-ray observations obtained as part of the MURALES survey and the 3CR *Chandra* Snapshot survey, respectively.

This sample of radio galaxies includes a variety of radio morphologies and optical classifications. Following the classification by Fanaroff & Riley (1974), it includes both radio galaxies with FR I (i.e., edge-darkened) and FR II radio morphologies (i.e., edge-brightened). Regarding their optical spectra (see Buttiglione et al. 2010), the sample includes HERGs, LERGs, BLRGs, and sources with uncertain optical classification. The inclusion of different optical classifications in the sample allowed me to study EELRs from two points of view:

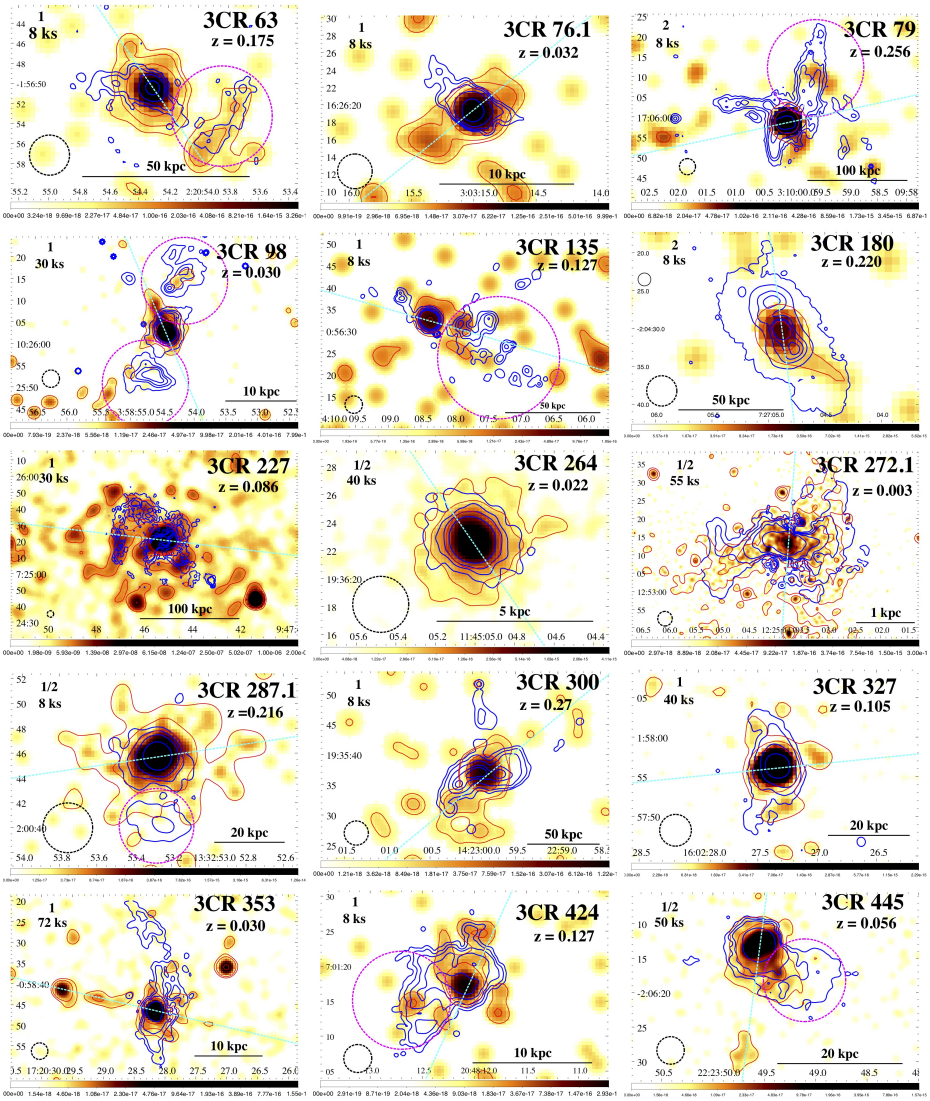

Figure 7.1: 0.5 – 3 keV X-ray emission with emission line contours overlaid, with binning factor and exposure times of the X-ray images in the upper left corner and a 2″ radius circle in the bottom left corner. Cyan dashed lines indicate the direction of the radio jets, while magenta dashed circles mark the regions used for the optical to X-ray flux comparison. Emission line used as well as the rest of image parameters are shown in Table 7.2.

1. Firstly, I can compare our results for HERGs and BLRGs with previous ones obtained by Balmaverde et al. (2012) through the comparison of *HST* and *Chandra* observations. Although Balmaverde et al. (2012) concluded that the dominant emission mechanism for EELRs in HERGs and BLRGs is nuclear photoionization, for 3CR 305 and 3CR 171, Hardcastle et al. (2010, 2012) claimed that their EELRs were most likely caused by radio-jet shocks heating of cold gas. Thus, new MUSE observations from the MURALES survey offer the opportunity to test these results by taking advantage of the unprecedented sensitivity provided by MUSE and by closely matching the optical resolution using *Chandra* sub-pixel analysis.

2. Then, I can compare results obtained for LERGs with those of HERGs and BLRGs.

This second goal is crucial since, while analyses of EELRs were previously restricted to HERGs, a different origin of EELRs of LERGs and HERGs would provide additional clues into the HERG/LERG classification scheme.

7.1 Sample selection

I initially selected all 33 radio galaxies from the MURALES survey since all of them have observations already available in the *Chandra* archive thanks to the 3CR *Chandra* Snapshot Survey. I then excluded (i) 10 sources with unresolved optical or X-ray diffuse emission (i.e., within a circle of 2″ radius in which the ∼90% of the on-axis *Chandra* PSF is enclosed), and (ii) 8 sources belonging to a galaxy cluster for which the thermal ICM dominates the X-ray emission.

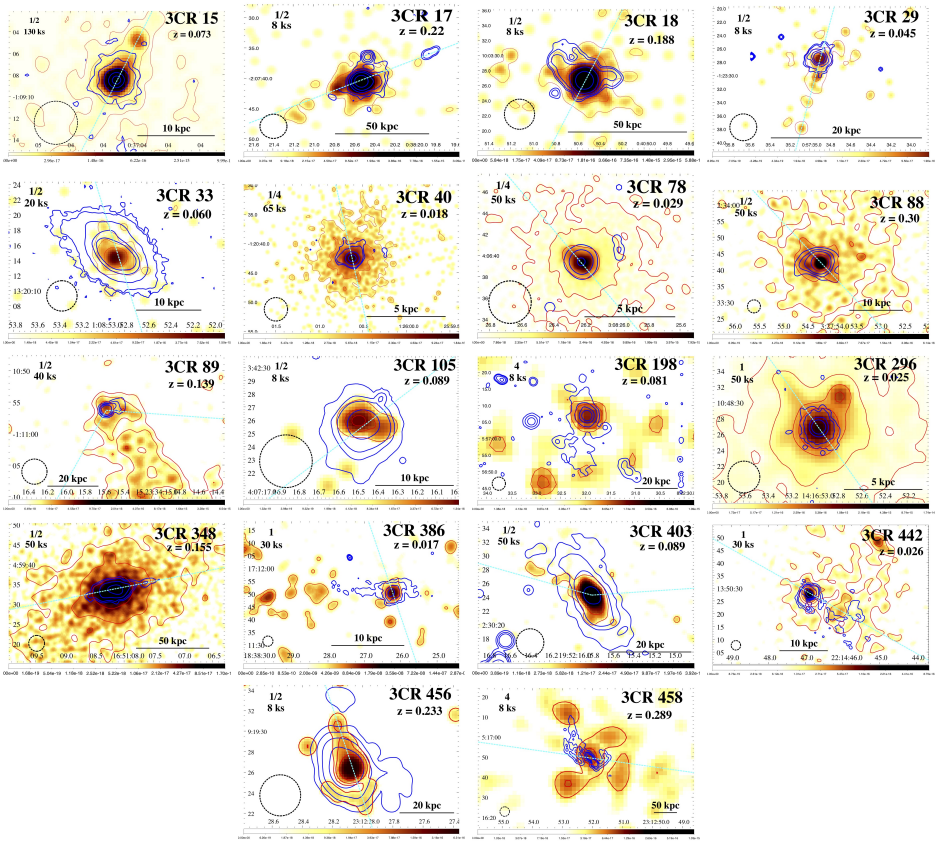

Figure 7.2: 0.5 – 3 keV X-ray emission with emission line contours overlaid, with binning factor and exposure times of the X-ray images in the upper left corner and a 2″ radius circle in the bottom left corner. Cyan dashed lines indicate the direction of the radio jets. Emission line used as well as the rest of image parameters are shown in Table 7.2.

Additionally, I excluded six sources from the original sample (i.e., not included in the original 33 sources), namely: 3CR 258, since its optical identification is unsure and it does not present strong emission lines in the wavelength range covered by MUSE (see Balmaverde et al. 2021); 3CR 273, due to the presence of a strong readout streak in the *Chandra* images; and 3CR 318.1, 3CR 196.1, 3CR 403.1, and 3CR 459, for which deeper

Table 7.1: Image parameters for X-ray and optical emission.

3CR Name	Optical emission line. (Å)	Seeing (arcsec)	Optical contour levels	X-ray pixel size (arcsec)	Smoothing Gaussian kernel (arcsec)	X-ray contour levels (photons)	X-ray exposure time (ks)	Radio freq. (GHz)	Beam size (arcsec)
15	[N II]λ6584 + Hα	0.65	3, 10, 50, 200, 500	0.25	1.48	0.2, 0.6, 2.0	130	8.4	0.34
17	[N II]λ6584 + Hα	0.49	3, 5, 10, 20, 100	0.49	1.48	0.1, 0.3, 1.0	8	4.8	0.42
18	[N II]λ6584	0.53	3, 5, 10, 20, 100	0.25	1.48	0.1	8	1.4	1.70
29	[N II]λ6584	0.51	10, 20, 50, 100, 200	0.49	1.48	0.07, 0.1, 0.3	8	4.8	5.09
33	[O III]λ5007	0.63	5, 10, 100, 500, 1000	0.25	1.48	0.1, 0.5, 1.0	20	4.8	1.35
40	[N II]λ6584 + Hα	0.40	3, 10, 100, 500	0.25	1.97	0.1, 0.3, 1.0	65	1.4	4.66
63	Hα	0.49	3, 10, 20, 100	0.49	1.48	0.1, 0.2, 1.0	8	1.4	1.36
76.1	[N II]λ6584	0.62	5, 10, 20, 50, 200	0.49	2.46	0.03, 0.07, 0.4	8	1.4	4.02
78	[N II]λ6584	0.53	3, 10, 50	0.12	0.98	0.1, 0.5, 1.0, 1.5	50	4.8	4.67
79	[O III]λ5007	0.66	5, 20, 50, 200, 1000	0.98	1.97	0.05, 0.2	8	1.4	1.50
88	[N II]λ6584	0.59	5, 20, 50, 200	0.25	1.97	0.1, 0.2, 0.5	50	4.8	4.42
89	[N II]λ6584	0.64	10, 50, 100, 200	0.25	1.97	0.1, 0.2	40	1.4	1.47
98	[O III]λ5007	0.66	10, 50, 100, 200	0.49	2.95	0.03, 0.06, 1.2	30	8.4	2.00
105	[O III]λ5007	0.71	5, 50, 100, 500	0.25	1.97	0.04, 0.1, 0.2	8	8.4	2.20
135	[O III]λ5007	0.52	5, 20, 50, 100	0.49	1.48	0.05, 0.1, 0.2	8	8.4	0.66
180	[O III]λ5007	1.45	5, 500, $2{\cdot}10^3$, $4{\cdot}10^3$, $6{\cdot}10^3$	2.95	1.48	0.05, 0.1	8	8.4	0.26
198	Hα	0.78	3, 10, 50, 200	1.97	1.48	0.06, 0.12, 0.2	8	4.8	25.88
227	Hα	0.91	5, 50, 100, 500	0.49	4.43	0.02, 0.06, 0.18	30	1.4	2.04
264	[N II]λ6584	0.85	5, 50, 100, 500	0.12	1.48	0.05, 0.5, 1.5	40	4.8	1.31
272.1	[N II]λ6584	5.40	10, 50, 100, 200, 500	0.25	1.48	0.1, 0.2, 0.5, 1.0	55	4.8	4.35
287.1	Hα	0.65	5, 20, 50, 200	0.25	1.48	0.07, 0.2, 1.0	8	4.8	4.55
296	[N II]λ6584	1.08	5, 50, 200, 500	0.12	1.97	0.1, 0.5, 1.5	50	8.4	0.75
300	[O III]λ5007	0.41	5, 20, 100, 500, 1000	0.49	2.46	0.03, 0.1	8	8.4	2.10
327	[N II]λ6584	0.70	5, 50, 200, 1000	0.49	1.48	0.1, 0.5, 2.5	40	8.4	2.20
348	Hα	1.76	5, 20, 100, 500	0.12	1.97	0.1, 0.25, 0.5	50	1.4	1.93
353	Hα	1.30	5, 20, 50, 200	0.49	1.97	0.1, 0.2, 0.5	72	8.4	0.44
386	[N II]λ6584	0.61	5, 20, 50, 200	0.49	2.46	0.04, 0.08, 0.16	30	1.4	4.06
403	[N II]λ6584	0.54	5, 20, 50, 500	0.25	1.97	0.07, 0.2, 0.5	50	4.8	1.37
424	[N II]λ6584	0.98	10, 50, 100, 200, 500	0.49	1.97	0.04, 0.07, 0.2	8	4.8	0.25
442	[N II]λ6584	0.61	5, 100, 200, 500, 2000	0.25	1.97	0.1, 0.2, 0.4	30	1.4	4.50
445	[N II]λ6584	1.48	5, 20, 50, 500	0.25	0.98	0.08,0.32,0.64	50	1.4	4.90
456	[N II]λ6584	1.27	5, 50, 200, 1000	0.12	1.97	0.02, 0.1, 0.5	8	4.8	0.54
458	[O III]λ5007	0.50	5, 50, 100, 200	1.97	1.48	0.1, 0.15, 0.2	8	4.8	2.33

Table 7.2: Column description: (1) Source name; (2) optical emission line used; (3) seeing of the optical observation; (4) optical contour levels shown as times the rms; (5) pixel size of the X-ray image; (6) size of the Gaussian Kernel used for smoothing the X-ray image; (7) X-ray contour levels; (8) X-ray exposure time; (9) frequency of radio maps used for the astrometry registration; (10) radio map beam size.

investigations have been already published or are in preparation (see Jimenez-Gallardo et al. 2021, 2022, Balmaverde et al. 2018 and Missaglia et al. 2022).

The final sample, shown in Fig. 7.1, includes 15 radio galaxies at $z < 0.3$, 7 HERGs, 3 BLRGs, 4 LERGs, and 1 with uncertain optical classification. From a radio morphology point of view, the sample includes 4 FR I and 11 FR II radio galaxies. Sources not included in the sample are shown in Fig. 7.2.

7.2 Optical and X-ray photometric analysis

I carried out the astrometric registration to align radio, optical and X-ray images following the same procedure described in Chapter 3. However, for 3CR 76.1, for which the radio centroid showed an offset of more than 1″ with respect to the Pan-STARRS[1] image, I aligned *Chandra* and MUSE images to the Pan-STARRS image. Shifts between X-ray and radio images are consistent with those previously reported for the 3CR *Chandra* Snapshot Survey (Massaro et al. 2011, 2013, 2015, 2018, Stuardi et al. 2018, Jimenez-Gallardo et al. 2020, and Missaglia et al. 2021).

Since *Chandra* ACIS data are undersampled, producing images of a point source with $FWHM$ ~0.7″ while having native detector pixel size of 0.492″, I recovered *Chandra* resolution by rebinning images by factors of 1/2 or 1/4, depending on the angular size of

[1] https://catalogs.mast.stsci.edu/panstarrs/

the EELR. This allowed me to match the optical (MUSE) and X-ray (*Chandra*) resolution to a degree not reached by previous studies (e.g. comparisons of *HST* and *Chandra* observations by Balmaverde et al. 2012).

7.2.1 X-ray and optical photometry

X-ray and optical fluxes of the extended regions were measured using a circle containing all X-ray and [O III]λ5007 extended emission and excluding a circular region of 2″ radius centered in the nucleus, since ∼ 90% of the on-axis *Chandra* PSF is enclosed in a circular region of 2″ radius. Similarly, I compared [O III]λ5007 and X-ray fluxes in circular regions selected based on the [O III]λ5007 for sources with extended optical features well distinguished from the nuclear emission. These additional regions are shown in magenta in Fig. 7.1. Background regions to measure X-ray fluxes were chosen as circular areas larger than regions selected for EELRs and located on the same CCD chip, far enough from the radio galaxy (i.e., at least a few tens of arcsec) to avoid the smearing of the PSF on CCD borders and contamination from the source. Background fluxes measured were then rescaled to EELRs region sizes.

7.3 EELRs in radio galaxies with different optical classifications

As shown in Fig. 7.1, most sources show a close morphological association between 0.5 - 3 keV and [O III]λ5007 emission, showing only significant differences in sizes and orientation in those sources for which the X-ray emission is due to radio counterparts, namely, 3CR 76.1 and 3CR 353.

To quantitatively compare the extended soft X-ray emission and the EELR, I calculated the [O III]λ5007 to 0.5 - 3 keV flux ratios of (i) all the extended emission (excluding a 2″ radius circle centered around the X-ray nucleus) and (ii) the extended emission in selected regions based on the [O III]λ5007 morphology and shown in Fig. 7.1, for different optical classifications.

While I found the same trend for [O III]λ5007 to 0.5 - 3 keV flux ratios as Balmaverde et al. (2012) when restricting the analysis to HERGs (with a median of [O III]λ5007 to soft X-ray ratio of ∼5.3 and values mostly confined to $0.2 \lesssim F_{[\mathrm{O\ III}]}/F_{0.3\text{-}5\ \mathrm{keV}} \lesssim 10$, see left panel of Fig. 7.3); for LERGs and BLRGs, the median of [O III]λ5007 to soft X-ray ratio is ∼0.19, with values mostly confined to $0.1 \lesssim F_{[\mathrm{O\ III}]}/F_{0.3\text{-}5\ \mathrm{keV}} \lesssim 0.4$, as shown in the right panel of Fig. 7.3. These trends for HERGs, LERGs and BLRGs, shown in Fig. 7.3, are also observed when considering isolated regions selected based on the [O III]λ5007 morphology.

To further corroborate Balmaverde et al. (2012) results, I compared [O III]λ5007 and soft X-ray fluxes of HERGs including the nuclear region. I again found a trend between optical and X-ray fluxes, with a median of the ratios of ∼2.8 and with most values constrained within a factor of two from the median, as also seen in Balmaverde et al. (2012).

Using a 3″ radius exclusion circle instead of a 2″ one for BLRGs only produced significantly different results for 3CR 445, for which a ratio consistent with those of HERGs was obtained. In this case, I argue that a larger exclusion region might be beneficial since

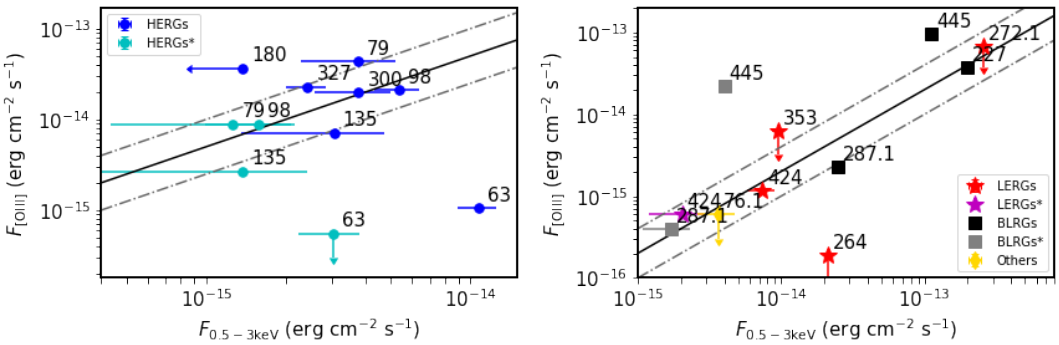

Figure 7.3: [O III]λ5007 flux versus 0.5 - 3 keV flux of the extended emission. Blue dots, red stars and black squares correspond to the total extended emission of HERGs, LERGs and BLRGs, respectively (excluding a 2″ region centered on the X-ray nucleus). Cyan dots, magenta stars and grey squares correspond to the emission in restricted regions (shown in Fig. 7.1). Yellow diamonds show the flux comparison for the total extended emission of one source with no clear optical classification. The solid lines correspond to constant ratios of $F_{[O\,III]}/F_{0.3\text{-}5\,keV} = 5$ (left) and $F_{[O\,III]}/F_{0.3\text{-}5\,keV} = 0.2$ (right); while the dotted lines correspond to $F_{[O\,III]}/F_{0.3\text{-}5\,keV} = 2.5$ and $F_{[O\,III]}/F_{0.3\text{-}5\,keV} = 10$ (left), and $F_{[O\,III]}/F_{0.3\text{-}5\,keV} = 0.1$ and $F_{[O\,III]}/F_{0.3\text{-}5\,keV} = 0.4$ (right).

3CR 455 is located at the edge of the CCD, at ~225″ (or ~246 kpc) from the aimpoint, which causes PSF smearing.

While I found generally lower values of $F_{[O\,III]}/F_{0.3\text{-}5\,keV}$ for LERGs, BLRGs, and sources with uncertain optical classification than for HERGs, all these sources, except for 3CR 76.1 and 3CR 445, show some degree of diffuse X-ray emission suggesting the presence of ICM in galaxy clusters. Additionally, these sources tend to have higher exposure times, with only 2 out of 7 HERGs having exposure times above 8 ks, while this fraction increases to 5 out of 8 for LERGs, BLRGs, and sources with uncertain optical classification. This also impacts uncertainties of the X-ray flux, with HERGs having uncertainties on average a factor 3 larger than other sources, as shown in Fig. 7.3.

7.4 Summary and discussion

I carried out a comparison of optical VLT/MUSE and X-ray *Chandra* observations of a sample of 15 radio sources observed during the MURALES survey, with resolved optical and X-ray diffuse emission, and for which thermal emission from ICM does not dominate the detected X-ray emission (excluding also 3CR 258, 3CR 272, 3CR 196.1, 3CR 318.1, 3CR 403.1, and 3CR 459). The final sample contains 7 FR II/HERGs, 1 FR II/LERG, 2 FR II/BLRGs, 3 FR I/LERGs, 1 FR I/BLRG, and 1 FR I with uncertain optical classification. The main goals of this comparison are the following:

1. To verify whether the close correspondence between soft X-ray and optical line morphology and emission claimed by Balmaverde et al. (2012) for HERGs and BLRGs using *Chandra* and *HST* observations is maintained when taking advantage of the unprecedented sensitivity provided by MUSE and being able to match much more closely the optical resolution using *Chandra* sub-pixel analysis.

Table 7.3: [O III]λ5007 and 0.5 - 3 keV luminosities for the selected sample

3CR Name	$L_{[O\ III],\ ext}$ (10^{40} erg s^{-1})	$L_{0.5\text{-}3\ keV,\ ext}$ (10^{40} erg s^{-1})	$F_{[O\ III]}/F_{0.5\text{-}3\ keV}$
63	9.1 ± 0.7	8.2 ± 3.7	0.098 ± 0.018
76.1	<0.1	0.9 ± 0.3	<0.16
79	881.1 ± 12.3	77.8 ± 30.3	11.54 ± 4.04
98	4.4 ± 0.1	1.1 ± 0.2	3.9± 0.8
135	30.3 ± 1.1	13.2 ± 7.3	2.3 ± 1.3
180	524.3 ± 10.9	<20.2	>26.3
227	70.4 ± 1.5	369.71 ± 16.02	0.19 ± 0.01
264	<0.02	2.34 ± 0.12	<0.01
272.1	<0.1	0.52 ± 0.01	<0.3
287.1	31.7 ± 1.2	349.89 ± 35.02	0.09 ± 0.01
300	458.2 ± 3.8	88.5 ± 27.9	5.3 ± 1.7
327	64.6 ± 3.2	6.9 ± 1.2	9.4 ± 1.6
353	<1.3	2.0 ± 0.2	<0.7
424	0.23 ± 0.01	1.4 ± 0.3	0.16 ± 0.04
445	72.3 ± 2.0	45.1 ± 1.9	0.86 ± 0.03

Column description: (1) source name; (2) [O III]λ5007 luminosity; (3) 0.5 - 3 keV X-ray luminosity; and (4) ratio of [O III]λ5007 to X-ray fluxes.

2. To investigate how this correspondence changes when considering LERGs, for which less luminous and smaller EELRs are expected if the difference between HERGs and LERGs is actually due to the accretion of cold or hot gas (see e.g., Baum et al. 1995, Hardcastle et al. 2007 and Buttiglione et al. 2010).

Similarly as Balmaverde et al. (2012), I found a close correspondence of X-ray and emission line morphologies of nearly all sources in the sample, the only exceptions being 3CR 76.1 and 3CR 353, for which the X-ray emission is aligned with the radio emission and, thus, it is most likely due to radio jets counterparts instead of being associated with the EELRs.

I compared the X-ray and [O III]λ5007 fluxes for the entire X-ray and [O III]λ5007 emission as well as for restricted regions, chosen based on the [O III]λ5007 morphology. I found the same trend as Balmaverde et al. (2012) for HERGs, with a median value of $F_{[O\ III]}/F_{0.3\text{-}5\ keV}$ ~5.3 and mostly restricted between ~0.2 and 10, also similar to ratios obtained for Seyfert galaxies, for which the origin of the soft X-ray emission is believed to be photoionization. Thus, newly obtained MUSE data support the conclusion previously achieved by Balmaverde et al. (2012) that the dominant emission process underlying EELRs in HERGs is nuclear photoionization.

On the other hand, while I did find a trend for the comparison of X-ray and [O III]λ5007 fluxes of LERGs and BLRGs, these sources present lower values of $F_{[O\ III]}/F_{0.3\text{-}5\ keV}$, with a median of ~0.19 and values mostly restricted between ~0.1 and 0.4. Thus, although showing smaller ratios of [O III]λ5007 to soft X-rays that could indicate a higher ionization state of the gas, the fact that a trend is still found points to a joint origin of the optical emission lines and diffuse X-ray emission. One possibility to explain these lower optical-to-X-ray ratios could be a significant contribution of jet-driven shocks to gas ionization. Nevertheless, these results should be taken with caution for the following reasons:

1. For all but one LERG in the sample, I could only obtain upper limits for the [O

III]λ5007. Therefore, deeper MUSE observations are needed to confidently characterize the EELR in LERGs.

2. Thermal X-ray ICM emission can be detected in most LERGs and BLRGs in the sample (except for 3CR 445). Thermal ICM X-ray emission could explain why LERGs and BLRGs in the sample do not follow the same trend as HERGs since the X-ray contribution of the ICM would yield higher X-ray fluxes than the one due only to the X-ray emission associated with the EELR. Nevertheless, in that case, it would not be expected to find a trend between optical and X-ray emission. Additionally, similar ratios are found when considering an ICM containing region as X-ray background, thus, subtracting the ICM component from the X-ray emission associated with the EELR. Therefore, if optical and X-ray emission have a common origin as the trend found suggests, the origin of the ionized gas could be the cooling of X-ray emitting plasma, as it is the case for some ionized gas filaments with X-ray counterparts observed in the brightest cluster galaxies of cool core clusters (see e.g., simulations by Qiu et al. 2020, 2021, and works such as Gaspari et al. 2012, 2013, 2015, 2017 and Voit et al. 2017).

Therefore, a larger sample of LERGs and BLRGs is needed to confirm whether the origin and emission mechanisms of their EELRs are, indeed, different than that of HERGs.

Lastly, it is important to highlight that although Balmaverde et al. 2012 claimed that BLRGs had [O III]λ5007 to soft X-ray ratios similar to those of HERGs, their optical and X-ray flux comparison only included one BLRG, 3CR 445, which is affected by PSF smearing, which could explain why the ratios I found for BLRGs are compatible with those of LERGs instead.

Therefore, although I can conclude that [O III]λ5007 to soft X-ray ratios for HERGs are compatible with the EELRs being caused by nuclear photoionization, further optical observations of additional LERGs and BLRGs are needed to establish the origin of their EELRs. This could also provide key pieces of evidence in the puzzle of the differences between HERGs and LERGs.

Bibliography

Balmaverde, B., Capetti, A., Grandi, P., et al. 2012, A&A, 545, A143

Balmaverde, B., Capetti, A., Marconi, A., et al. 2018, A&A, 612, A19

Balmaverde, B., Capetti, A., Marconi, A., et al. 2021, A&A, 645, A12

Baum, S. A., Zirbel, E. L. & O'Dea, C. P. 1995, ApJ, 451, 88

Bianchi, S., Guainazzi, M. & Chiaberge, M. 2006, A&A, 448, 499

Buttiglione, S., Capetti, A., Celotti, A., et al. 2010, A&A, 509, A6

Fanaroff, B. L. & Riley, J. M. 1974, MNRAS, 167, 31P

Fosbury, R. A. E. 1986, in Astrophysics and Space Science Library, Vol. 121, Large scale ionized gas in radio galaxies and quasars, ed. Giuricin, G., Mezzetti, M., Ramella, M. & Mardirossian, F., 297

Gaspari, M., Ruszkowski, M. &Sharma, P. 2012, ApJ, 746, 94

Gaspari, M., Ruszkowski, M. & Oh, S. Peng 2013, MNRAS, 432, 3401

Gaspari, M., Brighenti, F. & Temi, P. 2015, A&A, 579, A62

Gaspari, M., Temi, P. & Brighenti, F. 2017, MNRAS, 466, 677

Hardcastle, M. J., Evans, D. A. & Croston, J. H. 2007, MNRAS, 376, 1849

Hardcastle, M. J., Massaro, F. & Harris, D. E., 2010, MNRAS, 401, 2697

Hardcastle, M. J., Massaro, F. & Harris, D. E., 2012, MNRAS, 424, 1774

Jimenez-Gallardo, A., Massaro, F., Balmaverde, B., et al. 2021, ApJL, 912, L25

Jimenez-Gallardo, A., Sani, E., Ricci, F., et al. 2022, ApJ, submitted

Massaro, F., Chiaberge, M., Grandi, P., et al. 2009, ApJL, 692, L123

Massaro, F., Harris, D. E. & Cheung, C. C. 2011, ApJS, 197, 24

Massaro, F., Harris, D. E., Tremblay, G. R., et al. 2013, ApJS, 206, 7

Massaro, F., Harris, D. E., Liuzzo, E., et al. 2015, ApJS, 220, 5

Massaro, F., Missaglia, V., Stuardi, C., et al. 2018, ApJS, 234, 7

McDonald M., Veilleux, S., Rupke, D. S. N., et al. 2010, ApJ, 721, 1262

McDonald M., Veilleux, S. & Rupke, D. S. N. 2012, ApJ, 746, 153

Missaglia, V., Massaro, F., Liuzzo, E., et al. 2021, ApJS, 255, 18

Missaglia, V., Murgia, M., Massaro, F., et al. 2022, ApJ, submitted

Qiu, Y., Bogdanović, T., Li, Y., et al. 2020, Nature Astronomy, 4, 900

Qiu, Y., Hu, H., Inayoshi, K., et al. 2021, ApJL, 917, L7

Reynaldi, V. & Feinstein, C. 2013, MNRAS435, 1350

Spinrad, H., Djorgovski, S., Marr, J. & Aguilar, L. 1985, PASP, 97, 932

Stockton, A. & MacKenty, J. W. 1987, ApJ, 316, 584

Stuardi, C., Missaglia, V., Massaro, F., et al. 2018, ApJS, 235, 32

van Breugel, W. J. M., Fillippenko, A. V., McCarthy, P. J., et al. 1986, in Bulletin of the American Astronomical Society, Vol. 18, Spectroscopically Identical, High-Excitation Emission-Line Regions Associated with a Jet in the Radio Galaxy 3C 321, 1005

Voit, G. M., Meece, G., Li, Y., et al. 2017, ApJ, 845, 80

Chapter 8

Summary & Conclusions

In this thesis, I presented an overview of the multiphase gas in radio galaxies and the clues on feedback processes revealed by different gas phases, by comparing radio and X-ray emission at larger scales, and optical and X-ray emission at smaller scales.

Firstly, in Chapter 4, I focused on the completion of the 3CR *Chandra* Snapshot Survey, a survey dedicated to completing the X-ray coverage of the 3CR catalog which inspired numerous follow-up works such as the ones described in this thesis. In particular, I carried out the X-ray analysis of the highest redshift fraction of the 3CR catalog with $1.5 < z < 2.5$.

Chapter 5 was devoted to the study of the origin of extended soft X-ray emission detected surrounding FR II radio galaxies of the 3CR catalog while carrying out the 3CR *Chandra* Snapshot Survey. I distinguished two possible dominant emission mechanisms responsible for the extended X-ray emission: thermal ICM emission and non-thermal emission due to IC/CMB emission arising from radio lobes. Additionally, I tackled the issue of hotspot detection in sources with extended X-ray emission.

Then, in Chapter 6, I studied the origin of the multiphase gas in radio galaxies members of cool core galaxy clusters and showing signatures of radio feedback, such as cold filaments and X-ray cavities. Firstly, I present the multiwavelength analysis of the ionized gas filaments associated with cold X-ray filaments in 3CR 318.1, followed by the analysis of the ionized gas spatially associated with an X-ray cavity in 3CR 196.1. While, X-ray and ionized gas filaments are considered a common occurrence in radio galaxies in cool core clusters, even though their origin is still disputed, 3CR 196.1 could represent one of the first examples of ionized gas filling an X-ray cavity instead of spatially associated with its edges.

Finally, Chapter 7 was devoted to the study of the origin of EELRs in radio galaxies, using VLT/MUSE and *Chandra* observations of a selected sample of 15 3CR radio galaxies. This chapter explores the possibility of a common origin for the ionized gas and the X-ray emission associated with the EELR, studying the differences between different optical radio galaxy classifications and taking advantage of the unprecedented sensitivity of MUSE data and the sub-pixel analysis of *Chandra* observations which allowed me to match much more closely MUSE observations' resolution than previous analysis.

8.1 *Chandra* observations of high redshift 3CR radio sources

I analyzed Cycle 20 *Chandra* observations of the last nine identified (i.e., with optical counterparts) sources in the 3CR *Chandra* Snapshot Survey, namely 3CR 239, 3CR 249, 3CR 257, 3CR 280.1, 3CR 322, 3CR 326.1, 3CR 418, 3CR 454, and 3CR 454.1. This sample covers the highest redshift regime of the 3CR *Chandra* Snapshot Survey, with $1.5 < z < 2.5$.

Following the same analysis procedures as in previous 3CR *Chandra* Snapshot survey works, I detected X-ray nuclei in all sources in the sample except for 3CR 326.1 and 3CR 454.1, as well as X-ray counterparts of radio lobes in 6 out of the 9 sources in our sample, namely 3CR 239, 3CR 249, 3CR 257, 3CR 280.1, 3CR 322, and 3CR 326.1. In sources in which only one lobe X-ray counterpart was detected, the lobe detected was the brightest in the radio.

This work marks the completion of the identified fraction of the 3CR *Chandra* Snapshot Survey, whose observations made possible this thesis. Through the observing of 122 3CR radio sources with no previous archival *Chandra* observations, X-ray counterparts of 119 radio cores and of 11 radio lobes were detected. Additionally, thanks to this survey, the number of X-ray counterparts of radio jet knots was increased by ∼10 % and the number of sources with detected X-ray counterparts of hotspots was doubled. Lastly, thermal ICM emission was detected in 19 sources.

Results achieved so far, as well as the numerous follow-up observations made possible by the 3CR *Chandra* Snapshot Survey, illustrate perfectly the great value of this survey, whose completion made all chapters in this thesis possible.

8.2 Extended X-ray emission surrounding 3CR radio galaxies

I studied the extended soft X-ray emission with no GHz-counterpart seen surrounding FR II radio galaxies in the 3CR *Chandra* Snapshot Survey. The two main objectives of this analysis included:

1. Investigating the origin of this extended X-ray emission to elucidate whether the dominant emission process responsible for it is either non-thermal emission due to IC/CMB from lobes, thermal emission from ICM, or a combination of both.

2. Highlighting the nuances of hotspot detection against this extended X-ray emission.

This work was carried out by analyzing 0.5 - 3 keV, background and point source subtracted, exposure-weighted observations of 35 FR II radio galaxies with angular sizes above 5″ (measured in GHz radio maps) from the 3CR *Chandra* Snapshot Survey.

Regarding the first issue, I found that ∼90% of 3CR FR II radio galaxies are embedded in X-ray emission coincident with the radio galaxies, while ∼60% show extended X-ray emission perpendicular to the radio axis. Therefore, I concluded that IC/CMB is the most dominant emission process in ∼71% of sources in our sample, while thermal emission from the ICM dominates in ∼17% of them. In particular, IC/CMB was considered the dominant process whenever I found low-frequency, i.e., 150 MHz, radio emission tracing the extended X-ray emission since electrons responsible for IC/CMB emission from radio

lobes in the X-rays are also responsible for the synchrotron emission at tens of MHz. Nevertheless, I could not establish the emission mechanism responsible for the X-ray extended emission in ∼11% of the sample.

Additionally, while I found the same number of LERGs for which the dominant processes are IC/CMB from lobes and thermal ICM emission, in HERGs IC/CMB is the dominant process in six times more sources than thermal ICM emission. This suggests that FR II-LERGs tend to inhabit richer environments than FR II-HERGs.

Secondly, I confirmed the detection of 7 hotspots, whose detection had been previously claimed in the literature, excluding the possibility of them being fluctuations of the extended X-ray emission in which they are embedded. I was able to reject the detection of one of the hotspots previously identified in the literature and to claim the detection of new hotspots in two sources. This divergence from literature results illustrates the importance of taking into account the environment in which hotspots are embedded.

8.3 Signatures of radio feedback: cold X-ray filaments and X-ray cavities

I studied two manifestations of radio feedback in radio galaxies, the cold X-ray filaments spatially associated with ionized gas filaments in 3CR 318.1 and the ionized gas spatially associated with an X-ray cavity in 3CR 196.1. Thus, I carried out a joint radio, optical and X-ray analysis to better understand the origin and emission mechanisms underlying the multiphase gas in radio galaxies.

3CR 318.1:

Recent MUSE observations obtained during the MURALES survey revealed the presence of ionized gas filaments in 3CR 318.1, a LERG radio galaxy associated with the BCG of the cool core galaxy cluster MKW 3s.

From an optical point of view, intensity ratios of rest-frame emission lines provide conflicting results, with no unique ionization mechanism being able to reproduce the observed ratios. This seems a consistent occurrence in filaments in cool core galaxy clusters, which typically present lower values of [O III]/Hβ and higher values of [N II]/Hα, [O I]/Hα, and [S II]/Hα, than SDSS galaxies. This indicates that different emission mechanisms must be at play. I argue that, due to the similarities in line ratios between the filaments in 3CR 318.1 and other cool core galaxy clusters filaments, ionization mechanisms causing the optical emission in 3CR 318.1 filaments, must be the same as in other cool core galaxy clusters. Thus, filaments in 3CR 318.1 must be due to a combination of photoionization due to star formation, self-ionizing cooling ICM, and a contribution of ionization due to slow shocks, which, in the case of 3CR 318.1, must be small since ionized gas velocity dispersion along the filaments is $\sim$60 km s^{-1}.

Then, from a high-energy point of view, I detected an excess of X-ray emission above the ICM along the ionized gas filaments. Gas aligned with this X-ray filament is colder and appears to have lower metal abundance than the surrounding ICM, as previously seen in other ionized gas filaments in cool core clusters. Additionally, this filament is aligned with the direction of the radio jet, suggesting that the filament originated either from AGN-driven outflows or due to compression and catastrophic cooling. Nevertheless, the low velocity dispersion along the filaments implies that the most likely origin for 3CR 318.1 filaments is the AGN uplift scenario.

3CR 196.1:

The MURALES survey also unveiled the presence of ionized gas spatially associated with the X-ray cavity of 3CR 196.1, a LERG radio galaxy with a HYMOR radio morphology associated with the BCG of a cool core galaxy cluster. This is a rare occurrence, with ionized gas usually being associated with the edges of a cavity instead, thus, this work represents the first in-depth study of ionized gas potentially filling an X-ray cavity.

Through the analysis of the MUSE observations, I discovered the possible presence of a background ionized gas cloud due to the detection of additional Hα, [N II], and [S II] lines in the spectra of the central and cavity regions. The presence of these emission lines at $\sim$1000 km s^{s} to the red of the rest-frame components, together with the limited spatial ($\sim$1$''$) and spectral ($\sim$500 km s^{-1}) resolutions and the low signal to noise of the emission associated with the X-ray cavity, hindered the characterization of the ionized gas.

Velocity channel maps revealed the presence of blue ($\sim$-300 km s^{-1}) and red-shifted ($\sim$300 km s^{-1}) emission forming filaments, appearing to be wrapped around the southern radio lobe, as well as of an arched structure seemingly connecting the two filaments and tracing the inner edge of the X-ray cavity. Additionally, emission line ratios of these filaments indicate a LINER-like ionization state, often associated with large-scale outflows and shocks or with radio jet-shocked regions.

The main possible explanations for the detected ionized gas features spatially associated with an X-ray cavity instead of with its rim include:

1. The ionized gas is concentrated in filaments that wrap around the X-ray cavity instead of inside of it, however, projection effects make it appear to be co-spatial with the inside of the cavity. Although ionized gas filaments wrapping around an X-ray cavity are already present in the literature, I tend to disfavor this scenario since it will imply that the gas is seen where it has the lowest column density along the line of sight, instead of in the edges of the cavity, where its column density would be the highest.

2. The ionized gas is filling the X-ray cavity. In which case, other two scenarios can be distinguished:

   (a) The AGN could have undergone different outbursts and, therefore, the gas could have gone through multiple ionization events. This scenario is consistent with an AGN outburst occurring after the one responsible for the X-ray cavity since the age of the cavity ($\sim$12 Myr) is compatible with the typical cycling times in radio galaxies ($\sim$10 - 100 Myr).

   (b) The ionized gas forms filaments whose origin is the cooling of AGN outflows. This last scenario is compatible with simulations that show that ionized gas in the central region of cool core galaxy clusters can be uplifted by AGN outflows, forming ionized gas filaments that can be ring-shaped and perpendicular to the direction of the outflow (which would explain the arched feature seen connecting the two filaments and tracing the inner edge of the X-ray cavity).

Although the second two scenarios are preferred, I require longer *Chandra* and MUSE observations to characterize temperature and density profiles of the central ICM emission, as well as the ionized gas. Additionally, to be able to confirm the presence of ionized gas filling the X-ray cavity, despite the presence of a background ionized cloud in the cavity

region, I will need optical observations with higher spatial resolution. Nevertheless, if confirmed, the presence of ionized gas filling an X-ray cavity will be a new piece in the puzzle of feedback processes in radio galaxies.

8.4 The origin of EELRs in radio galaxies, a *Chandra*-MUSE comparison

The MURALES survey clearly revealed the presence of ionized gas in the form of EELRs extending up to ~100 kpc in the radio galaxies of the 3CR catalog with $z < 0.3$. Nevertheless, the origin of such gas is still disputed.

I tackled the problem of the ionization mechanisms and origin of EELRs in radio galaxies by carrying out a comparison of optical VLT/MUSE and X-ray *Chandra* observations of a sample of 15 radio sources observed during the MURALES survey, with resolved optical and X-ray diffuse emission, and for which thermal emission from ICM does not dominate the detected X-ray emission, and excluding sources with in-depth studies present in the literature.

Thus, with a sample of 15 radio sources containing 7 FR II/HERGs, 1 FR II/LERG, 2 FR II/BLRGs, 3 FR I/LERGs, 1 FR I/BLRG, and 1 FR I with uncertain optical classification, I aimed at:

1. Verifying whether the EELR in HERGs and BLRGs is due to nuclear ionization, as previously claimed by Balmaverde et al. (2012).

2. Investigating the origin of EELRs in LERGs, for which studies of their extended ionized gas are much rarer in the literature than for HERGs due to their EELRs being traditionally harder to detect than those of HERGs. Obtaining an overview of EELRs in LERGs could prove to be an additional clue to understanding the differences that drive the HERG/LERG classification.

I found a close correspondence of X-ray and emission line morphologies for nearly all sources in our sample, the only exceptions being 3CR 76.1 and 3CR 353, for which the X-ray emission is most likely originating from radio jet counterparts due to its alignment with the radio emission.

I found the same trend as Balmaverde et al. (2012) for HERGs when comparing X-ray and [O III]λ5007 fluxes, with similar values to the ratios obtained for Seyfert galaxies, for which the origin of the soft X-ray emission is believed to be nuclear photoionization. Thus, the dominant emission process underlying EELRs in HERGs is most likely nuclear photoionization.

While I did find a similarly strong trend for LERGs and BLRGs, these sources present lower $F_{[\mathrm{O\,III}]}/F_{0.3\text{-}5\,\mathrm{keV}}$ ratios, which could indicate a higher ionization state of the gas. However, the presence of a strong trend points out to a joint origin of the optical emission lines and diffuse X-ray emission, although different from that found for HERGs. These lower ratios could be due to a significant contribution of shocks to gas ionization, nevertheless, these results should be taken with caution for the following reasons:

1. Ratios obtained for most LERGs are only upper limits, thus, deeper MUSE observations are needed to confidently characterize the EELR in LERGs.

2. Thermal X-ray ICM emission can be detected in most LERGs and BLRGs in our sample (except for 3CR 445), which could be the explanation for obtaining the same level of X-ray emission as in HERGs. Nevertheless, in that case, I would expect the trend between optical and X-ray emission to disappear, since X-ray emission would have a different origin than optical emission. Additionally, results do not change significantly when taking into account the thermal ICM emission. Thus, if related to the ICM, the origin of the ionized gas could be the cooling of X-ray emitting plasma, as suggested for ionized gas filaments with X-ray counterparts seen in the brightest cluster galaxies of cool core clusters.

Therefore, while EELRs in HERGs seem to be dominated by nuclear photoionization, a larger sample of LERGs and BLRGs is needed to confirm whether the origin and emission mechanisms of their EELRs are, indeed, different than that of HERGs.

8.5 An overview of the puzzle

Regarding the open questions presented in § 1.5, I was able to conclude that:

1. The large-scale soft X-ray emission found surrounding FR II radio galaxies can be explained in most cases as being dominated by non-thermal processes. Additionally, low-frequency radio observations are crucial to unveil the origin of the extended X-ray emission and, thus, can be used together with short exposure X-ray observations to identify galaxy cluster candidates.

2. Jets strongly interact with their environments, not only via the creation of X-ray cavities, but also originating EELRs either via cooling of jet-driven outflows or via collisional ionization of jet-driven shock.

3. The origin of EELRs in radio galaxies appears to change according to their environment and classification. In particular, EELRs of radio galaxies inhabiting rich environments, whose X-ray diffuse emission is dominated by thermal processes, show signs of a strong contribution of ICM cooling. On the other hand, for those radio galaxies whose X-ray diffuse emission is not dominated by thermal processes, the origin of EELRs appears to be different in HERGs and LERGs, with EELRs in HERGs being dominated by nuclear photoionization and EELRs in LERGs, by collisional ionization.

Through the answers to these questions, I was able to conclude that, although a multi-frequency study of radio galaxies is essential, the extended X-ray emission in particular is a very powerful tool to study feedback processes in radio galaxies at small (< 100 kpc) and large (> 100 kpc) scales. In fact, such multi-frequency studies allowed me to highlight the very complex nature of ionized gas surrounding radio galaxies, with contributions of the AGN, star formation, and the ICM. Additionally, I was able to conclude that there appears to be a link between the origin of ionized gas in radio galaxies and different radio galaxy classifications and environments. Thus, I discovered that the origin of EELRs surrounding radio galaxies not only can shed clues on feedback mechanisms, but also on the HERG/LERG dichotomy.